

# CRAS 2020

---

Proceedings of the 10<sup>th</sup> Conference on  
New Technologies for Computer/Robot Assisted Surgery

September 28-30, 2020  
Barcelona, Spain



**Proceedings of the 10<sup>th</sup> Conference on  
New Technologies for Computer/Robot Assisted Surgery**

Proceedings of the 10<sup>th</sup> Conference on New Technologies for Computer/Robot Assisted Surgery,  
Barcelona, Spain, September 28 – 30, 2020

This work is subjected to copyright. It is published as an open-access publication under the “Creative Commons Attribution 4.0 International” license.

[www.cras-eu.org](http://www.cras-eu.org)





## **CRAS 2020**

### **Joining Efforts – Progressing Faster**

Robotic surgery is one of the most appealing fields of modern robotics. With over 3 decades of history, more than 3.800 systems installed worldwide and over 600.000 robot-assisted interventions conducted per year, the field of robotic surgery is well established. Despite these impressive figures and increasing popularity in research labs all over the world, the list of technological advances that made it into the operating room (OR) during this last decade remains limited. Long-awaited techniques such as augmented reality, 3D reconstruction, motion compensation, virtual guidance, haptic feedback, etc., are still under study in many labs all over the planet, progressing towards the market. CRAS strives to overcome this status-quo by strengthening the collaboration between the different research groups to boost the efficacy and shorten development cycles.

CRAS 2020 is the 10th edition of this successful event. Formerly labeled as a workshop, from this 10<sup>th</sup> edition onwards CRAS has graduated and will continue to move forward as a “conference”. The 10<sup>th</sup> edition was planned to be held at IBEC / UPC in Barcelona, Spain. However, due to the worldwide COVID-19 pandemic, the organizers were forced to convert it to an online event.

## Highlights

Surgical robotics is a key factor for the introduction of new surgical procedures not feasible otherwise, as well as for improving current procedures by providing new assistive tools that allow achieving higher precision and improved surgical performances. Robotics breaks into the Operating Room in an effective way in the XXI century and its progress, although still slow, has already reached a figure of 10.000 operation robots in hospitals worldwide. This year's edition, coinciding with the CRAS 10<sup>th</sup> anniversary, will evidence an explosion of new surgical robots and other devices in different specialties, which, until now, were produced by very few manufacturers. This market expansion will break with the otherwise slow progress and will favor reaching a wider range of clinical centers.

In this 10<sup>th</sup> edition, communications included advances in the following fields: novel medical devices and robotic systems, surgical robot control, novel sensing technologies, vision-based modeling and control, development and validation of surgical training systems, and artificial intelligence for planning, guidance and autonomous operations.

## CRAS 2020 Conference Chairs

### **Alicia Casals**

Universitat Politècnica de Catalunya  
Dep. ESAT  
Jordi Girona 1-3  
UPC-Campus Nord  
08034 Barcelona  
Spain

### **Emmanuel Vander Poorten**

University of Leuven  
Dept. of Mechanical Engineering  
Celestijnenlaan 300B  
B-3001 Heverlee  
Belgium

### **Paolo Fiorini**

Università di Verona  
Computer Science  
Department  
Ca' Vignal 2  
37134 Verona  
Italy

### **Leonardo Mattos**

Istituto Italiano di Tecnologia  
Dept. of Advanced Robotics  
Via Morego 30  
16163 Genoa  
Italy

### **Fanny Ficuciello**

Università degli Studi di Napoli Federico II  
PRISMA Lab - DIETI  
via Claudio, 21  
80125 Napoli  
Italy

## CRAS Organization Board

The organization board of CRAS consists - in alphabetical order - of the following members:

<b>Salih Abdelaziz</b> LIRRM	<b>Alperen Acemoglu</b> IIT	<b>Kaspar Althoefer</b> Queen Mary London	<b>F.R. Y Baena</b> ICL	<b>Christos Bergeles</b> KCL
<b>Gianni Borghesan</b> KU Leuven	<b>Marta Capiluppi</b> Univ. Verona	<b>Alicia Casals</b> UPC	<b>Zhuoqi Cheng</b> SDU	<b>Gastone Ciuti</b> SSSA
<b>Giulio Dagnino</b> ICL	<b>Jenny Dankelman</b> TU Delft	<b>Diego Dall'Alba</b> Univ. Verona	<b>Brian Davis</b> ICL	<b>Elena De Momi</b> POLIMI
<b>Kathleen Denis</b> KU Leuven	<b>Nikhil Deshpande</b> IIT	<b>Giancarlo Ferrigno</b> POLIMI	<b>Fanny Ficuciello</b> Univ. Napoli	<b>Paolo Fiorini</b> Univ. Verona
<b>Ioannis Georgilas</b> Univ. of Bath	<b>Edward Grant</b> NCSU	<b>Yassine Haddab</b> LIRRM	<b>Tamas Haidegger</b> Obuda Univ.	<b>Benoit Herman</b> UCLouvain
<b>Albert Hernansanz</b> UPC	<b>Tim Horeman</b> TU Delft	<b>Pierre Jannin</b> U.Rennes	<b>Chao Liu</b> LIRMM - CNRS	<b>Leonardo Mattos</b> IIT
<b>E. Mazomenos</b> Leeds	<b>Arianna Menciassi</b> SSSA	<b>Sara Moccia</b> Univ. Pol. delle Marche, IIT	<b>Guillaume Morel</b> ISIR	<b>Riccardo Muradore</b> Univ. Verona
<b>George Mylonas</b> UCL	<b>Florent Nageotte</b> Ben-Gurion Univ.	<b>Ilana Nisky</b> Ben-Gurion Univ.	<b>Mouloud Ourak</b> KU Leuven	<b>Sebastien Ourselin</b> KCL
<b>Nicolas Padoy</b> UNISTRA	<b>Veronica Penza</b> IIT	<b>Philippe Poignet</b> LIRRM	<b>Pierre Renaud</b> UNISTRA	<b>Benoit Rosa</b> UNISTRA
<b>Jerome Szewczyk</b> ISIR	<b>Bruno Siciliano</b> Univ. Napoli	<b>Giannarou Stamatia</b> ICL	<b>Stefanie Speidel</b> University Dresden	<b>Danail Stoyanov</b> UCL
<b>Selene Tognarelli</b> SSSA	<b>E. Vander Poorten</b> KU Leuven	<b>Tom Vercauteren</b> KCL	<b>Helge Wurdemann</b> UCL	<b>Nabil Zemiti</b> LIRRM

## Program

Overall Program CRAS 2020			
	Monday - 28.09	Tuesday - 29.09	Wednesday - 30.09
09.45 - 10.00	Opening Session		
10.00 - 11.00	Oral 1	Oral 3	Interactive 3
11.00 - 12.00	Keynote - C. Huet	Interactive 1	Interactive 4
12.00 - 13.00			
13.00 - 14.00			
14.00 - 15.00	Keynote - D. Rus	Keynote - A. Okamura	
15.00 - 16.00	Oral 2	Interactive 2	
16.00 - 17.00			Oral 4
17.00 - 18.00			Keynote - B. Hannaford
18.00 - 18.30			Awards & Closure

For details on the CRAS 2020 conference program, please refer to CRAS website

<https://cras-eu.org/program/>

## Open-Access License Information

All articles included in these proceedings are published as open-access publication under the ***“Creative Commons Attribution 4.0 International”*** license.

This means that the materials included here can be shared and adapted for any purpose. However, you must give appropriate credit, provide a link to the license, and indicate if changes were made. You may do so in any reasonable manner, but not in any way that suggests the licensor endorses you or your use.

For more details on the “Creative Commons Attribution 4.0 International” license, please refer to:

<https://creativecommons.org/licenses/by/4.0/>

**European Commission support to smart robots for healthcare: achievements and future perspective**

Dr. Cécile Huet

European Commission

The plenary lecture will cover a number of activities supported in the past, in particular through the Horizon 2020 funding programme, and will give some insights about the preparation of upcoming funding programmes, namely Horizon Europe (Research and innovation), and the digital Europe Programme (capacity building and deployment). It will also include some broader perspective on the relevant AI policy developments.



**Cécile Huet** is Deputy Head of the Unit “Robotics and Artificial Intelligence” at the European Commission. This unit funds and assists beneficial robotics and AI developments within Europe. The unit is in charge of one of the world’s largest civilian programme in robotics with a budget of €700 million EU funding from Horizon 2020, supplemented by €2.1 billion from the European robotics industry in the context of the Robotics Public-Private Partnership. The unit is coordinating the preparation of the AI activities in the next funding programmes, Horizon Europe and Digital Europe programmes. Currently the unit is working with the stakeholders on the next Partnership on AI, data and Robotics, defining the strategic research, development, innovation and deployment for Europe in these fields. Moreover, this unit is at the heart of the [Communication on Artificial Intelligence for Europe](#), the [Coordinated Plan on Artificial Intelligence](#) and the [Communication on Building Trust in Human-Centric Artificial Intelligence](#). Cécile joined the unit since its creation in 2004. Previously, she worked for the industry in signal processing after a post-doc at the University of California Santa Barbara and a PhD at University of Nice Sophia Antipolis. In 2015, she has been selected as one of the “[25 women in robotics you need to know about](#)”.

### Robots, AI, Pandemics, and Surgery

Prof. Daniela Rus

Massachusetts Institute of Technology

The COVID-19 pandemic has highlighted the role of AI and robotics in healthcare. There are tremendous opportunities to support the medical profession with intelligent tools to better diagnose, monitor, treat, and prevent disease. I will describe our recent work on robotic emergency ventilation systems for patients and UVC disinfecting robots, and discuss future opportunities for incision-free surgeries enabled by miniaturized robotic pills.



**Daniela Rus** is the Andrew (1956) and Erna Viterbi Professor of Electrical Engineering and Computer Science; Director of the Computer Science and Artificial Intelligence Laboratory (CSAIL); and Deputy Dean of Research for Schwarzman College of Computing at MIT. Prof. Rus brings deep expertise in robotics, artificial intelligence, data science, and computation. She is a member of the National Academy of Engineering, a member of the American Academy of Arts and Sciences, and fellow of the Association for the Advancement of Artificial Intelligence, the Institute of Electrical and Electronics Engineer, and the Association for Computing Machinery. She is also a recipient of a MacArthur Fellowship, a National Science Foundation Career award, and an Alfred P. Sloan Foundation fellowship. Rus earned her PhD in computer science from Cornell University.

**Advancing Human Sensorimotor Control for Surgery**

Prof. Allison M. Okamura

Stanford University

Robot-assisted surgery has a significant learning curve, because the human operators must adapt to kinematic mappings between human and robot, the dynamics of the manipulator and instruments, limited or altered sensory feedback, and learn the task itself. While performance metrics exist to certify users, it is generally unknown how to optimize training to speed up the learning and maximize the amount learned in skilled tasks. In this talk, I will demonstrate learning in novice and expert robot-assisted surgeons, discuss the mechanisms and roles of visual and haptic training, and propose methods for maximizing learning of complex instruments and tasks. Teleoperated robots enable visual and haptic perturbations, as well as detailed behavioral recordings, that facilitate the study of learning for a number of real-world skilled tasks not usually addressed in the neuroscience literature – ranging from surgery to driving a car.



**Allison M. Okamura** received the BS degree from the University of California at Berkeley and the MS and PhD degrees from Stanford University, all in mechanical engineering. She is currently Professor in the mechanical engineering department at Stanford University, with a courtesy appointment in computer science. She is an IEEE Fellow and Editor-in-Chief of the journal IEEE Robotics and Automation Letters. Her awards include the 2020 IEEE Engineering in Medicine and Biology Society Technical Achievement Award, 2019 IEEE Robotics and Automation Society Distinguished Service Award, and 2016 Duca Family University Fellow in Undergraduate Education. Her academic interests

include haptics, teleoperation, virtual environments and simulators, medical robotics, neuromechanics and rehabilitation, and soft robotics. She is passionate about engineering education and diversifying STEM. Outside academia, she enjoys spending time with her husband and two children, running, and playing ice hockey. For more information about her research, please see the Collaborative Haptics and Robotics in Medicine (CHARM) Laboratory website: <http://charm.stanford.edu>.



**Introducing Automation to Surgical Robotics: Challenges and Frontiers**

Prof. Blake Hannaford

University of Washington

With great success of teleoperated surgery in the medical profession, the research field is now working to demonstrate the utility of selectively introducing automated assistance for surgical robotics. Concepts from AI which readily translate into surgical robotics (though not necessarily in medical use) include computer vision, 3D shape recovery, augmented reality registration, and advances in control systems and networked teleoperation. Other concepts such as classical planners may not fit as well when a highly skilled human is still in the loop. Highly elongated, narrow, and lightweight structures of robotic surgical instruments are fundamentally limited in accuracy and precision – limitations that can surprise the engineer since human controllers so readily adapt. This talk will review some results from the lab on the determinants of precise positioning of robotic surgical instruments, as well as some ideas on possible AI frameworks needed to advance patient outcomes through selective automation.



**Blake Hannaford**, Ph.D., is Professor of Electrical Engineering, Adjunct Professor of Bioengineering, Mechanical Engineering, and Surgery at the University of Washington, in Seattle.

Blake Hannaford received the B.S. degree in Engineering and Applied Science from Yale University in 1977, and the M.S. and Ph.D. degrees in Electrical Engineering from the University of California, Berkeley. From 1986 to 1989 he worked on the remote control of robot manipulators in the Man-Machine Systems Group in the Automated Systems Section of the NASA Jet Propulsion Laboratory, Caltech and supervised that group from 1988 to 1989. Since September 1989, he has been at the University of Washington in Seattle, where he is Professor of Electrical and Computer Engineering. He was awarded the

National Science Foundation's Presidential Young Investigator Award, the Early Career Achievement Award from the IEEE Engineering in Medicine and Biology Society, and was named IEEE Fellow in 2005. He was at Google-X / Google Life Sciences / Verily from April 2014 to December 2015. His currently active interests include surgical robotics, surgical skill modeling, and haptic interfaces.



## CRAS 2020 Abstract index

<b>VR SIMULATION SYSTEM FOR IN-OFFICE HYSTEROSCOPY: A PILOT STUDY .....</b>	<b>14</b>
VLADIMIR POLIAKOV, DZMITRY TSETSERUKOU, KENAN NIU AND EMMANUEL VANDER POORTEN	
<b>PERSONALISED COMPUTER-ASSISTED TREATMENT OF KNEE OSTEOCHONDRAL LESIONS ENHANCED WITH AUGMENTED REALITY. A PROOF OF CONCEPT .....</b>	<b>16</b>
FABIO TATTI, HISHAM IQBAL, BRANISLAV JARAMAZ AND FERDINANDO RODRIGUEZ Y BAENA	
<b>CONTINUOUS-CURVATURE PATH PLANNING FOR ENDOVASCULAR CATHETERIZATION .....</b>	<b>18</b>
ZHEN LI, ANDREA PAGLIARI, NICOLÒ PASINI, CHIARA QUARTANA, VITTORIO ZACCARIA PASOLINI, JENNY DANKELMAN AND ELENA DE MOMI	
<b>A VISION-BASED TROCAR SITE FORCE SENSING TECHNIQUE .....</b>	<b>20</b>
JILMEN QUINTIENS, JEF DE SMET AND EMMANUEL VANDER POORTEN	
<b>VALIDATION OF A HIGH-FIDELITY NEONATAL PNEUMOTHORAX SIMULATOR WITH EXPERT NEONATOLOGISTS .....</b>	<b>22</b>
SABINA MAGLIO, ARIANNA MENCIASSI AND SELENE TOGNARELLI	
<b>PEDIATRIC NEUROSURGICAL ROBOT: FROM REQUIREMENTS TO DEVELOPMENT .....</b>	<b>24</b>
NABEEL KAMAL, ARMANDO CAMA AND LEONARDO S. MATTOS	
<b>ADAPTIVE NEURAL NETWORK FOR MODELLING AND CONTROL OF A SURGICAL ROBOTIC TOOL ATTACHED TO A SERIAL-LINK MANIPULATOR .....</b>	<b>26</b>
FRANCESCO CURSI AND PETAR KORMUSHEV	
<b>HIGH-FIDELITY SIMULATOR OF CERVIX CHANGES DURING LABOUR .....</b>	<b>28</b>
CARLOTTA LUCHINI, SELENE TOGNARELLI AND ARIANNA MENCIASSI	
<b>5G TELESURGERY – FEASIBILITY EXPERIMENT AND FIRST PUBLIC DEMO .....</b>	<b>30</b>
LEONARDO S. MATTOS, ALPEREN ACEMOGLU AND DARWIN G. CALDWELL	
<b>TOWARDS REAL-TIME EYE GEOMETRY ESTIMATION USING EYE TRACKER SENSOR .....</b>	<b>32</b>
NIKTE VAN LANDEGHEM, MEERE MALFAIT, MOULOUD OURAK, VIKTOR VÖRÖS AND EMMANUEL VANDER POORTEN	
<b>FLEXIBLE FRAMEWORK FOR REINFORCEMENT LEARNING IN SURGICAL ROBOTICS.....</b>	<b>34</b>
CLAUDIA D'ETTORRE, NERI NICCOLO DEI, SIVA KRISHNAN, SILVIA ZIRINO, GEORGIA CHALVATZAKI, AGOSTINO STILLI AND DANAIL STOYANOV	
<b>MANIPULABILITY ANALYSIS USING A COORDINATE INVARIANT INDEX WITH A REMOTE CENTER OF MOTION CONSTRAINT IN SURGICAL ROBOTICS .....</b>	<b>36</b>
CLAUDIA PECORELLA, BRUNO SICILIANO AND FANNY FICUCIELLO	
<b>FRAMEWORK FOR SOFT TISSUE MANIPULATION AND CONTROL USING DEEP REINFORCEMENT LEARNING .</b>	<b>38</b>
AMEYA PORE, ELEONORA TAGLIABUE, DIEGO DALL'ALBA AND PAOLO FIORINI	
<b>TOWARDS A COMPACT AUTO-FOCUSING SYSTEM FOR ENDOSCOPIC LASER SURGERY.....</b>	<b>40</b>
ANDRE GERALDES, PAOLO FIORINI AND LEONARDO MATTOS	
<b>VISION-BASED ESTIMATION OF DEFORMATION PROPERTIES FOR AUTONOMOUS SOFT TISSUES MANIPULATION .....</b>	<b>42</b>
MARCO PICCINELLI, ELEONORA TAGLIABUE, DIEGO DALL'ALBA AND PAOLO FIORINI	
<b>A HFMSM BASED COGNITIVE CONTROL ARCHITECTURE FOR ASSISTIVE TASK IN R-MIS .....</b>	<b>44</b>
NARCÍS SAYOLS BAIXERAS, ALESSIO SOZZI, NICOLA PICCINELLI, ALBERT HERNANSANZ, ALÍCIA CASALS, MARCELLO BONFÈ AND RICCARDO MURADORE	
<b>VISION-BASED DYNAMIC VIRTUAL FIXTURES FOR TOOLS COLLISION AVOIDANCE IN MIRS .....</b>	<b>46</b>
CRISTINA IACONO, ROCCO MOCCIA, BRUNO SICILIANO AND FANNY FICUCIELLO	
<b>A FRAMEWORK OF REAL-TIME FREEHAND ULTRASOUND RECONSTRUCTION BASED ON DEEP LEARNING FOR SPINE SURGERY .....</b>	<b>48</b>
RUIXUAN LI, KENAN NIU, DI WU AND EMMANUEL VANDER POORTEN	
<b>A SUPERVISORY CONTROLLER FOR SEMI-AUTONOMOUS SURGICAL INTERVENTIONS.....</b>	<b>50</b>
FABIO FALEZZA, NICOLA PICCINELLI, ANDREA ROBERTI, FRANCESCO SETTI, RICCARDO MURADORE AND PAOLO FIORINI	

<b>MULTI-TASK CONTROL STRATEGY EXPLOITING REDUNDANCY IN RMIS .....</b>	<b>52</b>
TOMÀS PIERAS, ALBERT HERNANSANZ, NARCÍS SAYOLS, JOHANNA PARRA, ELISENDA EIXARC, EDUARD GRATACÓS AND ALÍCIA CASALS	
<b>A CYCLE-GAN BASED TRANSFER LEARNING APPROACH FOR SURGICAL IMAGE SYNTHESIS.....</b>	<b>54</b>
EMANUELE COLLEONI, FRANCISCO VASCONCELOS AND DANAIL STOYANOV	
<b>TOWARDS THE DEVELOPMENT AND EVALUATION OF A HANDLE PROTOTYPE FOR A HANDHELD ROBOTIC NEUROSURGICAL INSTRUMENT .....</b>	<b>56</b>
EMMANOUIL DIMITRAKAKIS, GEORGE DWYER, LUKAS LINDENROTH, HOLLY AYLMOORE, NEIL DORWARD, HANI MARCUS AND DANAIL STOYANOV	
<b>MODULARIZATION OF MEDICAL ROBOTIC MANIPULATOR FOR ADAPTING SOFT ROBOTIC ARMS WITH VARYING NUMBERS OF DOFS .....</b>	<b>58</b>
CHUN-FENG LAI, FABIAN TRAUZETTEL, PAUL BREEDVELD, ELENA DE MOMI, GIANCARLO FERRIGNO AND JENNY DANKELMAN	
<b>DEEP REINFORCEMENT LEARNING FOR CONCENTRIC TUBE ROBOT CONTROL WITH GOAL BASED CURRICULUM REWARD.....</b>	<b>60</b>
KESHAV IYENGAR AND DANAIL STOYANOV	
<b>SOFTSCREEN – SOFT SHAPE-SHIFTING CAPSULE ROBOT FOR ENDOSCOPY BASED ON EVERSION NAVIGATION .....</b>	<b>62</b>
VANNI CONSUMI, LUKAS LINDENROTH, DANAIL STOYANOV AND AGOSTINO STILLI	
<b>ANGULAR METRICS AND AN EFFORT BASED METRIC USED AS FEATURES FOR AN AUTOMATIC CLASSIFYING ALGORITHM OF SURGICAL GESTURES .....</b>	<b>64</b>
MARCO BOMBIERI, DIEGO DALL'ALBA, SANAT RAMESH, GIOVANNI MENEGOZZO AND PAOLO FIORINI	
<b>ENDOSCOPIC OPTICAL COHERENCE TOMOGRAPHY VOLUMETRIC SCANNING METHOD WITH DEEP FRAME STREAM STABILIZATION .....</b>	<b>66</b>
GUIQIU LIAO, OSCAR CARAVACA MORA, BENOIT ROSA, DIEGO DALL'ALBA, PAOLO FIORINI, MICHEL MATHELIN, FLORENT NAGEOTTE AND MICHALINA GORA	
<b>FEASIBILITY OF USING A LONG SHORT-TERM MEMORY NETWORK FOR ROBOTIC CATHETER CONTROL.....</b>	<b>68</b>
DI WU, MOULOUD OURAK, MIRZA AWAIS AHMAD, KENAN NIU, GIANNI BORGHESEAN, JENNY DANKELMAN AND EMMANUEL VANDER POORTEN	
<b>SEGMENTATION OF LUMEN IN URETEROSCOPY IMAGES USING DEEP LEARNING.....</b>	<b>70</b>
JORGE LAZO, SARA MOCCIA AND ALDO MARZULLO	
<b>CONSTRAINT-BASED CONTROL OF A DISTALLY ACTUATED CONTINUUM ROBOT.....</b>	<b>72</b>
BEATRIZ FAROLA BARATA, GIANNI BORGHESEAN, DIEGO DALL'ALBA, JOS VANDER SLOTEN AND EMMANUEL VANDER POORTEN	
<b>STATISTICAL SHAPE MODELLING OF THE HUMAN NASAL CAVITY AND MAXILLARY SINUS FOR MINIMALLY INVASIVE SURGERY.....</b>	<b>74</b>
KENAN NIU, JULIE LEGRAND, LAURA VAN GERVEN AND EMMANUEL VANDER POORTEN	
<b>FORCE-BASED ENDOSCOPE POSITIONING FOR LAPAROSCOPIC SACROCOLPOPEXY .....</b>	<b>76</b>
JEF DE SMET, EMMANUEL VANDER POORTEN AND JAN DEPREST	
<b>VISION-GUIDED AUTONOMOUS ROBOTIC ELECTRICAL BIO-IMPEDANCE SCANNING SYSTEM FOR ABNORMAL TISSUE DETECTION AND TRACKING.....</b>	<b>78</b>
ZHUOQI CHENG, VERONICA PENZA, JESÚS ORTIZ, DARWIN CALDWELL AND LEONARDO MATTOS	
<b>DEVELOPMENT OF A RESISTIVE-BASED SENSOR FOR REAL TIME SHAPE DETECTION OF A SPRING BASED FLEXIBLE MANIPULATOR .....</b>	<b>80</b>
SUJIT KUMAR SAHU, IZADYAR TAMADON, BENOIT ROSA, PIERRE RENAUD AND ARIANNA MENCIASSI	
<b>A FLUID-DRIVEN MECHANISM FOR PERCUTANEOUS NEEDLE INSERTION AND FINE-MANIPULATION UNDER IMAGE GUIDANCE.....</b>	<b>82</b>
LUKAS LINDENROTH, AGOSTINO STILLI, SAURABH SINGH, STEVE BANDULA AND DANAIL STOYANOV	
<b>A VIRTUAL FETAL ENVIRONMENT FOR TTTS APPLICATIONS.....</b>	<b>84</b>
ALESSANDRO CASELLA, SARA MOCCIA, FILIPPO PICCINOTTI, DARIO PALADINI, EMANUELE FRONTONI, ELENA DE MOMI AND LEONARDO S. MATTOS	

<b>SMARTPROBE: AN EBI SENSING SYSTEM FOR HEAD AND NECK CANCER TISSUE DETECTION .....</b>	<b>86</b>
ZHUOQI CHENG, ANDREA LUIGI CAMILLO CAROBBIO, LARA SOGGIU, MARCO MIGLIORINI, LUCA GUASTINI, FRANCESCO MORA, MARCO FRAGALE, ALESSANDRO ASCOLI, STEFANO AFRICANO, DARWIN CALDWELL, FRANK RIKKI MAURITZ CANEVARI, GIAMPIERO PARRINELLO, GIORGIO PERETTI AND LEONARDO MATTOS	
<b>SYSTEMS-THEORETIC PROCESS ANALYSIS APPLIED AS A SOCIO-TECHNICAL SAFETY ANALYSIS TO SUPPORT FUTURE FETOSCOPE DESIGN .....</b>	<b>88</b>
ARIE ADRIAENSEN	
<b>ML BASED SOFT CAPACITIVE E-SKIN SENSOR FOR SOFT SURGICAL ROBOTS .....</b>	<b>90</b>
ABU BAKAR DAWOOD, HAREESH GODABA, AHMAD ATAKA AND KASPAR ALTHOEFER	
<b>UNSCENTED KALMAN FILTERING (UKF) WITH ELECTROCARDIOGRAM (ECG) SENSOR FUSION FOR HEART STATE ESTIMATION AND MOTION-COMPENSATION.....</b>	<b>92</b>
FLORIAN DE CLERCQ, GIANNI BORGHEAN, EMMANUEL VANDER POORTEN AND WOUTER OOSTERLINCK	
<b>PRELIMINARY ANALYSIS OF LEARNING A ROBOT-ASSISTED SURGICAL PATTERN-CUTTING.....</b>	<b>94</b>
YARDEN SHARON, DANIEL NAFTALOVICH, LIDOR BAHAR, HANNA KOSSOWSKY, Yael REFAELY AND ILANA NISKY	
<b>BITRACK: A FRIENDLY FOUR ARMS ROBOT FOR LAPAROSCOPIC SURGERY .....</b>	<b>96</b>
JOSEP AMAT, ALICIA CASALS AND MANEL FRIGOLA	

# VR Simulation System for In-Office Hysteroscopy: A Pilot Study

Vladimir Poliakov<sup>1</sup>, Dzmitry Tsetserukou<sup>2</sup>, Kenan Niu<sup>1</sup>, and Emmanuel Vander Poorten<sup>1</sup>

<sup>1</sup>*Robot-Assisted Surgery Group, Mechanical department, KU Leuven, Belgium*

<sup>2</sup>*Space Center, Skolkovo Institute of Science and Technology, Russia*

*vladimir.poliakov@kuleuven.be*

## INTRODUCTION

Hysteroscopy has been rapidly evolving for the past decade. Introducing office hysteroscopy, which allows outpatient treatment in clinic, has brought gynecology to yet another level [1]. Office hysteroscopy became available due to miniaturisation of instruments. Smaller instrument diameter makes it possible to pass through the cervical canal without prior dilation, thus reducing recovery time and mitigating risks related to the procedure as no anaesthesia is involved.

At the same time, omitting prior dilation imposes new challenges on the practitioner. The cervical canal is a very narrow passage with rather high curvature. Moreover, the canal might be obliterated by adhesions, which significantly impedes the process of introducing the instrument. Thus, a gynecologist has to pay great attention to avoid uterine perforation or a patient's discomfort [2]. In order to become proficient, clinicians spend many hours practicing this type of intervention. A wide range of options is available for surgical training in hysteroscopy, including artificial platforms: physical simulators, also known as box trainers, and virtual reality (VR) simulators. VR training has a great number of benefits compared to other types of surgical training [3]. It provides a great level of immersion and allows to render various scenarios and pathologies. Yet, to the best of our knowledge, no research has been done in VR training for hysteroscopic passage of the endocervix with in-office setup.

The hypothesis of this study was that VR training is capable of transferring the essential skills to overcome the difficulties when passing through the cervical canal. This extended abstract describes a VR surgical training system for hysteroscopy that was developed specifically for in-office hysteroscopy training and tested in the labo-

ratory setting. The proposed training system has a great potential to fill the research gap and to be applied in clinical practice.

## MATERIALS AND METHODS

To prove the hypothesis, a prototype platform has been designed. It features a simple navigation task, in which participants should pass through the endocervix to reach the uterine cavity.

The aim of the exercise was to enter the uterine cavity and collect all checkpoints while maintaining the level of applied force. Checkpoints are rendered as one-millimeter green spheres, which are evenly distributed along the surface of the cervical canal and the uterine cavity. A user can collect spheres by touching them with the tip of the hysteroscope: once a sphere is collected, it disappears. When all spheres are collected, the exercise is terminated.

**Hardware setup:** Figure 1 depicts the hardware layout of the system. The user operates a mock-up hysteroscope pivoting in a silicone phantom of the vagina. The Geomagic Touch haptic interface is attached to the hysteroscope on the other end, reading the position of the instrument and providing haptic feedback to the user. A PC (Intel Core I7-9850H, NVIDIA Quadro T1000 w/4GB GDDR6, 8GB RAM) runs the simulation and renders visual representation on a screen from the perspective of a virtual camera attached to the tip of the hysteroscope.

**Scene generation:** The geometrical model of the uterus is based on manual segmentation of the Visible Human cryosection dataset [4]. Mechanical properties were obtained from quasi in-vivo measurements performed by Omari et al. [5]. The mechanical model of the

uterus was represented by a finite-element tetrahedral model with the resolution of 1310 elements.

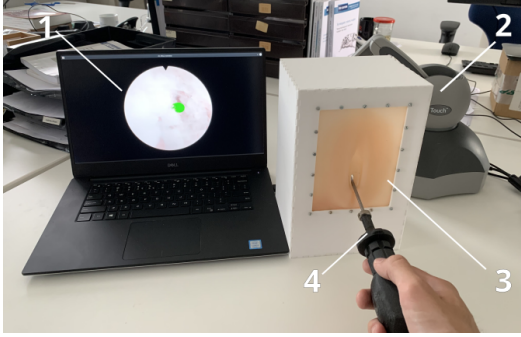


**Figure 1:** VR simulation setup, (1) user interface, (2) Geomagic Touch haptic device, (3) silicone phantom of the vagina, (4) hysteroscope

**Software architecture** of the simulator includes three main components: the physics engine, the visual renderer and the haptic loop. All mentioned components run in separate threads as all of them have different timing requirements. SOFA framework [6] is used as the physics engine of the system. It runs at the update rate of 150 frames per second (FPS). The Filament renderer [7] is used for graphical representation. The visual server runs at 50 FPS. Finally, the haptic loop utilizes the OpenHaptics [8] libraries and runs at 1kHz. Lagrange constraints generated by contact points in the physical simulation are passed to the haptic loop to provide realistic feedback.

**Experiments:** Three expert hysteroscopists and five novices with no prior experience participated in preliminary experiments to examine the proposed concept. Assessment of a subject’s performance was based on following metrics: total execution time ( $t_e$ ), trajectory length ( $l_t$ ), effective jerk (mean jerk excluding idle states) ( $j_e$ ), effective force (mean force excluding idle states) ( $f_e$ ), cumulative force (integrated force value) ( $f_c$ ), and force fast Fourier transform (FFT) ( $f_{FFT}$ ). The latter metric is the cumulative sum of the real component of applied force in the frequency domain.

To check statistical significance, the acquired dataset was tested using Mann-Whitney U-test. A metric was considered to be significant if its  $p$ -value was less than or equal to 0.05.

## RESULTS AND DISCUSSION

Table 1 represents the mean results of the experiment in the expert and novice groups.  $p$ -values between the groups are shown in the third column and denoted with an asterisk (\*) if a metric has statistical significance ( $p \leq 0.05$ ).

Overall the platform demonstrated the ability to distinguish between novice and expert users. Execution

time was 55% higher for novice users. Trajectory length difference was 46%. Cumulative force and force FFT were 48% and 23% higher for novice users, respectively.

Summing up, the proposed concept demonstrated its potential in training for in-office hysteroscopy. However, more features, such as obliteration of the cervical canal and surgical ripening of the cervix, still should be implemented to improve its content and face validity.

**Table 1:** Results of the experiments

Metric	Expert group	Novice group	$p$
$t_e$ [s]	$25.78 \pm 1.14$	$40.12 \pm 12.11$	0.0501*
$l_t$ [mm]	$147.66 \pm 3.84$	$215.86 \pm 19.74$	0.0167*
$j_e$ [m/s <sup>3</sup> ]	$2.88 \pm 0.22$	$3.29 \pm 0.62$	0.3805
$f_e$ [mN]	$505.50 \pm 10.01$	$498.52 \pm 42.82$	0.8878
$f_c$ [mN · s]	$6.18 \pm 0.64$	$9.17 \pm 0.73$	0.0173*
$f_{FFT}$	$3313 \pm 200.93$	$4079 \pm 43.88$	0.0173*

## REFERENCES

- [1] A. Hernandez, “In-office hysteroscopy,” in *Hysteroscopy*, A. Tinelli, L. Alonso Pacheco, and S. Haimovich, Eds. Cham: Springer International Publishing, 2018, pp. 33–40.
- [2] P. McGurgan and P. McIlwaine, “Complications of hysteroscopy and how to avoid them,” eng, *Best Practice & Research Clinical Obstetrics & Gynaecology*, vol. 29, no. 7, pp. 982–993, 2015, ISSN: 1521-6934.
- [3] M. M. Erian, G. R. McLaren, and A.-M. Erian, “Advanced hysteroscopic surgery training,” eng, *JSLs : Journal of the Society of Laparoscopic Surgeons*, vol. 18, no. 4, 2014.
- [4] M. Ackerman, “The visible human project,” *Proceedings of the IEEE*, vol. 86, no. 3, pp. 504–511, 1998.
- [5] E. A. Omari, T. Varghese, M. A. Kliever, J. Harter, and E. M. Hartenbach, “Dynamic and quasi-static mechanical testing for characterization of the viscoelastic properties of human uterine tissue,” *Journal of Biomechanics*, vol. 48, no. 10, pp. 1730–1736, 2015.
- [6] F. Faure, C. Duriez, H. Delingette, J. Allard, B. Gilles, S. Marchesseau, H. Talbot, H. Courtecuisse, G. Bousquet, I. Peterlik, and S. Cotin, “Sofa: A multi-model framework for interactive physical simulation,” in *Soft Tissue Biomechanical Modeling for Computer Assisted Surgery*, ser. Studies in Mechanobiology, Tissue Engineering and Biomaterials, vol. 11, Springer, 2012, pp. 283–321.
- [7] Google, *Filament rendering engine*, Accessed: 2020-05-10, 2020. [Online]. Available: <https://github.com/google/filament>.
- [8] 3DSystems, *Geomagic openhaptics*, Accessed: 2020-05-10, 2020. [Online]. Available: <https://www.3dsystems.com/haptics-devices/openhaptics>.

# Personalised Computer-Assisted Treatment of Knee Osteochondral Lesions Enhanced with Augmented Reality. A Proof of Concept

F. Tatti<sup>1</sup>, H. Iqbal<sup>1</sup>, B. Jaramaz<sup>2</sup>, and F. Rodriguez y Baena<sup>1</sup>

<sup>1</sup>*Department of Mechanical Engineering, Imperial College London*

<sup>2</sup>*Smith & Nephew Inc.*

{f.tatti,hisham.iqbal13,f.rodriguez}@imperial.ac.uk; branko.jaramaz@smith-nephew.com

## INTRODUCTION

Over 100,000 knee arthroplasties are performed annually in the United Kingdom, and the number is on the rise [1]. Procedures targeting focal cartilage lesions can avoid or postpone the need for a knee replacement, but they are still relatively uncommon [2]. One challenge presented by this class of procedures is the difficulty in achieving a good congruence between the implant's shape and patient anatomy, which is critical for success.

In this regard, Computer-Assisted Orthopaedic Surgery (CAOS) could be of assistance, as it provides valuable metrics that can inform the selection and placement of an implant and minimise the error between planning and execution. CAOS systems promise to bring more quantitative data and objective metrics into the operating theatre, informing the surgeons' decisions, thus allowing them to tailor each intervention to the patient's needs [3].

While CAOS systems can collect and process a great deal of information, how to best aggregate such information and present it to the surgeon is also a critical question. Currently, most CAOS systems rely on 2D touch screens for user interaction, which pose several problems, including the fact that surgeons have to switch their focus between the patient and the screen. Augmented reality is a promising alternative for the future, as it allows to display key information directly on site, avoiding the surgeon having to divert their attention from the patient [4].

In this work we present a proof of concept for a CAOS system, the aim of which is to achieve targeted patient-specific treatment of focal cartilage lesions. The system uses intraoperative information on the patient's anatomy and lesion to select an optimal implant and its pose. Augmented reality is used to display the anatomical information and surgical plan directly on or near the patient.

## MATERIALS AND METHODS

In the context of a government funded industry-academia partnership with a large orthopaedics robot manufacturer (Smith & Nephew, inc), we created a software module that generates a parametric description of the shape and size of an osteochondral defect (OCD), and used it to select an optimal implant and pose. The software broadcasts case-



**Fig. 1:** Holographic view of the implant's planned location overlaid on a model of the patient's femur.

specific data (i.e. implant pose and sizing) via UDP, along with live tracking information of the patient and surgical instruments, which in turn is utilised when rendering holographic content on an external augmented-reality headset.

The software module requires two inputs: a 3D model of the patient's femur and a vector of points representative of the defect's contour. The size and elongation of the defect are captured by fitting a 2D ellipse to its contour, while the anatomical shape is described by fitting an elliptic or hyperbolic paraboloid to the external surface. The 3D model of the femur is assumed to be constructed by means of a statistical shape model, therefore ignoring the presence of a defect and reconstructing the "missing" cartilage surface, as if the defect were not present.

The shape of the available implants is described using the same mathematical model employed for the defect geometry. We can therefore select the best implant for a given defect by comparing the defect's parametric description with that of the implants. The implant's best pose is then computed using the ICP algorithm to co-register the implant's and femur's outer surfaces.

## RESULTS

After implementing our prototype software in C++, we combined these tools with the existing capabilities of the Navio<sup>TM</sup> surgical system (Smith & Nephew



inc.), to create a complete surgical workflow. The stages of the complete workflow are the following: the surgeon is first tasked with collecting the position of anatomical landmarks with a tracked probe. These are used to register the position of the patient. The anatomy of the bone is then modelled by using the tracked probe to 'paint' the surface of the exposed femur. After this stage, the surgeon traces the outer edge of the defect and the collected information is then used to select the optimal implant and its pose. Finally, the system generates a plan for the bone that needs to be cut in order to correctly place the implant and the surgeon executes it using the system's burring tool.

Throughout all stages of the workflow, the information collected and generated is broadcast wirelessly to an augmented reality headset (HoloLens, Microsoft, inc.) worn by the surgeon, using UDP. We created custom HoloLens apps that retrieve the information and generate holographic content. We tested two modes of visualisation: one where the contents of the Navio<sup>TM</sup> touchscreen monitor are replicated on a virtual floating window that the surgeon can position freely in space, and another where information on the defect location, selected implant, and pose is presented holographically on a 3D twin model of the patient's femur, as in Fig. 1. Promising preliminary data on surgeons' interaction with the holographic display was presented in [5] and indicate that it is an acceptable means of interaction for surgeons and that it does not disrupt the flow of the procedure.

We also conducted preliminary testing of the workflow by simulating the presence of an osteochondral defect on plastic femur models. The testing was successful and demonstrated that the workflow can be used to select and position an appropriate implant for a given defect. Fig. 2 shows the successful planning and placement of an implant prototype.

## DISCUSSION

The goal of this study was to create and test a prototype of a novel CAOS workflow that pushes current system's capabilities in two ways: first, by using intraoperative information to inform the selection of an implant and its pose, and second by displaying this information to the surgeon on or near the operating site, by means of 3D holograms.

Our preliminary results are encouraging and suggest that the automated selection method provides valid information and that the augmented reality display is a valid means for displaying it.

While our system is an initial proof of concept, we believe it can be a first step in the direction of the coming generation of CAOS systems, which will enable new levels of assisted patient-specific planning, and use immersive technologies to make the interaction between surgeon and machine more natural and intuitive.



**Fig. 2:** Osteochondral defect repair workflow. Screenshot of the planning window (*top*) and final result (*bottom*).

## ACKNOWLEDGEMENTS

This study was funded by INNOVATE UK under project number 103950. HI also received funding from EPSRC and TJ Smith & Nephew Ltd. in the form of an industrial CASE Studentship.

## REFERENCES

- [1] National Joint Registry. Annual Report 2019.
- [2] Fuchs A, Eberbach H, Izadpanah K, et al. Focal metallic inlay resurfacing prosthesis for the treatment of localized cartilage defects of the femoral condyles: a systematic review of clinical studies. *Knee Surg Sports Traumatol Arthrosc.* 2018; 26:2722–32.
- [3] Picard F, Deakin A, Riches P, et al. Computer assisted orthopaedic surgery: Past, present and future. *Med Engineering and Physics.* 2019; 72:55–65.
- [4] Yoon J, Chen R, Kim E, et al. Augmented reality for the surgeon: Systematic review. *Int J Med Robotics Comput Assist Surg.* 2018; 14:e1914.
- [5] Iqbal H, Tatti F, Rodriguez y Baena F. Augmented-Reality within Computer Assisted Orthopaedic Surgery Workflows: A Proof of Concept Study. *CAOS* 2019; 184–188.

# Continuous-curvature path planning for endovascular catheterization

Zhen Li<sup>1,2</sup>, Andrea Pagliari<sup>1</sup>, Nicolò Pasini<sup>1</sup>, Vittorio Zaccaria Pasolini<sup>1</sup>, Chiara Quartana<sup>1</sup>, Jenny Dankelman<sup>2</sup>, Elena De Momi<sup>1</sup>

<sup>1</sup>Department of Electronics, Information and Bioengineering Department, Politecnico di Milano

<sup>2</sup>Department of Biomechanical Engineering, Delft University of Technology  
zhen.li@polimi.it; j.dankelman@tudelft.nl; elena.demomi@polimi.it

## INTRODUCTION

Navigation guidance can mitigate the skill and experience requirements for percutaneous treatment of Chronic Total Occlusions (CTOs). Planning for an appropriate path for flexible catheters safely is one of the major challenges for endovascular catheterization. However, state of the art publications rarely consider kinematic constraints (e.g. curvature limitation). In our previous work, we proposed a fast path planning approach under curvature constraints, and the approach explores a path along the vascular centerline-based structure and locally optimizes the path to satisfy curvature constraints. Furthermore, we develop the path planning approach in this work, ensuring the continuity of curvature at coincident points between the vascular centerline and the locally optimized path. Particularly, the present work focuses on path planning under the framework of ATLAS project.

## MATERIALS AND METHODS

### - Datasets preprocessing

The datasets are two-dimensional images with a pixel resolution of  $2822 \times 1539$ , presenting the lower limb arteries. They are obtained from five subjects via automatic stitching and convolutional neural network segmentation [1]. And then centerline-based information structure is extracted via medial axis skeletonization (Voronoi diagram) from the anatomical structure. It is feed to the further path planning simulation as an input and the simulation is carried out in the PyCharm platform on a computer with Ubuntu system.

### - Algorithm

#### 1) Planning under curvature constraints

We define that a path is composed of  $m$  points, and each point  $\mathbf{p}_i$  is represented by  $(x_1, \dots, x_n)$  that is the position representation in the  $n$ -dimensional Cartesian coordinate system. Curvature at  $\mathbf{p}_i$  is defined in Eq. (1). The curvature constraint is formulated as Eq. (2), where  $s^*$  is the allowed maximal curvature value depending on robot capability. For example,  $s^* \approx 0.08 \text{ mm}^{-1}$  of the designed steerable catheter prototype in [2].

$$s_i = \frac{\sqrt{\sum_{j \neq k}^n (\dot{x}_j \ddot{x}_k - \dot{x}_k \ddot{x}_j)^2}}{(\sum_{i=1}^n \dot{x}_i^2)^{3/2}} \quad (1)$$

$$s_i \leq s^* \text{ for } i = 1, \dots, m \quad (2)$$

In our previous work, we proposed a fast path planning approach under curvature constraints. Firstly, it explores

a path along the vascular centerline-based structure from a user-defined start point to an end point via traditional graph-based path searching algorithm. Then it locally optimizes the path to satisfy curvature constraints via genetic algorithm, converting the curvature constraint to a component of the objective function. For example, there is one curve segment should be optimized due to exceeding the limitation in Figure 1, marked with green color. There may be several curve segments exceeding the limitation along the centerline. In that case, parallel optimization is carried on to reduce computational time.

#### 2) Smoothing at coincident points

In this work, we focus on connection smoothing to ensure the differentiability and continuity of curvature at the coincident points. The optimized curve segment cannot be mounted to the centerline directly (see Figure 1B), since the derivative (slope)  $p^-$  at the left side of the coincident point  $\mathbf{p}$  has a great difference value from the one  $p^+$  at the right side. In other words, it results in a great rotation angle  $\theta$  in a short interval. It would exceed the robot kinematics and dynamics capability. Therefore, the differentiability should be respected.

To obtain a desired degree of smoothness, the coincident point not only needs to be differentiable, but also belongs to the class of  $C^1$  and  $G^2$  functions. The  $C^1$  continuity is essential to ensure tangent vectors of the two connected

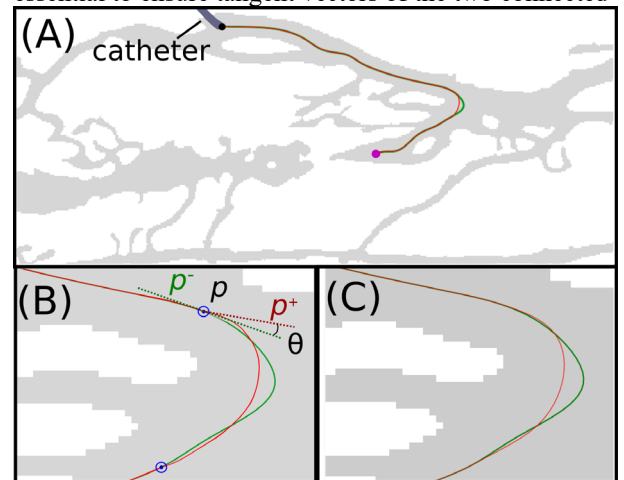


**Figure 1.** Path planning results on lower limb arteries: (A) the full view (B) the zoom-in view of the result before connection smoothing (C) the zoom-in view of the result via  $G^2$  quintic Hermite curve smoothing. The initial and goal location are the black and purple points, respectively. Green line represents the curve along vascular centerlines. Red line shows the final solution after optimization. Blues depict the coincident points.



segments are equal. The  $G^2$  continuity [3] means the 1<sup>st</sup> derivatives at the coincident points are collinear, and the curvature is continuous. The continuity of curvature is essential since it indicates non-sharp changes in bending extent of a catheter.

In this study,  $G^2$  continuous quintic Hermite spline is proposed for connection smoothing. And it is compared with  $C^1$  continuous cubic Hermite spline. With the cubic Hermite spline, four parameters are needed: two control points and their related derivatives. To obviate loops, cusps or folds, an optimized geometric Hermite has been considered. It is defined by optimizing the magnitudes of the endpoint tangent vectors in the Hermite interpolation process so that the strain energy of the curve is a minimum. With the quintic Hermite spline, not only the continuity of first derivative is ensured, but also curvature gaps in the connections will be reduced. In this case, the values of second derivatives are also needed to calculate such a polynomial.

## RESULTS

The proposed method is performed on the datasets, and the result is shown in Figure 1. It shows that  $G^2$  quintic Hermite curve method ( $M_2$ , Figure 1C) generates a smoother connection at the coincident points than the planning without smoothing ( $M_0$ , Figure 1B). Compared with the  $C^1$  cubic method ( $M_1$ ),  $M_2$  indicates a better performance in curvature continuity (see Figure 2). Moreover, the differentiability and curvature continuity are reported in Table I, and 40 trails for each set of ( $s^*$ ,  $M_i$ ) are performed. Two criteria are defined: difference of derivatives  $f_d = |p^+ - p^-|$  between both sides of the coincident point; difference of curvatures  $f_c = |s^+ - s^-|$ . By comparison, the differentiability and continuity of curvature is improved using the quintic Hermite interpolator. The reported values validate that a great improvement in the continuity of the curvature was obtained with the  $G^2$  quintic Hermite method, because its main strength is the control over the second derivative.

## CONCLUSION AND DISCUSSION

In this work, a continuous-curvature path planning method is proposed for endovascular catheterization. The direct connection between two curve segments would lead to non-differentiability at the coincident setpoints.  $G^2$  continuous quintic Hermite splines are proposed to handle the connection problem to ensure differentiability and continuity of the curvature itself. In the future, some other factors will be considered for developing intra-operative navigation: (i) the unpredictable environment deformation; and (ii) the uncertainties of model sensing (e.g. the tip position and vascular model).

## ACKNOWLEDGEMENT

This project has received funding from the European Union's Horizon 2020 research and innovation programme under the Marie Skłodowska-Curie grant agreement No 813782. The authors also thank Prof. Maria Francesca Spadea and others for datasets support.

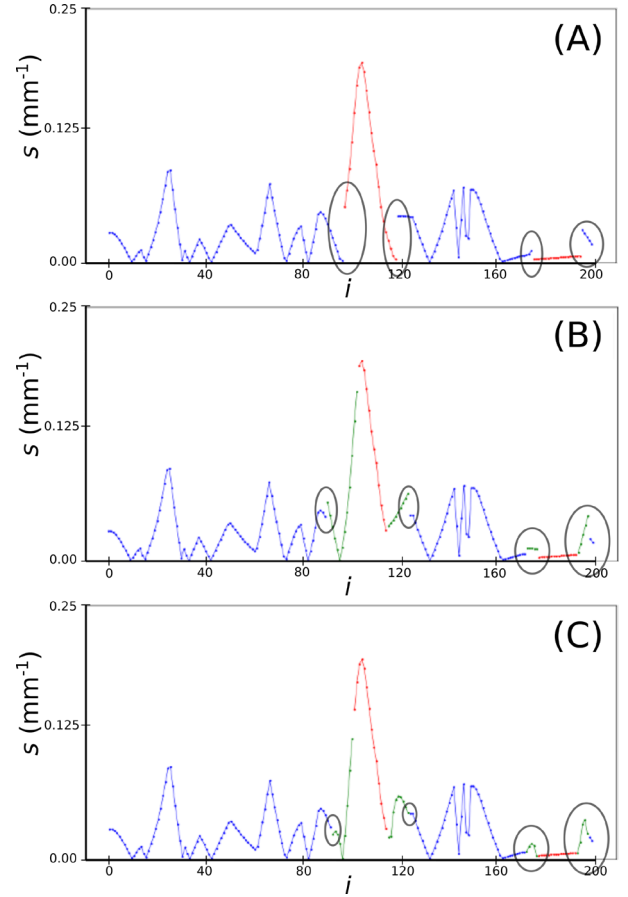


**Figure 2.** Curvature of the planned path via method (A)- $M_0$  (B)- $M_1$  (C)- $M_2$ . Blues represent curvature of the curve along vascular centerlines. Reds are curvature of the optimized path. Greens depict curvature after connection smoothing.

**Table I.** Performance comparison. The marks (\*,  $p < 0.05$  Kruskal-Wallis test) represent the statistical significance of ( $M_0, M_1$ ), ( $M_1, M_2$ ), ( $M_0, M_2$ ), respectively.

$s^*$		$M_0$	$M_1$	$M_2$	$p$
0.40	$f_d$	$6.06 \pm 3.14$	$0.30 \pm 0.19$	$0.20 \pm 0.04$	(***)
	$f_c$	$0.356 \pm 0.238$	$0.041 \pm 0.008$	$0.016 \pm 0.005$	(***)
0.46	$f_d$	$5.80 \pm 3.85$	$0.23 \pm 0.08$	$0.22 \pm 0.09$	(*)
	$f_c$	$0.365 \pm 0.243$	$0.041 \pm 0.013$	$0.011 \pm 0.011$	(***)
0.54	$f_d$	$5.25 \pm 3.28$	$0.23 \pm 0.09$	$0.20 \pm 0.08$	(***)
	$f_c$	$0.405 \pm 0.257$	$0.024 \pm 0.011$	$0.019 \pm 0.008$	(***)

## REFERENCES

- [1] P. Bruno, P. Zaffino, S. Scaramuzzino, S. De Rosa, C. Indolfi, F. Calimeri, and M. F. Spadea, "Using cnns for designing and implementing an automatic vascular segmentation method of biomedical images," in International Conference of the Italian Association for Artificial Intelligence. Springer, 2018, pp. 60-70.
- [2] A. Ali, A. Sakes, E. A. Arkenbout, P. Henselmans, R. van Starkenburg, T. Szili-Torok, and P. Breedveld, "Catheter steering in interventional cardiology: Mechanical analysis and novel solution," Proceedings of the Institution of Mechanical Engineers, Part H: Journal of Engineering in Medicine, vol. 233, no. 12, pp. 1207-1218, 2019.
- [3] R. Herzog and P. Blanc, "Optimal  $g^2$  hermite interpolation for 3d curves," Computer-Aided Design, vol. 117, p. 102752, 2019.

# A Vision-Based Trocar Site Force Sensing Technique

Jilmen Quintiens<sup>1</sup>, Jef De Smet<sup>1</sup>, Emmanuel B. Vander Poorten<sup>1</sup>

<sup>1</sup> KU Leuven, Department of Mechanical Engineering, Celestijnenlaan 300, Leuven, Belgium  
jilmen.quintiens@kuleuven.be

## INTRODUCTION

Minimally invasive surgery leads to high patient satisfaction, but puts an increased strain on the surgeon. Excessive loading of the patient's abdominal wall can lead to complications such as trocar site hernia (TSH). Therefore, the development of force sensors leads to tools and feedback systems, aiding in complication prevention [1]. However, mechanical sensors have various practical limitations. Therefore the application of vision-based force sensing can enable more cost-effective, intuitive and less invasive measurement systems [2].

Conventional visual force sensing techniques such as digital image correlation and visual-based finite element models are difficult to implement in the operating room: they are not flexible and often do not work real-time. Therefore a simplified model is suggested. In this *Circular Deformation Model*, a circular marking is applied on the abdominal tissues and its deformation modes are linked to tissue loading.

## MATERIALS AND METHODS

### (A) Physical setup

The experimental setup consists out of a box with a circular opening in the top lid. A synthetic body wall (EcoFlex 00-50, thickness=20 mm ; Young's modulus=82.7 kPa) was clamped inside the circular opening, modeling abdominal tissue. At the bottom of the box, a webcam (HP, 2300HD, resolution 1280×720 px) was fixated. The camera looked upon a circular silicon marking, adhered to the body wall ( $\pm 900$  px/cm<sup>2</sup>).

On the body wall, different loading tasks have been executed and the force was recorded with a sensor developed by De Smet et al. [3]. The tasks consisted of loading the body wall in all principal directions separately, in arbitrary in-plane directions and in three DoF directions.

### (B) Software for deformation tracking

An iterative algorithm has been developed where in each frame contour deformations are modeled as ellipses, of which the features are stored for the entire duration of the measurement. The algorithm comprises four main parts:

1) *Calibration*: Based on user input, parameters for both a circular region of interest and an edge thresholding scheme are determined.

2) *Canny edge thresholding*: Binary frames are computed based on a Canny edge detection scheme with hysteresis thresholding.

3) *Contour extraction and ellipse fitting*: Region growing algorithms extract contours from the image on

which elliptical shapes are registered by means of a least-squares approach.

4) *Cost assessment*: Elliptical likelihood is assessed with a cost function comprising internal cost (i.e. based on similarity with previous detections) and external cost (i.e. based on the elliptical attribute of constant cumulative contour point - focal points distance):

$$C_{int} = \alpha_c \sqrt{(x_{c,i} - x_{c,i-1})^2 + (y_{c,i} - y_{c,i-1})^2} + \alpha_r \sqrt{(R_i - R_{i-1})^2 + \alpha_r \sqrt{(r_i - r_{i-1})^2}}$$
$$\Delta F_{k,j} = \sqrt{(F_{kx} - x_j)^2 + (F_{ky} - y_j)^2}$$
$$C_{ext} = \alpha_{shape} \frac{\sum_{j=1}^n |\Delta F_{1,j} + \Delta F_{2,j} - R_i|}{n}$$

With current frame  $i$ , elliptical center  $(x_c, y_c)$ , extracted contour points  $(x_j, y_j)$ , long and short axis  $R$  and  $r$ , focal points  $F_1$  and  $F_2$  and weighting factors  $\alpha$ .

### (C) Signal alignment

Force and visual signals from the two independent measuring units are aligned in time. This is achieved by resampling, low pass filtering, rough and detailed alignment. Rough alignment is based on manual input, detailed alignment corrects small mismatches based on correlation maximization. Global relations between aligned visual and force signals, as well as linear approximate ranges, were investigated using the coefficient of determination  $R^2$ .

### (D) Model validation

Justification of elliptical shape approximation of deformed contours is investigated with two validating strategies: based on external cost in function of load amplitude; and based on power spectral density of higher harmonics in the discrete contour representation (where absolute elliptical shapes have one frequency per coordinate function).

## RESULTS

### (A) Model validation

As comparative standards, the costs of a perfect ellipse, a two-ellipse-hybrid with a wide ellipse representing compression and a small ellipse for tension, and an intermediate shape, all of similar resolution as the camera feed, were calculated, which amounted to 0.279 px, 12.281 px and 4.351 px respectively. Circular baseline contour cost lied around 1.15 px, a surplus attributed to shape imperfections. Cost rose with in-plane force amplitude, but not in a consistent relation. The increase was limited to a relative amount of maximal 25%-30%, with outliers up to >40%, but the absolute cost rarely surpassed 1.5 px. From a certain threshold on, cost maintained its increased level (Figure 1), but never reached costs indicating the alternate model outcomes.

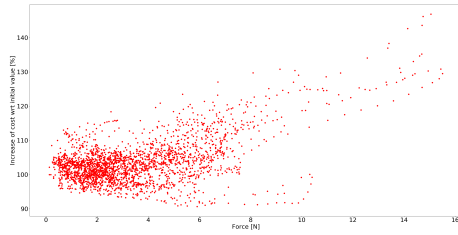


**Figure 1:** Elliptical cost in function of in-plane loading

A profound frequency analysis was prohibited because screen discretization resulted in an artefact where even perfect ellipses required higher harmonics for visually perfect reconstruction, making no standard available.

### (B) Force estimation

Perpendicular force related linearly with radial increase/decrease ( $R^2=0.95-0.97$ ), with gradients ranging from 0.41-0.51 N/px and zero deformation offsets ranging from 0.31-0.66 N. Also, a second degree parabola fitted the data as well ( $R^2=0.97-0.99$ ). In-plane force related linearly with center displacement ( $R^2=0.84-0.96$ ), with gradients ranging from 0.41-0.52N/px and zero deformation offsets ranging from 0.11-0.81N. Eccentricity (i.e. elliptical axes ratio) also showed peak to peak correspondence with in-plane loading, but the measure showed a higher sensitivity, where initial base shape deviations resulted in highly altered patterns and unintentional perpendicular loading gravely altered the eccentricity's value. These relations were used for arbitrary force reconstruction (example Figure 2). Results encompassed the signal's wave form, but were generally an overestimation. Linear regression did not give significant differences as compared to parabolic regression for the perpendicular force. In-plane forces were better reconstructed than three DoF forces since the radial parameter is also interdependent on in-plane loading.

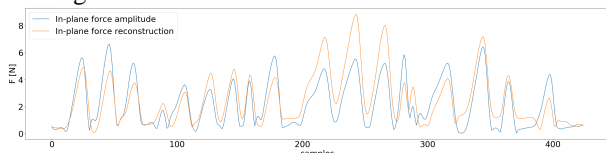


**Figure 2:** Example of a two DoF reconstruction

### (C) Non-linearities' influence

For high force amplitudes, the linear relation became more violated, pointing towards non-linear components influencing the relation. An iteration was performed where  $R^2$  was calculated based on high force samples only, with a varying threshold. For the first in-plane direction,  $R^2$  dropped from {0.94; -1.13} for  $F_{\text{thresh}} = \{7.5\text{N}; 7.6\text{N}\}$ . Number of samples for coefficient calculation were {14; 12}. For the other in-plane direction,  $R^2$  dropped from {0.89; 0.75; 0.19} for  $F_{\text{thresh}} = \{8.7\text{N}; 8.8\text{N}; 8.9\text{N}\}$ , with number of samples {54; 50; 49}. The perpendicular direction showed no sudden drop in  $R^2$  value, but rather a steady decline, where at 7.5N,  $R^2$  had decreased to 78% of its original value, and at 8.7N it had further decreased to 67%.

### (D) Force classification

Next to force estimation, force classification in high load / low load classes is also considered. Gaussian discriminant models, Fisher discriminant models and support vector machines with various kernel functions have been trained with elliptical attributes and cost as features, and their diagnostic value is predicted with repeated random sequence 10-fold cross-validation. With an estimated sensitivity of 85-86% and specificity of >99%, support vector machines with 3<sup>rd</sup> degree and radial base kernel functions show the most potential. Moreover they are relatively invariant to the class threshold force.

## CONCLUSION AND DISCUSSION

With the aim of practical force sensing during surgery, a pilot study to a vision-based force sensing technique is presented. Tissue deformation is modeled as elliptically shaped and elliptical attributes are related to loading. Linear relations can be deduced, but these are limited in valid range. Due to circumstances only a limited amount of measurements could have been executed. Lack of data could influence numerical significance. Moreover, these measurements were performed arbitrarily with different variance over the different tasks. Cross-talk (i.e. unintentional force components) occurred in single direction measurements, influencing the regression parameters. Hence, the repeatability of numerical results should be investigated. The circular marking on the body wall had a non-circular bias, making the fitted base shape elliptical instead of circular. This made the eccentricity relation more sensitive as different in-plane loading conditions could, depending on the orientation, both increase or decrease this parameter.

Framerates up to 40 fps are achieved. These were, however, based on a smaller resolution (640×480 px) than the HD capacity of the camera. Segmentation strategies can be improved in robustness, to account for field of view ambiguities. Possibilities are histogram based techniques or a Hough transform combined with parallel computing, reducing computational time.

Tissues are known to have hyper- and viscoelastic properties. More advanced reconstruction techniques, incorporating prior sample data, and soft-tissue models can be used to account for loading history dependence. Moreover, material parameters of the EcoFlex body wall are inherently different from the real abdomen (anisotropic, layered composition), implying possible different numerical results for real-life tissues. Introducing a more robust experimental setup for the acquirement of a larger dataset will be the first point of interest in a follow-up study. With this larger and more representative dataset, the compatibility with more elaborate soft-tissue models will be investigated.

## REFERENCES

- [1] T. Ortmaier, B. Deml, B. Kübler, G. Passig, D. Reintsema and U. Seibold, "Robot Assisted Force Feedback Surgery," in *Advances in Telerobotics*, Berlin, Springer, 2007, pp. 361-379.
- [2] M. A. Greminger and B. J. Nelson, "Vision-based force measurement," *IEEE Transactions on Pattern Analysis and Machine Intelligence*, vol. 26, no. 3, pp. 290-298, 2004.
- [3] J. De Smet, J. Deprest and E. B. Vander Poorten, "In Vivo Force Sensing During Laparoscopic Sacrocolpopexy Vaginal Vault Manipulation," *Journal of Medical Robotics Research*, vol. 4, no. 02, p. 1950003, 2019.

# Validation of a high-fidelity neonatal pneumothorax simulator with expert neonatologists

S. Maglio, S. Tognarelli, A. Menciassi<sup>1</sup>

<sup>1</sup>*The BioRobotics Institute, Scuola Superiore Sant'Anna  
s.maglio@santannapisa.it*

## INTRODUCTION

Pneumothorax (PTX) is the presence of air in the pleural space. It causes a partial or complete lung collapse and can lead to major clinical complications. The incidence of PTX in the neonatal period is higher than in any other period of life and leads to death in 20% of cases. Radiological survey showed a PTX incidence of 1-2% in term neonates of which most are asymptomatic and only 0.05-0.1% are symptomatic[1], [2].

The PTX is an emergency condition; few minutes of delay in intervention can lead to patient's death. Thus, it is advised to act immediately with the decompression procedure (DP) each time a PTX is suspected, even if it turns out that the suspect was wrong[3]. The emergency DP consists of positioning the infant supine and inserting a Butterfly 25G needle at the mid-clavicular line level in the 2<sup>nd</sup> or 3<sup>rd</sup> intercostal space (IS). The needle is inserted as close as possible to the lower rib to avoid any damage to the superior sensitive structures.

Simulation is an effective educational technique for medical students and residents, and a very useful retraining tool for expert neonatologists, where relevant clinical contents are reproduced to promote the deliberate practice[4]. It aims to improve interventional techniques and comfort during clinical procedures and to maintain the skills over time without placing the patient at risk. Literature demonstrated the use of high-fidelity simulators is valuable for all those cases where the development of specific and fine motor skills is needed, as in the case of PTX. High-fidelity simulator allows the reproduction of the required operative gestures on advanced manikins avoiding the occurrence of dangerous movements, thus risks and side effects for the patients[5]. A valid teaching and retraining simulation tool for PTX should present the following features: *i)* allow the identification of the correct IS through the anatomical references; thus, it should present an accurate simulation of the anatomy both in terms of dimensions and mechanical properties; *ii)* reproduction of the tissue penetration feedback and the entire IS; perceive the lower rib is fundamental to learn where the needle should be inserted; *iii)* reproduction of the syringe plunger return feedback when PTX is solved; this is crucial to understand when the procedure has to be stopped; *iv)* tools providing feedback on the proper execution of DP. Commercial PTX simulators, dedicated research prototypes and patents are currently available. To the best of the authors knowledge the existing commercial solutions consist or in specific adult manikins or in neonatal simulators that provide a poor simulation of PTX. In addition, research prototypes reported in

literature are almost low-fidelity simulators, and only one is for newborn[6], [7].

In this framework, the objective of this work is the development and assessment of a neonatal PTX simulator with expert neonatologists. The simulator validity was investigated as teaching and retraining tool by asking to the clinicians to perform on it an entire DP and evaluating the fidelity of the proposed simulator, both in terms of chest anatomy and PTX physiology.

## MATERIALS AND METHODS

Simulate the PTX means reproducing the pleural space: an airtight chamber delimited by the lung, diaphragm, chest wall and mediastinum (figure 1A). All these structures were reproduced in the simulator through Additive and Formative Manufacturing Technologies and using materials that better simulate the mechanical properties of human tissues, as Ecoflex series silicones and TPU (Thermoplastic polyurethane). The simulator presents a compliant TPU neonatal ribcage incorporated into a silicone chest wall, two lungs, a heart, a mediastinum and two dedicated areas for the needle insertion in the 3<sup>rd</sup> ISs (figure 1B). A simulated diaphragm was realized and glued to close the left and right pleural space at the manikin bottom and to connect them to the simulator hardware. Head, arms and a cover skin were then added to make the training procedure as realistic as possible (figure 1C).

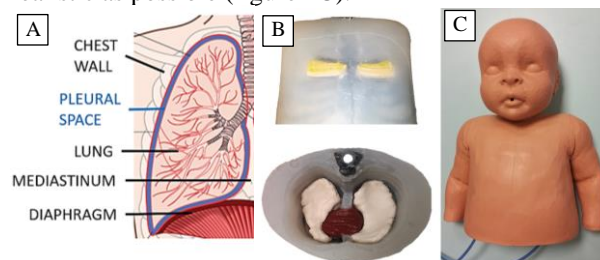


**Figure 1.** (A) Chest anatomy. (B) Simulator internal structures. (C) Complete simulator.

The simulator actively generates the tension inside the two pleural spaces through two air pumps, and it parametrically controls the internal pressure by means of two pressure sensors and the Arduino Uno microcontroller. Simulator management software and a user-friendly graphical-user interface (GUI) were implemented by using LabView software (figure 2). GUI permits to control the pressures inside the pleural space with both graphical and numerical outputs and it allows to activate the two air pumps for simulate the presence of air in the pleural space.

System validation process involved 10 expert neonatologists with, in average, 10 years of experience in



a 3B level Neonatal Intensive Care Units (NICU), and with previous experiences in simulation – they performed at least one DP on the simulator.

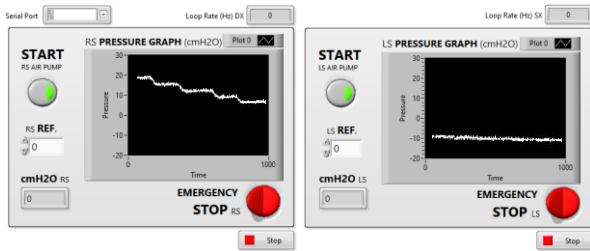


**Figure. 2.** Simulator interface. The left panel controls the right pleural space and the right panel controls the left one.

During the PTX DP, the physician uses a 10ml traditional syringe equipped with a three-ways valve connected to a thin and long tube whose end part consists of a Butterfly 25G needle. The syringe is filled with 2 ml of saline solution to easily visualize the air aspiration (figure3). Two surveys were submitted to the doctors before and after the DP. The pre-procedure survey aimed to quantify the physicians' previous experience and their general opinion about simulation. In the post-procedure survey, it was asked to evaluate the simulator features and its usefulness in teaching and periodical retraining courses. During each performed DP, a pleural pressure of 0mmHg was set and the pressure-time graph was showed to the physician for all the time.



**Figure. 3.** Neonatologist performing the DP on simulator.

## RESULTS

The proposed simulator presents all the features previously listed as required to be considered a valid teaching and retraining tool.

The physicians involved in the validation session belong to an homogeneous population: they have performed, in average, from 5 to 10 DPs during their career, 0 to 2 times during the last year and the last time they solve a PTX was less than six months ago.

In table 1 are reported the average scores of the main questions of pre- and post-procedure surveys. In brackets there are the scales of evaluation: (1-10) where a score 1 means a totally negative judgement or a question subject different from reality and 10 means a totally positive judgement or extreme fidelity of the question subject; (1<5<10) where 5 indicates an equal stiffness, scores >5 for stiffer tissues and scores <5 for softer tissues.

Pre-procedure survey	Score
Do you consider the simulation useful in clinical practice? (1-10)	9.5
Do you consider the simulation useful in teaching? (1-10)	9.6
Do you consider the simulation useful in periodical retraining? (1-10)	9.1

Post-procedure survey	
What is your overall assessment of the simulator? (1-10)	9.1
Is the simulator anatomy accurate? (1-10)	8.5
Is the ribcage stiffer, softer, or equal to reality (1<5<10)	6.1
Are the soft tissues stiffer, softer, or equal to reality (1<5<10)	5.7
Is the needle penetration feedback equal to reality (1-10)	7.5
Is the PTX volume equal to reality? (1-10)	8
Do you consider the high-fidelity simulation useful in teaching and retraining? (1-10)	9.5
Which is your overall judgment of the proposed simulator compared to tested commercial simulators? (1-10)	9.2

**Table. 1.** Surveys main questions and average scores.

## CONCLUSION AND DISCUSSION

PTX DP were simulated. An initial difficulty was observed in using the three-way valve, which highlighted the need of clear and real-time feedback on the procedure execution. This feedback is provided by the proposed simulator through the interface and more in detail with the pressure plots. Moreover, the simulator was recognized as an immersive training system allowing a complete skills development by the residents and becoming a valuable retraining tool for experienced physicians; every single phase of the DP can be trained and mastered with the simulator, unlike current commercial solutions. In fact, the latter do not present the fundamental feedback to understand the correct course of the procedure and its end, leading to a partial learning. Consequently, the learning gaps will only be filled when the DP is performed on the first patients, exposing them to avoidable and therefore unjustifiable risks.

In the future, for a more complete validation of the system, a specific experimental protocol involving residents will be carried out and a deep comparison of obtained results with the results from other commercial simulators could be also interesting.

## REFERENCES

- [1] H. H. Duong *et al.*, "Pneumothorax in neonates: Trends, predictors and outcomes," *J. Neonatal. Perinatal. Med.*, vol. 7, pp. 29–38, 2014.
- [2] H. Esme *et al.*, "The factors affecting persistent pneumothorax and mortality in neonatal pneumothorax," *Turk. J. Pediatr.*, vol. 50, no. 3, pp. 242–246, 2008.
- [3] T. L. Gomella, *Neonatology : Management, Procedures, On-Call Problems, Disease and Drugs*. 2004.
- [4] J. J. Fehr *et al.*, "The important role of simulation in sedation," *Curr. Opin. Anaesthesiol.*, vol. 29, pp. S14–S20, 2016.
- [5] N. J. Maran and R. J. Glavin, "Low- to high-fidelity simulation – a continuum of medical education?," *Med. Educ.*, vol. 37, no. s1, pp. 22–28, 2003.
- [6] V. Martinuzzi *et al.*, "Pneumothorax training system," *IMECE2015*, pp. 1–6, 2015.
- [7] A. O. Gupta and J. Ramasethu, "An innovative nonanimal simulation trainer for chest tube insertion in neonates," *Pediatrics*, vol. 134, no. 3, pp. e798–805, Sep. 2014.

# Pediatric Neurosurgical Robot: From Requirements to Development

Nabeel Kamal<sup>1</sup>, Armando Cama<sup>2</sup>, Leonardo S. Mattos<sup>1</sup>

<sup>1</sup>*Biomedical Robotics Lab, Advanced Robotics Dept., Istituto Italiano di Tecnologia*

<sup>2</sup>*Integrated Department of Medical and Surgical Neuroscience and Rehabilitation, Istituto  
Giannina Gaslini*

*{nabeel.kamal, leonardo.demattos}@iit.it, armandocama@gaslini.org*

## INTRODUCTION

Modern pediatric neurosurgery started with the work of Ingraham in around 1929 [1], which later led to the first textbook on pediatric neurosurgery published in 1954. Robotic surgery has seen its dawn almost twenty-five years ago, and the first reported surgical procedure was a neurological biopsy. This procedure removed the hesitation for using robots in ORs and the world has seen remarkable advances in surgical robotics ever since.

Neuromate was the first commercial neurosurgical robot, introduced in 1987. Now, commercial robotic systems can perform a wide range of the minimal invasive neurosurgical procedures such as stereo electroencephalography (SEEG), deep brain stimulation (DBS), targeted radiotherapy, and endoscopic third ventriculostomy (ETV). However, despite all the progress in this area, the literature on robotic neurosurgery in neo-natal and infants is nowhere to be found [2].

To this day, there are several solutions to carry out robotic neurosurgical procedures such as Medtech's ROSA®, Renishaw's Neuromate®, and iSYS's iSYS1. All of these systems are designed for adults. To the best of our knowledge, pediatric robotic neurosurgery using these systems has never been reported.

In the United States, there are 70,000 surgeries for treating hydrocephalus annually. 4 out of 1000 children are born with hydrocephalus [3], with estimated treatment costs amounting to nearly 2.0 billion US dollars. Surgeons perform these procedures manually, which is extremely difficult and risky for the babies. Therefore, there's a vast need for pediatric neurosurgical robots.

To understand why currently robots are not appropriate for infants, we should first understand the anatomy of the newly born baby skull: It is not fully developed (calcified), so it is soft. This means that the head fixation methods required by current neurosurgical robots (e.g. stereotactic frames) cannot be used in babies, as they can cause complications. Also, the large size of current neurosurgical robots is another significant issue, as they tend to significantly disrupt the regular workflow of the OR. This is critical pediatric neurosurgery as the workspace around the baby is very small, requiring the close presence of at least 3 clinicians, as shown in Fig. 1. Consequently, a new type of robot that can integrate seamlessly to the OR, causing minimal disruption and providing the required precision and workspace, is needed for pediatric neurosurgeries. Here, we present the

engineering requirements for one such system and propose a novel design to achieve them.

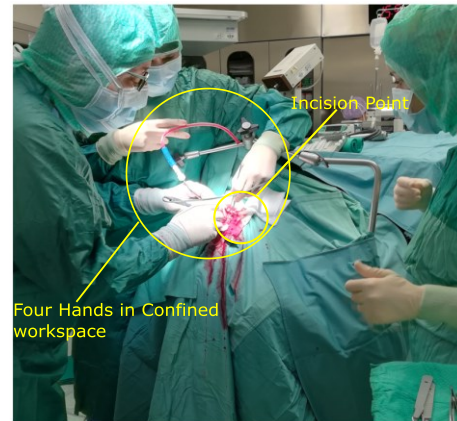


**Fig. 1:** Typical scenario of state-of-the-art pediatric neuroendoscopy.

## REQUIREMENTS

The engineering requirements for a new pediatric neurosurgical robot was defined by observing real surgeries and the environment of the operating room. In addition, the MRI of a newborn head was obtained and converted to a CAD model, as shown in Fig 2 (a). It was observed that the surgeries use one fixed entry point into the skull, through which a rigid surgical endoscopic sleeve is inserted (later on an endoscopic camera with surgical tools are inserted). The orientation of the endoscope is established before entry, based on a pre-operative plan and using intraoperative electromagnetic navigation. The references are Anterior-Posterior and Lateral-Medial angles. The endoscope is inserted by a very slow translation motion, which is constantly tracked using the navigation system. When the treatment area is reached, the endoscope is locked in place and the surgeon operates through the endoscope working channels.

In this work, the focus is on designing a new robot to enable precise and delicate insertion of the endoscope. It should also provide rigid and stable support for the subsequent manual surgical actions. The total size of the robotic system is also a key parameter. So the maximum size of the robot should be proportional to the surgical table, which is mentioned in Table.1. Therefore, from the description above it is clear that at least 3 DOFs are required to enable two rotations and one translation. Besides, the entry point configuration requires 3 more DOFs to place it precisely on the skull. Based on the MRI profile and the motions around it as shown in Fig 2(b),

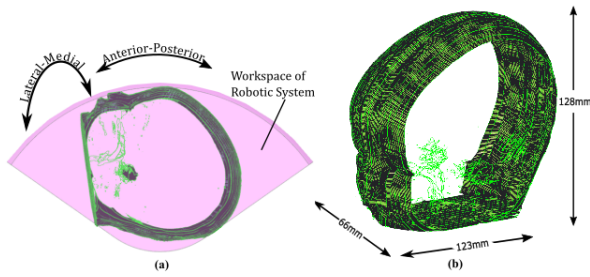


**Fig. 2:** (a) Required kinematic workspace (b) Real MRI of a baby's head converted to a CAD model.

**Table 1:** Design Parameters

Required Parameter	Value
Max. Robot Size	1000x1000x600 mm
Motions	AP= $-55^{\circ}$ to $55^{\circ}$
	LM= $-60^{\circ}$ to $60^{\circ}$
	Depth = 130 mm
	$\Delta X > 150\text{mm}$ , $\Delta Y > 70\text{mm}$ , $\Delta Z > 100\text{mm}$
Precision	100 microns

two circular and a translation motion are required for the intervention. The robotic system should allow  $-55^{\circ}$  to  $55^{\circ}$  in AP,  $-60^{\circ}$  to  $60^{\circ}$  in LM and at least 130 mm of depth motion.

Finally, another major requirement is to avoid interference with the neuro-navigation system.

### DESIGN OF THE ROBOTIC SYSTEM

Minimally invasive surgical robots typically required a Remote Center of Motion (RCM), which should be at the incision point to avoid damaging tissue around it. Here, we decided to use 3 DoFs to position a RCM point at the incision location, and another 3 DoFs to adjust the orientation and insertion of the surgical endoscope.

The RCM positioning is implemented with linear movements along the lateral and normal directions to the surgical bed ( $M_x$ ,  $M_y$ , and  $M_z$  on Fig. 3). The robotic system is designed to be mounted on the bed to minimize interference to the surgical workflow. It will be fabricated with non-magnetic material to avoid interfering with the intraoperative neuronavigation system. To help on this, we proposed a design that places most of the robot components under the operating table. The robot design resembles a Leksell frame, which can be easily integrated to the neurosurgery environment. It features a circular rail guide of 150 mm in diameter. An endoscope insertion mechanism is mounted on the rail of the circular guide. In order to provide rigid support, the circular guide rail is supported from both ends.

A fully decoupled mechanism design was selected to facilitate system control and the achievement of high precision and accuracy in positioning the robot end-effector. To achieve this, a slide-in frame system was designed as shown in Figure 3. The inner frame supports the circular guide rail. This frame slides in an outer U-Shape frame, enabling motion in  $M_z$ . Motion along  $M_y$  is enabled using two linear guides, which are used to keep

the motion of the inner frame intact. In the same manner, both of these frames move in the direction of  $M_x$ . This mechanism ensures three DOFs remain uncoupled.

The other three DOFs, i.e Anterio-Posterior, Lateral-Medial, and depth, are also shown in Figure 2 (a), above the bed. The RCM of the robotic arm is achieved mechanically by using the isocenter of the circular guide rail and its actuator.

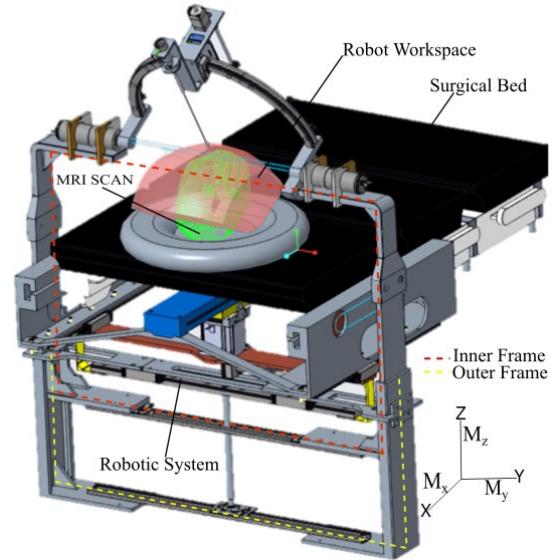


**Fig. 3:** Electro-Mechanical design of the robotic system.

### RESULTS AND DISCUSSION

A novel robotic platform has been designed and is under manufacturing based on a close collaboration with neurosurgeons. The overall volume occupied by the system is  $1016 \times 612 \times 167 \text{ mm}^3$ , but most of it is positioned under the operating bed. The mechanism above the operating table occupies a volume of only  $380 \times 612 \times 167 \text{ mm}^3$ . An initial proof-of-concept prototype was developed using stereolithography. The prototype allowed physical verification of the system with a pediatric neurosurgeon. After verifying the achieved workspace, as shown in Figure 2(a), surgeons confirmed the suitability of this design, mentioning it will likely be useful also for transnasal and trans mucus interventions. This robot was primarily designed for Endoscopic Third Ventriculostomy (ETV), but other potential indications can include Ventricular shunt, Biopsy and Deep Brain Stimulation (DBS). Next steps include the completion of the system fabrication, the design and implementation of its control system, and the execution of a series of testing and validation experiments.

### REFERENCES

- [1] L. K. Page, "History of pediatric neurosurgery in the United States and Canada," *Child's Nerv. Syst.*, vol. 7, no. 1, pp. 53–55, Feb. 1991.
- [2] J. J. Meehan, "Robotic Surgery for Pediatric Tumors," *Cancer J.*, vol. 19, no. 2, pp. 183–188, 2013.
- [3] M. J. McGirt, A. Zaas, H. E. Fuchs, T. M. George, K. Kaye, and D. J. Sexton, "Risk Factors for Pediatric Ventriculoperitoneal Shunt Infection and Predictors of Infectious Pathogens," *Clin. Infect. Dis.*, vol. 36, no. 7, pp. 858–862, Apr. 2003.



# Adaptive Neural Network for Modelling and Control of a Serial-Link Manipulator and a Surgical Robotic Tool

Francesco Cursi<sup>1,2</sup> and Petar Kormushev<sup>2</sup>

<sup>1</sup>*Hamlyn Centre, Imperial College London*

<sup>2</sup>*Robot Intelligence Lab, Imperial College London*

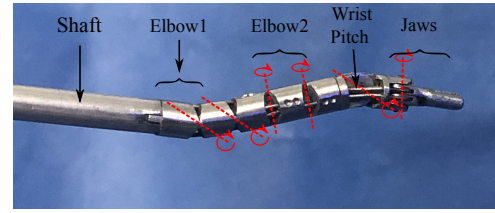
<sup>1</sup>*[f.cursi17,p.kormushev]@imperial.ac.uk*

## I. INTRODUCTION

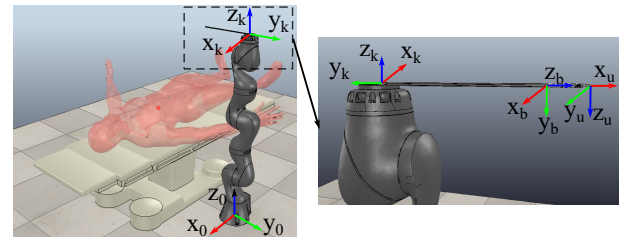
Accuracy and precision are of uttermost importance in many robotic applications, especially in minimally invasive surgery, where little (or preferably no) damage should be produced to the patient's body. In order to be able to perform surgeries, robots need to be safe, precise, and capable of adapting to different situations. However, modelling the kinematics of surgical robots may be very challenging. Machine learning and data-driven approaches have been having a huge impact on robot modelling, since analytical models may be hard to obtain due to the complexity of the systems [1]. In fields like robotic surgery the robot model need to be able to quickly adapt to the changing environment. As a matter of fact, significant modeling errors can occur during operation due to both neglected mechanical phenomena (e.g., nonlinear elasticity, wear or break of tendons) and perturbations, such as tool insertion and removal [2] or fluids (like blood) in the system that change the friction parameters. Traditional robot open-loop and closed-loop control techniques, which depend on an accurate models may not promise system stability or optimal control for the system. Therefore, an adaptive control strategy might be needed [3].

Another important aspect to consider in robotic surgery is the presence of a Remote Center of Motion (RCM). In order to guarantee RCM motion, serial-link manipulators can be used in conjunction with surgical tools to increase the number of Degrees of Freedom (DOFs) of the whole system [4]. Then, the RCM motion is guaranteed by properly controlling the whole system. Nevertheless, these control based techniques require the kinematic model of the system, both of the serial-link manipulator and the surgical tool.

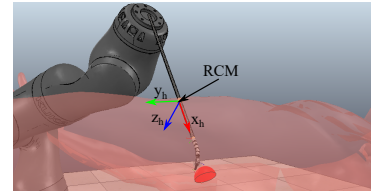
In this work we present an approach to effectively model a surgical robotic system and use the learned model, alongside the model of a known serial-link manipulator, to perform surgical tasks autonomously. Feedforward Artificial Neural Networks (ANN) are used to first build the forward kinematic model of the surgical robot offline. To deal with possible unpredictable changes in the model and not sufficient generalizability



(a) The Micro-IGES robot



(b) Total robot setup



(c) Remote Center of Motion

Fig. 1: The micro-IGES and the simulated environment.

of the ANN, an online adaptive strategy is also included. ANN have been chosen thanks to their ability to model complex functions and because their parametric nature allows to easily and analytically compute the network derivatives, which are needed for solving the inverse kinematics of the robot and for updating the model. The proposed method is shown in a simulation environment based on VREP simulator [5] for a tumor resection task (Figure 1).

## II. METHOD

### A. Micro-IGES Surgical Robotic Tool

The Micro-IGES [6] (Figure 1) is a surgical robotic tool, composed of a rigid shaft and a flexible section. In total it has 5 DOFs, plus the gripping. Each joint of the articulated part is driven by an antagonistic



pair of tendons, with each pair being connected to the corresponding driving capstan at the proximal drive unit. In this work, the motor to joint mapping is the same as in [7].

### B. Motion Control

In order to optimally exploit the hyper redundancy of the system, the Hierarchical Quadratic Programming framework (HQP) [8] is employed, which permits to specify motion tasks with different priorities: keeping the RCM fixed is the higher priority task; follow a desired path (in order to remove the tumor) is the secondary task. The control problem is then formulated as:

$$\begin{aligned} \dot{\mathbf{q}}_n &= \arg \min_{\dot{\mathbf{q}}} \frac{1}{2} \|\dot{\mathbf{h}}_n - \mathbf{J}_{h,n} \dot{\mathbf{q}}\|^2 \\ \text{s.t. } \mathbf{J}_{h,n-1} \dot{\mathbf{q}} &= \mathbf{J}_{h,n-1} \dot{\mathbf{q}}_{n-1} \quad , \\ \frac{\mathbf{q}_M - \mathbf{q}}{dt} &\leq \dot{\mathbf{q}} \leq \frac{\mathbf{q}_M - \mathbf{q}}{dt} \end{aligned} \quad (1)$$

where  $\mathbf{q}, \dot{\mathbf{q}} \in \mathbb{R}^{12}$  are the robot commands,  $\mathbf{J}_{h,n} = [\mathbf{J}_{Kuka} \ \mathbf{J}_{uIges}]$  the total robot Jacobian expressed in the base frame,  $n = 1$  corresponds to the task of guaranteeing RCM ( $\mathbf{J}_{h,1} = \mathbf{J}_{RCM}$ ) motion and  $n = 2$  is for the path tracking ( $\mathbf{J}_{h,2} = \mathbf{J}_{tot}$ ). For the primary RCM motion task,  $\mathbf{J}_{h,0} = \mathbf{0}$  and only joint limits are considered.

### C. Robot Modelling

The forward kinematic model of the Micro-IGES is first leaned offline, commanding the robot to follow a circular path, like the shape of the tumor to resect. ANN are employed for this purpose, mapping the motor values  $\theta \in \mathbb{R}^5$  to the 3D Cartesian tip position. The parametric nature of the ANN allows to analytically and easily compute the micro-IGES Cartesian Jacobian  $\mathbf{J}_{uIges}$ . To address the problem of possible unpredicted model inaccuracies, the neural network model is adapted online whenever the error between the expected tip position and the measured one (in a real scenario via electromagnetic trackers or vision) is larger than a certain threshold.

### III. RESULTS

To show the capabilities of the proposed adaptive modelling strategy and of the HQP control, the robot was required to follow a circular path, simulating a tumor resection, while guaranteeing the RCM motion. To simulate unpredicted model changes the Elbow 1 and Elbow 2 are assumed to be locked at  $10^\circ$  and  $20^\circ$  respectively. The proposed approach, however, does not have any knowledge about the changes in the model, but it only requires the measurement of the tip position for the adaptation. Results in Figure 2 show that the proposed approach is capable of relearning a good model and accurately perform the tracking task. The initial positioning error is due to the unmodelled locked joints. During the whole motion, the model was adapted 79 times. The mean absolute errors between the expected ANN output and the actual tip position along the  $x, y, z$  directions result to be  $[0.19 \ 0.28 \ 0.31] \text{ mm}$ , whereas

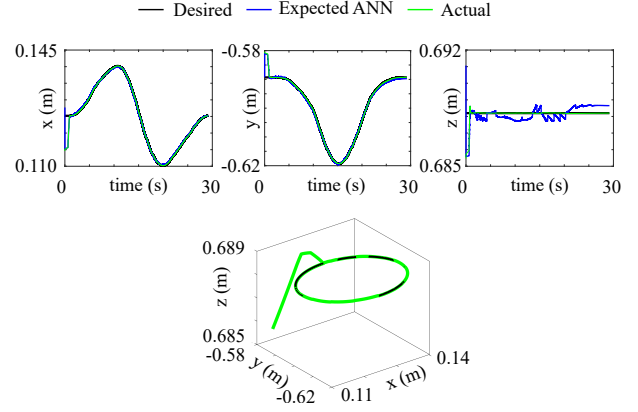


Fig. 2: Cartesian tip position for the path tracking simulating the tumor resection.

the mean absolute errors between the desired and the actual tip position are  $[0.05 \ 0.06 \ 0.01] \text{ mm}$ . With regards to the RCM, the mean absolute tracking errors are  $[0.51 \ 0.34] \cdot 10^{-3} \text{ mm}$  along  $y, z$  in the RCM frame (Figure 1c).

### IV. CONCLUSIONS

The proposed adaptive modelling approach resulted effective in relearning an accurate model of the robot, also in the case of unpredicted model changes. The control strategy proved capable of precisely perform the given motion tasks. Future work will focus on implementing the proposed approach on the real system, where the nonlinearities due to the tendon transmission make the modelling very challenging.

### REFERENCES

- [1] D. Nguyen-Tuong and J. Peters, "Model learning for robot control: a survey," *Cognitive Processing*, vol. 12, no. 4, pp. 319–340, 11 2011.
- [2] C. Kim, S. C. Ryu, and P. E. Dupont, "Real-time adaptive kinematic model estimation of concentric tube robots," in *IEEE International Conference on Intelligent Robots and Systems*, vol. 2015-December. Institute of Electrical and Electronics Engineers Inc., 12 2015, pp. 3214–3219.
- [3] D. Zhang and B. Wei, "A review on model reference adaptive control of robotic manipulators," pp. 188–198, 1 2017.
- [4] M. M. Marinho, M. C. Bernardes, and A. P. L. Bo, "Using General-Purpose Serial-Link Manipulators for Laparoscopic Surgery with Moving Remote Center of Motion," *Journal of Medical Robotics Research*, vol. 01, no. 04, p. 1650007, 12 2016.
- [5] "Coppelia Robotics V-REP: Create. Compose. Simulate. Any Robot." [Online]. Available: <http://www.coppeliarobotics.com/>
- [6] J. Shang, K. Leibrandt, P. Giataganas, V. Vitiello, C. A. Seneci, P. Wisanuvej, J. Liu, G. Gras, J. Clark, A. Darzi, and G.-Z. Yang, "A Single-Port Robotic System for Transanal Microsurgery—Design and Validation," *IEEE Robotics and Automation Letters*, vol. 2, no. 3, pp. 1510–1517, 2017.
- [7] K. Leibrandt, P. Wisanuvej, G. Gras, J. Shang, C. A. Seneci, P. Giataganas, V. Vitiello, A. Darzi, and G.-Z. Yang, "Effective Manipulation in Confined Spaces of Highly Articulated Robotic Instruments for Single Access Surgery," *Icra 2017*, vol. 2, no. 3, pp. 1–1, 2017. [Online]. Available: <http://ieeexplore.ieee.org/document/7855734/>
- [8] A. Escande, N. Mansard, and P.-b. Wieber, "Hierarchical quadratic programming : Fast online humanoid-robot motion generation," *International Journal of Robotics Research*, vol. 33, no. 7, pp. 1006–1028, 2014.

# High-Fidelity simulator of cervix changes during labour

C.Luchini, S.Tognarelli and A.Menciassi

*The BioRobotics Institute, Scuola Superiore Sant'Anna, Pisa, Italy*  
*c.luchini@santannapisa.it*

## INTRODUCTION

The cervix, which corresponds to the lower portion of the uterus, undergoes a structural transformation called *cervical remodelling* during labour. It is a continuous process that can be divided into four different phases: *softening* (corresponding to the softening of the cervical tissues), *effacement* (which is the gradual shortening of the cervix and it is usually evaluated in percentage from 0 to 100%), *dilation* (which coincides to the gradual opening of the cervix to accommodate the passage of the foetus head into the vagina and it is measured in centimetres from 0 to 10 cm) and *postpartum repair* (that is the recovery of tissue integrity). Cervix evaluation, in particular of its length, dilation and softness, is the only available intrapartum tool used by the medical doctors to manage delivery, and to take operative decisions, such as oxytocin use or caesarean delivery. Currently, the cervical assessment is still performed by a manual vaginal exploration during which the consistency, effacement and dilation are assessed only using index and medium fingers. This evaluation is therefore strongly subjective, thus reliability is very limited. Data reproducibility is the most important limit of the current methodology for delivery progress evaluation, also because several clinicians usually take part in the management of a single labour. Moreover, being manual capabilities strongly associated with experience, residents have to spend many hours in the delivery room for correctly learning how to make an accurate evaluation of the cervix, being no available alternatives in terms of training processes. To overcome this drawback, simulation plays a fundamental role in medical training. However, commercial simulators available on the market ([www.3bscientific.it](http://www.3bscientific.it), [www.birthinternational.com](http://www.birthinternational.com)) and prototypes reported in literature [1][2][3] are passive, static, low-fidelity and technically limited devices.

In this context, this work stemmed from the idea to design, develop and validate a High-Fidelity simulator for reproducing the changes that occur in the cervix during labour (i.e. softening, effacement and dilation). The device, developed with the collaboration of expert gynaecologists of the Azienda Ospedaliero Universitaria Pisana (AOUP), can be dynamic, modular, intuitive, easy to control, low cost and transportable.

## MATERIALS AND METHODS

The whole structure of the device (Figure. 1) is divided into three main sub-systems - each reproducing one of the changes that occur in the cervix, i.e. softening, effacement and dilation - assembled together in a support structure. During delivery, these phenomena occur in a

sequential way: first the cervix becomes soft, then the effacement occurs and, finally, dilation takes place. The same sequence of changes is reproduced in the system.

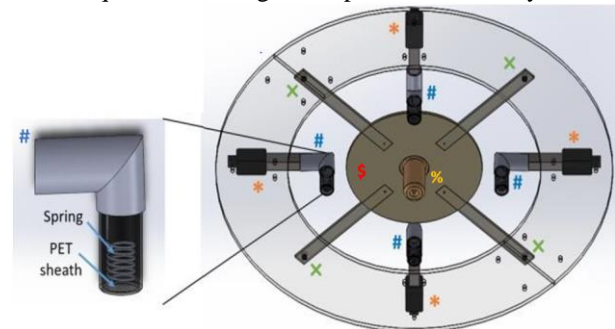


**Figure. 1. Rendering of the structure and its sub-systems.**

### A. Softening sub-system

The softening of the cervix is simulated by using granular jamming, a physical mechanism that allows to change a structure stiffness (central element in Figure 1). Key elements of granular jamming are: the membrane, the internal particles and the vacuum system. The membrane was realized through a moulding process with Ecoflex 0030 by Smooth-On (Smooth-On Inc., USA). The silicone membrane was filled with coffee powder, following the literature evidence [4], and a small flexible tube (2 mm in diameter), integrated into the coffee powder, was connected to an air pump motor for modulating the vacuum level. To control the softening process, the air pump was connected, through a Mosfet transistor, with Arduino MEGA 2560 microcontroller (Arduino AG, Italy). In order to assemble the softening module with the rest of the simulator, a 3 mm thick circular crown (\$) in Figure 1) was developed: it has a central hole for housing the body of the silicone structure and four bars equipped with four permanent magnets (x in Figure 1) used for attaching and detaching the softening sub-structure from the whole simulator.

### B. Effacement sub-system

Four independent structures (# in Figure 1) were realized for simulating the cervix effacement process. Human cervix shows a circular shape, however, the choice behind the idea to use four independent structures is for reducing the design complexity of the simulator while guaranteeing the ability to simulate both physiological and pathological shortening of cervix as for childbirth. The fundamental element of each single structure is a Nitinol (NiTi) Shape Memory Alloy (SMA) spring which allows for the realization of a sub-system that changes its length from 4 to 1 cm in a simple and quite fast way. The best trade-off between the anatomical cervical reduction that reaches 1 cm length starting from 4 cm, actuator force and activation current, led to using 1 mm diameter

NiTi wire for developing a torsion spring 8 mm in mean diameter featured by 4 active spring turns. Two commercial power supplies were included in the system, for powering the four SMA actuators. Experimental evidences showed that with a voltage of about 1.3 V and a current of about 3 A, the spring, once manually deformed for reaching the starting length of 4 cm, could return to its fabrication dimension in 0.5 seconds. However, because SMA actuators were not able to maintain a regular shape if repeatedly solicited, each NiTi spring was concentrically included into a preformed Polyethylene (PET) 5 mm in diameter sheath (# in Figure 1). In order to join the NiTi spring and the sheath and then close the two ends of the structure, two rapid prototyped bases equipped with two small gold rings permanently fixed into two holes, were fabricated. After connecting the spring to the rings, the two bases were glued to the ends of the sheath. The entire structure was then covered with Ecoflex 00-10 silicone to reproduce the same feeling of physiological tissue. The SMA actuators were controlled by an Arduino MEGA 2560 microcontroller together with an electronic circuit containing a relay module as the power supplies cannot be directly connected to the Arduino as they generate too high current.

### C. Dilation sub-system

Four linear actuators (\* in Figure. 1) are used to simulate the cervix dilation. Four L12-50-100-12-P Micro Linear Actuators made by Actuatorix Motion Devices (Actuatorix Motion Device Inc., Canada) were selected, as they are small in size and show an intuitive control. In addition, each motor has 5 cm of stroke, so by fixing them at 90° each other, the 10 cm cervix dilation, required to accommodate the passage of the baby head into the vagina, was obtained. In order to join the dilation sub-system with the effacement one, a Silicone Ecoflex 00-50 membrane 2 mm thick was obtained by moulding technique. The effacement sub-system was manually inserted into this membrane and fixed to the mobile end of the motor exploiting a dedicated 3D printed mock-up already screwed to the motor. Lastly, between one sub-system and the other, a preformed PET sheath, covered with Ecoflex 00-10 silicone and suitably fixed to the entire system, was added so that the circular shape (typical of the human cervix) remained with the variation of the dilation.

## RESULTS

The single components described in the previous paragraphs were assembled to reproduce the human cervix anatomy and physiology. In particular, the linear actuators with the effacement sub-system were fixed to a PMMA circular crown, fabricated by using the Laser Cutter machine (Universal Laser Systems Inc., USA), so that in the rest position (stroke of each motor equal to zero) the cervix dilation is 10 cm, and when the stroke of the motors is maximum (5 cm for each motor) a closed cervix is simulated. The softening sub-system was assembled with the rest of the structure thanks to four magnets included in both sub-systems. In order to easily transport the simulator, all the electronic components

were inserted inside a PMMA box made again by laser cutting. The overall assembly of the simulator is shown in Figure 2. To control the entire system, an intuitive user interface (GUI) was created with LabVIEW 2019 (National Instruments, USA). The GUI was made up of three blocks for easily managing the three sub-systems (Figure 3) thus for guaranteeing the sequential behaviour of the human cervix: softening, then effacement and, at the end, dilation, as it happens in nulliparous mother during labour. In order to validate the proposed system a preliminary assessment phase was carried out involving four ten-year experience gynaecologists. Medical doctors confirmed the effectiveness of the proposed device, both in terms of used materials and technologies.

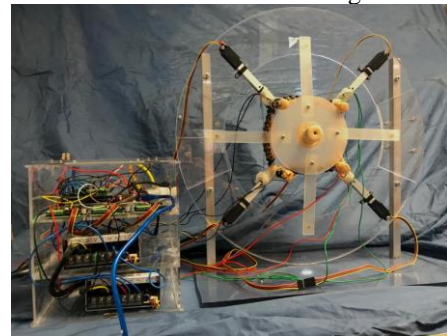


Figure 2. Assembly of the simulator.

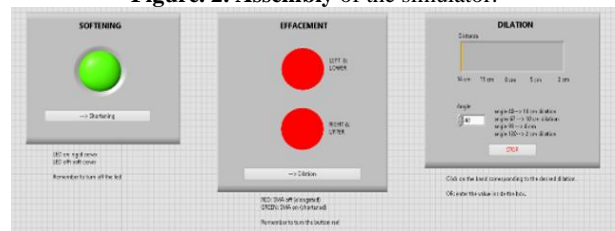


Figure 3. The User Interface.

## CONCLUSION AND DISCUSSION

Analysing the state of the art of both commercial simulators and prototypes, it emerges that currently there are no systems that faithfully reproduce actively and dynamically the changes of the cervix during the labour. This work has the aim of creating a system capable of covering this gap, using different technologies and principles, such as granular jamming, SMA, 3D printing, laser cutting and linear actuators. The realized simulator paves the way for more innovative and technological training and teaching programs in gynaecology and obstetrics. Future efforts will be dedicated to carry out a well-structured validation protocol involving both resident and expert gynaecologists.

## REFERENCES

- [1] York *et al.*, "Creation and Initial Assessment of a Second Trimester Uterine Model" *Simul. Healthc.*; 2014.
- [2] K. L. Shea *et al.*, "Vaginal Examination Simulation Using Citrus Fruit to Simulate Cervical Dilation and Effacement" *Cureus*; 2015.
- [3] M. J. Luk *et al.*, "A dynamic Cervix Phantom Robot for Latent Labor Simulation" *Soft Robot.*; 2018
- [4] A. Cavallo *et al.*, "A Soft Retraction System for Surgery Based on Ferromagnetic Materials and Granular Jamming" *Soft Robot.*, 2019.



# 5G Telesurgery – Feasibility Experiment and First Public Demo

Leonardo S. Mattos, Alperen Acemoglu, and Darwin G. Caldwell

*Biomedical Robotics Lab, Advanced Robotics Dept., Istituto Italiano di Tecnologia*

*{leonardo.demattos,alperen.acemoglu,darwin.caldwell}@iit.it*

## INTRODUCTION

The remote surgery idea has been around for over 30 years [1]. This dream was finally achieved in 2001 with the Operation Lindbergh, the first transatlantic surgical intervention performed on a human [2]. However, this feat proved hard to replicate, especially due to high costs and the limited availability of both surgical robots and appropriate telecommunication links. This scenario is quickly changing with technological progress and the popularization of robotic surgery. Now, the new 5G mobile telecommunication standard promises to satisfy all requirements for telesurgery applications.

Here, we present an initial positive verification of this possibility based on an experimental 5G network and an experimental surgical robot: IIT's laser microsurgery system was adapted for remote operation and ROS (robot operating system) was used as the middleware, connecting a surgeon to the remote surgical robot over Vodafone's 5G network in Milan (Italy). This setup was then used for feasibility tests on a human cadaver and presented live during the first public demonstration of 5G telesurgery.

## MATERIALS AND METHODS

The complete surgical robotic system used in this telesurgery experiment is presented in Fig. 1. This setup was developed based on IIT's robot-assisted laser microsurgery technologies, created in collaboration with ENT surgeons from the University of Genova to address current limits in transoral laser microsurgery (TLM). TLM is a particularly challenging procedure performed to treat delicate structures in the larynx, such as the vocal cords. It is performed under high-magnification optics and requires the use of a surgical laser and a microsurgical forceps for tissue manipulation. Here, an entire TLM setup was adapted for teleoperation as described below.

The patient-side setup was installed at the cadaver lab of San Raffaele's hospital in Milan. It included a robotic laser micromanipulator (CALM [3]), a microsurgical forceps manipulated by a Franka Emika Panda robot, a Karl Storz VITOM 3D exoscope, a Deka SmartXide C60 surgical laser, and teleconference equipment (webcam and speakers). These devices were interfaced to a patient-side PC for integrated control and high-level communication with the surgeon console. This was performed using a 5G Radio Access Network.

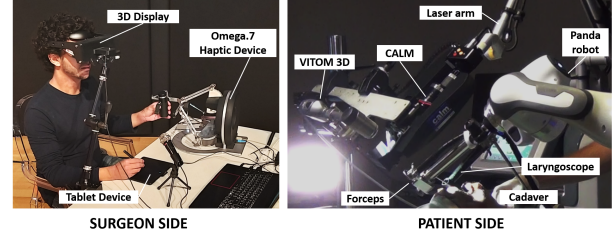


**Fig. 1:** The two sides of the telesurgery setup, located 15 Km away from each other in this experiment.

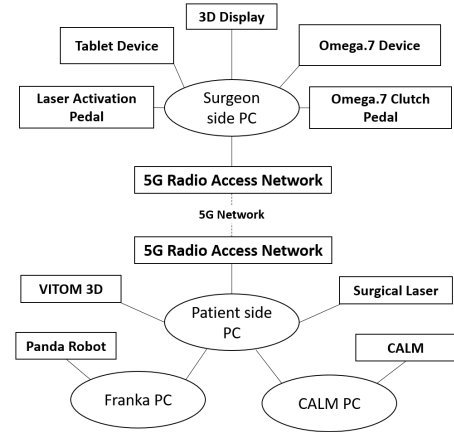


**Fig. 2:** Diagram of the 5G telesurgery setup.

The surgeon-side setup was at the Vodafone Village theater, located 15 Km away from the hospital. This side of the setup featured a laptop, a 3D display, a tablet for laser aiming control, and an Omega.7 haptic device for microsurgical forceps control. In addition, two footswitches were used: one to activate the surgical laser and the other to work as a clutch for the Omega device. All devices were connected to the laptop, which in turn was connected to the patient-side setup using a 5G Radio Access Network. A diagram illustrating the system setup connections is shown in Fig. 2.

The 5G telecommunication system used was an experimental network installed in Milan by Vodafone in the context of the “5G for Milan” project. This network is being constantly upgraded as 5G technologies develop. Nonetheless, at the time of this experiment (November 8, 2019), it was already able to provide 650 Mbps (download), 60 Mbps (upload) and one-way latency below 20 ms. In addition, a secured connection was established using a private dedicated access point name (APN). All communi-

**Table 1:** Summary of major real-time data streams

Stream	Bandwidth	Surgeon $\longleftrightarrow$ Patient
Commands	10 Kbps	$\longrightarrow$
Teleconf A/V	$\approx 3Mbps$	$\longrightarrow$
3D HD video	2x 10 Mbps	$\longleftarrow$
Teleconf A/V	$\approx 3Mbps$	$\longleftarrow$

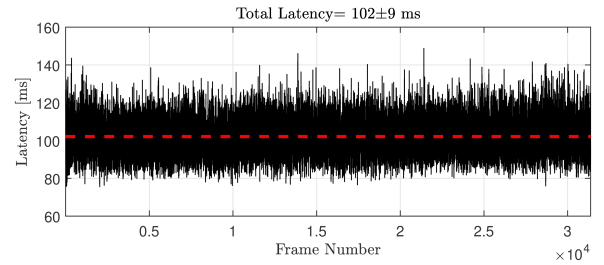
cations were confined to Vodafone’s core network for maximum reliability, security and performance. The major data streams transmitted over the 5G network are listed in Table 1. They included both time-critical signals (the two full HD videos captured by the 3D exoscope and the commands issued by the user interface devices) and non-critical teleconference data. The surgical videos were captured at 30 fps and encoded using H.264 to 10 Mbps, which was found to be a very good compromise between image quality and required bandwidth. All data streams passed through the same 5G connection.

The telesurgery experiment included preliminary microsurgery tests on silicon phantoms of human vocal cords; a public live demonstration to over 300 people using one of these phantoms; and a human cadaver trial. Expert ENT surgeons were in control of the telesurgery system during all trials, and four of them participated to the experiment. The quantitative evaluation metrics used included video transmission latency, time between received video frames, and number of lost communication packages. In addition, qualitative assessment was provided by the surgeons regarding the system usability, teleoperation efficiency, and capability to perform typical microsurgical tasks.

## RESULTS

The video transmission latency data collected during the experiments is illustrated in Fig. 3. The figure shows a representative period of 17.4 minutes, demonstrating a stable streaming performance with a total latency of  $102 \pm 9$  ms. The minimum and maximum recorded latency values were, respectively, 75.69 and 148.30 ms. The mean time between received video frames was  $33.43 \pm 5.57$  ms, and no packages were lost during this period.

The qualitative feedback received from the surgeons indicated high system usability and teleoperation efficiency. All surgeons were able to precisely control the robotic devices without any prior training on the system. The system latency was noted by all of them, but they were able to quickly adapt to it, so this was not remarked as a problem that would prevent telesurgery. This was corroborated by the fact that they were able to perform typical microsurgical tasks with great precision, including tissue grasping, tensioning and excision using the surgical laser. System setup and bed-side assistance proved to be managed effectively through the teleconference system, which enabled clear communication between

**Fig. 3:** Video transmission latency, measured between the moment an image is captured and the moment it is displayed to the surgeon. Red line shows the mean value.

the remote surgeon and the local assistants.

During the live public demonstration, the surgeon performed the excision of a simulated tumor on the vocal cord phantom, remotely manipulating the forceps to grasp the tissue and the laser to precisely cut it away. Then, during a subsequent private test session, the surgeons successfully performed different types of laser cordectomies on the cadaver vocal cords, excising tissue that was subsequently removed from the surgical site by a bed-side assistant.

## DISCUSSION

Based on the results of this experiment, it is clear that 5G has real potential to be an enabling technology for telesurgery. The developed system proved to successfully exploit this new technology to enable remote laser microsurgery, allowing delicate and precise control of the robotic instruments in realistic surgical scenarios. This was true despite the round-trip latency noticed by the surgeons, which can be conservatively approximated to twice the one-way video latency, i.e., 200 ms on average with a maximum of 300 ms in the worst moments. These latency values are already in the acceptable range for teleoperation, but are bound to greatly decrease in the near future as 5G technologies mature.

This first feasibility test was also highly successful in terms of raising public awareness about surgical robotics and their vast potential to improve healthcare. With 5G, it is now possible to envision a quick progress of telemedicine, with applications ranging from telementoring to telesurgery becoming mainstream. However, this will require further R&D to guarantee the safety and robustness of telesurgery systems, and new public policies to deal with the responsibilities and ethics of such procedures.

## References

- [1] T. L. Ghezzi and O. C. Corleta, “30 years of robotic surgery,” *World journal of surgery*, vol. 40, no. 10, pp. 2550–2557, 2016.
- [2] J. Marescaux, “Code name: Lindbergh operation,” *Ann chir*, vol. 127, no. 1, pp. 2–4, 2002.
- [3] A. Acemoglu, N. Deshpande, J. Lee, D. G. Caldwell, and L. S. Mattos, “The calm system: New generation computer-assisted laser microsurgery,” in *Proceedings of the International Conference on Advanced Robotics (ICAR ’19)*. IEEE, 2019.

# Towards Real-Time Eye Geometry Estimation using Eye Tracker sensor

N. Van Landeghem<sup>\*1</sup>, M. Malfait<sup>\*1</sup>, M. Ourak<sup>1</sup>, V. Vörös<sup>1</sup>, E. Vander Poorten<sup>1</sup>

<sup>1</sup>Department of Mechanical Engineering, University of Leuven, Belgium

*emmanuel.vanderpoorten@kuleuven.be*

## INTRODUCTION

Retinal vein occlusion (RVO) is one of the most common causes of vision loss [1]. This phenomenon is observed when an occlusion occurs in the retina vessel. This case is considered a very serious condition. When detected in an early stage, further vision loss could be prevented with different treatments, such as ocular massage, but often the already lost vision cannot be improved [2]. Microcannulation is a new type of minimally invasive surgery that exists out of injecting a drug into the retinal vein to dissolve the blood clot. The treatment is thought to potentially restore the vision. During retinal vein cannulation (RVC), instruments are inserted into the eye through a keyhole. The needle is to be positioned with very good precision in order to operate on the targeted micrometer scale structures [3]. Several factors influence the success rate of this procedure. These factors include: the physiological tremor of the surgeon [4], movement of the patient during the operation [5], the limited work space, an insufficient depth perception and visual feedback [3].

The introduction of robotics in minimally invasive micro-cannulation proved to increase the success rate of this procedure [6]. Different co- and tele-manipulated robots that are able to reduce the forces on the eye surface, increase the stability of the needle and eliminate the tremor of the surgeon, have been developed by multiple research facilities [3].

Although the use of robots has improved the development of the clinical intervention, multiple challenges still remain. Mainly, the limited visualization and depth perception increase the risk of double puncturing, that might severely damage the retina [3]. The purpose of this research is to model the eye geometry with external sensors. The model could then be used to create a virtual wall. This will limit the robot from reaching too far in the eye. In this way, for example, haptic feedback can be introduced such that the surgeon feels when he is approaching the virtual wall.

Multiple attempts have been done in the search of an external sensor that could provide such information about the eye's position in space. The first one is 3D reconstruction of the retina using a stereo-microscope [8]. The second one is the estimation of the distance from the needle tip through impedance sensing or optical coherence tomography (OCT)[9]. The third approach is

by modeling the retina using the OCT C-scan reconstruction [10]. In this paper, eye gaze tracking technology will be explored to reconstruct a model of the human eye as a new sensing technique.

## MATERIALS AND METHODS

The hardware used during this work is the eye tracking sensor Tobii X2-30. This sensor estimates in real time (i.e., up to 60 Hz) multiple parameters of both left and right eye such as: pupil diameter, gaze point and eye position. This data allows to extract other information from the eye such as the 3D position of the center of the pupil (gaze origine - GO) and the 3D position of the visual target on the screen (gaze position - GP) as shown in Figure 1. During the procedure, the user is positioned at approximately 65 cm from the eye tracker and a chin rest is used to stabilize his head during the experiment to make sure that only the eyes are moving.

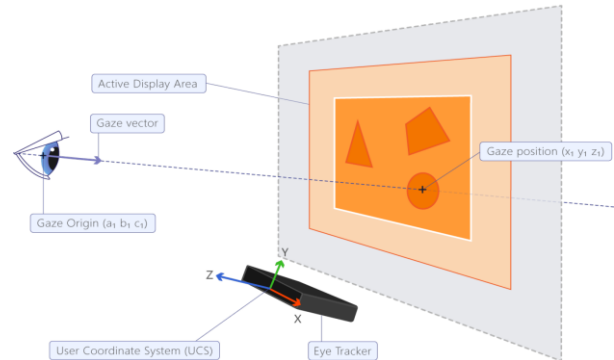


**Figure 1.** Overview of the setting and information that can be gathered using the Tobii sensor [7]

For this work, two assumptions are made to evaluate the proposed technology: (a) the center of rotation of the eye is considered static while moving the eye and (b) the geometrical model of the eyeball is considered spherical. Based on these assumptions, the data set of the GO will belong to the surface of the spherical eye model. These data points are used to estimate the radius and the center of the sphere. To gather this data, the user is asked to follow with his/her eyes a certain pattern on the screen. During this process,  $n$  points of GO are recorded for a given GP on the screen and used as inputs for the model.

A mathematical model was developed to estimate the best fitting sphere based on the least square method. Given that the eye tracker's output tends to present significant noise and outliers, the RANSAC function was used to filter out the outliers and find the most

(\*) Both authors equally contributed to this work  
Proceedings of the 10th Conference on  
New Technologies for Computer/Robot Assisted Surgery (CRAS 2020)

representative data points to construct the model. Figure 2 depicts the general proposed method to get the best fitting geometry.

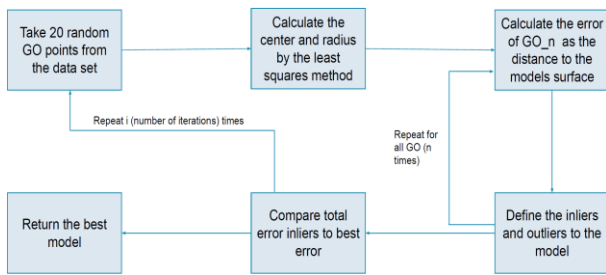


**Figure. 2.** Pupil tracking proposed diagram

The sphere was calculated a number of times set by the user. On each iteration 20 random (give the best results) data points were taken to calculate the radius and center of the best fitting sphere with the least square method. The inliers (based on a threshold given by the user) and average error per inlier was calculated for each model, and the best model was returned by the function.

## RESULTS

The mathematical model was tested under three different simulation: with ideal data, with added noise and with 5 outliers added to the ideal data. The performance of the model was evaluated in terms of the average error found on the radius and the center of the estimated sphere for 100 iterations. The impact of the RANSAC inputs was also investigated for a simulation with added noise.

Figure 3 depicts the 160 ideal GP and 5 outliers used as input, while Figure 4 shows a graphical representation of the estimated sphere with 5 outliers added to the measurements. The modeling errors were found to be  $2.29 \times 10^{-13}$  mm. When a noise level of 0.1 mm was added to the pupil's center data set, the average error on the estimated radius and center of the sphere were of 0.101 mm and 0.069 mm respectively. The introduction of outliers had an influence on the model and RANSAC had to be introduced to compensate for it.

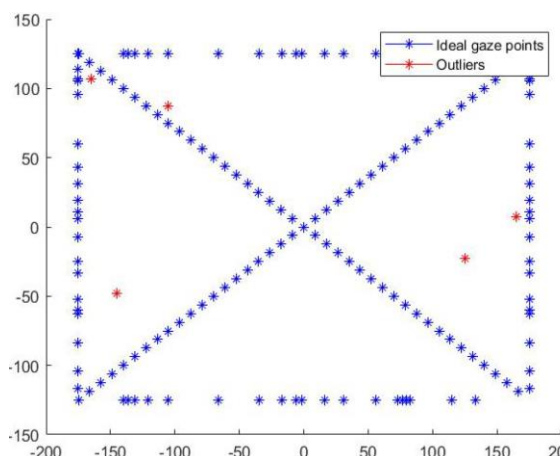


**Figure. 3.** Screen with GP, 160 ideal data points and 5 outliers

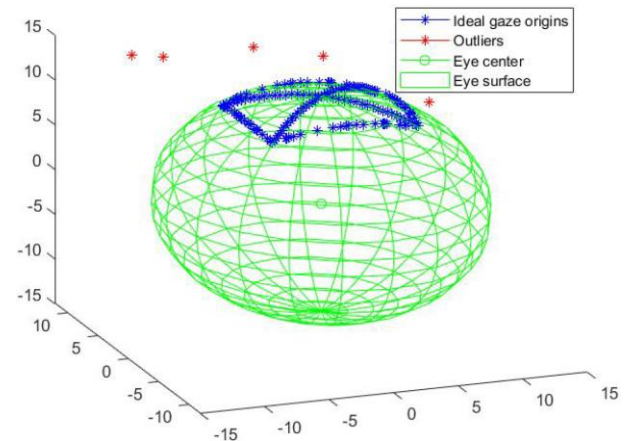


**Figure. 4.** Eye surface modeled with the proposed method, 160 ideal data points and 5 outliers.

## CONCLUSION AND DISCUSSION

A new technique to model the geometry of the eye is proposed based on eye tracking sensor. A mathematical method was developed to estimate the best fitting model based on the sensor information using the pupil coordinates. The model uses the least square method to calculate the geometrical model. Furthermore, RANSAC was implemented to overcome the sensitivity of the least square method to outliers. Future work is foreseen to evaluate the precision and reliability of this method on variable eye shapes and real human eyes.

## REFERENCES

- [1] Hiroyuki Iijima. Mechanisms of vision loss in eyes with macular edema associated with retinal vein occlusion. *Japanese Journal of Ophthalmology*, 2018.
- [2] Sohan Singh Hayreh. *Ocular Vascular Occlusive Disorders*. Springer International Publishing, 2015.
- [3] J Abbott, *et al.* *Handbook of Robotic and Image-Guided Surgery*, chapter Robotic Retinal Surgery, pages 627 – 672. Elsevier, 2019.
- [4] C.N Riviere, *et al.* A study of instrument motion in retinal microsurgery. In *Proceedings of the 22nd Annual International Conference of the IEEE Engineering in Medicine and Biology Society*, volume 1, pages 59–60 vol.1. 2000.
- [5] C.Mccannel, *et al.* Snoring is associated with unexpected patient head movement during monitored anesthesia care vitreoretinal surgery. *Retina*, 32(7):1324–1327, 2012.
- [6] Shinichi Tanaka, *et al.* Quantitative assessment of manual and robotic microcannulation for eye surgery using new eye model. *The international journal of medical robotics and computer assisted surgery*, 2014.
- [7] Tobii Pro SDK. URL:<http://developer.tobii.com/commonconcepts/coordinatesystems.html>.
- [8] P. Thomas, *et al.* "Automatic tool landmark detection for stereo vision in robot-assisted retinal surgery." *RAL*, 2017.
- [9] L. Schoevaerdts, *et al.* "Electrical Bio-Impedance Proximity Sensing for Vitreo-Retinal Micro-Surgery." *RAL*, 2019.
- [10] P. Cornelissen, *et al.* "Towards Real-time Estimation of a Spherical Eye Model based on a Single Fiber OCT." *ICAR* 2019.



# Flexible Framework for Reinforcement Learning in Surgical Robotics

C. D'Ettorre<sup>1</sup>, N. N. Dei<sup>2</sup>, S. V. Krishnan<sup>3</sup>, S. Zirino<sup>4</sup>, G. Chalvatzaki<sup>5</sup>, A. Stilli<sup>1</sup>, D. Stoyanov<sup>1</sup>

<sup>1</sup>Wellcome/EPSRC Centre for Interventional and Surgical Sciences, University College London, UK

<sup>2</sup>DIEF, Department of Industrial Engineering, Università degli Studi di Firenze, Italy

<sup>3</sup>Department of Mechanical Engineering, Indian Institute of Technology Kharagpur, India

<sup>4</sup>DEIB, Department of Electronics, Information and Bioengineering, Politecnico di Milano, Italy

<sup>5</sup>FG-IAS, FB-Informatik, TU Darmstadt, Germany

c.dettorre@ucl.ac.uk

## INTRODUCTION

In the context of Robot-Assisted Minimally Invasive Surgery (RAMIS), this work aims to contribute to the development of a flexible simulated environment to train the da Vinci surgical robot (Intuitive Surgical, Inc., Sunnyvale, CA) with reinforcement learning (RL). The framework is tested on a pick and place task in which the robotic tool aims to pick the Pneumatically Attachable Flexible (PAF) rail [6] and to place it on a target organ. This surgical subtask requires fine manipulation and continuous adaptation at multiple levels: picking the rail from the most convenient configuration for task success, adjusting the tool's orientation according to the observed environment and its changing conditions and so on. These problems can be effectively answered by developing learning algorithms that will adjust the robot's behaviour in crucial parts of the task for a successful placement of the rail. This work builds on the da Vinci Reinforcement Learning (dVRL) [3] and aims to advance it with new objects, a PyRep [4] model and a GUI for recording demonstrations from the da Vinci Research Kit (dVRK) [5] master console. These additions contribute to the development of a flexible and reliable framework, which are fundamental properties to address the issues of generalising and reproducing research work in RL [2] and to speed up RL research in the field of RAMIS.

## MATERIALS AND METHODS

**System specifications:** this work relies on CoppeliaSim [7] version 4.0.0 as physics simulator. The environment inherits from the goal-oriented environment of OpenAI Gym [1].

**Simulation Environment:** building on the previous work in [8], the environment is characterised by one Patient Side Manipulator (PSM) equipped with a Large Needle Driver (LND) tool. The model of the robotic arm has been developed in the PyRep framework to create a modular system. This enables to execute Python code and run the simulation synchronously, thus making the process of editing the scene and choosing the training algorithms simpler and faster compared to using a Python client that uses remote procedure calls to interact with the simulation. Moreover, a PyRep model, through a remote

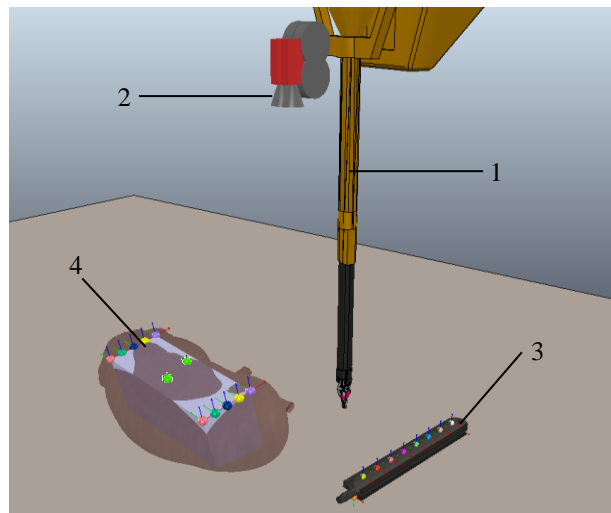


**Figure. 1** The simulation environment comprised of a dVRK PSM (1), stereoendoscope camera (2), the PAF rail (3) and the kidney model with its markers (4). The emerging lilac cuboid in the kidney is its approximation. Here, the rail is placed.

API, allows accessing features of the robot model that were previously inaccessible, because coded in Lua. The scene also presents an anatomically realistic kidney model [9], the PAF rail and a stereo-endoscope, as shown in Figure 1. A realistic texture was overlaid using explanted porcine kidney pictures. The PAF rail model, previously presented in [6], is characterised by a suction channel and a grasping pin running throughout its length. Eight grasping sites distinguish the graspable area for the sake of simplicity. The physics simulator works with approximated cuboid shapes to decrease the computational load because the detailed objects have complex meshes. The resulting surface approximation error is under 2 mm for the kidney. Furthermore, employing simple shapes facilitates the place task and laying the rail on a plane surface is more convenient. Rigid reactions to collisions allow to perform the pick and place task without issues like permeation of shapes and avoid unrealistic starting positions at reset. It is important to note how the proposed flexible framework allows the organ to be easily resized.

**Pick and place task:** the environment has been developed to allow randomisation of the initial positions



of the objects, guaranteeing stochasticity. The randomisation volumes are normalized according to the initial position of the robot. Specific markers (dummies) have been used to mark the objects in the scene. The kidney has five couples of dummies on its top surface, randomly used as targets (coloured markers in Fig. 1). The rollout of the task is composed of the following phases:

1. Definition of the scene objects' initial positions;
2. The LND opens the gripper and approaches the grasping site on the PAF rail;
3. The pick task is concluded when the gripper closes and correctly grasps the rail;
4. The rail is moved towards the target;
5. The place task is concluded when the rail lays in the designed area on the kidney's surface.

The pick task is considered successful when the distance between the LND and the grasping site is below a certain threshold, set to 3 mm in this case. For the place task, two dummies positioned below the rail at opposite sides of its suction area must reach the targets on the kidney with a distance below such threshold. Opposite sides dummies on the rail are checked since, from experience, it is more likely that the suction is better performed when the opposite sides of the rail lay on the desired surface. **Stereo-endoscope setup and calibration:** two vision sensors have been added to the environment in order to reproduce the stereo-endoscope of the dVRK. The camera parameters have been replicated as the real ones [10], except for the resolution, set to half of the original value to avoid excessively long simulation time. The two cameras have been calibrated through MATLAB computer vision toolbox after creating a dataset of checkerboard images by extracting frames from the sensors in CoppeliaSim. The kidney reconstruction is a critical step for adding visual servoing in the simulated environment. Two dummies have been positioned on the top of the kidney to facilitate the analysis of the results. The reconstruction pipeline implemented via OpenCV libraries follows these steps: first, the images are rectified and then the kidney and the dummies are segmented from the frames. This is achieved by calculating the per-element bit-wise conjunction of the image with colour masks, that specify which pixels fall between upper and lower HSV limits. Then, feature points were detected with the SURF algorithm [11] and matched across the two views of the sensors. Linear triangulation was exploited using the method in [12] to reconstruct the 3D positions of these points.

**GUI for demonstrations:** using demonstrations is fundamental when solving an RL problem in robotics with vast continuous domains [3]. The simulation scene has been connected to ROS to control the simulated robot using the dVRK master console. In detail, a CoppeliaSim API is used to publish the state of the robot joints and gripper. The simulator subscribes to relevant topics so that the robot joints motion can be controlled via ROS. Although developed, this GUI has not been employed to obtain demonstrations from the dVRK master console due to limitations raised by the SARS-CoV-2 pandemic.

## RESULTS

To learn the desired task, the robot has been trained on the pick and place phases separately. Currently, more research on the RL training is being carried out, confronting different state-of-the-art algorithms and focusing on improving results. Regarding the 3D reconstruction of feature points, the accuracy has been evaluated through the error computed in terms of Euclidean distance between a detected dummy and its known coordinates, obtaining a result of 10.8 mm. Basic tasks, such as opening the simulation containing the dVRK model using PyRep, have been carried out successfully. Initial tests for the modification of the robot scene are being carried out.

## CONCLUSION AND DISCUSSION

In the view of contextual learning, this work lays the preliminary foundations for a ground for training where the agent can be robust to varying conditions, which is very common in the real surgical context. More research is being conducted, focusing on the training, transfer of the test case to the real system as well as implementing an accurate visual servoing in the 3D reconstruction and, lastly, building a preliminary framework to accelerate further research that will ultimately allow to deploy practical autonomous robotic assistance in surgery.

## REFERENCES

- [1] G. Brockman *et al.*, "OpenAI Gym", CoRR, vol. abs/1606.01540, 2016.
- [2] H. Nguyen *et al.*, "Review of Deep Reinforcement Learning for Robot Manipulation", 2019 Third IEEE International Conference on Robotic Computing (IRC), Naples, Italy, 2019.
- [3] F. Richter *et al.*, "Open-Sourced Reinforcement Learning Environments for Surgical Robotics", 2019, arXiv:1903.02090 [cs.RO].
- [4] S. James, *et al.*, "PyRep: Bringing V-REP to Deep Robot Learning", 2019, arXiv: 1906.11176 [cs.RO].
- [5] Z. Chen *et al.*, "Software Architecture of the Da Vinci Research Kit", 2017 First IEEE International Conference on Robotic Computing (IRC), Taichung, 2017.
- [6] A. Stilli *et al.*, "Pneumatically Attachable Flexible Rails for Track-Guided Ultrasound Scanning in Robotic-Assisted Partial Nephrectomy—A Preliminary Design Study", in IEEE Robotics and Automation Letters, vol. 4, April 2019.
- [7] E. Rohmer *et al.*, "V-REP: A versatile and scalable robot simulation framework", IEEE/RSJ International Conference on Intelligent Robots and Systems, Tokyo, 2013.
- [8] G. A. Fontanelli *et al.*, "A V-REP Simulator for the da Vinci Research Kit Robotic Platform", 2018 7th IEEE International Conference on Biomedical Robotics and Biomechatronics (Biorob), Enschede, 2018.
- [9] R. Hayrullin, "Kidney", Sketchfab, 2019, vshorturl.at/uKR27
- [10] D. L. Chow *et al.*, "Supervisory control of a DaVinci surgical robot", IEEE Int. Conf. Intell. Robot. Syst., 2017.
- [11] Bay H. *et al.*, "SURF: Speeded Up Robust Features", Computer Vision – ECCV 2006.
- [12] R. Hartley *et al.*, "Multiple View Geometry in Computer Vision", Cambridge University Press, 2003.

# Manipulability Analysis using a Coordinate Invariant Index with a Remote Center of Motion Constraint in Surgical Robotics

Claudia Pecorella<sup>1</sup>, Bruno Siciliano<sup>1</sup>, Fanny Ficuciello<sup>1</sup>

<sup>1</sup>Department of Electrical Engineering and Information Technology

University of Naples Federico II

claudia.pecorella, bruno.siciliano, fanny.ficuciello@unina.it

## I. INTRODUCTION

Medical robotics application is currently a growing field of robotics, aimed to improve precision, enhance dexterity, reduce invasiveness of operation and overall time of intervention with a following reduction of the recovery time for the patient. In these applications, multiple tasks are assigned to the robot to ensure a safety and adaptable behaviour of it, e.g. joint limits and obstacle avoidance, or manipulability maximization. One of the big challenges in robotics assisted surgery is the constrained manipulation of tissue through a pivot point, referred to as Remote Center of Motion (RCM). The significance of employing a robot is that it compensates for the reduced number of DOFs that result from the RCM constraint, enhancing dexterity.

When multiple tasks are assigned to the robot, besides kinematic singularities, also singularities between tasks can occur, namely tasks conflicts better known as *algorithmic singularities*. When this kind of singularity occurs, the accomplishment of tasks with lower priorities could be compromised. In a medical application this could represent a danger for the patient, and thus it is necessary to monitor the kinematic performances of the manipulator throughout the execution of the task, being aware of the feasibility of it. We define a coordinate invariant index, aimed to give an objective and consistent measure of the robot manipulability.

## II. METHODS

In the context of robotics-assisted minimally invasive surgery the robot tool is inserted into the patient body through an incision point,  $P_{trocar}$ . The Trocar point is defined as a fix point in the world frame through which the shaft of the tool has to pass, and constitute the remote center of motion for the manipulator. In section II-A the constrained kinematic as in [1] is presented, followed by the proposed coordinate invariant index in Section II-B and the obtained results in Section III.

### A. Kinematic Constraint at a RCM

We will denote with  $P_{RCM} \in \mathbb{R}^3$  the RCM point that must coincide with the trocar point  $P_{trocar} \in \mathbb{R}^3$ . The RCM is assumed to belong to a shaft attached at the end effector of the manipulator, and can be located anywhere on the tool. Following the formulation proposed in [1], the position of the RCM over time is given by:

$$\mathbf{p}_{RCM} = \mathbf{p}_i + \lambda(\mathbf{p}_{i+1} - \mathbf{p}_i) \quad 0 \leq \lambda \leq 1 \quad (1)$$

where  $\mathbf{p}_i$  and  $\mathbf{p}_{i+1}$  denote the boundaries of the shaft. The dependencies of the points coordinates from joint variables and time are omitted for brevity.

Differentiating (1), and exploiting the differential mapping between the joint space and the operational space, we obtain:

$$\dot{\mathbf{p}}_{RCM} = \mathbf{J}_{RCM}(\mathbf{q}, \lambda) \begin{pmatrix} \dot{\mathbf{q}} \\ \dot{\lambda} \end{pmatrix} \quad (2)$$

where  $\mathbf{J}_{RCM}$  is the Jacobiano of the RCM, given by:

$$\mathbf{J}_{RCM} = \begin{pmatrix} \mathbf{J}_i + \lambda(\mathbf{J}_{i+1} - \mathbf{J}_i) \\ \mathbf{p}_{i+1} - \mathbf{p}_i \end{pmatrix} \quad (3)$$

To satisfy the RCM constraint, it has to be  $P_{RCM}(t) \equiv P_{trocar}(t)$ , therefore  $\dot{\mathbf{p}}_{RCM} = \mathbf{0}$ .

Indicating with  $\mathbf{t} = \mathbf{f}(\mathbf{q})$  a generic desired task, and considering the differential kinematic between task and joints velocities, it is possible to derive the differential kinematic of the extended task which includes the above mentioned RCM constraint.

$$\dot{\mathbf{t}}_{EXT} = \begin{pmatrix} \dot{\mathbf{t}} \\ \mathbf{0}_{3 \times 1} \end{pmatrix} = \begin{pmatrix} \mathbf{J}_t & \mathbf{0}_{n_t \times 1} \\ \mathbf{J}_{RCM} \end{pmatrix} \begin{pmatrix} \dot{\mathbf{q}} \\ \dot{\lambda} \end{pmatrix} = \mathbf{J}_{EXT} \begin{pmatrix} \dot{\mathbf{q}} \\ \dot{\lambda} \end{pmatrix} \quad (4)$$

where  $n_t$  is the dimension of the task space.

To guarantee exponential decoupled convergence of the extended task to a desired value, we employed the following kinematic control:

$$\begin{pmatrix} \dot{\mathbf{q}} \\ \dot{\lambda} \end{pmatrix} = \mathbf{J}_{EXT}^\dagger \begin{pmatrix} \mathbf{K}_t & \mathbf{0}_{n_t \times 3} \\ \mathbf{0}_{3 \times n_t} & \mathbf{K}_{RCM} \end{pmatrix} \mathbf{e}_t \quad (5)$$

where  $\mathbf{e}_t$  is the vector containing the error of the task and of the rcm, i.e.  $\mathbf{e}_t = (\mathbf{t}_d - \mathbf{t} \quad \mathbf{p}_{trocar} - \mathbf{p}_{RCM})^T$ .

In (5) additional tasks could be considered and projected into the null-space of the extended jacobian  $\mathbf{J}_{EXT}$ .

### B. Coordinate Invariant Manipulability Index

As mentioned in the introduction, it is crucial to monitor the proximity of a singularity and check the feasibility of a stack of tasks. Most of the kinematic performance measures proposed in the last decades are related to the concept of manipulability, dexterity and isotropy. In a singular configuration the considered performance measure is zero, and it increases as soon as the robot moves out of the singularity.

Manipulability measures are related to the concept of manipulability ellipsoids, proposed in [2], and its volume was assumed to be a measure of uniformity of the mapping between joint and task spaces. The ellipsoids are used to analyse

pure kinematic feasibility to arbitrarily generate end-effector velocity or force in a certain joint configuration. It is not often remarked, but manipulability ellipsoids are dependent from the joint coordinate choice [3], i.e. arbitrarily manipulability could be inferred for the same configuration depending on the chosen coordinates in the joint space. Therefore, it is of crucial importance the choice of the kernel of the quadratic form which describes the ellipsoids' equation in order to have an objective measure.

Considering the mass matrix  $\mathbf{M}(\mathbf{q})$  of the manipulator as a metric tensor to redefine the sphere related to the joint velocities, we have the same ellipsoid no matter the parametrization chosen for  $\dot{\mathbf{q}}$  [3]. Following this reasoning, it is possible to define velocity and force ellipsoids in the Cartesian space, as in (6) and (7). The kernel in these equations is given by the inertia in the Cartesian space ( $\mathbf{\Lambda} = (\mathbf{J}\mathbf{M}^{-1}\mathbf{J}^T)^{-1}$ ) and its inverse. This matrix is the induced metric in the Cartesian space, obtained by using  $\mathbf{M}$  as a metric in the Joint configuration space.

$$\dot{\mathbf{x}}^T(\mathbf{J}\mathbf{M}^{-1}\mathbf{J}^T)^{-1}\dot{\mathbf{x}} = 1, \quad (6)$$

$$\mathbf{f}^T(\mathbf{J}\mathbf{M}^{-1}\mathbf{J}^T)\mathbf{f} = 1. \quad (7)$$

The velocity and force ellipsoids in (6) and (7) incorporate a strong physical meaning: their principal axis describe the capability of the robot to produce end-effector velocities/forces in certain directions taking into account not only the kinematic structure of the robot, but also the dynamic constraints intrinsically expressed by the inertia matrix  $\mathbf{\Lambda}$ ; furthermore, they are independent of the joint parametrization, which comes as consequence of choosing a proper metrics in the Joint Configuration Space [3]. Only ellipsoids obtained by choosing a proper metric in the Joint Configuration Space reflects physical properties of the robot. Other ellipsoids could infer for the same configuration arbitrarily high or poor manipulability, depending on the joint coordinates and the units chosen to parametrize the Joint Configuration Space.

The manipulability measure related to the classical ellipsoid expression is given by the square root of the determinant of the ellipsoid's kernel, i.e.  $w = \sqrt{\det(\mathbf{J}\mathbf{J}^T)}$ . Considering the above mentioned metric, we consider the inertia matrix as a coordinate invariant measure of manipulability:

$$w = \sqrt{\det(\mathbf{\Lambda}^{-1})}. \quad (8)$$

### III. RESULTS

Here we want to compare our approach with the one proposed in [4], during the execution of a trajectory which could be compared to the first arch of circle made during a suture, while satisfying the RCM constraint. In [4] a modified variant of the measure of isotropy as the Frobenius condition number of the Jacobian matrix is proposed. They argue that due to the slow motion of a surgical task, they can decompose it in a *reach*, only translational, or *orient* motion. In this way the resulting manipulability index is unit-invariant.

As can be seen from Figure 1, the two indexes have a different behaviour throughout the trajectory. In Figure 1a and 1c the trend of the manipulability index computed as in [4]

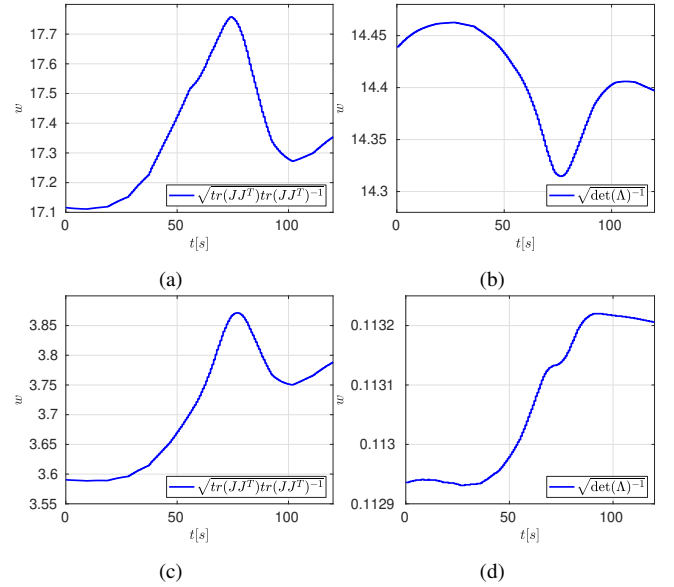


Fig. 1: Comparison of the manipulability indexes: in 1a and 1c manipulability computed considering the Frobenius norm, 1c considering only the translational jacobian; in 1b and 1d the manipulability computed with our approach, 1d - as in 1c - considering only the translational jacobian.

are depicted, more in detail in 1c it is depicted the trend of the measure considering only the translational Jacobian. In Figure 1b and 1d our proposed index is reported. The two indexes not only have different values, but also have opposite trends when the whole Jacobian is considered, and in both cases, if the measure is considered only for the reach motion, we have a smaller value of the manipulability.

### IV. CONCLUSIONS AND DISCUSSION

A coordinate invariant manipulability index has been proposed, which could be useful for the on-line detection of algorithmic singularities. Further research direction would be to investigate an appropriate reactive control schemes (to be decided according to the specific application) to manage the conflict situations. We aim to evaluate the proposed manipulability index in a human-robot interaction framework, adopting an impedance control algorithm to hand guide the manipulator. In addition, we want to consider a stack of tasks, so to consider also other crucial aspects such as distance from joint limits, obstacle avoidance and manipulability maximization. In this framework, we aim to study the feasibility of the stack with the imposed RCM constraint.

### REFERENCES

- [1] N. Aghakhani, M. Geravand, N. Shahriari, M. Vendittelli, and G. Oriolo, "Task control with remote center of motion constraint for minimally invasive robotic surgery," in *IEEE Int. Conf. on Robotics and Automation*, 2013, pp. 5807–5812.
- [2] T. Yoshikawa, "Manipulability of robotic mechanisms," *Int J Robot Res*, vol. 4, no. 2, pp. 3–9, 1985.
- [3] J. Lachner, V. Schettino, F. Allmendinger, M. D. Fiore, F. Ficuciello, B. Siciliano, and S. Stramigioli, "The influence of coordinates in robotic manipulability analysis," *Mechanism and Machine Theory*, vol. 146, 2020.
- [4] H. Azimian, R. V. Patel, and M. D. Naish, "On constrained manipulation in robotics-assisted minimally invasive surgery," in *2010 3rd IEEE RAS EMBS International Conference on Biomedical Robotics and Biomechanics*, 2010, pp. 650–655.

# Framework for soft tissue manipulation and control using Deep Reinforcement Learning

Ameya Pore<sup>1</sup>, Eleonora Tagliabue<sup>1</sup>, Diego Dall'Alba<sup>1</sup>, Paolo Fiorini<sup>1</sup>

<sup>1</sup>*Department of Computer Science, University of Verona, Italy,  
ameya.pore@univr.it*

## INTRODUCTION

The future generation of surgical robotic systems will provide an increased level of autonomy. All minimally invasive surgical (MIS) procedures are composed of a series of repetitive subtasks like dissection, suturing and knot tying, that extensively deal with the manipulation of soft tissues. Automation of these subtasks would bring several benefits to MIS, among which enhanced precision in tool control and increased dexterity, which would eventually lead to improved operator comfort. Some attempts to automate these repetitive sub-tasks have been already proposed [1]. However, these approaches use hand-crafted control policies which work well in laboratory conditions but perform poorly within the highly-variable surgical environment. Hence, autonomous surgical systems should be able to manipulate highly deformable and dynamic soft tissues in a robust and efficient way.

Deep Reinforcement Learning (DRL) offers a good framework to model such hard-to-engineer behaviours [2]. DRL has shown promising success in industrial robotic systems to extract useful feature representations from images and learn to perform an optimal action [2]. Most of the works based on DRL for soft-tissue manipulation have focused on 2D deformations such as clothing articles [1], [3]. To tackle issues such as clinical safety, ethics, economical and hardware risks, various studies have proposed to train autonomous agents in a simulated environment. Then the learned policies can be transferred to a real system based on a sim-to-real approach [4].

In the context of clinical applications, soft tissues are usually simulated using finite element models (FEM) due to their high accuracy in simulating soft tissues dynamics [5]. However, high accuracy implies high computational time, which makes it impractical to employ FEMs in DRL framework, where a huge number of trial and error attempts are needed. A possible alternative to FEM is represented by non-physics based methods, such as Position-Based Dynamics (PBD). PBD has been demonstrated to model anatomical tissues deformations to an acceptable degree of accuracy while keeping the computation time low [6].

In this work, we introduce a soft-tissue simulation framework that replicates the preliminary steps of partial nephrectomy procedure. Furthermore, we show that an end-to-end reinforcement learning algorithm can be trained in the simulation without any user demonstration to accomplish a tissue manipulation task. To the best of our knowledge, this is one of the first attempts of using DRL agents to manipulate soft tissues for autonomous surgical action execution.

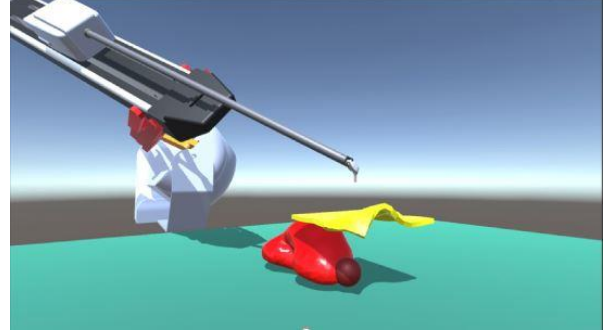


**Figure 1.** Environment scene developed in Unity3D for robot-assisted nephrectomy procedure. The scene consists of a single PSM arm, kidney, tumour and renal fascia (fat tissue). For visual simplicity, high contrast colours are used to depict various objects

## MATERIALS AND METHODS

**Simulation details:** Our simulation environment relies on the Unity3D engine (Fig 1). In addition to the high flexibility and modularity offered by this development platform, which allows adding custom objects and sensors to the scene, Unity enables the modelling of soft objects exploiting the efficient PBD implementation provided by NVIDIA FleX. All the deformable structures present in our environment (kidney, tumour and surrounding fat tissue) have been modelled using FleX, and deformation parameters have been tuned with an ad-hoc experiment to provide realistic behaviour [6]. In the proposed virtual environment, we modelled a single slave arm of the da Vinci Research Kit (dVRK) setup, that is, a Patient Side Manipulator (PSM) equipped with a Large Needle Driver (LND) instrument having jaw gripper to grasp objects. We implemented a closed-form inverse kinematics of the PSM to enable the Cartesian space control of the manipulator. We define the tissue grasping condition based on proximity; in particular, we check when the distance between LND tooltip and the fat surface is less than 2mm. We set a bound to the maximum limit of movement of the end-effector (EE) by a predefined delta movement  $\Delta$  parameter.

**Reinforcement learning:** RL is a trial and error optimisation technique that defines a Markov decision process (MDP) where an agent learns by interacting with the environment. An MDP is characterised by a state space  $S$ , action space  $A$ , and a reward function  $R : S \times A \rightarrow R$  that encapsulates the goal. At each time step  $t$ , the environment produces a state observation  $s_t \in S$ , the agent then samples an action  $a_t \sim \mu(s_t)$ ,  $a_t \in A$  and  $\mu : S \rightarrow A$  represents a behaviour policy. As a consequence, the environment then yields a reward  $r_t$  sampled from  $R$  and the agent moves to a new state  $s_{t+1}$  sampled from a transition probability function

$P(S' = s_{t+1} | S = s_t, A = a_t)$ . The agent's goal is to maximise the expected future discounted reward:

$$G_t = E_{s_0 \rightarrow T, a_0 \rightarrow T-1, R_0 \rightarrow T-1} \left[ \sum_{i=0}^{T-1} \gamma^i R_i \right]$$

where  $T$  is the time horizon and  $\gamma \in [0,1]$  is the discount factor.

**Experiment:** The experiment aim is to move the PSM arm from an initial position  $P_0$  to a position close to the tumour  $T_0$ , grasp the fat and retract it to a predefined target position  $P_F$ . The state and action space of the environment at timestep  $t$  is  $S_t = [P_t, P_F, T_0, G]$ ,  $A_t = [-1,0,1] * \Delta$ , where  $P_t, T_0, G$  are the position of the EE, tumour and gripper state, respectively. The reward function is:

$$r(s_t) = \begin{cases} -d(P_t, T_0) * k & \text{if gripper close} \\ -d(P_t, P_F) * k & \text{if gripper open} \end{cases}$$

Where  $d$  denotes the distance function, and  $k$  is a constant that depends on the volume in which PSM can move. The gripper state changes automatically when a grasping event is detected. Each episode consists of 1500 steps. We use Proximal Policy Optimisation (PPO), which is the state-of-the-art DRL algorithm supported by MLAgents framework provided by Unity [7].

## RESULTS

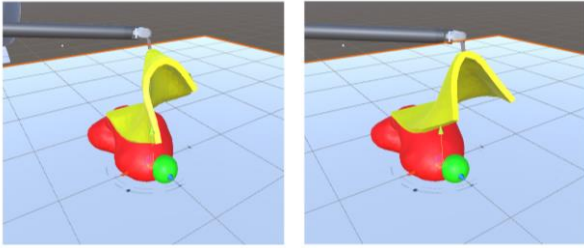


**Figure 2.** Learnt policy from two different starting position of the PSM arm.

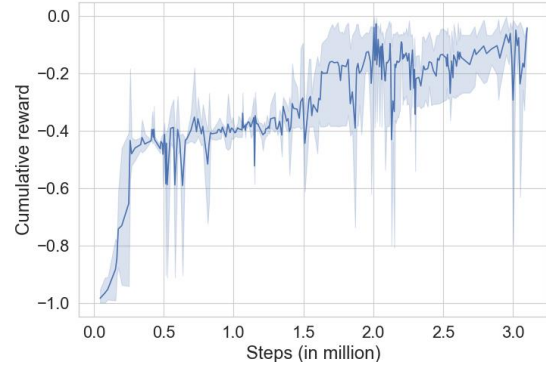
Fig 2. highlights the final state of the learnt behaviour where the PSM arm approaches, grasps the fat tissue and consequently exposes the underlying tumour. The figure depicts the dynamic and flexible nature of the soft tissue that is rendered in the simulator.

Fig 3. shows the learning curve, that is, the number of steps taken to reach a higher cumulative reward. The agent requires 3 million steps to learn the manipulation task. This result is comparable to the training steps required to grasp rigid objects [8]. From the reward trend, it emerges that the agents require 500 thousand steps to learn the approach behaviour towards the fat, the subsequent 1.5 million steps to learn the interaction with the fat and finally 1 million steps to learn the retract behaviour. Note that the behaviour is learnt without any visual cues and purely on the basis of positional information. The training is carried out on an NVIDIA TitanX GPU with 16 parallel workers and takes 3hrs in real-time.

## CONCLUSION AND DISCUSSION

This work is a preliminary step towards developing autonomous agents for controlling surgical tools and manipulating soft tissues. Future work would be focused on autonomous control using visual cues and developing

a metric to evaluate the trajectory/behaviour learnt. We



**Figure 3.** The obtained learning curve. The cumulative reward is normalised in the range  $[-1,0]$ . The shaded area spans the range of values obtained when training the agent starting from three different initialisation seeds.

plan to extend the work towards using model-based approaches and incorporating imitation based learning using expert demonstration to bootstrap the number of training steps. Subsequent directions would be carried out to transfer the learned knowledge to a real-robotic system.

## ACKNOWLEDGEMENTS

This project has received funding from the European Research Council (ERC) under the European Union's Horizon 2020 research and innovation programme (grant agreement No. 742671 "ARS") and under the Marie Skłodowska-Curie (grant agreement No. 813782 "ATLAS"). We acknowledge the support of NVIDIA Corp. for the donation of the Titan X GPU.

## REFERENCES

- [1] Murali, Adithyavairavan, et al. "Learning by observation for surgical subtasks: Multilateral cutting of 3d viscoelastic and 2d orthotropic tissue phantoms." *2015 IEEE International Conference on Robotics and Automation (ICRA)*. IEEE, 2015.
- [2] Arulkumaran, Kai, et al. "Deep reinforcement learning: A brief survey." *IEEE Signal Processing Magazine* 34.6 (2017): 26-38.
- [3] Tsurumine, Yoshihisa, et al. "Deep reinforcement learning with smooth policy update: Application to robotic cloth manipulation." *Robotics and Autonomous Systems* 112 (2019): 72-83.
- [4] Peng, Xue Bin, et al. "Sim-to-real transfer of robotic control with dynamics randomisation." *2018 IEEE international conference on robotics and automation (ICRA)*. IEEE, 2018.
- [5] Zhang, Jinao, Yongmin Zhong, and Chengfan Gu. "Deformable models for surgical simulation: a survey." *IEEE reviews in biomedical engineering* 11 (2017): 143-164.
- [6] Tagliabue, Eleonora, et al. "Position-based modeling of lesion displacement in Ultrasound-guided breast biopsy." *International journal of computer assisted radiology and surgery* 14.8 (2019): 1329-1339.
- [7] Juliani, Arthur, et al. "Unity: A general platform for intelligent agents." *arXiv preprint arXiv:1809.02627* (2018).
- [8] Richter, Florian, Ryan K. Orosco, and Michael C. Yip. "Open-sourced reinforcement learning environments for surgical robotics." *arXiv preprint arXiv:1903.02090* (2019).



# Towards a Compact Auto-Focusing System for Endoscopic Laser Surgery

A. Gerales<sup>1</sup>, P. Fiorini<sup>2</sup>, L.S. Mattos<sup>1</sup>

<sup>1</sup>Biomedical Robotics Lab, Istituto Italiano di Tecnologia,

<sup>2</sup>Department of Computer Science, University of Verona  
andre.gerales@iit.it

## INTRODUCTION

Despite their broad use in surgical interventions, traditional laser systems require a direct line-of-sight to the surgical target. In contrast, endoscopic laser systems allow minimally invasive access by using flexible optical fibers for delivering the laser much closer to the surgical site. This presents significant advantages including better visualization of the target, control over the laser delivery angle and the ability to reach targets inaccessible by a straight-line trajectory [1]. Unfortunately, the limited space in endoscopic laser tools has so far prevented the integration of complex optical systems for controlling the focusing and scanning of the laser beam, such as those commonly seen in traditional laser systems.

Without focusing units, current endoscopic laser tools use optics with fixed focal length or use no optics at all, placing the tip of the fiber in close proximity of the tissue being ablated. When fixed focus is used, the distance between the tool and the target must be constantly adjusted by the surgeon, which not only hinders the precision of the ablation procedure, but also increases the surgeon's mental workload. On the other hand, placing the tip of the fiber too close to the target results in excessive thermal damage to the surrounding tissue, often leading to tissue carbonization [2]. This suggests that the performance of endoscopic laser tools could be significantly improved by incorporating a compact optical system with variable focal length.

One key technology for enabling such focusing system are varifocal mirrors (VM), which consist in optical elements whose surface can be dynamically deformed. This allows changing their focal length without the need of physical displacement. In a recent work [3], we developed an elliptical MEMS varifocal mirror with microfluidic actuation for focusing a CO<sub>2</sub> laser beam in an off-axis configuration. Here we propose a compact auto-focusing (AF) system based on such mirror and a sensorless actuation method for controlling the VM.

## MATERIALS AND METHODS

Fig. 1 shows a schematic representation of the proposed AF system. In this system, the laser beam coming from the optical fiber is collimated by the collimating lens and focused by the combination of the VM and a prefocusing lens with focal length  $f_L$ . When the VM is flat, the focal length of the system  $f_{sys}$  is equal to  $f_L$ . However, when

the VM is deflected in convex or concave shape,  $f_{sys}$  becomes greater or lower than  $f_L$ , respectively.

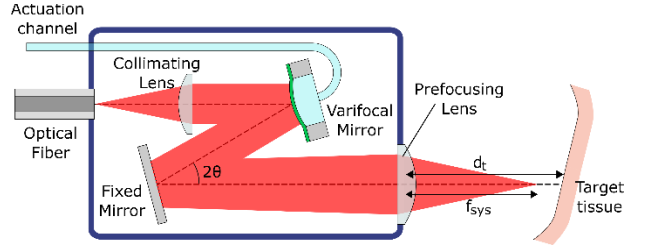


**Fig. 1** Schematic diagram of the proposed AF system.

The focal length  $f_{sys}$  of the system is determined by the focal lengths of the VM ( $f_M$ ) and the prefocusing lens ( $f_L$ ), as well as by the distance  $d_L$  that the laser travel between them. When  $d_L = f_L$ ,  $f_{sys}$  is obtained as:

$$f_{sys} = f_L - P_M f_L^2, \quad (1)$$

where  $P_M = 1/f_M$  is the optical power of the VM. This condition is important, as it makes the numerical aperture of the focused beam independent of  $P_M$ , allowing to shift the focal point of the laser without changing the diameter of the focused spot. The optical power of the VM is determined by the pressure  $\Delta p$  applied to the actuation channel and is given as  $P_M = 4w_0/(R_x R_y)$ , with  $w_0$  being the central deflection of the mirror and  $R_x$  and  $R_y$  being its semi-major and semi-minor axes. The relationship between  $w_0$  and  $\Delta p$  can be obtained as:

$$\Delta p = 2hR_k\sigma w_0 + \frac{2hER_k^2}{3(1-\nu)}w_0^3, \quad (2)$$

where  $h$  is the thickness of the membrane mirror,  $E$  and  $\nu$  are the Young's modulus and Poisson's ratio of the membrane material,  $\sigma$  is its residual stress and  $R_k$  is given by  $R_k = (R_x^2 + R_y^2)/(R_x^2 R_y^2)$ .

Based on this model, the focal length of the system can be completely determined by the applied actuation pressure. Therefore, one method for controlling the proposed AF system is to measure the distance to the target  $d_t$  using 3D surface reconstruction [4] and to set  $f_{sys} = d_t$ . The advantage of this method is that it does not require using a beam splitter or other sensors commonly used in AF systems [5], since the 3D reconstruction can be performed with the stereo camera already present in the endoscope. This sensorless control approach is critical for allowing the AF system to remain compact.

## RESULTS

To evaluate the proposed AF controller, we assembled the VM into the AF tool shown in Fig. 2. Here the actuation pressure  $\Delta p$  was controlled by a microinjection system and the laser beam used was a 10 mW fiber-coupled LED. The AF tool was attached to a linear positioning stage (PS) placed in front of a fixed target, which consisted of a sheet of paper. Using the PS, the distance between the AF tool and the target was changed from 15 to 50 mm, while the focal length of the system was adjusted by the AF controller. The distance to the target was obtained directly from the encoder of the PS (simulating an ideal distance sensor) and the diameter of the focused laser spot was measured by a high-speed camera. The precise values of the parameters of (2) were obtained empirically before the experiment, using a wavefront sensor, as described in [3].

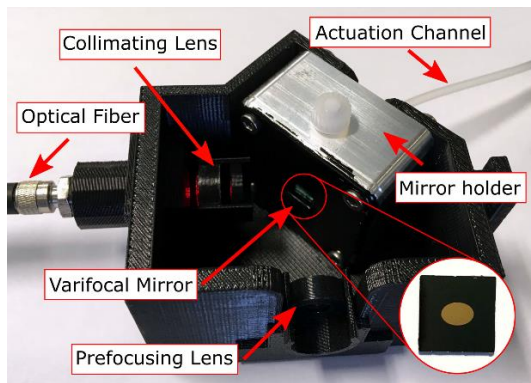


**Fig. 2** Developed prototype of an auto-focusing system based on a MEMS varifocal mirror.

Fig. 3 shows the measured laser spot diameter when the AF tool was moved with and without using the AF controller. Without the AF controller,  $f_{sys}$  was kept equal to 32 mm, which caused the laser beam to defocus as the target moved away from this point. At the maximum defocusing, the spot diameter reached 1.2 mm. On the other hand with the AF controller enabled, the spot diameter remained between 620 and 646  $\mu\text{m}$ , which corresponds to 2% of variation over the central value of 633  $\mu\text{m}$ . This confirms that the mirror deflection model is accurate and validates the proposed AF controller.

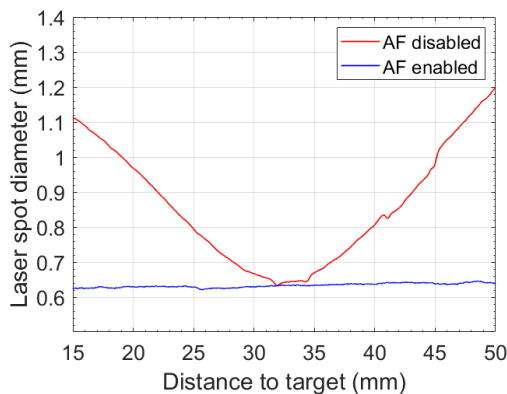


**Fig. 3** Obtained laser spot diameter with and without the proposed AF controller.

## DISCUSSION

Based on the obtained results, it is possible to draw some conclusions about the proposed AF system. In terms of performance, the developed AF tool was able to focus the laser beam with high precision for a distance range compatible with endoscopic laser surgery. The obtained laser spot diameter was higher than typical values for fiber laser tools (around 250  $\mu\text{m}$ ), but it can be further reduced by increasing the numerical aperture of the laser beam. The motion of the AF tool was performed at low speed (1 mm/s) due to the limitations of the positioning stage. Further experiments would be required in order to verify the performance of the system in the presence of fast motion. Finally, the use of a simulated distance sensor may have contributed to the precision of the AF controller. However, using a 3D reconstruction method such as reported in [4], it is possible to measure the distance to the target with an average error of 0.2 mm. Considering all that, we believe that the obtained performance of the AF system makes it a promising solution for endoscopic laser tools.

In terms of compactness, the fabricated AF tool is relatively large, mainly due to the mirror holder (which is 40 mm long), but it can still be miniaturized. The overall diameter of the tool depends mainly on the diameter of the optical elements being used. Since the dimensions of the varifocal mirror are 3 x 4.24 mm, it is reasonable to assume that the diameter of the entire tool can be made within 12 mm. This would make the tool compatible with standard surgical endoscopes, assuming it to be incorporated in the endoscope design. The length of the system, in the other hand, depends mainly on the prefocusing lens, since its distance to the VM must be equal to  $f_L$ . Reducing  $f_L$  can make the tool shorter, but it also affects the focal length range  $\Delta f_{sys}$  of the tool. Therefore the optimization of  $f_L$  must take into account the required focal length range for one specific application.

## REFERENCES

- [1] Wang Z, Chocat N. Fiber-optic technologies in laser-based therapeutics: threads for a cure. *Current pharmaceutical biotechnology* 11.4 (2010): 384-397.
- [2] Janda P, et al. Comparison of thermal tissue effects induced by contact application of fiber guided laser systems. *Lasers in Surgery and Medicine: The Official Journal of the American Society for Laser Medicine and Surgery* 33.2 (2003): 93-101.
- [3] Gerales A, Fiorini P, Mattos LS. An Auto-Focusing System for Endoscopic Laser Surgery based on a Hydraulic MEMS Varifocal Mirror. 2019 19th International Conference on Advanced Robotics (ICAR). IEEE, 2019.
- [4] Cao BX, et al. Automatic real-time focus control system for laser processing using dynamic focusing optical system. *Optics Express* 25.23 (2017): 28427-28441.
- [5] Schoob A, et al. Tissue surface information for intraoperative incision planning and focus adjustment in laser surgery. *International journal of computer assisted radiology and surgery* 10.2 (2015): 171-181.

# Vision-based estimation of deformation properties for autonomous soft tissues manipulation\*

M Piccinelli<sup>1</sup>, E Tagliabue<sup>1</sup>, D Dall’Alba<sup>1</sup>, P Fiorini<sup>1</sup>

<sup>1</sup>*Dept. of Computer Science, University of Verona  
eleonora.tagliabue@univr.it*

## INTRODUCTION

The latest research in robotic surgery has increasingly focused on the automation of surgical tasks. The main challenge faced by an autonomous surgical robot is to learn how to safely interact with the deformable anatomical environment, whose dynamic behaviour is complex and thus difficult to predict. In this context, simulation plays an important role in supporting the decisions that the autonomous system has to make. In addition to providing an environment where the planned actions can be safely tested pre-operatively, simulation can also be exploited intra-operatively to complement information coming from sensors. Furthermore, some recent works have proposed to exploit Deep Reinforcement Learning (DRL) methods to learn robot manipulation tasks on a realistic replica of the surgical environment before transferring the policies to the real system, coping with the shortage of real clinical data which would be needed for agent training [1].

Among the different strategies that can be employed to simulate the deformable behaviour of living tissues, position-based dynamics (PBD) has proved able to achieve fast and unconditionally stable simulations, both representing important requirements in robotics applications [2]. However, in order to rely on simulation results, it is essential to guarantee that the simulated environment represents an accurate replica of the real-world scenario where the robot will be acting. A-priori knowledge of each organ dynamic behaviour is almost impossible to obtain from pre-operative information. Even though this information was available, a direct way to convert real mechanical properties into PBD parameters does not exist. A possible approach to tackle the issue is to estimate soft tissues properties with an ad-hoc optimization technique on the scenario of interest exploiting information coming from sensor data [2, 3].

In this work, we present a method to estimate the deformability properties of soft tissues employing visual observations, during a representative manipulation task performed with the da Vinci Research Kit (dVRK). The preliminary results obtained on a phantom experiment have shown that the proposed method is able to estimate parameters which minimize the gap between the real and the simulated configurations. This work represents a first promising step towards the improvement of simulations realism, to an extent that will make their exploitation into real clinical scenarios possible.

## MATERIALS AND METHODS

In this work, we optimize the elastic properties of soft tissues during a simple manipulation task, where a single

dVRK Patient Side Manipulator (PSM) grasps and lifts a rectangular silicone patch with one fixed side, whose elastic properties replicate those of connective tissues. The grasping points are distributed over the non-fixed sides and the internal surface (Figure 1). We perform a total of 10 acquisitions where the dVRK lifts the deformable tissue to a maximum height of 48 mm, with three intermediate steps ( $L=3$ ). For each experiment, we acquire the point cloud representing the real state of the soft tissue surface with an Intel RealSense D435 RGB-D camera. The joint states of the robot manipulator at the considered timestamps are also saved since they will be needed to reproduce the arm movements in the simulated environment. Color-based segmentation is applied to the raw point clouds to extract only the points belonging to the deformable tissue. Then, a post-processing is performed to clean the point clouds and remove acquisition noise. Each point cloud is then matched with its corresponding arm configuration, based on the acquisition timestamps.

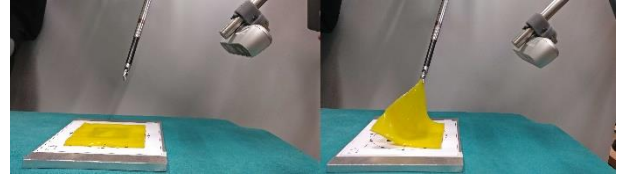


**Figure 1:** One optimization experiment. Left: rest configuration. Right: deformed configuration. The dVRK PSM grasps and lifts the tissue, whose deformed surface is acquired with the depth sensor.

The simulated environment is based on Unity3D, where the dVRK robotic arm is simulated with dVRK-XR (dVRK Mixed Reality Extension) [4]. An important preliminary step to the optimization process consists on the rigid alignment of the simulated and the real scenes. This is done by mapping the poses of the PSM in a common reference space by reaching several points on a custom calibration board, which is placed at the centres of the two reference systems. The calibration has a 1.3 mm error. Soft tissue simulation is obtained exploiting NVIDIA FleX implementation of position-based dynamics, where deformable objects are modelled as systems of particles divided into several clusters. The parameters with the highest impact on objects deformable behaviour are those describing the position of the different clusters in space and their relative constraints: cluster spacing, radius and stiffness. Therefore, these are the parameters of interest in our optimization. To properly simulate the tissue, particles’ diameter is set to 3 mm and volume sampling is set to 2,

\*This project has received funding from the European Research Council (ERC) under the European Union’s Horizon 2020 research and innovation programme (grant agreement No. 742671 "ARS")



resulting in a two-layer structure with the same width of the tissue. All the other simulation parameters are kept fixed for the whole process, using the same values as [2].

Parameters	Lowest	Highest	Optimal
Cluster Spacing	0.05	1	0.153
Cluster Radius	0.025	0.5	0.113
Cluster stiffness	0.1	0.9	0.631

**Table 1:** Upper and lower bounds defining the search space for the parameters of interest, and optimization results.

For each experiment, the previously collected joint states are fed to the simulated PSM arm. Direct kinematics allows to get the position of the end effector, which grasps the FleX object surface, modifying the position of those particles that are within a pre-defined distance from the end effector. The other particles follow the grasped ones and the object assumes a deformed configuration which depends on the current simulation parameters.

The optimization process is performed with the genetic algorithm scheme, which avoids being trapped in local optimal solutions, exploiting the implementation provided by MATLAB global optimization toolbox [2]. The algorithm explores a wide range of values over the entire search space (Table 1). To prevent the algorithm from trying unacceptable configurations, we define a custom constraint which ensures that generated clusters always overlap (i.e., cluster radius is at least half of cluster spacing). To be sure that the optimal parameters are able to generalize, the optimization process is performed considering different grasping experiments ( $N = 6$ ). The goal of this process is to estimate the set of parameters that gives the best matching between the real and the simulated data. To achieve this, our method minimizes the following error metric  $e$ :

$$e = \sum_{n=1}^N \sum_{l=1}^L \sum_{m=1}^M \|X_{GND}(l, n) - X_{SIM}(l, n)\| \quad (1)$$

It corresponds to the sum of the Euclidean distances ( $\|*\|$ ) between each of the  $M$  particles composing the simulated data ( $X_{SIM}$ ) and the closest point of the ground truth ( $X_{GND}$ ).

## RESULTS

The optimization process converges to the values reported in Table 1. The final optimization error is 109.5 mm, which corresponds to an average error of 2.8 mm per particle. This error is obtained as ratio between the final optimization error and the total number of particles considered in the process ( $L \cdot N \cdot M$ ). In order to assess the goodness of the estimated parameters, we introduce a new evaluation metric which allows to consistently compare real and simulated data. Since ground truth provides information only relative to the visible portion of the tissue, we reproduce the same partial view of the object that the RGB-D sensor experiences on the real setup. The error is calculated in the same way as Equation 1, but the number of considered particles is now represented by  $M'$ , which includes only those particles

which are visible from the RGB-D sensor. Furthermore, the evaluation error is computed on a broader set of experiments which includes samples not considered during the optimization. The final evaluation error is 2.6 mm ( $\pm 1.2$ ). Considering that this metric includes also the calibration error, we are able to reach an overall error which is lower than the width of the considered tissue, achieving a simulation which is highly representative of reality, as can be qualitatively seen in Figure 2.

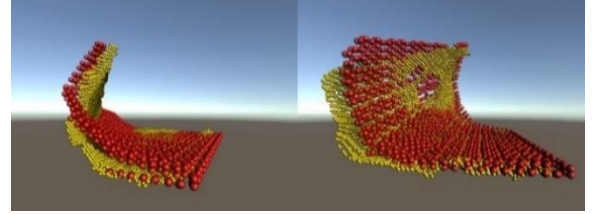


**Figure 2:** Ground truth point cloud (yellow) and deformed soft tissue with the estimated parameters (red). Figure shows two different experiments corresponding to the two greatest input deformations.

The obtained error is higher for samples with higher input deformation, suggesting that the considered set of parameters might not be able to capture the entire tissue dynamics. The obtained parameters allow our simulation to achieve a degree of accuracy which has made it possible to successfully employ it in a sim-to-real reinforcement learning framework [1].

## CONCLUSION AND DISCUSSION

Leveraging only on vision and kinematic data, which are commonly acquired in a surgical scenario, the proposed optimization method has shown promise for estimating the elastic properties of soft tissues, relying on a set of representative manipulation actions. This method has proved able to minimize the gap between simulation and reality, achieving a sufficient accuracy level to successfully learn soft tissue manipulation tasks in simulation by a DRL agent. Future work will focus on comparing the presented method with different simulation methods, for example based on continuum mechanics (i.e. SOFA framework), and testing them with more complex geometries and tasks, moving towards more realistic clinical settings.

## REFERENCES

- [1] E. Tagliabue, A. Pore, D. Dall’Alba, E. Magnabosco, M. Piccinelli, and P. Fiorini “Soft Tissue Simulation Environment to Learn Manipulation Tasks in Autonomous Robotic Surgery”, IROS, 2020.
- [2] E. Tagliabue, D. Dall’Alba, E. Magnabosco, C. Tenga, I. Peterlik, and P. Fiorini, “Position-based modeling of lesion displacement in ultrasound-guided breast biopsy.” IJCARS, 2019.
- [3] P. Guler, K. Pauwels, A. Pieropan, H. Kjellstrom and D. Kragic, “Estimating the Deformability of Elastic Materials using Optical Flow and Position-based Dynamics” 2015 IEEE-RAS 15th Int Conf on Humanoid Robots
- [4] L. Qian, A. Deguet, and P. Kazanzides, “dVRK-XR: Mixed Reality Extension for da Vinci Research Kit,” in Hamlyn Symposium on Medical Robotics, 2019.

# A hFSM based cognitive control architecture for assistive task in R-MIS

Narcís Sayols<sup>1</sup>, Alessio Sozzi<sup>2</sup>, Nicola Piccinelli<sup>3</sup>, Albert Hernansanz<sup>1</sup>, Alicia Casals<sup>1</sup>,  
Marcello Bonfè<sup>2</sup> and Riccardo Muradore<sup>3</sup>

<sup>1</sup>*Universitat Politècnica de Catalunya, Barcelona, Spain*

<sup>2</sup>*Department of Engineering, University of Ferrara, Italy*

<sup>3</sup>*Department of Computer Science, University of Verona, Italy*  
*narcis.sayols@upc.edu*

## INTRODUCTION

Nowadays, one of the most appealing and debated challenge in robotic surgery is the introduction of certain levels of autonomy in robot behaviour [1] implying technical advances in scene understanding and situation awareness, decision making, collision-free motion planning and environment interaction. The growth of R&D projects for autonomous surgical robotics (e.g. EU funded I-SUR, MURAB and SARAS) demonstrates the confidence and the expectations of the medical community on the benefits of such technologies. SARAS aims to develop assistive surgical robots for laparoscopic MIS, autonomously operating in the same workspace of either a teleoperated surgical robot or a manually driven surgical tool. The auxiliary robots autonomously decide which task perform to assist the main surgeon, planning motions for executing the task considering the dynamics of human driven tools and patient's organs (predictable only within a short time horizon). This paper proposes a control architecture for surgical robotic assistive tasks in MIS using a hierarchical multi-level Finite State Machine (hFSM) as the cognitive control and a two-layered motion planner for the execution of the task. The hFSM models the operation starting from atomic actions to progressively build up more complex levels. The two-layer architecture of the motion planner merges the benefits of an offline geometric path construction method with those of online trajectory reconfiguration and reactive adaptation. At a global level, the path is built according to the initial knowledge of the operating scene and the requirements of the surgical tasks. Then, the path is reconfigured with respect to the dynamic environment using artificial potential fields [2]. Finally, a local level computes the robot trajectory, preserving collision-free property even in presence of obstacles with small diameter (i.e. the manually driver surgical instruments), by enforcing a velocity modulation technique derived from the Dynamical Systems (DS) based approach of [3].

## MATERIALS AND METHODS

The surgical tasks of the auxiliary robots in the surgical environment are modelled as a three-level hFSM:

- **Surgeme level:** this level are sequences of simple movements that can be performed by the robot (the *surgemes*) to form actions.
- **Action level:** this level is made of a sequence of actions (a simple tool task with a defined objective) to perform operation phases.
- **Phase level:** a real surgical procedure is decomposed into a sequence of phases (a complex of surgical actions with a defined intention or objective with a clear beginning and end).

A scheme of the three levels of the hFSM for the Bladder Mobilization task is shown in figure 1.

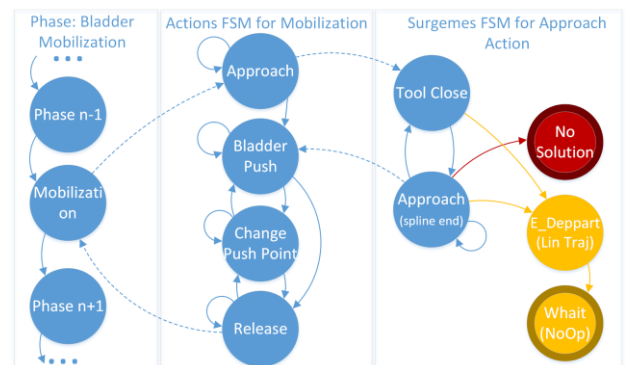


**Figure. 1** Scheme of the hierarchical FSM

The transitions between the phases and the actions can be triggered using algorithms of scene understanding, action recognition and action prediction or by direct commands of the main surgeon. The transitions between the surgemes are triggered by the inner controls of the robot or by the motion planner as soon as the relative task is accomplished. Once the surgeme to be executed is determined by the cognitive control, the motion planner generates the trajectory (if the surgeme requires a movement) to accomplish the task. The first layer of the motion planning module, called Dynamic trajectory reconfigurator (DTR), generates a trajectory defined by a set of free of collision control points (CPs) using the current and goal points as well as collision risk information computed as in [4] and the constraints on the motion such as direction to follow at the end or the

beginning of the motion. The DTR computes an initial smooth trajectory (C1 third order polynomial) from the current pose to the goal pose (which can be dynamically updated by the hFSM during the trajectory) with the constraints given by the hFSM. This layer returns a set of equally spaced CPs that represent the trajectory. At each control step, the DTR reconfigures the CPs to ensure that the trajectory is collision free in the dynamic environment. These CPs are adapted using artificial potential fields. Each CP is represented as a mass affected by the attraction force to its original position, a repulsion force generated by the other elements in the workspace and a force in the direction of the neighbouring CPs to maintain the coherence in the movement. Moreover, a Depth Map 2D matrix (DM) is computed at each CP to ensure that the whole tool (not only the tip) follow a collision free trajectory. The elements (i,j) of the DM matrix represent the maximum depth reachable for the tool in the direction  $\theta_i, \phi_j$  (spherical coordinates). The CP is transformed into spherical coordinates with origin in the insertion point of the tool (RCM) to be compared with the values in the DM; if the depth value of the CP is higher than the corresponding element of the DM, the trajectory passing through that CP would lead a part of the tool to collide with an obstacle, so the CP receives an attraction force towards the RCM in order to be moved to a new position. Finally, the DTR uses the collision free CPs to generate a Catmull-Rom spline that represents the trajectory. The coefficients of this spline are sent to the second layer. The DTR ensures that the CPs are collision free but does not guarantee that the trajectory between two consecutive CPs is collision free too; in fact, the surgical scenario includes cylindrical tools with very thin diameter which can be smaller than the distance between two adjacent CPs. Thus, the second layer, called local modulation planner, is the responsible to compute free collision trajectories between each consecutive pair of CPs exploiting an approach based on the algorithm described in [5]. This algorithm modulates the desired velocity of the robot to obtain a new velocity which drives the robot on a collision free trajectory. The modulation is performed by means of a matrix computed analytically from the geometric features of the obstacles. Since the modulation changes the original trajectory of the robot given by the CPs, a recomputation of the spline is necessary at the end of the modulation to obtain the new trajectory until the next CP. This new spline will be used in the next control step  $t+1$  to compute the desired velocity.

## RESULTS

The method has been validated by performing a realistic surgical task both in a simulated environment and on a real setup. The phase chosen for the validation is the bladder mobilization of the Robotic Assisted Radical Prostatectomy. Figure 1 shows the decomposition of this phase in actions and surges. In this phase, the SARAS tools must push down the bladder to make space for the main surgeon avoiding any type of collision with the

main tools and the environment. This phase has been chosen because it contains almost all type of surges and the trajectory planning has to perform different types of constraint in the movement. This phase is composed of four consecutive actions. In the first action (Approach), the tool is placed over a determined point of the bladder surface. Then the tool pushes the bladder down (Bladder push), creating free space for the surgeon. The pushing position and depth can be changed if required with the Change push point action. Finally (Release), the tool releases the bladder and exits to a safe pose. An emergency action is included to place the tool in a safety pose and exit the action. A snapshot of the approach trajectory (Spline end surge for a spline trajectory with constraint on the direction at the end of the motion) of the Approach action is shown in Figure 2.

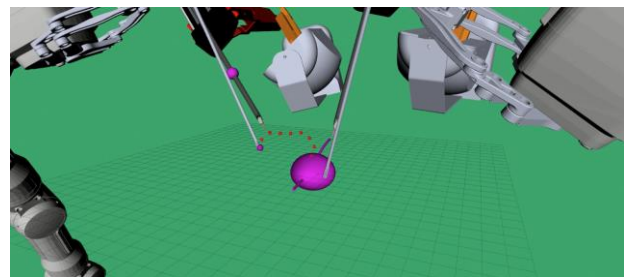


**Figure. 2** Example of the trajectory computed and dynamically updated for approaching a virtual bladder

## CONCLUSION AND DISCUSSION

We proposed a cognitive control architecture for autonomous execution of assistive task in R-MIS. This architecture is based on a three-level hFSM that models the surgical operation and on a two-layer motion planner which ensures the correct execution of the motions. The proposed architecture has been successfully validated on a realistic surgical task both in a simulated environment and on a real setup.

## REFERENCES

- [1] Fanny Ficuciello, Guglielmo Tamburrini, Alberto Arezzo, Luigi Villani, Bruno Siciliano, "Autonomy in surgical robots and its meaningful human control", Paladyn, Journal of Behavioral Robotics, 2019, De Gruyter, vol.10, 1, 30-43
- [2] R. R. Murphy, "Potential Fields Methodology", Introduction to AI robotics (1st Ed.), MIT Press, 2000, 105-153.
- [3] Khansari-Zadeh, S. M. and Billard, Aude, "A Dynamical System Approach to Realtime Obstacle Avoidance", Autonomous Robots, Springer Verlag, 2012, vol.32, 4,433-454.
- [4] A. Hernansanz and A. Casals and J. Amat, "A multi-robot cooperation strategy for dexterous task oriented teleoperation", Robotics and Autonomous Systems, 2015, vol. 68, 156-172.
- [5] Sozzi, A., Bonfè, M., Farsoni, S., De Rossi, G. and Muradore, R, "Dynamic Motion Planning for Autonomous Assistive Surgical Robots", Electronics, MDPI, 2019, vol. 8, 957.



# Vision-Based Dynamic Virtual Fixtures for Tools Collision Avoidance in MIRS

C. Iacono, R. Moccia, B. Siciliano, and F. Ficuciello

*Department of Information Technology and Electrical Engineering, Università degli Studi di Napoli Federico II*

## INTRODUCTION

During the execution of a surgical procedure, in Minimally Invasive Robotic Surgery (MIRS), two or more tools can come dangerously close to each other. The surgeon has a limited vision on the surgical site, which reduces dexterity and increases the cognitive workload. Moreover, collisions can cause tools or tissues damage. Haptic feedback could significantly affect the performances of novice surgeons, reducing training duration and improving the effectiveness of the procedures. A large number of surgical tasks can benefit from the introduction of haptic feedback, such as robotic polypectomy [1]. Collisions between surgical tools in MIRS can be avoided with the application of shared control techniques, such as Virtual Fixtures. Forbidden Region Virtual Fixtures (FRVF) can be used to restrict the motion of the robot's tool through a repulsive force rendered to the surgeon. The da Vinci Research Kit (dVRK) is already used to test VF-based methods [1] [2]. Since dVRK robot joints are driven through cables that introduce elasticity, backlash and nonlinear friction [3], tools pose obtained through direct kinematics is affected by errors. Therefore, to ensure a correct application of the VF, a method for tool tracking is strictly needed. In our work, we propose a surgical tool collision-avoidance method, to improve safety in surgical procedures. The method is tested on the dVRK and includes marker-less surgical tool tracking using an Extended Kalman Filter (EKF) that couple vision and kinematics information to enhance the robustness of VF application.

## MATERIALS AND METHODS

The dVRK robot is composed of two Patient Side Manipulators (PSMs) and an Endoscope Camera Manipulator (ECM) commanded by two Master Tool Manipulators (MTMs). The surgical scene can be seen by the surgeon thanks to an endoscope, including a stereo camera with 5 mm baseline. Each PSM has a reference base frame,  $\mathcal{F}_b : (O_b - x_b y_b z_b)$ , positioned at the PSM Remote Center of Motion (RCM). The direct kinematics of the dVRK allows computing the current pose of each gripper frame  $\mathcal{F}_g : (O_g - x_g y_g z_g)$  respect to the corresponding base frame. The tools tip frames  $\mathcal{F}_t : (O_t - x_t y_t z_t)$  of each PSM have their origins in the PSM tool tips. The method directly uses laparoscopic images to track the surgical instrument. A deep learning solution for instrument semantic binary segmentation is employed. The system adopts the U-Net modification proposed in [4], called TernaNet that is trained using the dataset provided for MICCAI 2017 Endoscopic Vision Sub-Challenge: Robotic Instrument

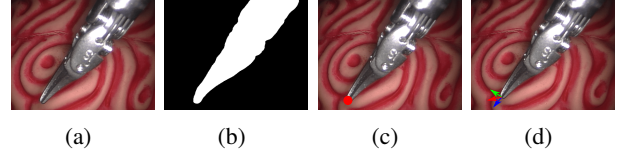


Fig. 1: Segmentation method: (a) Original frame; (b) Binary mask; (c) Point identification in the image plane; (d) Reference frame definition.

Segmentation. The tool tip position on the image plane is computed from the binary mask, reducing the search area range re-projecting the tip kinematic position on the image plane. Then, the 3D position of the PSM2 tip, expressed in the camera frame  $\mathcal{F}_c$ , is reconstructed by using a triangulation method with direct linear transform. The tool orientation is computed solving PnP problem, which allows computing the orientation of the object from a set of  $n$  correspondences between 3D points and their 2D projections. For the estimation and tracking of the instrument pose, the Extended Kalman Filter (EKF) is used, combining visual information from the endoscope with the robot kinematics. The prediction step provides a preliminary estimation of the instrument pose through the linear and angular velocities of the gripper provided by the manipulator kinematics. Then, the vision-based estimated pose is used in the filter correction step. The filter provides an estimate of the tool tip pose  $\zeta = [p_t, q_t]^T$ , being  $p_t$  the true tool position, and  $q_t = [\eta_t, \epsilon_t]^T$  its quaternion-based true orientation in the base frame  $\mathcal{F}_b$ . The process dynamics for the state vector  $\zeta$  and the measurement model are given by:

$$\begin{cases} \dot{p}_t = v_g + S(\omega_g) r_{gt} + n_p \\ \dot{q}_t = \frac{1}{2} \Omega(\omega_g) q_t + n_q \\ y = \zeta + m \end{cases} \quad (1)$$

where  $[v_g, \omega_g]^T$  are the linear and angular velocity of the gripper frame,  $S(\cdot)$  is the skew-symmetric operator,  $r_{gt}$  is the position vector of the tool tip respect to the gripper,  $n = [n_p, n_q]^T \sim \mathcal{N}(0, N)$  and  $m \sim \mathcal{N}(0, M)$  are the process and measurement noise respectively and

$$\Omega(\omega) = \begin{bmatrix} 0 & -\omega^T \\ \omega & S(\omega) \end{bmatrix}. \quad (2)$$

Then, the control and measurement matrices used in the EKF implementation are easily computed:

$$F = \begin{bmatrix} S(\omega_g) & O_3 \\ O_3 & S(\omega_g) \end{bmatrix}; \quad H = \begin{bmatrix} I_3 & O_3 \\ O_3 & I_3 \end{bmatrix}. \quad (3)$$

The collision avoidance between the two tools is ensured by the application of a FRVF. To this purpose, the VF is

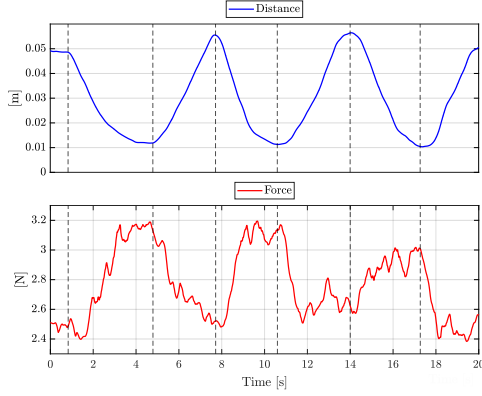


Fig. 2: First evaluation experiment. Duration: 20 seconds. Time histories of: (Blue) Distance between surgical tools; (Red) Related estimated force norm.

defined as the swept surface along one of the tool axis. The VF has a cylindrical shape with a radius which is double the tool radius. The minimum distance between the PSM tool tip position  $\mathbf{x}$  and the cylindrical FRVF of the other tool corresponds to the length of the line segment which joins perpendicularly the point to the axis minus the radius of the cylinder. A constraint enforcement method is defined, consisting in the application of a spring-damper like force:

$$\mathbf{f}_{vf}(\tilde{\mathbf{x}}, \dot{\tilde{\mathbf{x}}}) = -\mathbf{K}_{vf}\tilde{\mathbf{x}} - \mathbf{D}_{vf}\dot{\tilde{\mathbf{x}}} \quad (4)$$

where  $\tilde{\mathbf{x}} = \mathbf{x}_d - \mathbf{x}$  is the displacement between the point  $\mathbf{x}_d$ , belonging to the constraint geometry having minimum distance from  $\mathbf{x}$ . The matrices  $\mathbf{K}_{vf}$  and  $\mathbf{D}_{vf}$  are properly designed diagonal and positive definite. The external force is not directly measurable, it is estimated by resorting to a non-linear dynamic observer [2]. Finally, the force imposed by the Virtual Fixture is mapped on the MTM, that is controlled through an impedance controller, to generate the force cues.

## RESULTS

The collision avoidance strategy is evaluated in two different tasks. During the first evaluation test, the PSM1 tool is fixed and the PSM2 is moved by the user in teleoperation mode towards PSM1. Figure 2 shows the distance between the two surgical tools, computed considering the proposed tracking method, and the related repulsive haptic force norm rendered to the user through the master side (MTM) during the task. The maximum reached force is 3.2 N. The second evaluation test consists in a human subject study to show significant differences in performance caused by the introduction of force feedback. The study involves 12 subjects divided into two groups, 6 experienced and 6 novice surgeons, based on self-evaluation about their experience in the use of daVinci Robotic system for minimally invasive surgical procedures. During each test, the subject keeps the PSM1 centered in the middle of a circle with a diameter of 20 mm. Meanwhile, the PSM2 has to follow the circular path for 270° from a definite starting point. In the first experiment, the subjects perform the test 5 times moving the surgical tool in free

TABLE I: Maximum force and t-test results on minimum distance for novice and expert users. The result of the test is 1 if the test rejects the null hypothesis at the 5% significance level, and 0 otherwise.

Novice	test	p	$F_M$ [N]	Expert	test	p	$F_M$ [N]
1	1	0.0044	2.4416	1	0	0.1352	3.4527
2	1	0.0127	3.0749	2	0	0.0856	2.8175
3	1	0.0030	3.3411	3	0	0.8286	3.5239
4	1	0.0219	2.8188	4	0	0.8757	2.6180
5	1	0.0206	3.9998	5	0	0.1140	3.0035
6	1	0.0012	3.4170	6	0	1	2.8800

motion and 5 times with the proposed collision avoidance constraint applied. The minimum distance between the tools is considered as performance parameter and it is computed using the proposed tracking method, in the VF constraint test the maximum force felt during the task is also computed. To demonstrate the statistical relevance of the results, a comparison is made between the mean values of minimum distance, through a statistical unpaired t-test, with a significance level  $\alpha = 0.05$ . As presented in Table I, the test shows statistically significant differences between the means for all subject in the novice group and an increase in the minimum distance values of  $\sim 10\%$  in collision tests with respect to free-hand tests.

## CONCLUSIONS AND DISCUSSION

This paper introduces a method based on haptic guidance and virtual fixtures that allows avoiding surgical tools collision in MIRS. A marker-less algorithm allows estimating the PSM position and orientation, using kinematic and visual information. The PSM estimated pose is used to generate a FRVF, that aims to avoid collision between the two instruments through a repulsive force felt at the MTM during the surgical task execution. The proposed strategies are evaluated through multiple experiments on dVRK, showing good results in improving novice surgeon's performance. Therefore, the method can be considered effective both in a training stage of novice surgeon, as well as when the level of expertise increases. The goal for future works is to improve the accuracy of the tool pose estimation. For this purpose, more advanced methods for hand-eye calibration and 3D reconstruction will be considered. Moreover, the application of the method can be extended to the collision avoidance of both PSMs and the ECM, when automatic movement of the ECM is imposed.

## REFERENCES

- [1] R. Moccia, M. Selvaggio, L. Villani, B. Siciliano, and F. Ficuciello, "Vision-based Virtual Fixtures Generation for Robotic-Assisted Polyp Dissection Procedures," *Proc. IEEE International Conference on Intelligent Robots and Systems*, 2019.
- [2] M. Selvaggio, G. A. Fontanelli, F. Ficuciello, L. Villani, and B. Siciliano, "Passive Virtual Fixtures adaptation in minimally invasive robotic surgery," *IEEE Robotics and Automation Letters*, vol. 3, no. 4, pp. 3129–3136, 2018.
- [3] G. A. Fontanelli, F. Ficuciello, L. Villani, and B. Siciliano, "Modelling and identification of the da Vinci Research Kit robotic arms," *Proc. IEEE/RSS International Conference on Intelligent Robots and Systems*, pp. 1464–1469, 2017.
- [4] A. A. Shvets, A. Rakhlin, A. A. Kalinin, and V. I. Iglovikov, "Automatic Instrument Segmentation in Robot-Assisted Surgery using Deep Learning," *Proc. 17th IEEE International Conference on Machine Learning and Applications*, pp. 624–628, 2018.

# A Framework of Real-time Freehand Ultrasound Reconstruction based on Deep Learning for Spine Surgery

Ruixuan Li<sup>1</sup>, Kenan Niu<sup>1</sup>, Di Wu<sup>1</sup>, Emmanuel Vander Poorten<sup>1</sup>

<sup>1</sup>Robot-Assisted Surgery Group, Mechanical department, KU Leuven, Belgium,  
ruixuan.li@kuleuven.be

## INTRODUCTION

In modern society, a great number of people suffer from spinal diseases, such as degenerative spine diseases (DSD). The incidence of DSD is about 3.63% of world population, affecting 266 million individuals. Currently, advanced medical imaging has provided high resolution medical images. However, ionizing radiation of CT and high cost of MRI limit their clinical applications. Ultrasound (US) is capable of detecting bone through soft tissue and tracking bone kinematics [1], which becomes a good alternative to visualize the anatomy of the spine. It provides an affordable and non-ionizing imaging modality. However, disease diagnosis with 2D US images is time consuming and skill-intensive.

To interpret US images, the real-time 3D reconstructed spine model can thus reduce the mental effort for clinicians. To reconstruct a 3D spine model, the contours of vertebrae need to be segmented from US images. Traditional image segmentation algorithms have already achieved good results with an average accuracy of less than 0.3 mm. However, the computation time is about 4.1 seconds for one image [2]. Recently, advanced deep learning networks have been applied in medical ultrasound imaging processing. The U-Net is an efficient network to segment ultrasound images [3]. In this study, we applied the U-Net with several modifications for real-time US segmentation. The goal of this study is to improve pre-operative DSD diagnosis so that the proposed accurate 3D US image reconstruction framework could be applied for intraoperative surgery. This framework can also be coupled with automatic robotic ultrasound imaging system in the future.

The following section presents materials and methods of the proposed US scanning system. Section Results addresses the experiments performances and quantitative results. Finally, results are discussed, and conclusions are drawn.

## MATERIALS AND METHODS

A vertebra model was generated from preoperative CT scanning. Then, it was manufactured by 3D printing and immersed in a water tank for image acquisition. To acquire US image data associated with 3D positioning information, the medical ultrasound system (SonoSite, USA) was equipped with a video capture card (Epiphan Systems Inc. Palo Alto, Canada) and an electromagnetic tracking system (NDI Aurora, Canada). In addition, a PC workstation with Nvidia P2000 GPU was employed for training deep learning network and visualization.

Figure 1 illustrated the workflow to reconstruct the spine model. The US images and spatial information were collected simultaneously with ROS. Then the obtained images were automatically segmented by U-Net and published as ROS topic. Combining with Aurora ROS topic, information was sent to reconstruction algorithm.

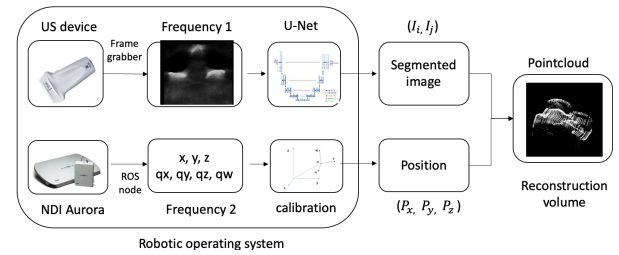


**Figure. 1.** Workflow for the reconstruction system

To capture a full view of the vertebra, US probe was held on the top of the vertebra and kept perpendicularly to the vertebra. 90 images were collected by video capture card and masked manually. Subsequently, these images were augmented to generate more datasets by mirroring on vertical axis and shifting in horizontal direction within 0.05 mm separately. Eventually, the model was trained with 360 augmentation images, in which 36 images were used as validation datasets. The implementation of U-Net consisted of five layers, and the size of input images was 256\*256. The network was trained for 50 epochs with a learning rate of 1e-4. The U-Net based bone segmentation algorithm could predict the segmentation outputs from raw images without additional pre-processing. Then, predicted images were evaluated using recall and precision segmentation metrics. Furthermore, the dice similarity coefficient (DSC) was also calculated by comparing with manually labelled images.

For freehand tracking, an EM sensor was used to provide translation and rotation information  $T_{s \rightarrow g}$ . After attaching the EM sensor on US probe, spatial calibration and temporal calibration were performed. The purpose of the spatial calibration was to establish the transformation between sensor coordinate and US image coordinate  $T_{i \rightarrow s}$  of transducer surface. The crosswire phantom was applied for spatial calibration with the Least Square method [4]. Furthermore, temporal calibration was implemented to eliminate the sampling latency time between EM data and US image data. A synchronizing filter was used within ROS framework by comparing timestamps of incoming messages to output messages in one callback.

Once data were calibrated, the pixels in 2D US images were transformed into 3D volume in the global coordinate system. In reconstruction process, the



segmented contour pixel  $(u_x, u_y)$  was converted into point cloud  $(x, y, z)$  in the global coordinate, where  $T_{s \rightarrow g} \cdot T_{i \rightarrow s}$  is the transformation matrix from image coordinates to sensor coordinate in Eq. (1).

$$\begin{bmatrix} x \\ y \\ z \\ 1 \end{bmatrix} = T_{s \rightarrow g} \cdot T_{i \rightarrow s} \begin{bmatrix} u_x \\ u_y \\ 0 \\ 1 \end{bmatrix} \quad (1)$$

Subsequently, the calibrated image sequences in 12Hz and corresponding positions in 50Hz were transmitted simultaneously to reconstruction algorithm to form 3D volume. In previous research, the interpolation method was widely developed to render volume [5]. But this paper focused on geometry features of the interest region of spine. Thus, to visualize the features, PointCloud Library (<https://pointclouds.org/>) based program was developed. The collected point clouds had the potential to have meshes as smooth surface for future requirements.

## RESULTS

The numerical evaluation results of U-Net segmentation are shown in Table 1 compared with ground truth obtained from manual segmentation. The inference time for 30 US images is about 5 seconds.

**Table 1.** Validation of U-Net image segmentation

	Recall	Precision	DSC
Experiment 1	0.90	0.91	0.91
Experiment 2	0.94	0.95	0.94
Experiment 3	0.93	0.93	0.93
Experiment 4	0.86	0.91	0.83
Experiment 5	0.97	0.99	0.95

Figure 2 gives an example of the predicted results of the vertebra spinous process generated by the trained model. Figure 2.c shows the reconstructed point clouds of 3D spine model contains all significant geometry features such as spinous process and articular process, which matches with 3D printed vertebra model in Figure 2.d. This result can visually show the features of the spine. The entire framework could operate at 5Hz to generate an updated point cloud.

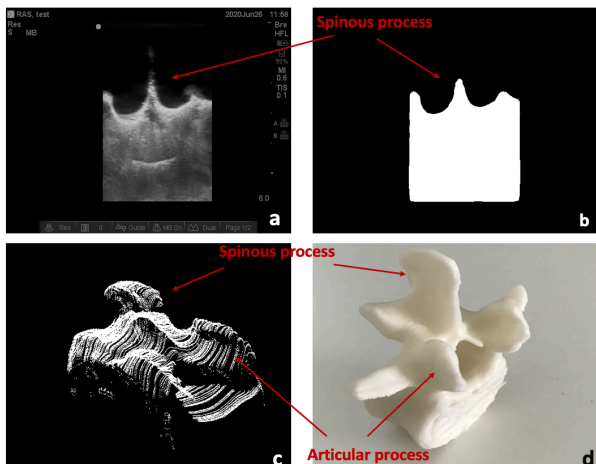


**Figure 2.** Example of U-Net US segmentations. a) Raw US image; b) U-Net segmented image; c) Reconstruction model; d) 3D printed vertebra model.

## CONCLUSION AND DISCUSSION

In this article, a workflow was presented to reconstruct 3D spine shape model for medical purposes, mainly for pre-operative spine disease diagnosis. US images and position data were efficiently coupled in ROS and processed by the proposed framework. Moreover, the contour of spinous and articular process were successfully segmented and reconstructed with spatial information. U-Net network is capable of efficiently and accurately segmenting ultrasound images. Except pre-operative applications, such framework also has a great potential to be applied in intraoperative surgery to generate 3D structure of the anatomy within a short time. Finally, the outcome can be illustrated in 3D by visualization toolkit.

However, a limit of this study is the small amount of training data. Therefore, the performance of U-Net still has potential to be improved, when the larger training data is available. Besides, 3D printing material can generate a strong reflection of ultrasound wave, resulting in bony shadow in B-mode images. To mimic the actual human bone, future research should use bionic material phantom or animal specimen. In the future, robot arms can be utilized in this framework for surgical application. Highly automatic robotic control can reduce the work burden and obtain the optimal probe position rather than freehand scanning. Besides, IMU tracking is another promising tracking solution to get rid of magnetic field. Finally, future work should also focus on developing deep learning network for spine shape model reconstruction.

## REFERENCES

- [1] K. Niu *et al.*, 'In situ comparison of A-mode ultrasound tracking system and skin-mounted markers for measuring kinematics of the lower extremity', *J. Biomech.*, 2018, doi: 10.1016/j.jbiomech.2018.03.007.
- [2] R. Jia, S. J. Mellon, S. Hansjee, A. P. Monk, D. W. Murray, and J. A. Noble, 'Automatic bone segmentation in ultrasound images using local phase features and dynamic programming', *Proc. - Int. Symp. Biomed. Imaging*, vol. 2016-June, pp. 1005–1008, 2016, doi: 10.1109/ISBI.2016.7493435.
- [3] O. Ronneberger, P. Fischer, and T. Brox, 'U-net: Convolutional networks for biomedical image segmentation', in *Lecture Notes in Computer Science (including subseries Lecture Notes in Artificial Intelligence and Lecture Notes in Bioinformatics)*, 2015, vol. 9351, pp. 234–241, doi: 10.1007/978-3-319-24574-4\_28.
- [4] L. Mercier, T. Langø, F. Lindseth, and D. L. Collins, 'A review of calibration techniques for freehand 3-D ultrasound systems', *Ultrasound Med. Biol.*, vol. 31, no. 4, pp. 449–471, 2005, doi: 10.1016/j.ultrasmedbio.2004.11.015.
- [5] Q. H. Huang, Z. Yang, W. Hu, L. W. Jin, G. Wei, and X. Li, 'Linear tracking for 3-D medical ultrasound imaging', *IEEE Trans. Cybern.*, vol. 43, no. 6, pp. 1747–1754, 2013, doi: 10.1109/TSMCC.2012.2229270.

# A supervisory controller for semi-autonomous surgical interventions

Fabio Falezza , Nicola Piccinelli , Andrea Roberti , Francesco Setti ,  
Riccardo Muradore , and Paolo Fiorini

*Department of Computer Science, University of Verona, Verona, Italy*  
*{name.surname}@univr.it*

## INTRODUCTION

Nowadays the main research interests in the field of Robotic Minimally Invasive Surgery (R-MIS) are related to robots' autonomy [1]. Techniques like trajectory planning, collision avoidance [2, 3], decision making and scene understanding [4] require technical advances in order to be applied to such an environment. In this paper, we propose a deterministic supervisory controller for a surgical semi-autonomous robotic platform.

The proposed method uses a three-level Hierarchical Finite State Machine (HFSM) to define all the possible behaviours of the autonomous system. The transitions of the HFSM are triggered by the *Observers*, a set of functions fed with the state of the system (robot kinematics, anatomical structures, etc.) that output a logical description of the surgery state. We tested the supervisory controller performing the “bladder neck incision” phase of a Radical Prostatectomy (RARP) procedure.

## SUPERVISORY CONTROLLER

We propose a hierarchical HFSM with three layers defined as: (1) **Procedure**, which encompasses a complete surgical procedure and is composed of a set of surgical phases and transitions between them; (2) **Phase**, which defines a complex of surgical actions with a defined intention or objective having a clear beginning and end; (3) **Action**, which defines a simple tool task with a specific objective and defined as a set of surgemes and their interactions, i.e. the atomic actions within a surgery that cannot be decomposed further. The medical knowledge used to define the HFSM is provided by surgeon interviews and literature review. The control and supervision of the procedure, phases and actions is conducted by means of finite state machines (FSM). This methodology enables a strict control of the status of each phase, action and surgeme executed by each robotic tool during a procedure. The procedure is modelled as a FSM, where each state represents a phase. Following with the decomposition, each phase FSM contains an action FSM whose states are surgemes representing atomic actions performed by a robot or a surgical tool.

The supervisory controller is in charge of providing commands to the robot controller and to trigger the transitions of the HFSM. Three sub-modules compose the controller: *Supervisor* uses the knowledge of the surgical pro-

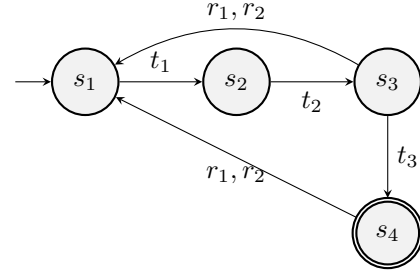


**Figure 1:** The finite state machine of the first action (approach catheter) of the bladder neck incision. Labels  $s_i$ ,  $r_i$  and  $t_i$  are defined in Table 1.

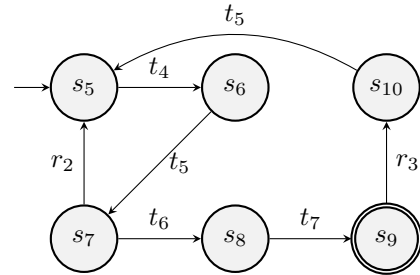


**Figure 2:** The finite state machine of the second action (grasp catheter) of the bladder neck incision. Labels  $s_i$ ,  $r_i$  and  $t_i$  are defined in Table 1.

cedure to choose the atomic movement (i.e. surgeme); *Observer* converts the information generated by the perception of the environment to the trigger events encoded into the surgical procedure; and *Dispatcher* is in charge of dispatching the surgeme execution to the lower level robot controller (i.e. the trajectory reconfiguration and obstacle avoidance modules).

## EXPERIMENTAL SETUP

The experimental setup consists of a *da Vinci* surgical robot controlled through the *da Vinci* Research Kit (dVRK), a SARAS robotic arm [1] acting as the assistant surgeon and an Intel RealSense d435 RGB-D camera mounted on the *da Vinci* camera arm (ECM).

The HFSM used in the experiment is composed of one phase FSM and two action FSMs shown in Fig. 1 (*wait until the catheter is detected before moving SARAS arm towards it*) and Fig. 2 (*grasping and pulling movements*). A detailed description of the surgemes and the transition triggers are presented in Table 1.

Label	State description
$s_1$	Move to safe position
$s_2$	Wait until catheter is recognised
$s_3$	Follow the catheter position
$s_4$	Approach the grasping position
$s_5$	Idle, wait in the grasping position
$s_6$	Open the grasper
$s_7$	Reach the grasping position
$s_8$	Close the grasper
$s_9$	Pull up the grasper
$s_{10}$	Open the grasper

Label	Trigger description
$t_1$	Robot tool is in safe position
$t_2$	Catheter has been recognised
$t_3$	Catheter has been pulled-up
$t_4$	Robot tool is ready to start grasping
$t_5$	Robot tool is open
$t_6$	Catheter is on the grasping position
$t_7$	Robot tool is close
$r_1$	Catheter tracking is lost
$r_2$	Reset command by surgeon
$r_3$	Target position not reachable

**Table 1:** Description of the surges and triggers generated by the Observer.

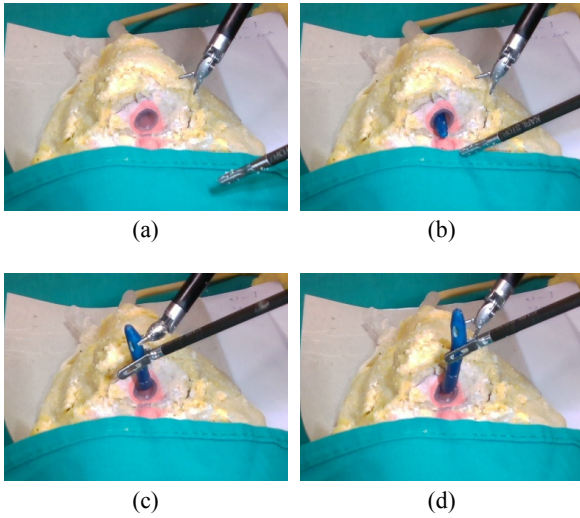


**Figure 3:** The automatic catheter grasping experimental validation. a) the initial position of the autonomous system, b) the arm starts moving to the catheter, c) the arm approaches the grasping point, d) once the catheter is grasped the main surgeon releases it.

The detection and tracking of the catheter is done using the OpenCV library. To detect the catheter we use a template matching technique, the resulting features are then tracked frame by frame using Lucas-Kanade optical flow. The position and the velocity of the catheter are projected in 3D (using the depth map of the RGBD camera) providing to the supervisory controller the odometry of the grasping point. The proposed tracking method is further improved by restricting the search area around the *da Vinci* arm during the catheter extraction.

## RESULTS

The proposed method, as shown in Fig. 3, is able to accomplish the catheter detection and grasping autonomously. Fig. 3a shows the robot in the initial position, corresponding to the state  $s_1$  of the FSM of Fig. 1. When the vision module recognises the catheter, the SARAS tool reaches the approach grasping position ( $s_4$ ) provided by the features in the 3D system space, as shown in Fig. 3b. The surgeon extracts the catheter with the *da Vinci* arm (PSM) and pulls it up to the desired posi-

tion, triggering the transition from state  $s_5$  and  $s_6$ . Therefore, the SARAS tool starts moving towards the grasping point and can proceed with the grasping action shown in Fig. 3c. After that, the SARAS arm pulls the catheter autonomously as shown in Fig. 3d. Pictures in Fig. 3 refer to the full video available at <https://youtu.be/mTAWF56iEek>.

## CONCLUSION

In this work, we proposed a supervisory controller for semi-autonomous surgical robots. The controller has been tested with realistic phantom on a specific phase of a radical prostatectomy. Further improvements of the proposed method are: the integration of machine learning approaches to provide phases and actions segmentation as input to the observer, and the extensions to the full RARP.

## ACKNOWLEDGEMENTS

This work has received funding from the European Research Council (ERC) under the European Unions Horizon 2020 research and innovation programme under grant agreement No. 742671 (ARS) and from the European Union’s Horizon 2020 research and innovation programme under grant agreement No. 779813 (SARAS).

## REFERENCES

- [1] Elettra Oleari et al. “Enhancing surgical process modeling for artificial intelligence development in robotics: The SARAS case study for minimally invasive procedures”. In: *2019 13th International Symposium on Medical Information and Communication Technology (ISMICT)*. IEEE. 2019, pp. 1–6.
- [2] Alessio Sozzi et al. “Dynamic Motion Planning for Autonomous Assistive Surgical Robots”. In: *Electronics* 8.9 (2019), p. 957.
- [3] Michele Ginesi et al. “Autonomous task planning and situation awareness in robotic surgery”. In: *arXiv preprint arXiv:2004.08911* (2020).
- [4] Giacomo De Rossi et al. “Cognitive Robotic Architecture for Semi-Autonomous Execution of Manipulation Tasks in a Surgical Environment”. In: *2019 IEEE/RSJ IROS*. IEEE. 2019, pp. 7827–7833.

# Multi-task control strategy exploiting redundancy in RMIS

Tomàs Pieras<sup>1</sup>, Albert Hernansanz<sup>1</sup>, Narcís Sayols<sup>1</sup>, Johanna Parra<sup>2</sup>, Elisenda Eixarch<sup>2,3</sup>, Eduard Gratacós<sup>2,3</sup>, Alícia Casals<sup>1</sup>

<sup>1</sup>Research Centre for Biomedical Engineering, CREB. Universitat Politècnica de Catalunya, UPC

<sup>2</sup>Research Fetal i+D Fetal Medicine Research Center, BCNatal - Barcelona Center for Maternal-Fetal and Neonatal Medicine (Hospital Clínic and Hospital Sant Joan de Déu)

<sup>3</sup>Universitat de Barcelona Centre for Biomedical Research on Rare Diseases, CIBER-ER

tomas.pieras@upc.edu

## INTRODUCTION

Intrauterine fetal surgery allows a minimally invasive surgery (FMIS) approach to the treatment of congenital defects. This surgical technique allows the correction of the Twin-to-Twin Transfusion Syndrome (TTTS) [1]. TTTS is a severe complication in monochorionic twins' pregnancies that occurs when there is communication (anastomoses) between the fetuses' blood systems, which leads to cardiovascular disturbances and results in their death in 90% of cases. A minimally invasive approach is less harmful and allows the preservation of the tissues of the amniotic sac. Fetoscopic Laser Photocoagulation (FLP) is a MIS intervention to ablate all the intertwin anastomoses to make independent the twins' vascular systems from each other [2].

A single master single slave teleoperation platform was developed to assist the surgeon during FLP, Fig. 1. The master is composed of a 6DoF haptic device and an interactive user interface containing fetoscopic view, interactive navigation map, etc. The slave is composed of 6DoF robot holding a fetoscope, an active trocar insertion depth control and an automated coagulation laser control system. The platform has been tested by 14 surgeons with different fetoscopic surgical experience, obtaining the face validity. Two main issues have been detected. First, the need of a redundant robot to overcome the kinematic restrictions imposed by the Remote Center of Motion (RCM) and the workspace placement, defined by the placenta position. Second, the need of active human-robot interaction during pre and post-operative phases

(insertion and extraction of the fetoscope) and during surgery to enable a safe shared workspace between medical staff (e.g. auxiliary surgeon with an echographer probe) and robot.

Following the generalized framework for control of redundant manipulators in RMIS proposed in [3], this paper proposes a multi-task control strategy exploiting redundancy to improve dexterity and reachability as well as enable human-robot interaction to deal with human-robot collisions and co-manipulation while performing the surgical task. This work is based on a 7 DoF KUKA LWR 4, a redundant and collaborative robot.

## MATERIALS AND METHODS

FLP surgery can be described with a Finite State Machine (FSM) with five main states: System Set-up (SS), anastomoses localization (AL), coagulation (AC), review (AR) and tool removal (TR). The developed multi-task control modulates the behavior of the system according to the specific requirements of each state. A hierarchical multi-layer control ensures the control of the tool tip pose (main task) guided by co-manipulation (SS and TR) or telemanipulation (AL, AC and AR). Three secondary tasks are active when necessary: dexterity optimization using redundancy (all states), joint compliance (all states) and obstacle avoidance (AL, AC and AR). Fig. 2 shows the multi-layer control schema for the different phases.

Two robot guidance modes are proposed: telemanipulation and co-manipulation.

Robot redundancy is obtained adding an extra joint (q3) to the kinematic chain. Redundancy allows the use of the

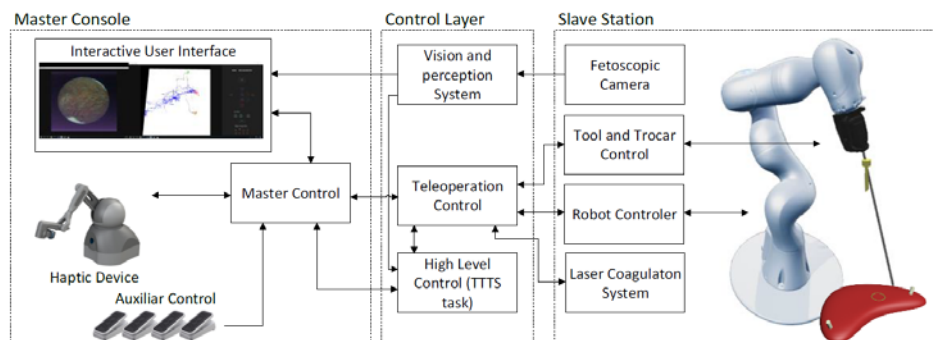


Figure 1. Schematic representation of the robot-assisted TTTS surgery-oriented teleoperation platform



Jacobian's null-space projection, where the proposed subtasks can be performed without modifying the main task (tool position). The subtasks performed in null-space have a strict priority hierarchy. From highest to lowest: joint compliance, obstacle-avoidance and dexterity optimization.

Joint compliance control allows safe human-robot interaction. This admittance-based control allows the surgeon to free occupancy space (passive behavior) and react safely to unintended collisions (active behavior) by changing the stiffness parameter. The obstacle-avoidance control defines lateral boundaries that represent the allowed lateral occupancy space of the robot. The lateral boundaries are modelled as masses attached to a spring-damper system, affected by repulsive forces. The medical staff is treated as obstacles that generate a repulsive force to the boundaries based on the distance. The joint configuration of the robot must remain inside the lateral bounds. Finally, as redundancy offers infinite configurations for a given tool pose, it can be exploited to increase the reachability workspace and maximize dexterity, within the joint limits defined by the higher priority subtasks. The proposed dexterity optimization method dynamically finds the joint configuration that gives the maximum manipulability from a set of redundant configurations around the current joint position  $q_3(t) \in [q_3(t-1) - \Delta_{max}, q_3(t-1) + \Delta_{max}]$ , where  $\Delta_{max}$  is the maximum allowed joint movement at each control step. To maintain a coherence in the movement around the workspace,  $q_3$  upper and lower boundaries are set proportional to the radial distance to the RCM in the XY plane. This policy forces the robot to decrease its  $q_3$  value near the centre, allowing it to escape local maxima that would compromise the robot's performance.

## RESULTS

Several scenarios have been used to test the proposed control, simulating different realistic placenta positions: posterior and lateral. The workspace of the robot is constrained by the RCM, which defines a cone-shape workspace. In posterior placenta the tool is inserted (origin of the tool orientation) in vertical whereas lateral placenta forces the tool to enter with some inclination. The joint compliance control has been tested in simulation with different stiffness parameters, where the robot dynamics behave as expected upon an external force. The obstacle-avoidance control has been tested in simulation with an obstacle trajectory of approaching and retreating. The robot's lateral occupancy space is reduced when the obstacle is close. A performed reachability workspace analysis proved that in posterior placenta the reachability (points reached inside the workspace) increases a 30% using redundancy, but there is not a significant volume increase (<5%). In the lateral placenta, the reachability increases up to an 80% and the volume up to 70%. The dexterity optimization algorithm is tested for a set of randomized paths. The results show that the manipulability increases up to 600% in some regions with respect to the results of the same test with a 6 DoF robot, whereas isotropy increases up to 80%. Best

results are obtained in the vicinity of a singularity where the use of  $q_3$  avoids falling into a singularity. None of the subtasks performed in the null space compromised the main task, which in all tests reached all destination points with an error less than 1 mm.

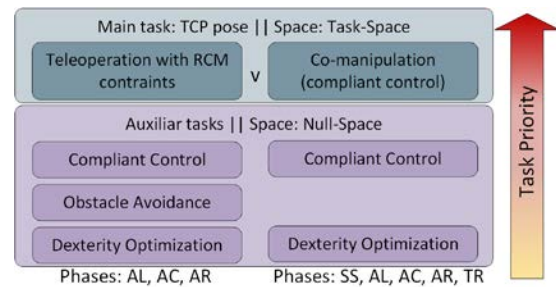


**Figure 2.** Multi-Layer control schema

## CONCLUSION AND DISCUSSION

The inclusion of a redundant and collaborative robot in the FMIS teleoperation platform has demonstrated a noticeable improvement of the system in several aspects. The hierarchical multi-task control strategy enables an adaptive system behavior depending on the specific requirements of each phase of the surgical procedure. The main task ensures the correct fetoscope position using any of the two tool guidance modes: co-manipulation and teleoperation. The secondary tasks are applied depending on the desired robot behavior. Redundancy increases the reachable workspace, optimizes dexterity (local optimization) and singularity avoidance, ensuring the applicability of the system independently of the placenta position. Dexterity improvement eliminates singularities inside the workspace. In addition to redundancy the collaborative capabilities offer benefits in two aspects. First, enables the system to be implemented in real surgical environments, where the robot occupancy volume is shared with medical staff (e.g. the echographer). The ability to measure the forces exerted on the arm enables the possibility to change its position to free up working space while the main task (fetoscope position) is accomplished. Second, improves the set-up and tool removal phases, reducing the surgery room occupancy time. Finally, the obstacle avoidance and compliant control ensure the safety of the medical staff during surgery. The new multi-task control schema jointly with the use of Kuka LWR 4 will speedup the process to start tests with animal models.

## REFERENCES

- [1] Gratacos E., Deprest J., Current experience with fetoscopy and the Eurofoetus registry for fetoscopic procedures, Eur J Obstet Gynecol Reprod Biol. 2000, vol. 92 pp. 151-159.
- [2] WAPM consensus group on Twin-to-twin transfusion syndrome, Baschat A., et al., Twin-to-twin transfusion syndrome (TTTS)\*, Journal of Perinatal Medicine, 2011, 39(2), 107-112
- [3] Sandoval J., Vieyres P., and Poisson G., Generalized Framework for Control of Redundant Manipulators in Robot-Assisted Minimally Invasive Surgery, IRBM, 2018, vol. 39(3) pp. 160-166



# A cycle-GAN based transfer learning approach for surgical image synthesis

E. Colleoni<sup>1</sup>, F. Vasconcelos<sup>1</sup>, D. Stoyanov<sup>1</sup>

<sup>1</sup>*Department of Computer Science, University College London, United Kingdom*

## INTRODUCTION

Learning-based technologies and, in particular, deep learning, have revolutionised the way researchers and engineers approach surgery and computer assisted interventions, avoiding time-consuming and task-specific solutions to existing tasks and introducing new technologies, such as virtual and augmented realities. However, this comes at the expense of a large number of training data, that is the fundamental requirement even for basic tasks, e.g. surgical tool segmentation or pose estimation. A possible solution to this issue could be to generate new data starting from a given dataset, that, as a matter of facts, should lead to an infinite number of data. In particular, Generative Adversarial Networks [3] (GANs) achieved state of the art performances for image generation, being able to create realistic textures and objects. However, GANs suffer from very unstable training and usually fail in reproducing realistic image content. Many of these issues have been tackled with the introduction of cycle consistency Generative Adversarial Network (cycle-GAN) [2]. In their work [2], Zhu et al. proposed a novel GAN composed by two generators and two discriminators that connect two different but correlated set of images (e.g. night to day light pictures, horse to zebra images, simulated to real surgical tool): one generator takes an image from one set and transforms it into an image from the other set, while the other generator performs the opposite transformation. This methodology leads to a more stable training thanks to cycle consistency and allows an efficient transformation between two set of images without the need for labels or paired samples. In this extended abstract we propose a novel framework for labelled surgical dataset generation: in order to produce realistic data from simulation images, our method takes images from a virtual simulator (where segmentation ground truth is automatically provided) and from a real ex-vivo dataset and uses a cycle-GAN to learn the style transformation between them. Once style transfer is applied on simulation images, they are blended on a real surgical background to finally produce complete synthetic frames. The produced dataset is evaluated for tool segmentation, showing that state of the art performances can be obtained by training a segmentation model only on synthetic data.

## MATERIALS AND METHODS

The proposed data generation methodology is divided in two successive steps. First, we process images acquired using a daVinci simulator [1] on CoppeliaSim<sup>1</sup> (Fig.1.a) in order to produce real-looking surgical tools (Fig.1.b). The processed images are then blended on a surgical

background to finally produce complete synthetic surgical frames (Fig.1.c). In this section we first describe our training data, the employed cycle-GAN architecture and the tool-blending procedure and finally we present our experimental protocol.

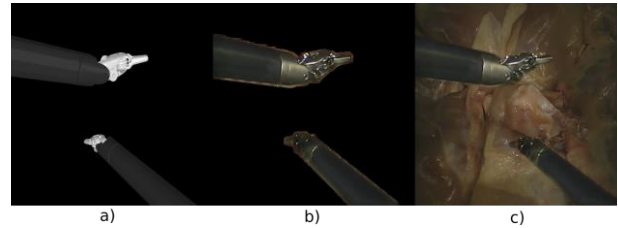


**Figure. 1.** Main steps of the proposed procedure. Starting from images containing simulated surgical tools (a), a cycle-GAN based style transfer method is applied to give the tools real appearance (b). Finally, the produced tools are blended on a surgical background (c).

### *Transfer learning and tool blending*

**Real set:** The proposed cycle-GAN is trained to transfer the real-looking style from ex-vivo frames, i.e. the real set, to simulation images (simulation set).

Starting from raw frames, we produced our real set by extracting tools from the background using segmentation labels. Such separation procedure is necessary since we experimentally observed that applying style transfer directly on full images leads to an unstable training and poor visual results.

**Simulation set:** The simulation set was generated using a daVinci virtual simulator [1] that reproduces both tool geometry and kinematic and can acquire images with a virtual camera.

**Network architecture and training strategies:** Cycle-GANs are composed by two generators (set1 to set2 transform and vice versa) and two discriminators. The architectures of generators and discriminators in our work are based on [2]. Generators have an encoder-decoder structure: two initial down sampling blocks (2D convolution + Instance normalization + Relu activation) reduce the image width and length by 4 and increase the number of channels to 256. The result is then processed into 9 successive residual blocks and the image is finally up sampled to the initial shape and number of channels. The discriminators architecture is composed by four down sampling blocks that reduces the input dimensions by 16 and increase the number of channels to 512. The result is finally processed using a 2D convolution to generate a 64x64 grayscale image.

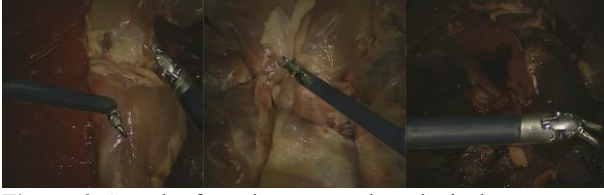


**Figure 2.** Samples from the generated synthetic dataset.

In order to stabilize training, we applied spectral normalization before each convolution, we applied historical averaging during the discriminators training and we set  $lr_D = 4lr_G$ , where  $lr_D$  and  $lr_G$  are the discriminator and generator learning rates respectively. The loss function employed to train our models is the same as [2] and we chose Adam with  $lr_G=0.0002$ ,  $\beta_1=0.9$  and  $\beta_2=0.999$  as our optimizer.

**Tool blending:** Once style transfer has been applied on simulation images (Fig.1.b), we can exploit simulation tool masks to properly paste the tool on a surgical background (Fig.1.c). This assumes that, during style transfer, the content of the image has not been modified and so that the simulated and the transformed images share the same segmentation mask. The final image is produced following the formula:  $I_{final} = M * I_{tran} + (1 - M) * I_{background}$ , where  $I_{tran}$  is the transformed image,  $M$  is the relative binary segmentation mask,  $I_{background}$  is the surgical background image and ‘\*’ and ‘+’ are per-pixel multiplication and sum respectively.

#### Experimental Protocol

To train our cycle-GAN, we produced the real set starting from 14 ex-vivo surgical videos [6] for a total amount of 660 frames. Then we created the simulation set by producing other 660 simulation images using our daVinci simulator.

With the trained cycle-GAN, we generated 3000 synthetic frames using 10 different surgical backgrounds from [6]. Images have dimension 512x512x3. A sample of the produced synthetic frames is shown in Fig.2.

In order to quantitatively validate the proposed data generation method, we trained two models based on the same architecture, the first on synthetic data only and the second on real data [6] respectively. The performances of these two models were then tested on four real test videos provided by [6]. We chose RASNet [4] as our state of the art tool segmentation architecture.

Segmentation performances were evaluated in terms of median Intersection Over Union (*IoU*) score:

$$IoU = \frac{TP}{TP+FP+FN}$$

where TP is the number of pixels correctly classified as tool pixels while FP and FN are the number of pixels misclassified as tool and background respectively.

## RESULTS

Results obtained by RASNet trained on real and synthetic data are shown in Table 1. The model trained on transformed data showed the best performances on the first three test videos, with an improvement range from

4.30% (Video 3) to 10.85% (Video 1), w.r.t. the one trained on real data. Even considering that the real data model performed better than the one trained on our synthetic dataset on Video 4, both the models obtained *IoU* scores above 90%, with less than 3% difference.

## CONCLUSION AND DISCUSSION

The obtained results suggest that our cycle-GAN was able to properly select and transfer features from real to simulation tools in order to produce high quality synthetic data. This is shown particularly by the performances obtained on Video 1, 2 and 3, where the model trained on synthetic frames outperformed the one trained on real ex-vivo images. The major limitation of this work is the need for ground truth segmentation masks to separate tools and background to produce the real set for our cycle-GAN training. The development of a complete unsupervised methodology for surgical data generation could be a natural extension of this work, allowing the generation of huge datasets with little human effort. Another future direction for our work could be to produce frames that could better represent the real surgical scenario, i.e. with blood on the tools and projected shadows on the background.

	Real data	Synthetic data
<b>Video 1</b>	79.25	<b>90.1</b>
<b>Video 2</b>	78.44	<b>87.18</b>
<b>Video 3</b>	84.56	<b>88.86</b>
<b>Video 4</b>	<b>95.09</b>	92.39

**Table 1.** Results achieved on 4 test videos [6] by two RASNets trained on real data and synthetic data. Performances are evaluated in terms of median *IoU* score (%).

## REFERENCES

- [1] Fontanelli, Giuseppe Andrea, et al. "A v-rep simulator for the da vinci research kit robotic platform." *2018 7th IEEE International Conference on Biomedical Robotics and Biomechatronics (Biorob)*. IEEE, 2018.
- [2] Zhu, Jun-Yan, et al. "Unpaired image-to-image translation using cycle-consistent adversarial networks." *Proceedings of the IEEE international conference on computer vision*. 2017.
- [3] Goodfellow, Ian, et al. "Generative adversarial nets." *Advances in neural information processing systems*. 2014.
- [4] Ni, Zhen-Liang, et al. "RASNet: Segmentation for tracking surgical instruments in surgical videos using refined attention segmentation network." *2019 41st Annual International Conference of the IEEE Engineering in Medicine and Biology Society (EMBC)*. IEEE, 2019.
- [5] Gatys, Leon A., Alexander S. Ecker, and Matthias Bethge. "Image style transfer using convolutional neural networks." *Proceedings of the IEEE conference on computer vision and pattern recognition*. 2016.
- [6] Colleoni, Emanuele, Philip Edwards, and Danail Stoyanov. "Synthetic and Real Inputs for ToolSegmentation in Robotic Surgery." *arXiv preprint arXiv:2007.09107* (2020).

# Towards the Development and Evaluation of a Handle Prototype for a Handheld Robotic Neurosurgical Instrument

Emmanouil Dimitrakakis<sup>1</sup>, George Dwyer<sup>1</sup>, Lukas Lindenroth<sup>1</sup>, Holly Aylmore<sup>2</sup>, Neil L. Dorward<sup>3</sup>,  
Hani J. Marcus<sup>3</sup>, and Danail Stoyanov<sup>1</sup>

## I. INTRODUCTION

The Expanded Endoscopic Endonasal Approach (EEEA) is a Minimally Invasive Surgery (MIS) technique that is performed through the sinus and aims at the removal of lesions from a number of areas at the base of the brain [1]. Although a promising alternative to transcranial approaches that require craniotomies and brain retraction, the EEEA comes with its limitations and 74% of surgeons identified the limited surgical manipulation that the standard non-articulated instruments offer as the biggest challenge [2]. This procedure could potentially be improved using robotic instrumentation that provides articulation at the tip.

The purpose of this preliminary study is to create an ergonomic handle for a handheld surgical robotic tool intended for the EEEA. A handheld tool was chosen rather than a tele-operated robotic platform, due to its compactness and its ability for easier integration into the surgical workflow. In previous work, a 3 degrees-of-freedom articulated robotic end-effector for this tool was developed, with the purpose of pairing it with the ergonomic handle in future work. This paper will present the design and development of an ergonomic handle for a robotic neurosurgical tool. The guidelines for developing ergonomic handles will be outlined followed by our proposed handle design and simulation environment.

## II. MATERIALS AND METHODS

### A. Ergonomic guidelines

Long-term use of incorrectly designed tools can cause conditions such as the carpal-tunnel syndrome and the hand-arm vibration syndrome [3], meaning that appropriate ergonomic tool design is essential. According to [4], it is difficult to define a clear and universal consensus on specific components or instructions that make a handle design ergonomic and comfortable to use. Despite this difficulty, however, there are still some characteristics that are found to be contributing towards an ergonomic design. These instructions and suggestions on ergonomic guidelines are summarized in table I.

### B. Handle implementation

Following these instructions, we developed a handle design that was inspired by most commercially available hand-

**TABLE I:** Some of the ergonomic guidelines suggested from the current literature.

Instructions towards an ergonomic handle design
<i>The surgeon's hand size should not hugely affect the design [5]</i>
<i>The handle type should be finger-operated [5]</i>
<i>The thumb actuates the robot joints (eg joystick or rotary switch) [6]</i>
<i>The index finger actuates the robot gripper (eg trigger) [6]</i>
<i>The tool geometry should include a large palmar grip surface [7]</i>
<i>The Handle - shaft angle should be 45° [7]</i>
<i>A partially opened hand should hold the instrument at rest [7]</i>

held robotic tools that are used in surgery. It is finger-operated, employing a thumb-controlled joystick that actuates the robot joints, mainly its pitch and yaw rotations, and an index finger-controlled standard trigger that actuates the robot gripper. The roll motion is carried out by the surgeon's hand. It contains a large handle surface that provides the surgeon with palmar grip and the handle-shaft angle is 45°. To account for different hand sizes and to make sure that the instrument at rest is maintained by a hand that is also kept at rest, we introduced a 'rotating joystick body' that is modifiable and can be rotated into the position that each surgeon feels more comfortable with. Figure 1 shows the handle with its rotating body in 7 different discrete positions.

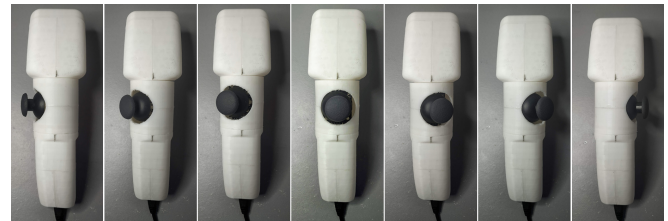


**Fig. 1:** Seven discrete joystick positions on a printed rotating-body handle prototype.

The level/resting position of the hand is shown in Figure 2A. In Figure 2B, the thumb is shown in 'adduction' (left) and 'abduction' (right). It is evident from this figure that the resting position of the hand requires the thumb to be in an 'abduction' position, not so close to the rest of the fingers.

If we were to place the joystick at the exact centre of the handle, the thumb would be at an 'adduction' position and the surgeon would feel uncomfortable and easily tired. By placing the joystick on a rotating body, the surgeon can

<sup>1</sup>Wellcome/EPSCRC Centre for Surgical and Interventional Sciences (WEISS), University College London (UCL), London, UK

<sup>2</sup>University College London, London, UK

<sup>3</sup>National Hospital for Neurology and Neurosurgery, London, UK  
e.dimitrakakis@ucl.ac.uk



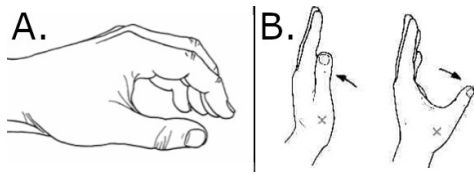


**Fig. 2:** A. The hand at its resting position, and B. thumb adduction (left), thumb abduction (right) [8].

rotate the joystick to the left if they are to use it with their right hand and to the right, if they are to use it with their left hand. The angle of rotation, namely the angle by which the surgeon needs to rotate the joystick body to feel comfortable, depends on the surgeon's hand size.

In Figure 3 it is shown how this handle can cater to different hand sizes and can be used independently of right- or left-handedness. It is worth mentioning that in Figures 3.A and 3.B the rotating body has been rotated by approximately  $15^\circ$ , whereas in Figures 3.C. and 3.D by approximately  $35^\circ$

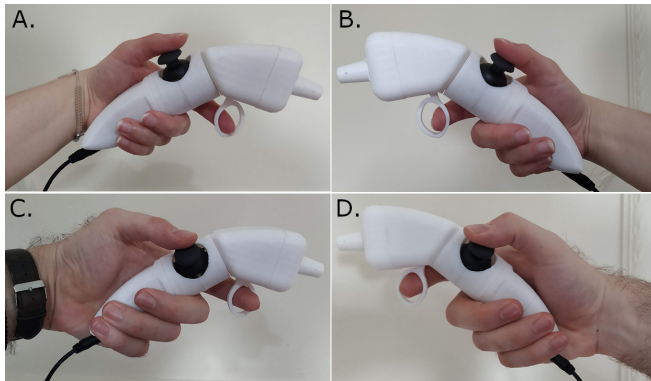


**Fig. 3:** The handle held by A. a small left hand, B. a small right hand, C. a large left hand, and D. a large right hand.

### C. Simulator implementation

For the simulator, we decided to use CoppeliaSim (formerly V-REP), a versatile and powerful robot simulation platform [9]. Objects inside the CoppeliaSim simulator are controlled remotely by Robot Operating System (ROS) nodes and other custom solutions. The simulation task we decided to develop in this environment is a ring-transfer task, with the developed handle controlling a surgical forceps. An endoscope-resembling camera was also implemented inside the simulation that is user-controlled through a 3D-printed endoscope. Both the shafts of the developed handle and the endoscope were physically constrained in space in accordance to the EEEA workspace constraints.

To evaluate the efficacy and comfort of the device, we performed the ring transfer task using the handle to move the robotic end-effector, and using keyboard inputs to move the robot shaft in space. This will be substituted by an optical tracking system in the future that maps the surgeon's handle movements in 3D space to the simulation environment. All six rings could be transferred from the one set of spikes to the next, with comfort and ease. This, however, will be extensively tested in future work when a number of evaluation

and comparison tests will be carried out to investigate the efficacy of the tool. A series of pictures of the simulated task moving the first two of the six rings can be seen in Figure 4.

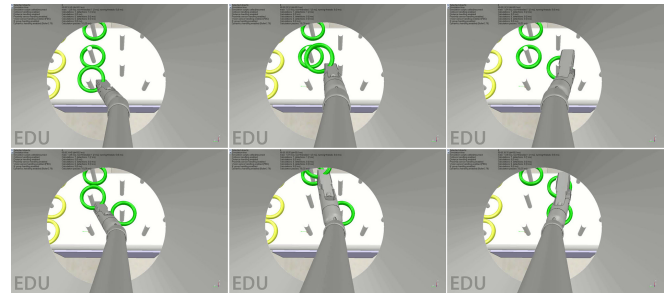


**Fig. 4:** The ring transfer task inside the CoppeliaSim simulation environment using the handle prototype.

### III. CONCLUSION AND DISCUSSIONS

In this preliminary study we developed an ergonomic handle prototype for a handheld robotic neurosurgical instrument. Alongside the handle, a simulation in the CoppeliaSim environment was developed to evaluate the prototype. The end-goal of the study is to evaluate the efficacy of the handle, before the implementation of the final robotic instrument prototype. This is why as a continuation of this abstract, we plan on developing additional handles with different design strategies, and additional simulation tasks, and conduct a clinician user-study where experts are going to decide which handle design is the most appropriate for the EEEA.

### REFERENCES

- [1] A. R. Dehdashti, A. Ganna, I. Witterick, and F. Gentili, "Expanded endoscopic endonasal approach for anterior cranial base and suprasellar lesions: indications and limitations," *Neurosurgery*, vol. 64, no. 4, pp. 677–689, 2009.
- [2] H. J. Marcus, T. P. Cundy, A. Hughes-Hallett, G.-Z. Yang, A. Darzi, and D. Nandi, "Endoscopic and keyhole endoscope-assisted neurosurgical approaches: a qualitative survey on technical challenges and technological solutions," *British journal of neurosurgery*, vol. 28, no. 5, pp. 606–610, 2014.
- [3] P. Stoklasek, A. Mizera, M. Manas, and D. Manas, "Improvement of handle grip using reverse engineering, cae and rapid prototyping," in *MATEC Web of Conferences*, vol. 76. EDP Sciences, 2016, p. 02029.
- [4] A. DiMartino, K. Doné, T. Judkins, J. Morse, J. Melander, D. Oleynikov, and M. S. Hallbeck, "Ergonomic laparoscopic tool handle design," in *Proceedings of the Human Factors and Ergonomics Society Annual Meeting*, vol. 48, no. 12. SAGE Publications Sage CA: Los Angeles, CA, 2004, pp. 1354–1358.
- [5] L. Santos-Carreras, M. Hagen, R. Gassert, and H. Bleuler, "Survey on surgical instrument handle design: ergonomics and acceptance," *Surgical innovation*, vol. 19, no. 1, pp. 50–59, 2012.
- [6] M. A. Van Veelen, D. W. Meijer, R. H. M. Goossens, and C. J. Snijders, "New ergonomic design criteria for handles of laparoscopic dissection forceps," *Journal of Laparoendoscopic & Advanced Surgical Techniques*, vol. 11, no. 1, pp. 17–26, 2001.
- [7] A. G. González, D. R. Salgado, L. García Moruno, and A. Sánchez Ríos, "An ergonomic customized-tool handle design for precision tools using additive manufacturing: a case study," *Applied Sciences*, vol. 8, no. 7, p. 1200, 2018.
- [8] L. D. Lehmkuhl and L. K. Smith, *Brunnstrom's clinical kinesiology*. Davis, 1984.
- [9] E. Rohmer, S. P. N. Singh, and M. Freese, "Coppelasim (formerly v-rep): a versatile and scalable robot simulation framework," in *Proc. of The International Conference on Intelligent Robots and Systems (IROS)*, 2013, www.coppeliarobotics.com.

# Modularization of medical robotic manipulator for adapting soft robotic arms with varying numbers of DOFs

Chun-Feng Lai<sup>1</sup>, Fabian Trauzettel<sup>1</sup>, Paul Breedveld<sup>1</sup>, Elena De Momi<sup>2</sup>, Giancarlo Ferrigno<sup>2</sup>, Jenny Dankelman<sup>1</sup>

<sup>1</sup>*Department of Biomechanical Engineering, Delft University of Technology,*

<sup>2</sup>*Department of Electronics, Information and Bioengineering, Politecnico di Milano  
c.lai-1@tudelft.nl*

## INTRODUCTION

Medical robotics systems are widely used nowadays and gaining more and more attention from both research societies and surgeons, providing new solutions to different minimally invasive surgeries. Despite higher costs, hospitals are embracing the new technology for reasons like providing more dexterity than traditional laparoscopy and better ergonomics, which relieve the surgeon's mental burden [1, 2]. Most of the designs of currently available medical robots consist of rigid parts not suitable for interventions such as flexible endoscopy. The tips of flexible endoscopes are usually actively steered by tendons while their bodies are passively flexible and will bend with the surrounding lumen.

The Bio-Inspired Technology group (BITE) at Delft University of Technology is designing new mechanical solutions that allow instruments to navigate through vulnerable anatomic surroundings and get to hard-to-reach locations. Inspired by nature, innovative soft robotic arms with varying numbers of steerable segments were designed and manufactured with 3D printing technology [3], allowing rapid manufacture and easy adjustment for different clinical needs. However, to build robotic actuators for these varying designs is time consuming, especially when a new design has to be changed according to the required number of degrees of freedom (DOF) that has to be controlled. Modular actuation has a strong advantage on addressing this issue as modular actuators can be easily duplicated and stacked for different DOF to make them suitable for new designs. Therefore, in this paper, a miniature soft robotic arm controlled by modularized actuation segments is proposed. These segments can work independently and/or together to steer the soft robotic arm. This study aims to investigate whether the proposed design is able to steer a cable-driven soft robot and is suited for designs with different numbers of steerable segments (DOF).

## MATERIALS AND METHODS

The proposed manipulator design is modular with respect to the number of actuation segments in the soft robotic arm. These modularized actuation units correspond to the number of steerable segments required, each unit being able to steer one steerable segment. In each unit, we used four stepper motors (NEMA17, 17HS4401) with drivers (DRV8825, AZDelivery)

connecting to one microcontroller (ATmega328P, Arduino UNO) with shield circuit (Arduino CNC shield v3). Mechanical supports and parts are identical in each segment. The stepper motors connect to the soft robotic arm by tendons and are arrayed with offset angles in order to minimize the space required for each motor. Microcontrollers in different segments are connected via I2C, the first leading microcontroller being the master and the others serving as slaves. To prove the concept, a soft robotic arm with two steerable segments (4 DOFs) is used. The 1<sup>st</sup> to 32<sup>nd</sup> microsteppings are used to increase resolution of the movement of the tip. A manipulator with two modularized actuation segments is built and employed with two control strategies. The first strategy consists of simply using two independent joysticks to steer two deflection angles of their corresponding segments. The second strategy is the follow-leader-control, meaning the first leading segment is remotely controlled by a joystick. When the deflection of the first tip is being determined by the user, the following part will then move the same way as the leading one by a feedforward control strategy.

## RESULTS

The 4 DOF soft robotic arm manipulator that was built is shown in Figure 1. The dimensions of the modularized actuation part are 300x200x100mm. Two modules were assembled and connected to the soft robotic arm, which possesses 2 steerable segments with an outer diameter of 8 mm and a total length of 85 mm. The manipulator can successfully control the movement of each segment by two joy sticks as shown in Figure 2.

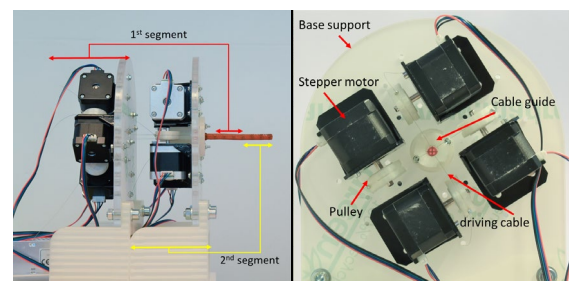


**Figure 1.** The left figure shows the assembly of two modularized actuation segments together with a 4 DOF soft robotic arm. The right figure shows the actuation elements in one actuation module.



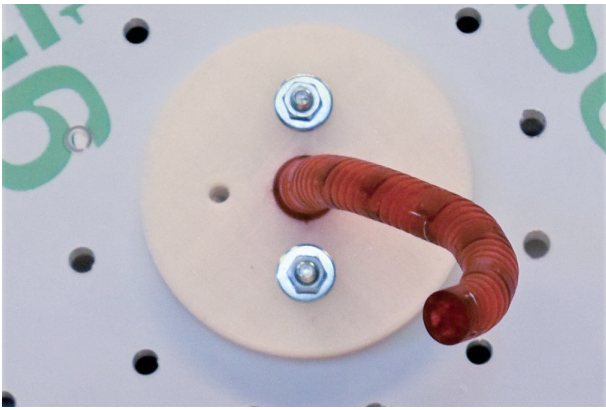


**Figure 2.** Front view from the manipulator showing robotic arm being driven by two-joystick.

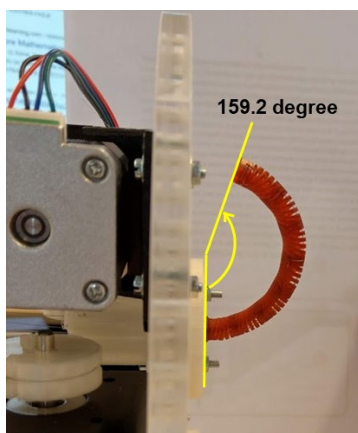


**Figure 3.** Side view from the manipulator showing the maximum deflection it can achieve.

The resolution of tip movement and the maximum deflection of both steerable segments together are  $0.38^\circ$  and  $159.2^\circ$ , respectively, as measured with a digital camera and image processing software. In Figure 4(A)-(F), the follow-the-leader strategy is shown from the top view. The second segment can approximately follow the position of the first leading segment in large steps, however, its positioning in small steps is not smooth. While the control model assumes the tendons are routed parallel to the axis of the catheter, the tendons actually follow a very steep helical path, leading to small errors. Backlash was observed between actuator pulleys and tendons when the actuator reversed direction to steer the tip in the opposite direction.

## CONCLUSION AND DISCUSSION

The modularized actuation unit can successfully drive a steerable segment of a tendon-actuated soft robotic arm independently and also together with other segments. Follow-the-leader control is achieved but with displacement error in the tip and in the following segment. With an improvement of the utilized mathematical model as well as the use of tendon force monitoring to compensate for actuator backlash, the error

is likely to be reduced. To steer a multiple-segment soft robotic arm, a controller other than two joy sticks should be designed to have a better ergonomics since human operators are not used to control more than two segments at once. The advantage of a modularized actuation unit is its expandability and flexibility in adapting to robotic arms with varying DOFs. In the presented manipulator, it is proven that a robot with modularized actuation can be easily extended to more segments. Ignoring the physical limits on the maximum overall size of an actuation unit, the theoretical maximum number of controllable segments would be 128, as dictated by the maximum number of 7-bit addresses on an I2C bus. Further research will focus on decreasing the number of required actuators, miniaturization of the system, adding sensors that provide position and force feedback to reduce errors and also on the control model of the soft robotic arm.

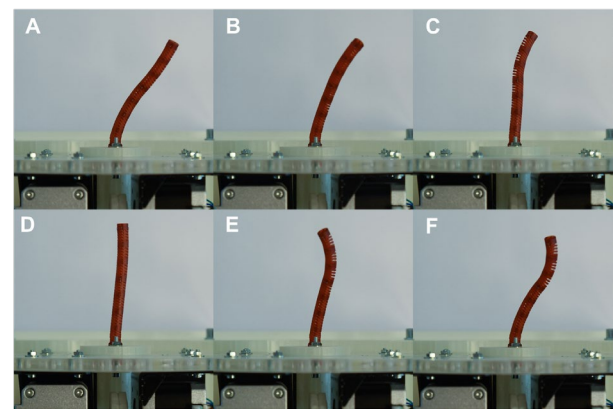


**Figure 4.** Top view of follow-the-leader motions in different steps. From (A) to (C), the leading segment was steered to the right, and followed by the second segment. From (D) to (F), the leading segment was steered to the origin and followed by the second segment.

## ACKNOWLEDGEMENT

This project has received funding from the European Union's Horizon 2020 research and innovation programme under the Marie Skłodowska-Curie grant agreement No 813782.

## REFERENCES

1. Hubert, N., et al., *Ergonomic assessment of the surgeon's physical workload during standard and robotic assisted laparoscopic procedures*. The International Journal of Medical Robotics and Computer Assisted Surgery, 2013. 9(2): p. 142-147.
2. Peters, B.S., et al., *Review of emerging surgical robotic technology*. Surgical endoscopy, 2018. 32(4): p. 1636-1655.
3. Culmone, C., et al., *Exploring non-assembly 3D printing for novel compliant surgical devices*. Plos one, 2020. 15(5): p. e0232952.

# Deep Reinforcement Learning for Concentric Tube Robot Control with Goal Based Curriculum Reward

K. Iyengar<sup>1</sup>, D. Stoyanov<sup>1</sup>

<sup>1</sup> Wellcome/EPSRC Centre for Interventional and Surgical Sciences, University College London, UK,

keshav.iyengar@ucl.ac.uk

## INTRODUCTION

Concentric tube robots (CTRs) are composed of pre-curved, super-elastic tubes that behave like continuum robots with a rotation and translation degree of freedom per tube [1]. The tubes interact with each other when rotating and translating to bend and twist in a manner resulting in curvilinear paths as seen in Figure 1. CTRs are clinically employed in minimally invasive surgery (MIS) in applications of actuated steerable needles or teleoperated manipulators. Ophthalmological, endonasal and fetal surgery have been explored interventions that may benefit highly from the dexterity, compliance and flexibility of CTRs [2]. In such applications, the main benefit is having a flexible articulated instrument while maintaining a small incision point to minimize trauma at the entry point.

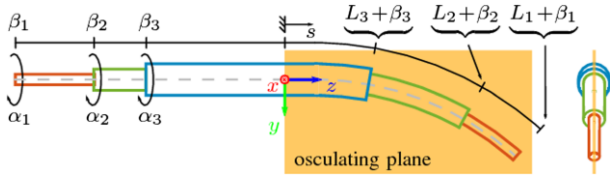


**Figure. 1.** Concentric tube robot kinematic inputs for 3 tubes adapted from [6].

Compared to rigid link robots, the kinematic modelling of CTRs is more complex due to the non-linear interactions of the tubes. Previous model-based work has thoroughly investigated various solutions with respect to computation complexity and accuracy. A geometrically exact model [3] is one such solution but has its limitations in terms of transverse shear, elongation and friction. A generally applicable modelling technique has not yet emerged.

In this work, we present a goal based curriculum reinforcement learning approach to learn the inverse kinematics of CTRs. Reinforcement learning is an iterative paradigm where an agent aims to learn the optimal sequence of actions to achieve a goal summarized by a reward signal. We focus on simulation results in this work because transfer learning is an active research area with various strategies such as domain randomization being explored. Although previous work has investigated model-free kinematics for CTRs [4,5,6,7], our contributions in this work are a novel training strategy with goal based curriculum and confirming previous reinforcement learning approach

results [7] with a more accurate kinematics model [3] used for simulation.

## MATERIALS AND METHODS

As described in [7], we formulate a Markov Decision Process (MDP) with states, actions and reward function. The state is defined as rotation ( $\alpha_i$ ) and extension ( $\beta_i$ ) position for each tube  $i$  in trigonometric form [6], desired goal,  $g$ , achieved goal or robot tip position,  $\hat{g}$  and goal tolerance  $\delta(t)$ . The trigonometric form,  $\gamma_i$ , is defined as

$$\gamma_i = \{\gamma_{1,i}, \gamma_{2,i}, \gamma_{3,i}\} = \{\cos \alpha_i, \sin \alpha_i, \beta_i\}$$

Thus, we can define the state at timestep  $t$  as

$$s_t = \{\gamma_1, \gamma_2, \gamma_3, g - \hat{g}, \delta(t)\}$$

The extension joint,  $\beta_i$  can directly be obtained from  $\gamma_{3,i}$  and the rotation joint  $\alpha_i$  can be obtained by

$$\alpha_i = \text{atan2}(\gamma_{2,i}, \gamma_{1,i})$$

The kinematic input variables ( $\alpha, \beta$ ) are shown in Figure 1 where  $L_i$  is the overall length of tube  $i$ . Actions are defined as changes in rotation and extension positions in a single timestep. The desired goal,  $g$ , is defined as a Cartesian point in the achievable workspace. The desired goal,  $\hat{g}$ , is the tip position of the robot determined with forward kinematics in simulation. The reward at timestep  $t$ , is defined with a reward function as follows,

$$r_t = \begin{cases} 0, & e_t \leq \delta(t) \\ -1, & \text{otherwise} \end{cases}$$

where  $\delta(t)$  is the goal tolerance as a function of timesteps and  $e_t$  is the Cartesian error from the robot tip to desired goal.

To investigate a goal-based curriculum, we propose three goal tolerance functions. Using a starting goal tolerance  $\delta_{\text{initial}}$ , and final goal tolerance  $\delta_{\text{final}}$ , with  $N_{ts}$  being the total number of timesteps to apply the function, we can fully define these functions. The first function is a constant tolerance,

$$\delta(t) = \begin{cases} \delta_{\text{final}}, & t \leq N_{ts} \\ \delta_{\text{final}}, & \text{otherwise} \end{cases}$$

The second function is a linear,

$$\delta(t) = \begin{cases} at + b, & t \leq N_{ts} \\ \delta_{\text{final}}, & \text{otherwise} \end{cases}$$

$$a = (\delta_{\text{final}} - \delta_{\text{initial}})/N_{ts}$$

$$b = \delta_{\text{initial}}$$

The final function is exponentially decaying with  $a$  as an initial tolerance and  $r$  as the rate of decay.

$$\delta(t) = \begin{cases} a(1-r)^t, & t \leq N_{ts} \\ \delta_{\text{final}}, & \text{otherwise} \end{cases}$$

$$a = \delta_{\text{initial}}$$

$$r = 1 - (\delta_{\text{final}}/\delta_{\text{initial}})^{N_{ts}^{-1}}$$

For the second function, the tolerance remains at  $\delta_{\text{final}}$  for  $t > N_{ts}$  till the end of training. We train a three tube robot system with parameters listed in Table 1, where stiffness is 5 GPa and torsional stiffness is 2.3 GPa with deep deterministic policy gradient [8] and with hindsight experience replay [9]. We use parameters found in [7] with multi-variate Gaussian noise. Each experiment was trained for a total of 300,000 and  $N_{ts} = 150,000$ ,  $\delta_{\text{final}} = 1$  mm and  $\delta_{\text{initial}} = 20$  mm and 19 parallel workers.

$L$ (mm)	$L_{\text{curved}}$ (mm)	$d_{\text{inner}}$ (mm)	$d_{\text{outer}}$ (mm)	Pre- curvature
215.0	14.9	1.0	2.4	15.82
120.2	21.6	3.0	3.8	11.8
48.5	8.8	4.4	5.4	20.04

**Table 1.** Simulation robot parameters. From inner to outer.

## RESULTS

To compare convergence of training of the experiments we plot error through training with the shaded standard deviation area in Figure 2 and the cumulative episode rewards through training in Figure 3.

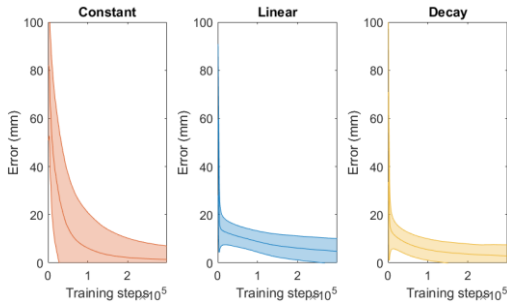


**Figure 2.** Comparing error during training for constant, linear and decay functions.

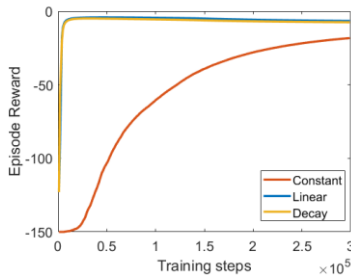


**Figure 3.** Comparing error during training for constant, linear and decay functions

The final error found at the end of training was 1.4mm for the constant function, 4.8mm for linear and 2.9mm for the decay function in Cartesian space. With 2 million training steps, these methods are in-line with [7] which was on par with other simulation results [4].

## CONCLUSION AND DISCUSSION

Conducting this study we reached two conclusions. First, Although the final error for the constant function is lower than linear or decay, varying the goal tolerance had a large effect in the beginning of training by reducing errors very quickly with high rewards as compared to the constant function. Second, there is less deviation in the linear and decay function during the initial stages of training.

In this study, a novel training methodology for concentric tube robots with reinforcement learning based on goal tolerance has been suggested to be useful at the initial stages of training. Expanding on work conducted in [7] that used simplified kinematics, this study trains with accurate kinematics of CTRs. In future work we will experiment with combining functions to improve convergence speed and lower errors.

## REFERENCES

- [1] P. E. Dupont, J. Lock, B. Itkowitz, and E. Butler, "Design and control of concentric-tube robots," *IEEE Trans. Robot.*, vol. 26, no. 2, pp. 209–225, 2010, doi: 10.1109/TRO.2009.2035740.
- [2] J. Burgner-Kahrs, D. C. Rucker, and H. Choset, "Continuum Robots for Medical Applications: A Survey," *IEEE Transactions on Robotics*, vol. 31, no. 6. Institute of Electrical and Electronics Engineers Inc., pp. 1261–1280, 01-Dec-2015, doi: 10.1109/TRO.2015.2489500.
- [3] D. C. Rucker, B. A. Jones, and R. J. Webster, "A geometrically exact model for externally loaded concentric-tube continuum robots," *IEEE Trans. Robot.*, vol. 26, no. 5, pp. 769–780, 2010, doi: 10.1109/TRO.2010.2062570.
- [4] C. Bergeles, F.-Y. Lin, and G. Z. Yang, "Concentric Tube Robot Kinematics Using Neural Networks," in *The Hamlyn Symposium on Medical Robotics*, 2015, no. June, pp. 13–14, doi: 10.1109/MPUL.2012.2182857.
- [5] A. Kuntz, A. Sethi, R. J. Webster, and R. Alterovitz, "Learning the Complete Shape of Concentric Tube Robots," *IEEE Trans. Med. Robot. Bionics*, vol. 3202, no. c, pp. 1–1, 2020, doi: 10.1109/tmr.2020.2974523.
- [6] R. Grassmann, V. Modes, and J. Burgner-Kahrs, "Learning the Forward and Inverse Kinematics of a 6-DOF Concentric Tube Continuum Robot in SE(3)," in *IEEE International Conference on Intelligent Robots and Systems*, 2018, pp. 5125–5132, doi: 10.1109/IROS.2018.8594451.
- [7] K. Iyengar, G. Dwyer, and D. Stoyanov, "Investigating exploration for deep reinforcement learning of concentric tube robot control," *Int. J. Comput. Assist. Radiol. Surg.*, vol. 15, no. 7, pp. 1157–1165, 2020, doi: 10.1007/s11548-020-02194-z.
- [8] T. P. Lillicrap *et al.*, "Continuous control with deep reinforcement learning," 2015.
- [9] M. Andrychowicz *et al.*, "Hindsight experience replay," in *Advances in Neural Information Processing Systems*, 2017, vol. 2017-Decem, pp. 5049–5059.



# SoftSCREEN – Soft Shape-shifting Capsule Robot for Endoscopy based on Eversion Navigation

Vanni Consumi<sup>1</sup>, Lukas Lindenroth<sup>1</sup>, Danail Stoyanov<sup>1</sup> and Agostino Stilli<sup>1</sup>

<sup>1</sup>Wellcome/EPSRC Centre for Interventional and Surgical Sciences, University College London, UK

## INTRODUCTION

Colorectal cancer (CRC) is the third most commonly diagnosed malignancy and the second most common cause of cancer-related deaths worldwide [1]. Conventional colonoscopy represents the gold standard for the evaluation of diseases of the colon and for CRC diagnosis [2]. However, this screening procedure is considered invasive – discomfort, pain and potential tissue damage can occur for patients. Ingestible endoscopic capsules have been developed to overcome the drawbacks of standard colonoscopy. Despite the advantages offered by these wireless devices, their main limitation is that their motion depends on natural bowel peristalsis only and it is not possible to control capsule motion and camera orientation [3]. Magnetic capsules instead rely on external magnetic fields to overcome the lack of controllability of standard ingestible capsules, however, they require bulky and expensive equipment to be actuated with enough precision and force [4].

To actively and reliably control the movements of an endoscopic capsule system a number of embedded locomotion approaches have been explored, with robotic solutions being proposed by multiple research groups [4]. Systems based on rigid mechanical elements, like the robots presented in [5], can cause damage to the soft walls of the navigated GI tract despite their active motion capabilities. For this reason motion techniques based on treaded tracks [6] and elastic caterpillars [7] have been suggested. In [6], the rigid endoscopic capsule has four soft tracks powered by a worm-gear transmission and has successfully demonstrated benefits in terms of navigation speed, however, due to the fixed geometry of the proposed system, the four tracks are never simultaneously in contact with the walls, significantly reducing the controllability of the system. The robotic endoscopic system shown in [7] instead makes use of elastic tracks that passively deform to match the local lumen of the colon. This arrangement ensures a central positioning of the capsule body, however, its motion is strongly affected by the gravity action as well as by the lack of direct control on the geometry of the system, hence, of the interaction forces between the tracks and the wall of the GI tract.

In this paper the Soft Shape-shifting Capsule Robot for Endoscopy based on Eversion Navigation (SoftSCREEN) is presented for the first time – a novel capsule-sized system that propels itself through the GI tract by means of a series of continuously everting elastic tracks distributed all around its body. A proof-of-concept 2:1 scaled prototype for validation of navigation and shape-shifting capabilities, is proposed as shown in Fig. 1. The system consists of a rigid cylindrical body (Fig. 1-b, light blue) which encases a worm gear powered by a motor. The motion is provided by six elastic tracks engaging with the worm gear teeth, regularly distributed

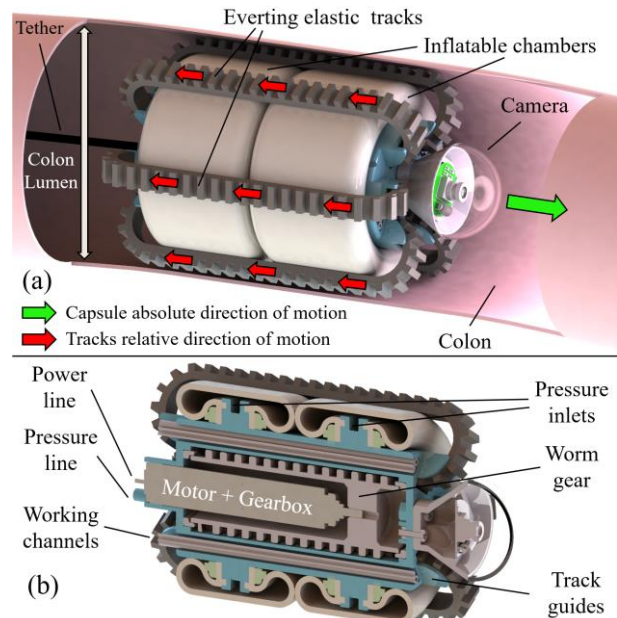


Figure 1 – (a) SoftSCREEN System motion principle: the inflation of the chambers ensures the contact of the tracks onto the colon walls. (b) Section of the 2:1 scaled prototype.

around the capsule lateral surface. Differently from other track-based capsule designs, the geometry of the SoftSCREEN system can be changed by pressurising the two toroidal chambers displayed in white in Fig. 1. When the chambers are inflated, the elastic tracks are deformed in the part not engaged in the worm gear. This design feature allows to match the local lumen of the GI tract, ensuring constant traction of all the tracks. The proposed inflatable mechanism allows also for self-alignment of the system with the central axis of the targeted section, thus providing a stable configuration for the camera embedded for navigation and screening. The revolution of the worm gear leads to the revolution of the tracks around the inflatable chambers and along the length of the capsule, enabling navigation (Fig. 1-a). The colon lumen diameter varies in a range between 30 to 90 mm; therefore, the 2:1 scaled prototype diameter at rest should not exceed 60 mm, while deforming up to 180 mm. The main focus of this work is the validation of the navigation capabilities of this novel design – challenges like down-scaling, durability, sterilization, single-use sub-systems, compliance with medical devices regulations, although all of critical importance for the development of the final system, are not discussed here due to space constraints.

## MATERIALS AND METHODS

The CAD model of the prototype is shown in Fig. 1-b. A rigid chassis encloses a 10 mm diameter brushless DC motor (Maxon 315170 motor, 332426 gearbox) paired with a worm gear, both arranged longitudinally. The elastic tracks (Fig. 2-a) are made of Dragon Skin™ 20



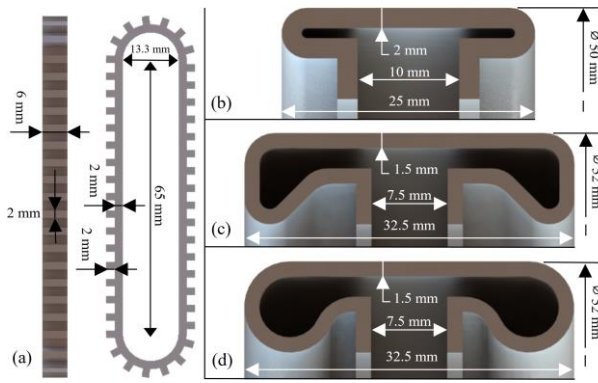


Figure 2 – (a) track dimensions, (b) simple chamber profile. (c) squared chamber profile and (d) rounded chamber profile.

silicone (Smooth-On Inc., Easton, PA, US), have a planar low-friction internal surface to slide on the chambers and a series of teeth on the external surface to engage with the worm gear inside the chassis, while providing the desired friction when interacting with the walls of the colon. As the tracks, the chambers are made of Dragon Skin™ 20. As shown in Fig. 1-b, the chambers are secured to the chassis by means of flanges embedded in the chassis, custom rings (in green) and screws, creating an air-tight connection. Air in pressure is supplied to the chambers by the circumferential pressure inlets shown in Fig. 1-b: these are connected to the pressure supply through a 1 mm diameter longitudinal pipe built into the chassis. Additionally, space for six 2 mm diameter channels is available for pressure lines, tendons or electrical cables. In this paper we present a preliminary design study focusing on Finite Element Method (FEM) static analysis of the chambers and of the tracks, using Dragon Skin™ 20 silicone as material – the mechanical parameters of which have been obtained from [8]. The aim of this study is to optimize the design of the chambers to achieve the desired radial expansion (180 mm), without exceeding the diameter at rest of 60 mm. In Fig. 2-b/c/d we present three designs: in (b) we minimise the radial encumbrance at rest, in (c) we maximise the section area and in (d) we maximise the internal curvature. These profiles have the following geometrical features (expressed as middle line perimeter of the section profile, deformable silicone volume, thickness): (b) 39.42 mm, 11.83 cm³, 2 mm; (c) 66.39 mm, 13.94 cm³, 1.5 mm; (d) 68.9 mm, 14.77 cm³, 1.5 mm. A larger section area ensures more material to deform, while a large and uniform curvature prevents localised areas of high stress, that could lead to rupture of the chamber. Profile (c) has a longer section perimeter and internal curvature radius of 1 mm/1.5 mm. Profile (d) has shorter section perimeter but features a uniform internal curvature radius of 3 mm. Finally, with respect to profile (b), both (c) and (d) are as wide as the chassis and have closer flanges to further increase the amount of deformable material, with slightly decreased thickness.

## RESULTS

Due to computational limitations of the FEM software used (Ansys 19.0, ANSYS Inc., US) the proposed profiles were tested deforming them only up to a third of their desired deformation in two scenarios: single chamber free inflation (3D study) and chambers-track interaction (2D study), modelling also the track (Dragon Skin™ 20)

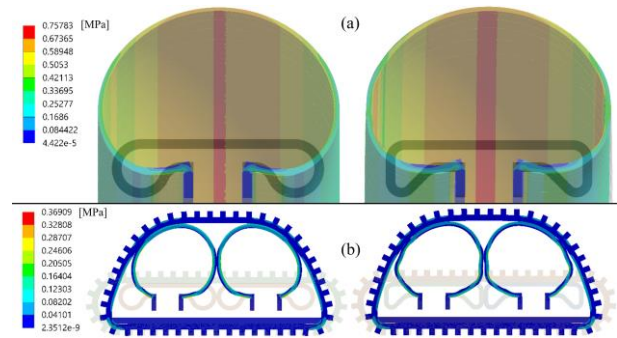


Figure 3 – (a) 2D track/chamber simulation for circular (left) and squared profile (right). (b) 3D free inflation for circular (left) and squared profile (right).

and the chassis (steel). The results of the simulations are illustrated in the Fig. 3. Fig. 3-a shows the circular profile on the left as the best for the free inflation, with a maximum stress of 0.675 MPa, while the right profile exhibited maximum stress 0.758 MPa, with a radial deformation of 21 mm in both cases. In the chambers-track interaction case (Fig. 3-b) instead, the squared profile showed less localized maximum stress, peaking at 0.326 MPa, while the circular one peaked at 0.369 MPa, in both cases for a radial deformation of 20.3 mm.

## CONCLUSION AND DISCUSSION

In this work, a novel design for an endoscopic shape-shifting robotic capsule is presented. A proof-of-concept system is presented, investigating a 2:1 tethered version, focusing on colonoscopy. The large deformation of the inflatable and elastic elements composing the envisioned variable geometry mechanism pose the biggest design challenge. A preliminary FEM analysis of different designs for the inflatable chambers showed that a large and continuous curvature radius results in lower maximum stress in the free inflation scenario, while the larger amount of material in the squared profile results in a lower stress in the chamber-track interaction scenario. Regardless of the geometry, in both cases the maximum stress measured for a third of the desired deformation is ten times smaller than the tensile stress of the silicone rubber tested (3.8 MPa). These results will be validated in real prototypes in the sooner future.

## REFERENCES

- [1] International Agency for Research on Cancer - World Health Organization, "Cancer Today - Data visualization tool for exploring the global cancer burden in 2018," 2019. <https://gco.iarc.fr/today/home> (accessed Mar. 16, 2019).
- [2] W. C. Y. Leung *et al.*, "Alternatives to colonoscopy for population-wide colorectal cancer screening," *Hong Kong Med. J.*, vol. 22, no. 1, pp. 70–77, 2016, doi: 10.12809/hkmj154685.
- [3] R. E. (2015) Koulaouzidis A, Iakovidis DK, Karargyris A, "Wireless endoscopy in 2020: Will it still be a capsule?," *World J Gastroenterol* 2020(21)5119–5130.
- [4] G. Ciuti *et al.*, "Frontiers of robotic endoscopic capsules: a review," *J. micro-bio Robot.*, vol. 11, no. 1–4, pp. 1–18, 2016.
- [5] C. Quaglia, E. Buselli, R. J. Webster III, P. Valdastris, A. Mencias, and P. Dario, "An endoscopic capsule robot: a meso-scale engineering case study," *J. Micromechanics Microengineering*, vol. 19, no. 10, p. 105007, 2009.
- [6] G. A. Formosa, J. M. Prendergast, S. A. Edmundowicz, and M. E. Rentschler, "Novel Optimization-Based Design and Surgical Evaluation of a Treaded Robotic Capsule Colonoscope," *IEEE Trans. Robot.*, 2019.
- [7] D. Kim, D. Lee, B. Kim, and B.-I. Lee, "A self-propelled robotic colonoscope using elastic caterpillars," in *IEEE ISR 2013*, 2013, pp. 1–4.
- [8] L. Marechal, P. Baland, L. Lindenroth, F. Petrou, C. Kontovounisios, and F. Bello, "Toward a Common Framework and Database of Materials for Soft Robotics," *Soft Robot.*, 2020.

# Angular metrics and an effort based metric used as features for an automatic classifying algorithm of surgical gestures

M. Bombieri<sup>1</sup>, D. Dall'Alba<sup>1</sup>, S. Ramesh<sup>1</sup>, G. Menegozzo and P. Fiorini<sup>1</sup>

<sup>1</sup>*Department of Computer Science, University of Verona,  
{marco.bombieri\_01,diego.dallalba,paolo.fiorini}@univr.it*

## INTRODUCTION

To improve the quality with which a surgical procedure is performed it is necessary to have effective and systematic surgical training techniques: [2] the better the quality of the training, the lower the risk of incurring serious post-operative complications [1]. Automated surgical gestures classification and recognition are important precursors to achieving the goal of objective evaluation of surgical skills. [2]. Many works have been done to discover and validate metrics based on the motion of instruments that can be used as features for automatic classification of surgical gestures [3]. Most of the motion metrics proposed are derived from the ones developed for Minimally Invasive Surgery (MIS): which are based on motion analysis performed in cartesian space (e.g. tool-tip velocities and accelerations). The introduction of Robotic-Assisted MIS (RAMIS) with improved control and dexterity of surgical instruments could enable the introduction of more complex and descriptive metrics: the motion of teleoperated RAMIS reflects the motion of the operating human surgeon and the robot senses its kinematic variables. Some recent research works have introduced metrics specifically designed for RAMIS, based on orientation information [3], gripping, and interaction forces with the environment [4]. To the best of our knowledge, these metrics have been devised and applied in the cartesian space and not in joints space. In this work, we present a series of angular metrics that can be used together with cartesian-based metrics to better describe different surgical gestures. These metrics can be calculated both in cartesian space and in joint space and are used as input features to an automatic surgical gesture classification algorithm. To evaluate the proposed metrics we introduce a novel surgical dataset that contains both cartesian and joints spaces data acquired with da Vinci Research Kit (dVRK) [5]. The dataset consists of 40 subsequent suturing exercises performed by a single expert operator. The obtained results confirm that the application of joint space metrics improves the accuracy of gesture classification: five out of the ten most important features are from joint space and six of them are orientation based features; this confirms that our proposed orientation based metrics in joint space are a good set of features. The results also show that specific joints have a greater importance in the automatic classification of surgical gestures.

## MATERIALS AND METHODS

In this work we extended the Cartesian metrics introduced in [3] to consider their application to the joint space. In the following formulas, we will show how to calculate metrics on a generic joint  $k$ . The calculation of the average metric on more joints is a trivial extension. In the joints space we introduce the *Angular Displacement Joint* (ADIJ) metric as:

$$ADIJ_k = \sum_{i=1}^{N-1} |\theta_{i+1} - \theta_i| \quad (1)$$

where  $\theta_i$  and  $\theta_{i+1}$  are angles corresponding to joint  $k$  in two successive samples and  $N$  is the number of samples. Another metric is the *Time Angular Displacement Joint* (TADJ):

$$TADJ_k = \frac{1}{T} \sum_{i=1}^{N-1} |\theta_{i+1} - \theta_i| \quad (2)$$

where  $T$  is the duration of the specific surgical action considered. Also, in the joint space we define the metric *Rate Of Change Joint* (ROCJ):

$$ROCJ_k = \frac{1}{N-1} \sum_{i=1}^{N-1} \omega_i \quad (3)$$

where  $\omega_i$  is the instantaneous angular velocity of the joint  $k$  and  $N$  is the number of samples corresponding to the specific action considered.

Our data contain also information about current joint effort (e.g joint motor current, joint force or torque) as a scalar value  $\tau_i$ . Based on this information we introduce the *mean effort* (MEJ) which represents how the joint  $k$  interacts with the environment:

$$MEJ_k = \frac{1}{N-1} \sum_{i=1}^{N-1} \tau_i \quad (4)$$

A strong limitation for the evaluation of the proposed metrics is that surgical datasets publicly available in the literature, such as JIGSAWS [6], do not contain information in joints space. Therefore we acquire a new surgical dataset called YEAST (Yet Another Surgical Training Dataset) that contains both information. The acquired dataset consists of 40 trials of the same suturing task performed by a single expert user (see Figure 1) using a full dVRK setup and it is publicly available at <https://gitlab.com/altairLab/yeast-dataset>. For each trial, kinematics and endoscopic video data from stereo cameras are recorded. Different data streams have been synchronized and geometrically calibrated to provide coherent and consistent information. The surgical

gestures executed in the dataset have been manually annotated following the JIGSAWS convention [6].

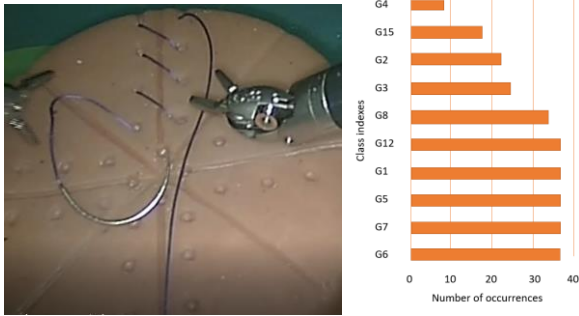


Figure 1 Left: Example of endoscopic view during suturing task. Three pass continue suture is performed using large needle driver on silicone phantom. Right: Histogram showing the number of samples for each gesture.

We investigate the ability of the proposed metrics to discriminate surgical gestures in two steps. First, we compute for each annotated gesture, the metrics using recorded kinematic values from the beginning to the end of the movements. Then, we analyze which are the most significant metrics for the classifier. To do so, we select the same Random Forest Classifier (RFC) proposed in [7]. Due to the high imbalance of the number of instances for each gesture, as shown on Figure 1 (Right), we validate our classifier using Stratified K-Folds (SKF) methodology (i.e. the folds are created in a way that they contain at least one instance for each class in both training and testing phase).

## RESULTS

We analyze the contribution of cartesian and joint space metrics for the task of surgical gesture classification. The mean accuracy is obtained using SKF methodology on three groups of metrics: cartesian space metrics, joints space metrics, and combined cartesian space and joints space metrics. The highest average classification accuracy of 86.51% is obtained using both cartesian and joint data. We obtain an accuracy of 83.01% if we use only joint space metrics and an accuracy of 75.27% if we use only cartesian space metrics. In Figure 2 we report Precision, Recall and F-Score for each gesture recognized using only cartesian space metrics or cartesian space metrics and joints space metrics together.

## CONCLUSION AND DISCUSSION

The accuracy, Precision, Recall and F-Score we obtain considering only joint metrics is better than that obtained considering only the cartesian metrics. This confirms that the proposed metrics are useful in order to obtain a better classification of the gestures. Results in Figure 2 suggest that the combined analysis of both cartesian and joint metrics allows us to get better performances during the classification phase. This is due to some translational gestures are well described by motion metrics in the cartesian space while orientation gestures are better described by metrics in the joint space.

Gestures	Cartesian Space			Cartesian + joints Space		
	Precision	Recall	F-Score	Precision	Recall	F-Score
G1	0.7148	0.6429	0.6639	<b>0.8556</b>	<b>0.8357</b>	<b>0.8363</b>
G2	<b>0.9029</b>	<b>0.9200</b>	<b>0.9044</b>	0.8762	0.9000	0.8810
G3	0.8529	0.8800	0.8600	<b>0.8600</b>	<b>0.9200</b>	<b>0.8873</b>
G4	0.0000	0.0000	0.0000	0.0000	0.0000	0.0000
G5	0.6495	0.6464	0.6337	<b>0.7844</b>	<b>0.8357</b>	<b>0.7907</b>
G6	0.8950	0.9429	0.9115	<b>0.9092</b>	<b>0.9714</b>	<b>0.9374</b>
G7	0.8051	0.9464	0.8655	<b>0.8833</b>	<b>1.0000</b>	<b>0.9366</b>
G8	0.6267	0.6524	0.6217	<b>0.8444</b>	<b>0.8429</b>	<b>0.8359</b>
G12	0.7853	0.7571	0.7577	<b>0.9095</b>	<b>0.8679</b>	<b>0.8857</b>
G15	0.7333	<b>0.5500</b>	<b>0.6248</b>	<b>0.8333</b>	0.4167	0.5343

Figure 2: Precision, Recall and F-Score for each gesture computed with only cartesian space metrics or in cartesian space metrics and joints space metrics together. The highest scores are shown in bold.

The classification method, however, fails for some gestures, mainly because the number of occurrences of such gestures is very low as shown by Figure 1 (Right). Other errors are instead attributable to the intrinsic similarity of some surgical gestures.

More detailed analysis show that the joints of the instrument unit have a greater importance for the purpose of gestures classification than the joints of the base unit. This work is a first step towards extending available objective evaluation metrics to joint space, providing also a new dataset suitable for benchmarking the performance of different methods. Future works will focus on the automatic segmentation of the surgical gestures to permit an automatic assessment of surgical skills based on the proposed metrics. We are also working on extending the dataset with more expert demonstrations.

## ACKNOWLEDGEMENTS

This research is funded by the ERC project ARS under the EU H2020 research and innovation programme (grant agreement No 742671) and under the Marie Skłodowska-Curie (grant agreement No. 813782 "ATLAS").

## REFERENCES

- [1] Birkmeyer, J. D., et al. "Surgical skill and complication rates after bariatric surgery." *New England J. of Med.* 369.15 (2013).
- [2] DiPietro, R., et al. "Segmenting and classifying activities in robot-assisted surgery with recurrent neural networks." *Int. J. of computer assisted radiology and surgery* 14.11 (2019).
- [3] S., Yarden, T. S. Lendvay, and I. Nisky. "Instrument orientation-based metrics for surgical skill evaluation in robot-assisted and open needle driving. (2017).
- [4] Trejos, A. L., et al. "Development of force-based metrics for skills assessment in minimally invasive surgery." *Surgical endoscopy* 28.7 (2014).
- [5] Kazanzides, P., et al. "An open-source research kit for the da Vinci Surgical System." 2014 IEEE int. conf. on robotics and automation (2014).
- [6] A., Narges, et al. "A dataset and benchmarks for segmentation and recognition of gestures in robotic surgery." *IEEE Transactions on Biomedical Engineering* 64.9 (2017).
- [7] Pedregosa, F., et al. "Scikit-learn: Machine learning in Python." *Journal of machine learning research* 12.Oct (2011).



# Endoscopic Optical Coherence Tomography Volumetric Scanning Method with Deep Frame Stream Stabilization

Guiqiu Liao<sup>1,2,\*</sup>, Oscar Caravaca Mora<sup>1,\*</sup>, Benoit Rosa<sup>1</sup>, Diego D'Allaba<sup>2</sup>, Alexandre Asch<sup>1</sup>, Paolo Fiorini<sup>2</sup>, Michel de Mathelin<sup>1</sup>, Florent Nageotte<sup>1</sup>, Michalina J. Gora<sup>1</sup>

<sup>1</sup> ICube Laboratory, University of Strasbourg,

<sup>2</sup> ALTAIR Robotics Laboratory, The University of Verona

\* This authors contributed equally to this work  
guiqiu.liao@icube.unistra.fr;

## INTRODUCTION

Optical coherence tomography (OCT) is increasingly used in biomedical and clinical imaging due to its combination of high-speed optical sectioning and high resolution. Side-viewing OCT probes with proximal scanning have been successfully used in the diagnosis of intravascular diseases, the intravascular stent strut assessment, as well as in the digestive tract. The rotational distortion of proximal-scanning endoscopic optical coherence tomography is significant due to the friction of optical fiber between the wire wall and the variable torque of the optical fiber. It can be further increased in the case of a steerable catheter used for large area scanning using a flexible robotized endoscope [1]. The robotized steerable OCT user can navigate the probe using telemanipulation with bending, translation and rotation of the steerable OCT catheter.

This work is focused on correction of image artifacts presented in three-dimensional OCT imaging in rotational scanning. The results show a significant reduction of the image precession when implementing a robotic pullback instead of the conventional internal pullback of the optical probe. In this case the whole OCT catheter is in motion during the 3D-scanning eliminating the torsion caused by the internal friction between the sheath and the rotating probe, so that the precession is 90% reduced in comparison with the conventional pullback scanning. In order to fully reduce remaining precession, which can be attributed to motor speed instability, an image processing technique based on deep learning is also integrated.

## MATERIALS AND METHODS

In this work, a steerable OCT instrument with an outer diameter of 3.5 mm is used for volumetric imaging [1]. The steerable instrument is terminated with a 2 cm long transparent sheath to allow three-dimensional OCT imaging using a side-focusing optical probe with two external scanning actuators. The instrument is connected to an OCT imaging system built around the OCT Axsun engine, with a 1310 nm center wavelength swept source laser and 100 kHz A-line rate. The OCT steerable catheter is compatible with one of two instrument channels of a robotized flexible intervention endoscope [2]. The distal end of the robotized endoscope can be bent

in 2 degrees of freedom, translated and rotated. The steerable OCT catheter can be translated, rotated and bent in one plane. In addition, the rotation and translation of the inner OCT probe can also be controlled by a servo system.

Conventional internal pullback scanning was effectuated to image a 20 mm long 3D printed rectangular tube target in VeroWhite material (Figure 1(E)). In the next step the same pullback was effectuated using a robot. To estimate stability of the image, ImageJ was used to manually measure the rotation of the 4 internal corners of the rectangular tube for each 1 mm of spacing with respect to the first frame.

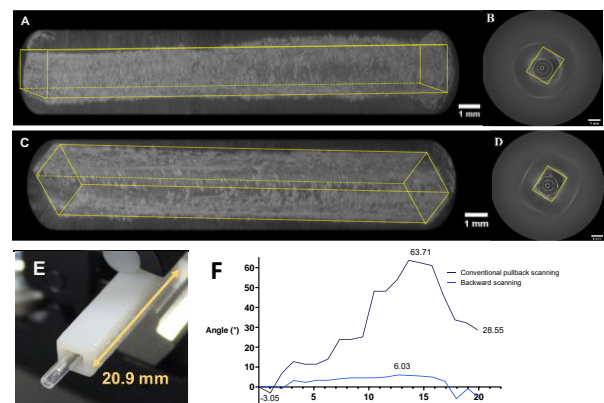


**Figure 1.** Results of 3D reconstruction of the rectangular tube and the sum of the frames by performing regular pullback scanning (A, B)), and results of robotic pullback scanning (C, D). (E) Rectangular tube target for testing. (F) Angular rotation versus the pullback scanning distance (mm) for regular pullback and tool pullback with steerable catheter.

To further improve the alignment on the robotic volumetric scanning data, a deep convolutional neural network (CNN) based video stabilization algorithm was applied to eliminate the image rotation distortion between B-scans. This algorithm takes image sequence as input to get image correction vectors. To train the algorithm, a data set of 3.6 million image pairs is generated with 1800 true OCT images. Each image pair is generated by distorting original images with a random Non-uniform Rotational Distortion (NURD) warping vector. The training pipeline is implemented with Python codes, Pytorch framework is used for network implementation. After training the deep network for  $14 \times 10^4$  iterations, it's



deployed with a NVIDIA QT1000 graphics card to process the OCT data collected with the proposed scanning system. We calculated the standard deviation (STD) value and en-face projections [3] of videos to evaluated the efficiency of the stabilization algorithm.

## RESULTS

A conventional OCT pullback scanning presented image rotation between 2D radial frames from  $-3.04^\circ$  clockwise at 1.06 mm to a maximum rotation angle of  $63.71^\circ$  counterclockwise at 14 mm, ending in an angle of  $28.55^\circ$  at 20 mm (Fig. 1 F). When performing volumetric robotic scanning of the steerable OCT tool the image rotation was reduced to the range of  $6.03^\circ$  to  $-5.83^\circ$  at 13 mm and 18 mm correspondingly. This constitutes an improvement of approximately 90% in reduction of precession when performing backward scanning. The actual scanning length was 20.9 mm and the speed of the pullback motion of the robotic instrument was 2.7 mm/s. Figure 1 shows the 3D reconstruction in both scanning methods. The conventional OCT pullback scanning presents major deformation in Figure 1(A) due to a large rotation angle, while such deformation is highly reduced in the case of robotic volumetric scanning in Figure 1(C). Figures 1(B, D) show the sum of all the frames to better demonstrate the difference of precession for each scanning method.

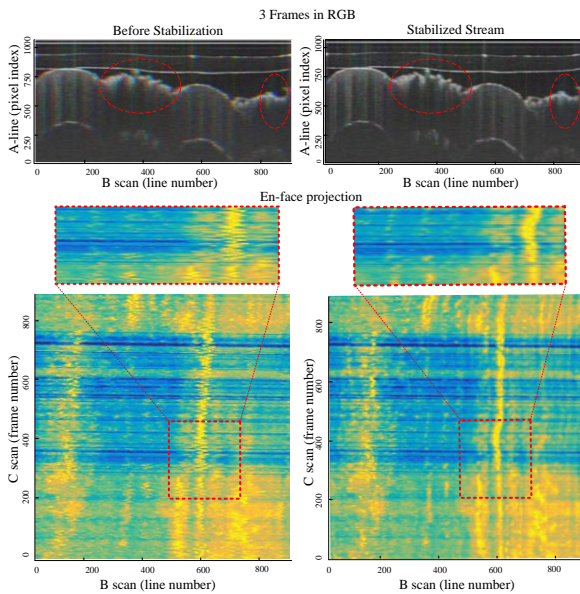


**Figure. 3.** Top row is the comparison of 3 adjacent frames in RGB channels, the bottom row is the comparison of A-line accumulated images with the videos containing 900 frames. The dashed circles mark out areas prohibiting significant NURD and corresponding stabilized result. The dashed boxes are enlarged for better visualization.

The STD value of the video before applying stabilization algorithm is  $7.33 \pm 0.52$ , which means it still experience fluctuation with a maximum value of 9.15. After applying the deep video stabilization algorithm to the

data, the STD value of the video decreases to  $6.19 \pm 0.08$ , which has both lower mean value and variation.

In Figure 3, the top row shows 3 consecutive frames encoded in the red, green and blue (RGB) channels and superimposed to one individual image. The stabilization algorithm reduces the “colorful” part of unstable original frames significantly, while maintaining the texture characteristics of the original OCT images. It is also presented in en-face projections of the 3D OCT data set where each A-line is accumulated to one single value by mean intensity projecting (bottom row in Figure 3). In this case an X axis corresponds to a circumferential scanning and a Y axis to a longitudinal volumetric scanning. The frame size of one OCT image is  $1024 \times 832$ , which contains 832 A-lines. We transform 900 frames into a  $900 \times 832$  matrix, and for display reason the matrix is normalized and the mean value is subtracted. Before stabilization, the image on the bottom left of figure 3 shows more unsmooth fluctuation. The right bottom image shows the A-line accumulation of stabilized robotic scanning data, which has less fluctuation, whereas its overall texture matches the overall texture of the bottom left image. This indicates that the algorithm can stabilize the video without changing other information in OCT images.

## CONCLUSION AND DISCUSSION

We have demonstrated the potential benefit of implementing the pullback scanning with the robotic tool, our results show reduction of precession of the OCT images by about 90% in comparison with the regular internal pullback, significantly reducing as well distortion in 3D reconstruction.

With a deep learning based method applied to the robotic scanning data, the stabilization of OCT frame stream is further improved, representing by the reduced STD value and the lower fluctuation in the en-face projection. Other scanning methods using the automatic capabilities of the robot will be explored in the future work.

## REFERENCES

- [1] O. Caravaca Mora et al., “Steerable OCT catheter for real-time assistance during teleoperated endoscopic treatment of colorectal cancer,” *Biomed. Opt. Express*, Dec. 2019.
- [2] A. De Donno et al., “Introducing STRAS: A new flexible robotic system for minimally invasive surgery,” *Proc. - IEEE Int. Conf. Robot. Autom.*, 1213–1220, 2013.
- [3] Abouei, A. et al., “Correction of motion artifacts in endoscopic optical coherence tomography and auto fluorescence images based on azimuthal en face image registration,” *Journal of Biomedical Optics*, vol. 23, no. 01, p. 1-14, 2018.

## Acknowledgements

This work was supported by the ATIP-Avenir grant, the ARC Foundation for Cancer research, the University of Strasbourg IdEx, and funding from the European Union’s Horizon 2020 research and innovation programme under the Marie Skłodowska-Curie grant agreement No 813782.

# Feasibility of using a Long Short-Term Memory Network for Robotic Catheter Control\*

Di Wu<sup>1,2</sup>, M. Ourak<sup>1</sup>, M. Ahmad<sup>1</sup>, K. Niu<sup>1</sup>, G. Borghesan<sup>1,3</sup>, J. Dankelman<sup>2</sup>, E. Vander Poorten<sup>1</sup>

<sup>1</sup>KU Leuven, Department of Mechanical Engineering, Leuven, Belgium

<sup>2</sup>TU Delft, Department of Biomechanical Engineering, Delft, the Netherlands

<sup>3</sup>Core Lab ROB, Flanders Make, Belgium

## INTRODUCTION

Coronary artery disease (CAD) is one of the major cardiovascular diseases threatening human health worldwide and is responsible for around 20% of deaths in the developed countries [1]. Patients suffering from CAD experience different levels of chest pain, shortness of breath, fatigue, or irregular heartbeat. Cardiac catheterization is widely performed to treat CAD. In this procedure, a flexible catheter is steered along the aorta until it reaches the left and right coronary arteries. Next, a guidewire is employed to cannulate the occlusion area [2].

Accurate control of flexible catheters is vital in interventions. Nevertheless, precise steering is difficult in practice. Amongst other factors, hysteresis is a major cause of imprecision regardless of actuation technologies. Hysteresis generates a complex non-linear multi-valued relation between input commands and the response of the catheter distal tip. In the past, researchers endeavored to model and compensate for the hysteresis in catheters based on mathematical modeling [3], where a complex identification process is imperative. In comparison, Neural Networks (NNs) are appealing for their ability to accurately represent complex nonlinear behavior, albeit dependent on the specific application. This makes them feasible for modeling and compensating nonlinear systems. In this work, the feasibility of employing a NN to deliver precise catheter control in presence of a hysteresis-affected actuation system is investigated.

## METHODS

The output of a system suffering from hysteresis depends on both the current and past inputs, typically described as a time series of hysteresis loops. Long Short-Term Memory (LSTM) proposed in [4] is an effective tool for processing sequential information since it takes historical information into account and utilizes this knowledge to predict the behavior at future time steps. Therefore, LSTM is logical to be used in this work. In the following, the LSTM was first trained based on real hysteresis data collected from an experimental setup and then validated on that setup as well.

Pneumatic Artificial Muscles (PAMs) show good promise in intervention tools thanks to its advantages e.g. large bandwidth, easy fabrication, and lightweight. Nevertheless, hysteresis is a major challenge when using PAMs, thus

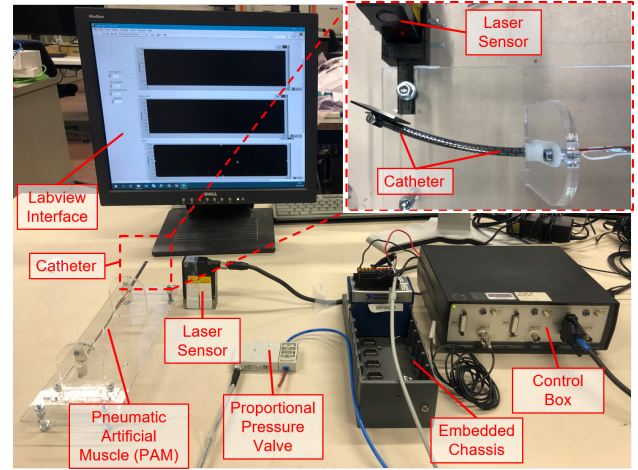


**Fig. 1.** The experimental setup for hysteresis data collection and LSTM performance validation. A close-up demonstrates the bending configuration of the catheter when the PAM is inflated.

compensation of hysteresis originating therefrom based on LSTM is investigated. To collect training data for the LSTM, an experimental setup was developed (Fig. 1). The setup contains a one-DOF Nitinol distal catheter segment with an embedded PAM. The PAM is attached off-center to the catheter tip. When increasing the pressure, the PAM contracts and pulls via a steel cable on the catheter tip, causing a bending moment. A laser sensor is used to measure the catheter tip displacement. A proportional pressure valve is employed to regulate the pressure applied to the PAM. The pressure and displacement data is collected at a sampling frequency of 250 Hz and visualized on LabVIEW®.

To fully excite the system, pressure signals as descending sine waves following:

$$p(t) = e^{-\tau t} (2.5 \times \sin(2\pi f t - \frac{\pi}{2}) + 2.5) \quad [\text{bar}] \quad (1)$$

were used to induce multi-loop hysteresis. The resulting catheter tip displacement - pressure data collected therefrom were then used to train the LSTM. In Eq. (1), the variable  $\tau$  regulated the descending speed of the sine wave and it was set to -0.05. The variable  $f$  was the excitation frequency in Hz and it was switched among 0.2, 0.4, 0.6, 0.8. Consequently, there are four groups of data containing 34413 data points in total for training the LSTM.

To estimate the pressure for controlling flexible catheters, the displacement data were used as input to the LSTM, while the predicted pressures are the output. The training of the LSTM was performed on a 4 GB NVIDIA CUDA-capable GPU. The LSTM was trained for 50 epochs, and the training time is around 20 to 30 minutes. For prediction, the average

\*This work was supported by the ATLAS project. ATLAS has received funding from the European Union's Horizon 2020 research and innovation programme under the Marie Skłodowska-Curie grant agreement No 813782. Corresponding author: Di Wu, di.wu@kuleuven.be

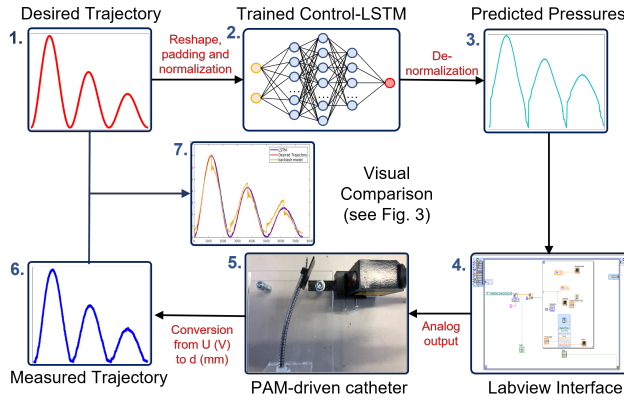


**Fig. 2.** The validation procedure for investigating the performance of the LSTM: 1) Creating a desired trajectory; 2) The desired trajectory is pre-processed and fed into the LSTM; 3) The LSTM predicts the corresponding pressures; 4) The predicted pressures are read by Labview and applied to the catheter as feedforward control; 5) The catheter tip motion is measured by a laser sensor; 6) Measured voltages are converted to catheter tip displacements; 7) Both measured and desired trajectories are visualized and compared.

inference time for a single point is 2.5 ms.

To evaluate the trained LSTM, an experimental procedure shown in Fig. 2 was conducted and illustrated as follows: 1) desired trajectory of the catheter tip is created by the users. In this work, a descending sinusoid trajectory following Eq. (2) is tested:

$$d(t) = e^{-0.05t}(4.5 \times \sin(0.2\pi t - \pi) + 4.5) \quad [\text{mm}] \quad (2)$$

2) displacement data are reshaped into a window size of 120, containing previous 120 samples  $d^{(t-119)}, d^{(t-118)}, \dots, d^{(t-1)}$  and  $d^{(t)}$ , and they are fed into the trained LSTM to predict  $p^{(t)}$ ; 3) predicted pressure is produced by LSTM and saved into a spreadsheet; 4) Labview reads the pressures from the spreadsheet and sends this to the PAM-driven catheter through an analog output as a feedforward control. The pressure control frequency is 250 Hz; 5) a laser sensor measures the motion of the catheter tip as voltage signals; 6) the measured voltage signals are converted to catheter tip displacements; 7) both the desired trajectory and the measured trajectory are visualized and compared on the same plot. Root Mean Square Error (RMSE) and Maximum Absolute Error (MAE) are used to quantitatively evaluate the performance of hysteresis compensation.

A controller based on a backlash model introduced in [5] was established for comparison with the LSTM-based controller. The backlash model is a rate-independent model that has a non-continuous function describing the dead zone. Measured trajectories resulting from both controllers are visualized and compared.

## RESULTS

The experiments on both the LSTM and backlash models were run ten times. One example of ten experimental results is visualized in Fig. 3. It can be observed that the LSTM-based controller is able to achieve effective hysteresis compensation, and the measured trajectory can precisely track the desired trajectory. One can see that the backlash model-based controller tries to compensate for the hysteresis by applying large pressure variations when approaching the

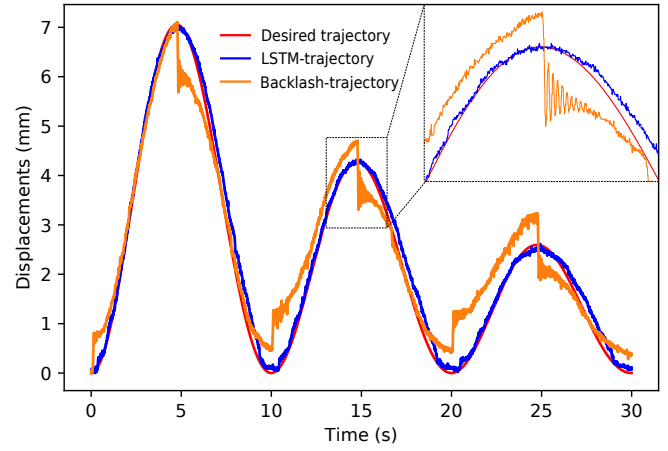


**Fig. 3.** Trajectories achieved by LSTM (blue) and backlash model (orange) compared to the desired trajectory (red).

**TABLE I:** MEAN AND STANDARD DEVIATION OF RMSE AND MAE OF 10 GROUPS OF EXPERIMENTS

Models	RMSE (mm)		MAE (mm)	
	Mean	STD	Mean	STD
LSTM	0.214	0.007	0.626	0.033
Backlash model	0.499	0.014	1.350	0.042

extrema points. However, this controller has difficulties in estimating the exact pressure-change that is needed, leading to significant over/under-shoots followed by some oscillations. The average mean and standard deviation over ten groups of the experiments (Table I) of the LSTM are 0.214 mm and 0.626 mm, respectively, which are less than half of the error achieved by the backlash model (RMSE = 0.499 mm and MAE=1.350 mm).

## CONCLUSION AND DISCUSSION

This study proposes to compensate for the hysteresis in a flexible catheter using LSTM. The proposed LSTM was first trained based on four groups of descending sine waves, then the LSTM is utilized to predict the pressures based on a given trajectory. The performance of the LSTM was validated on a descending sine wave (RMSE = 0.214 mm, MAE = 0.626 mm). The results indicate that the LSTM is able to effectively compensate hysteresis in a PAM-driven catheter. The errors are less than half of those achieved by the backlash model. Future work focuses on validating the generalization ability of the LSTM on other trajectory patterns that are completely different from the training data, e.g. ascending sine waves, sine waves with time-varying frequency, triangle waves.

## REFERENCES

- [1] A. Cassar, D. R. Holmes Jr, C. S. Rihal and B. J. Gersh, "Chronic coronary artery disease: diagnosis and management," *In Mayo Clinic Proceedings*, Vol. 84, No. 12, pp. 1130-1146, Dec. 2009.
- [2] A.K., Malakar, D. Choudhury, B. Halder *et al.*, "A review on coronary artery disease, its risk factors, and therapeutics," *Journal of cellular physiology*, Vol. 234, No.10, pp.16812-16823, 2019.
- [3] T. N. Do, T. Tjahjowidodo, M. W.S. Lau, *et al.*, "Hysteresis modeling and position control of tendon-sheath mechanism in flexible endoscopic systems," *Mechatronics*, vol. 24, no. 1, pp.12-22, Feb. 2014.
- [4] S. Hochreiter and J. Schmidhuber, "Long Short-Term Memory," *Neural Computation*, vol. 9, no. 8, pp. 1735-1780, Nov. 1997.
- [5] A. Devreker *et al.*, "Fluidic actuation for intra-operative in situ imaging," *In 2015 IEEE/RSJ International Conference on Intelligent Robots and Systems (IROS)*, pp. 1415-1421, 2015



# Segmentation of Lumen in Ureteroscopy Images using Deep Learning

Jorge F. Lazo<sup>1,2</sup>, Aldo Marzullo<sup>3</sup>, Sara Moccia<sup>4,5</sup>, Benoit Rosa<sup>2</sup>, and Elena De Momi<sup>1</sup>

<sup>1</sup> *Department of Electronics, <sup>2</sup>Information and Bioengineering, Politecnico di Milano, Milan, Italy*

<sup>2</sup> *ICube, Université de Strasbourg, Strasbourg, France*

<sup>3</sup> *Department of Mathematics and Computer Science, University of Calabria, Cosenza, Italy*

<sup>4</sup> *Department of Information Engineering, Università Politecnica delle Marche, Ancona, Italy*

<sup>5</sup> *Department of Advanced Robotics, Istituto Italiano di Tecnologia, Genoa, Italy*

jorgefrancisco.lazo@polimi.it

## I. INTRODUCTION

Ureteroscopy is a minimally invasive procedure which is used to explore the upper urinary tract, allowing the diagnosis and treatment of different conditions, such as kidney stones or urothelial carcinoma. Navigation and diagnosis inside the urinary tract are highly dependent upon the operators experience, and some image-related conditions such as the presence of image artifacts, floating debris, occlusions in the video, or image noise could add additional challenges for non-experienced operators. The development of computer vision methods for surgical assistance aims to deal with these limitations by highlighting relevant information which can enhance the performance of the surgeon and minimize the probability of complications.

The task of lumen segmentation is a fundamental part in the development of these assistance systems since this is the reference which marks the path that the endoscope should follow. However, this is not a simple task since there is a high variability in the the inter-patient anatomical structures, as well as the inner-patient variability, in terms of the different shapes in which the lumen is deformed at different points in the urinary tract.

Previous implementations of lumen segmentation has been proposed for colonoscopy images, being the majority of them based on the design of handcrafted feature extractors which require the tuning of several parameters [1], [2]. The most recent study proposes the use of a FCN-8 network [3] for the general segmentation of elements appearing of colonoscopy images, among them the lumen.

To the best of our knowledge, Convolutional Neural Networks (CNNs) have not been applied to semantic segmentation of the lumen in ureteroscopy images. We attribute this with the lack of a publicly available annotated dataset of ureteroscopy images, which is needed in order to train and validate such kind of networks. To tackle this we collected and annotated our own dataset from ureteroscopy images.

In this paper we propose the application of a variation of the well-known CNN architecture U-Net for the task of lumen segmentation by adding batch normalization layers at

the output of each of the convolutional layers and changing the loss function to the Dice similarity coefficient loss ( $L_{DSC}$ ).

## II. PROPOSED METHOD

Inspired by the model proposed in [4] originally developed for axon segmentation in microscopy images, we propose the implementation of a lumen-segmentation network based on U-Net architecture. We applied batch normalization at the output of every convolutional layer. In our specific case, the use of batch normalization provided stability and convergence of the learning process given the high variability in the structures, brightness and image resolution among the images of the dataset we used. A set of experiments was carried out using the original implementation of U-Net without batch normalization. It was observed that during training without batch normalization, without a proper initialization of the weights the network got stuck in a point where only white, or only black images were obtained as outputs and with  $DSC$  values below 0.25 in average.

The second modification with respect to [4] is a change in the chosen loss function. The one used in this implementation was the ( $L_{DSC}$ ) defined as:

$$L_{DSC} = 1 - \frac{2TP}{2TP + FN + FP} \quad (1)$$

where  $TP$  is the number of pixels that belong to the lumen, which are correctly segmented,  $FP$  is the number of pixels miss-classified as lumen, and  $FN$  is the number of pixels which are classified as part of lumen but actually they are not. Adam optimization was used during the training. The learning rate, and mini batch size for each of the models was chosen by trying the different combinations between several possible values of the hyper-parameters and using a 5-fold cross validation strategy. Once the hyper-parameter values were chosen, the training process was done dividing the data set for training/validation in a ratio 65/35. The Wilcoxon T-test on the  $DSC$  was used to determine statistical significance between the different models trained.

For this study, 7 video dataset from 4 patients were collected. The videos were acquired from the European Institute



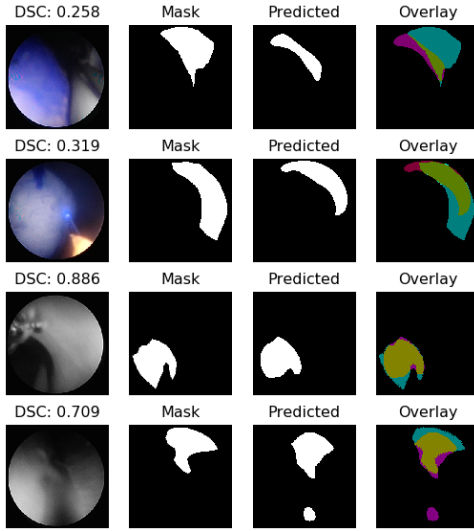


Fig. 1: Sample of results obtained using U-Net with BN with its respective *DSC* score. The colors in the Overlay images are as follows, TP: Green, FP: purple, FN: Blue, TN: Black.

of Oncology (IEO) at Milan, Italy and the KU Leuven University Hospital. All patients gave their informed consent for data collection and use of it for research. The data collection followed the ethical protocol approved by the IEO and in accordance with the Helsinki Declaration. The videos are from ureteroscopy procedures targeting upper tract tumor ablation and kidney stone removal. From these videos, a total number of 1,445 frames were extracted and manually annotated using our own GUI developed in Matlab for this purpose. The video-frames from patient one were set apart to be used as test dataset. We compare the obtained results with the FCN-8 architecture that has been used for lumen segmentation in colonoscopy images [5].

The performance metrics chosen to quantitatively evaluate the results, were the *DSC*, the Precision (*Prec*) and Recall (*Rec*), which are defined as

$$DSC = 1 - L_{DSC} \quad (2)$$

$$Prec = \frac{TP}{TP + FP} \quad (3)$$

$$Rec = \frac{TP}{TP + FN} \quad (4)$$

### III. RESULTS AND DISCUSSION

The boxplots of the *DSC* are depicted in Fig. 2. From these result is possible to see that U-Net has the best performance overall. The average values of *DSC*, *Prec* and *Rec* for this network were of 0.65, 0.48 and 0.82 respectively. In comparison with FCN-8 in the gray-scale dataset U-Net achieves a *DSC* 0.25 better than the FCN-8 network ( $p < 0.05$ ) and in the case of the RGB dataset achieves an average value 0.18 ( $p < 0.01$ ) better than FCN-8. In general for both models it was seen that the training in gray-scale images achieve

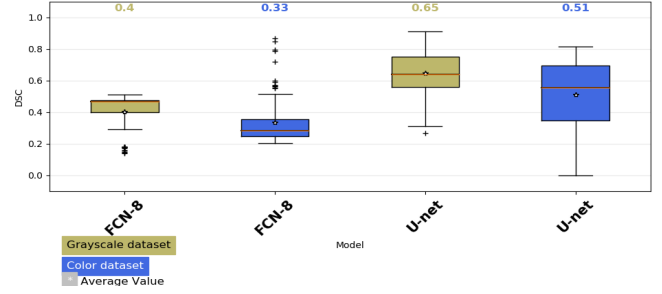


Fig. 2: Box plots of *DSC* obtained with the different CNNs tested.

better results among the same models. In the case of U-Net a difference of 14% was observed ( $p < 0.001$ ) while in the case of FCN-8 the difference was of 7% ( $p < 0.05$ ). This might be related to the color-space itself of the dataset. Considering that the gray-scale image dataset might have enough information to perform the binary classification of pixels into lumen and no-lumen, the addition of two channels would require the adjustment of more parameters, which implicitly would require a higher amount of data. Some sample of the segmented images are depicted in Fig. 1

### IV. CONCLUSION

In this paper, we addressed the task of lumen segmentation in the ureter, for this purpose we proposed the implementation of a Deep CNN. The network used consisted of a standard version of U-Net with the addition of batch normalization at the output of each of the convolutional layers. The method was tested in different image spaces finding that for this task the network performs better in gray-scale images and then compare with a FCN-8 model which previously has been used for lumen segmentation in colonoscopy images. We show that the network performs better than the previous model implemented for this task. This demonstrates that it could be a suitable model for further development in the task of lumen segmentation of the ureter.

### REFERENCES

- [1] G. Gallo and A. Torrisi, "Lumen detection in endoscopic images: a boosting classification approach," *International Journal On Advances in Intelligent Systems*, vol. 5, no. 1, 2012.
- [2] D. Wang, X. Xie, G. Li, Z. Yin, and Z. Wang, "A lumen detection-based intestinal direction vector acquisition method for wireless endoscopy systems," *IEEE Transactions on Biomedical Engineering*, vol. 62, no. 3, pp. 807–819, 2014.
- [3] J. Verma, M. Nath, P. Tripathi, and K. Saini, "Analysis and identification of kidney stone using k th nearest neighbour (knn) and support vector machine (svm) classification techniques," *Pattern Recognition and Image Analysis*, vol. 27, no. 3, pp. 574–580, 2017.
- [4] O. Ronneberger, P. Fischer, and T. Brox, "U-net: Convolutional networks for biomedical image segmentation," in *International Conference on Medical Image Computing and Computer-Assisted Intervention*. Springer, 2015, pp. 234–241.
- [5] D. Vázquez, J. Bernal, F. J. Sánchez, G. Fernández-Esparrach, A. M. López, A. Romero, M. Drozdal, and A. Courville, "A benchmark for endoluminal scene segmentation of colonoscopy images," *Journal of Healthcare Engineering*, vol. 2017, 2017.

# Constraint-Based Control of a Distally Actuated Continuum Robot\*

Beatriz Farola Barata<sup>1,2</sup>, Gianni Borghesan<sup>1,3</sup>, Diego Dall'Alba<sup>2</sup>, Jos Vander Sloten<sup>1</sup>, and Emmanuel Vander Poorten<sup>1</sup>

<sup>1</sup>*Robot-Assisted Surgery Group, Department of Mechanical Engineering, KU Leuven, Belgium*

<sup>2</sup>*Altair Robotics Laboratory, Department of Computer Science, University of Verona, Italy*

<sup>3</sup>*Core Lab ROB, Flanders Make, Belgium*

beatriz.barata@kuleuven.be

## INTRODUCTION

Endovascular catheterization is a minimally invasive procedure typically carried out with the use of catheters, inserted in the vasculature and steered towards a desired site. Preventing damage to the vasculature relies on the precise navigation of the catheter's tip, while minimizing the contact between the instrument and the vasculature [1]. Robotic technology is increasingly investigated in such task, as it promises a high level of precision. Robots could further perform complex coordinated motion in 3D space. Developing a safe and precise controller that accounts for the large amount of variability is far from trivial. In order to tackle the associated challenges, different control approaches have been introduced, such as multi-task control frameworks [2].

This work proposes a constraint-based velocity-resolved control approach for a steerable catheter, with a distal bending segment. Figure 1 shows the steerable catheter with distal bending segment (in red) between the base  $\mathbf{p}_b$  and the tip  $\mathbf{p}_t$  of the catheter. The controller is tested inside a virtual aortic vessel model.

Given the vessel centerline, locally approximated as a line  $cl$ , the controller is designed such that the catheter tip navigates within a safe zone (defined by a safe distance  $\mathbf{d}_s$ ) around  $cl$ ; and the mid-node of the bending segment backbone  $\mathbf{p}_n$  (situated between  $\mathbf{p}_t$  and  $\mathbf{p}_b$ ) keeps minimal contact with the vessel wall. The goal of this work is to propose and assess a control framework for the aforementioned control problem.

## MATERIALS AND METHODS

The robot is controlled with a velocity-resolved constraint-based scheme [3]. This kind of approach requires the following elements: *i*) a forward kinematic and differential forward kinematic functions relating the actuator space and task space, *ii*) control equations solved with a quadratic programming (QP) approach, and *iii*)

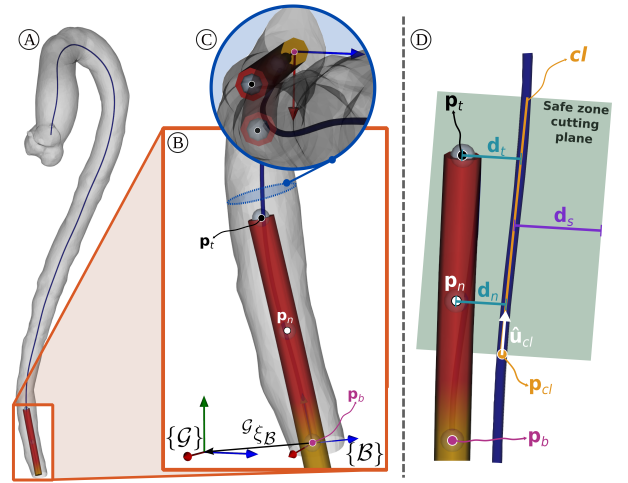


**Figure 1:** System's overview in the simulated aortic model (A), with a focus on the different components of the robot and relevant frames in (B). Representations of the control outcome in the  $xy$  plane (C) and of the overall control approach with relevant variables (D) are shown.

task specification. The kinematic relation between  $\mathbf{y}$  (output space) and  $\mathbf{q}$  (actuator space) and the obtained control actions (based on the generalized Jacobian matrix  $\mathbf{J}$ ) are described as follows:

$$\mathbf{y} = \mathbf{g}(\mathbf{q}), \quad \dot{\mathbf{y}} = \mathbf{J}(\mathbf{q})\dot{\mathbf{q}} = \frac{\partial \mathbf{g}(\mathbf{q})}{\partial \mathbf{q}} \dot{\mathbf{q}} \quad (1)$$

In our case, position and velocity constraints (*i.e.* task functions) are defined. A velocity constraint imposes that a particular velocity is followed by the time derivative of an expression  $\mathbf{g}(\mathbf{q})$ . Desired velocities  $\dot{\mathbf{y}}_d^o$  are computed as:

$$\dot{\mathbf{y}}_d^o = \mathbf{K}_p(\mathbf{y}_d - \mathbf{y}) \quad (2)$$

where  $(\mathbf{y}_d - \mathbf{y}) = \mathbf{e}$  (error) and  $\mathbf{y}_d$  and  $\mathbf{y}$  represent the desired and measured positions, respectively.  $\mathbf{K}_p$  (dimensions:  $[1/s]$ ) are the gains of the controller. A similar reasoning can be applied to inequalities, see [3].

\*This work was supported by the ATLAS project. The ATLAS project has received funding from the European Union's Horizon 2020 research and innovation programme under the Marie Skłodowska-Curie grant agreement No 813782.

**Forward and differential kinematics:** The task spatial relation is described by two mapping functions, the robot kinematics ( $cc$ ), and the distance function ( $dst$ ). These, combined and differentiated, provide the kinematics in function of ( $\mathbf{q}$ ):

$$\mathbf{d} = \mathbf{g}_{dst}(\mathbf{g}_{cc}) \quad (3)$$

$$\mathbf{J}(\mathbf{q}) = \mathbf{J}_{dst}(\mathbf{p}_c) \mathbf{J}_{cc}(\mathbf{q}) \quad (4)$$

where  $\mathbf{J}$  is the task Jacobian matrix, and  $\mathbf{p}_c$  denotes any node on the robot's bending segment backbone.

The catheter has three control variables  $\mathbf{q}$  from its three degrees of freedom (DoFs): the bending angle  $\theta$ , the bending direction angle  $\phi$  of the distal segment, and the insertion  $\rho$ .

$\mathbf{g}_{cc}(\mathbf{q})$  is characterized as the constant curvature kinematics (no external loads assumed), further discussed in [4]. The catheter's bending segment is thus modeled as a circular arc, with  $l$  as the arc length:

$$\mathbf{g}_{cc}(\mathbf{q}) = {}^G\xi_{\mathcal{B}} \begin{bmatrix} \frac{l \cos \phi (1 - \cos \theta)}{\theta} \\ \frac{l \sin \phi (1 - \cos \theta)}{\theta} \\ \frac{l \cos \theta}{\theta} \end{bmatrix} \quad (5)$$

${}^G\xi_{\mathcal{B}}$  denotes the orientation of frame  $\{\mathcal{B}\}$ , attached to the base ( $\mathbf{p}_b$ ) of the bending segment and in which the constant curvature kinematics are determined, with respect to the global reference frame  $\{\mathcal{G}\}$  (see fig. 1).

$\mathbf{g}_{dst}$  is the task-specific function mapping, formulated as follows:

$$\mathbf{g}_{dst}(\mathbf{p}_c) = \frac{\|(\mathbf{p}_c - \mathbf{p}_{cl}) \times \hat{\mathbf{u}}_{cl}\|}{\|\hat{\mathbf{u}}_{cl}\|} \quad (6)$$

where all elements are expressed in the global frame  $\{\mathcal{G}\}$  with  $\mathbf{p}_{cl}$  being a point on the approximated centerline  $cl$  and  $\hat{\mathbf{u}}_{cl}$  its direction vector ( $cl = \mathbf{p}_{cl} + \hat{\mathbf{u}}_{cl} t$ ,  $t \in \mathbb{R}$ ).

**QP-based continuum robot control strategy:** A QP optimization problem is formulated for deriving the control variables velocities  $\dot{\mathbf{q}}$  from desired output variations, considering different task functions:

$$\underset{\mathbf{x}}{\text{minimize}} \quad \mathbf{x}^T \mathbf{H} \mathbf{x} \quad (7a)$$

$$\text{subject to} \quad \mathbf{L}_b \leq \mathbf{A} \mathbf{x} \leq \mathbf{U}_b \quad (7b)$$

$$\mathbf{l}_b \leq \mathbf{x} \leq \mathbf{u}_b \quad (7c)$$

where  $\mathbf{x}$  denotes the vector  $[\dot{\mathbf{q}} \ \varepsilon]$  ( $\varepsilon$  is a vector of slack variables).  $\mathbf{H}$  is a diagonal matrix comprising both the control variables and the slack variables weights [3]. From eq. (1) and eq. (2), the robot's tasks, relative to the tip and mid-node (with their respective Jacobian matrices), are implemented in the QP algorithm (eq. (7b)) as position constraints (frame  $\{\mathcal{G}\}$ ):

$$\mathbf{J}(\mathbf{q}) \dot{\mathbf{q}} \sim \mathbf{K}_p \mathbf{e} + \varepsilon \quad \text{where } \sim \in \{=, \leq, \geq\} \quad (8)$$

**Task specification using constraints:** Three position and one velocity constraints, detailed in Table 1, are enforced so the catheter tip navigates in a user-defined safe zone while minimizing contact between the vessel and the catheter body.

**Table 1:** Implemented constraints overview. Note that constraints are divided into two priority levels: hard (higher priority) and soft (lower priority) [3].

# Constraint	Type	Target
1 – Tip safety	Hard inequality	$\mathbf{g}_{dst}(\mathbf{p}_t) \leq 6$ [mm]
2 – Tip towards centerline	Soft equality	$\mathbf{g}_{dst}(\mathbf{p}_t) = 0$ [mm]
3 – Mid-node towards centerline	Soft equality	$\mathbf{g}_{dst}(\mathbf{p}_n) = 0$ [mm]
4 – Forward insertion	Soft inequality	$\dot{\rho} \geq 1$ [mm/step]

**Experiment:** From the task specification, an experiment was carried out in which, during insertion, the measured distances,  $\mathbf{d}_t$  and  $\mathbf{d}_n$ , of the catheter tip and mid-node from the centerline were recorded. Constraints 2, 3 and 4 (soft constraints) were given weighting factors of 0.6, 0.7 and 0.5, respectively.

## RESULTS

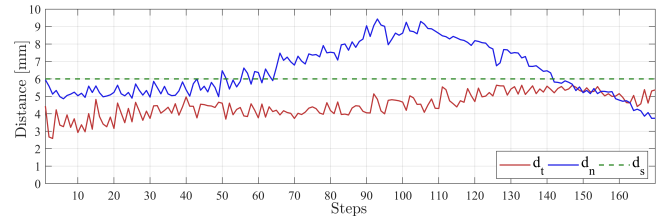


**Figure 2:** The graph shows the distances  $\mathbf{d}_t$  and  $\mathbf{d}_n$  as a function of the simulation steps considering the task specification.  $\mathbf{d}_s$  depicts the safe zone distance for the catheter's tip. The obtained results are relative to the initial section of the aortic model.

## CONCLUSION AND DISCUSSION

Overall, the controller demonstrated safe navigation and minimal contact between the vessel and the robot. The catheter tip was kept within the safe zone and the mid node of its distal segment showed no contact with the simulated environment (the aortic model is considered to have a radius of 16 mm). Having one active segment leads to a trade-off: one node's convergence to the centerline often translates into the other's divergence (fig. 2). The proposed task specification was successfully verified.

## REFERENCES

- [1] E. Rijanto, A. Sugiharto, S. Utomo, R. Rahmayanti, H. Afrisal, and T. Nanayakkara, "Trends in robot assisted endovascular catheterization technology: A review," in *2017 International Conference on Robotics, Biomimetics, and Intelligent Computational Systems (Robionet-ics)*, 2017, pp. 34–41.
- [2] M. T. Chikhaoui and J. Burgner-Kahrs, "Control of continuum robots for medical applications: State of the art," in *ACTUATOR 2018; 16th International Conference on New Actuators*, 2018, pp. 1–11.
- [3] E. Aertbeliën and J. De Schutter, "Etsl/etc: A constraint-based task specification language and robot controller using expression graphs," in *2014 IEEE/RSJ International Conference on Intelligent Robots and Systems*, 2014, pp. 1540–1546.
- [4] T. Mahl, A. Hildebrandt, and O. Sawodny, "A variable curvature continuum kinematics for kinematic control of the bionic handling assistant," *IEEE Transactions on Robotics*, vol. 30, no. 4, pp. 935–949, 2014.

# Statistical Shape Modelling of the Human Nasal Cavity and Maxillary Sinus for Minimally Invasive Surgery

Kenan Niu<sup>1\*</sup>, Julie Legrand<sup>1\*</sup>, Laura Van Gerven<sup>2</sup>, Emmanuel Vander Poorten<sup>1</sup>

<sup>1</sup>Robot-Assisted Surgery Group, Mechanical department, KU Leuven, Belgium

<sup>2</sup>Head Neck Surgery, Department of Otorhinolaryngology, University Hospitals Leuven, Belgium

\*these authors contributed equally to this work and should be both considered as first author

[kenan.niu@kuleuven.be](mailto:kenan.niu@kuleuven.be)

## INTRODUCTION

Sinus surgery is a procedure to open the pathways of the sinuses or restore pathological changes inside sinuses, such as inverted papilloma, fungus balls or carcinoma. Currently, rigid surgical instruments are widely used by surgeons. Given the complex anatomical structures, it is often highly challenging to target certain anatomical spots in a confined space, for example the anterior or lateral walls of the maxillary sinus. In some more complex cases, the surgeon needs to resort to open surgery. Due to the nature of anatomical structures of the nasal cavity and maxillary sinus, a large curve is always present in the expected surgical trajectory to reach the maxillary sinus (Fig 1). Therefore, it reveals that a flexible surgical instrument is necessary to perform sinus surgery under a minimally invasive manner, especially for the maxillary sinus. Before inserting surgical instruments into the maxillary sinus, an antrostomy is often performed by surgeon in order to create a passage to connect the maxillary sinus and the nasal cavity. In this context, the surgical instrument inserted from nostril is able to access the maxillary sinus. However, currently available design parameters are scarce. Most of them were obtained using conventional 2D measures in CT images, which resulted in large deviations from actual anatomical structures [1].

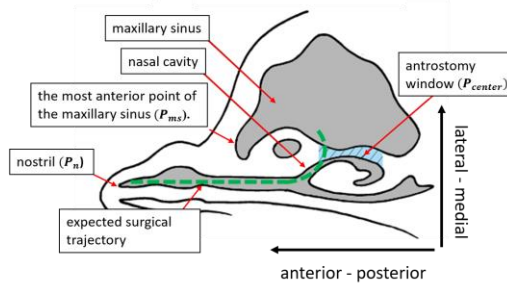


**Figure. 1.** The illustration of anatomical landmarks and structures in the nasal cavity and maxillary sinus.

Statistical shape model (SSM) have been widely used in medical image processing, such as image segmentation, registration and reconstruction [2]. Except describing the variations in image domain, SSM is also capable of describing geometrical variations and features from various shapes and anatomical structures. Therefore, SSM of the nasal cavity and maxillary sinus has great potential to derive geometrical variations for which the impacts of shape variations on the specifications of

flexible instrument can be investigated. However, to the authors' knowledge, there is few study that uses SSM to investigate the design parameters for surgical instruments, especially for the flexible instruments.

In this abstract, a statistical shape model of the nasal cavity and maxillary sinus was generated. Subsequently, a shape analysis was performed to derive essential design parameters from the established SSM. Preliminary results were reported demonstrating the capability of SSM to extract essential parameters which were hardly obtained from 2D measurements.

## MATERIALS AND METHODS

After obtaining ethical approval (S63078), CT scans were collected from 20 healthy subjects that had no experience of pathological history on the sinuses. The CT scans were acquired using a Cone Beam CT (VGI EVO, NewTom, Verona, Italy) with 0.25 mm x 0.25 mm pixel resolution in plane and slice thickness between 0.25 and 1 mm. The CT images were manually segmented using Mimics (20.0 version, Materialise, Leuven, Belgium) to get 3D surface meshes of the nasal cavity and maxillary sinus. Moreover, the antrostomy window was created deliberately during image segmentation. The segmented surface meshes were exported as STL files, resulting in 20 left side and 20 right side surface meshes. The surface meshes of right sinuses were mirrored to the left ones. Eventually, 40 surface meshes of left sinuses were obtained. To build a SSM using principal component analysis (PCA) [3], point correspondences need to be established by registering all surface meshes. To realize it, an arbitrary mesh was selected as the reference mesh. An elastic registration was performed to register the reference mesh to the rest of meshes [4], which resulted in the replicated meshes, termed point correspondence meshes (PCMs). Subsequently, SSM can be built by applying PCA on the vertices of all PCMs together with the reference mesh.

$$U = \bar{U} + b\Phi \quad (1)$$

Where  $U$  is a new shape instance and  $\bar{U}$  represents the mean shape.  $\Phi = (\phi_1, \phi_2 \dots \phi_t)$  is the matrix of the first  $t$  eigenvectors and  $b = (b_1, b_2 \dots b_t)$  is the vector that describes the weights of eigenvectors. The range of  $b$  is commonly limited to  $-3\sqrt{\lambda}$  to  $3\sqrt{\lambda}$ , where the variance of  $b$  equals to corresponding eigenvalue ( $\lambda$ ).

After establishing SSM, the impacts of shape variations on two important parameters were investigated, namely maximum bending angle (MBA) and outer-diameter of



flexible instrument. To calculate maximum bending angle, several landmarks were manually identified on SSM, such as nostril ( $P_n$ ), the most anterior point of the maxillary sinus ( $P_{ms}$ ). The rest of points were selected on the outer surface of the antrostomy window to locate the position of antrostomy window, termed  $P_{aw}$ . The center point of  $P_{aw}$  was calculated as  $P_{center}$  in Fig 1. The maximum bending angle can be estimated by calculating the intersection angle of two 3D vectors between  $\overrightarrow{P_n P_{center}}$  and  $\overrightarrow{P_{center} P_{ms}}$ .

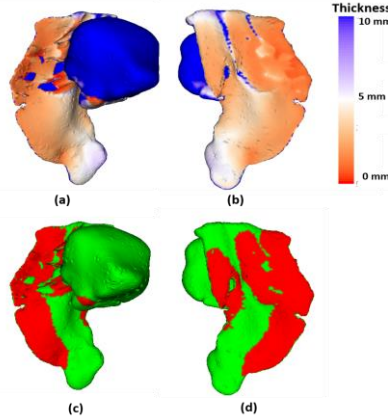


**Figure 2.** An example of nasal cavity width in a color map with different viewpoints in a and b, and a 3 mm threshold to distinguish areas: green ( $> 3$  mm) and red ( $< 3$  mm) (c and d).

The width of the nasal cavity constrains the outer diameter of the designed flexible instrument. To calculate it, the reverted normal vector on the surface mesh pointed to the inside of the nasal cavity. When a point was found on the opposite surface along the reverted normal vector, the distance between the found point and original triangle surface was calculated to represent the nasal cavity width in local area. To intuitively visualize the calculated widths, the data were mapped to a color map from orange (0 mm) to blue (10 mm). When taking 3 mm outer-diameter as an example, a threshold was set at 3 mm to map widths in two different colors: green regions representing the width is more than 3 mm; and red regions representing less than 3 mm width. In this context, green areas can be considered as a safe region for an instrument with less than 3 mm outer diameter.

Because all selected landmarks were selected from SSM, when various shape modes of SSM changed from  $-3\sqrt{\lambda}$  to  $3\sqrt{\lambda}$ , the positions of these points will be updated accordingly as well as the calculated design parameters. This feature provides a convenient way to explore defined design parameter. The mean and standard deviation (SD) of the absolute differences of the design parameters from various shape modes with respect to the data from the mean shape were reported.

## RESULTS

SSM was built from 40 surface meshes. The mean shape and first three shape modes were shown in Fig 3. The size of the maxillary sinus was scaled equally in the shape mode1. Shape mode2 mainly included the morphological changes vertically. Shape mode3 represented the morphological change horizontally. The extracted maximum bending angle was  $155.33^\circ$  for mean shape,

shown in Table 1. Except mode1, the rest modes caused at least 1 degree change in MBA. From nasal cavity width analysis results, for example, an outer-diameter 3 mm instrument could be considered in designing flexible instrument.

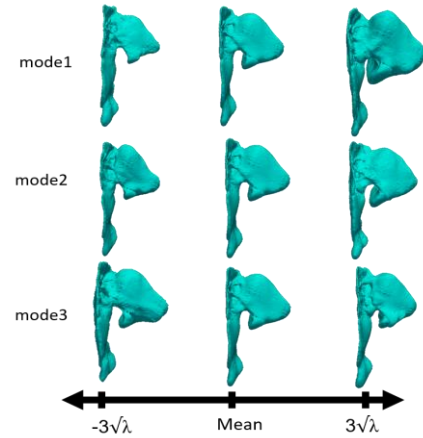


**Figure 3.** The visualization of the mean shape and the first three shape modes of the nasal cavity and maxillary sinus changing from  $-3\sqrt{\lambda}$  to  $3\sqrt{\lambda}$ .

**Table 1.** The extracted maximum bending angle (MBA) in the mean shape (MS) and the mean $\pm$ SD of absolute parameter differences between MS and the first three shape modes.

	MS	mode1	mode2	mode3
MBA( $^\circ$ )	155.33	$0.33 \pm 0.33$	$1.52 \pm 0.93$	$1.03 \pm 0.64$

## CONCLUSION AND DISCUSSION

A statistical shape model of the nasal cavity and maxillary sinus has been established to derive quantitative design parameters for designing flexible instrument. This approach thus shows great potential to analyze the impact of designing flexible instrument in a confined 3D space. However, in this abstract, only two design parameters have been investigated from 20 CT data, which limit its generality in terms of age, race and gender. More design parameters and datasets will be investigated in the future, such as the length of rigid part from the nostril to antrostomy window, the sizes of antrostomy window and maxillary sinus. After exploring and covering more comprehensive design parameters, the proposed approach can be further developed for flexible instrument design in sinus surgery and potentially for other medical applications where complex anatomical structures are present in robot assisted minimally invasive surgery.

## REFERENCES

- [1] A. Souza *et al.*, "Anatomy of maxillary sinus and its ostium: A radiological study using computed tomography," *CHRSIMED J. Heal. Res.*, vol. 3, no. 1, p. 37, 2016.
- [2] T. Heimann *et al.*, "Statistical shape models for 3D medical image segmentation: A review," *Med. Image Anal.*, vol. 13, no. 4, pp. 543–563, Aug. 2009.
- [3] T. F. Cootes *et al.*, "Active shape models - their training and application," *Comput. Vis. Image Underst.*, vol. 61, no. 1, pp. 38–59, Jan. 1995.
- [4] F. Danckaers *et al.*, "Correspondence Preserving Elastic Surface Registration with Shape Model Prior," in *2014 22nd International Conference on Pattern Recognition*, 2014, pp. 2143–2148.

# Force-based Endoscope Positioning for Laparoscopic Sacrocolpopexy

J. De Smet <sup>1</sup>, E. Vander Poorten <sup>1</sup>, J. Deprest <sup>2</sup>

<sup>1</sup> KU Leuven, Department of Mechanical Engineering, Leuven, Belgium

<sup>2</sup> KU Leuven, Department of Development and Regeneration, Leuven, Belgium  
jef.desmet@kuleuven.be

## INTRODUCTION

During laparoscopic sacrocolpopexy (LSC) vaginal vault prolapse is repaired by suturing one side of a synthetic mesh between the vaginal cuff and/or cervix while stapling the other side to the anterior longitudinal ligament [1]. It is considered the preferred treatment for vaginal vault prolapse [2], with good (82.5 %) long-term subjective success rates [3]. However, technical difficulties such as the loss of haptic feedback, and non-ergonomic postures make it a long and stressful intervention [4].

To get a proper view on the vaginal vault, a laparoscopic assistant is asked by the surgeon to move back and forth between a number of fixed camera positions. Miscommunication between surgeon and assistant may lead to improper positioning of the endoscope and can further increase stress levels and surgery time. Therefore, LSC may benefit from a robotic camera assistant which can learn the required endoscope positions in advance, such that the view on the surgical site is correctly presented.

To ensure safe robotic endoscope positioning, this work presents a force-based *teach by demonstration* algorithm to assist the surgeon during LSC.

## METHODS

The controller has six states: *idle*, *resetting*, *teaching*, *processing*, *initiating* and *copying*. For brevity, only the *teaching*, *processing* and *copying* states are discussed here.

### Teaching and Processing

During the *teaching* state the user guides the end-effector in operational space while recording its end-effector pose  $T$  and twist  $t$  with respect to the world frame at a frequency of 1 kHz. The recorded data is stored in a *bag* file.

The *processing* state reads the *bag* file and reduces the amount of data samples. It iterates over the recorded pose samples while calculating the difference between consecutive positions  $\Delta p_i = \|p_i - p_{i-1}\|$  and rotation matrix derived *Euler angles*  $\Delta \epsilon_i = \|\epsilon_i - \epsilon_{i-1}\|$ . When

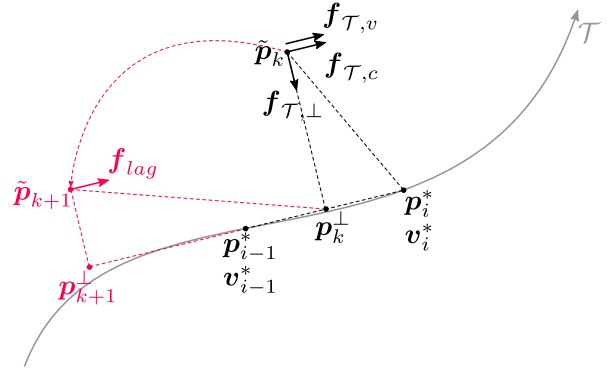


Figure 1: The copying state of the teach by demonstration controller.

either  $\Delta p$  or  $\Delta \epsilon$  exceed a specified threshold, 1 mm or 0.01 rad respectively, the pose sample  $T_i$  is saved along with its corresponding twist sample  $t_i$ . The set of processed data is called the trajectory  $\mathcal{T}$ :

$$\mathcal{T} = \{(T, t) \mid \Delta p \geq 0.001 \vee \Delta \epsilon \geq 0.01\}. \quad (1)$$

### Copying

After processing, the robot can start copying the trajectory. Both recorded pose and twist are used to enhance the quality of the copied trajectory. Figure 1 shows the copying state for the force components of the controller's output wrench  $w_{copy}$ .

Consider two sets of consecutive samples

$$\left. \begin{array}{l} \text{position: } p_i^*, p_{i-1}^* \\ \text{linear velocity: } v_i^*, v_{i-1}^* \end{array} \right\} \in \mathcal{T}, \quad (2)$$

the measured current position  $\tilde{p}_k$  and its projection  $p_k^\perp$  on  $\overrightarrow{p_{i-1}^* p_i^*}$ . A constant force  $f_{\mathcal{T},c}$  towards the current desired position  $p_i^*$  is calculated as:

$$f_{\mathcal{T},c} = \frac{p_i^* - p_k^\perp}{\|p_i^* - p_k^\perp\|} c. \quad (3)$$

Where  $c$  is a constant value. In the current implementation it is set to 1.5, which is enough to overcome tro-

car friction while keeping forces low enough to ensure safety.

Besides a constant force along  $\mathcal{T}$ , one would also like to compensate for disturbances that possibly move the end-effector away from the trajectory. Therefore, a force  $f_{\mathcal{T},\perp}$  is added which moves the end-effector towards  $\mathcal{T}$ :

$$f_{\mathcal{T},\perp} = K_{\perp} \left( (p_i^* - \tilde{p}_k) - (p_i^* - p_k^{\perp}) \right). \quad (4)$$

The diagonal values of  $K_{\perp}$  ( $3 \times 3$ ) are currently set to  $200 \text{ Nm}^{-1}$  which is fairly stiff.

To cope with the variation in speed, a velocity-based force component  $f_{\mathcal{T},v}$  is added to the summation:

$$f_{\mathcal{T},v} = K_v v_i^*. \quad (5)$$

Lastly, since the stiffness along the trajectory ( $f_{\mathcal{T},c} + f_{\mathcal{T},v}$ ) is quite low, it is easy to push back the end-effector by a significant distance. To avoid lagging too much behind, an additional force component  $f_{lag}$  is added. This component tries to align the end-effector with the furthest progressed position along the trajectory. I.e. a variable  $p_{k,max}^{\perp} = p_k^{\perp}$  is assigned every time  $p_k^{\perp} > p_{k,max}^{\perp}$ . Figure 1 shows this for position sample  $\tilde{p}_{k+1}$  which is pushed back past the previous desired position  $p_{i-1}^*$ . The additional force is calculated as:

$$f_{lag} = K_{lag} (p_{k,max}^{\perp} - p_{k+1}^{\perp}). \quad (6)$$

$K_{lag}$  is the ( $3 \times 3$ ) diagonal stiffness matrix for lagging compensation and can be set to similar values as  $K_{\perp}$ .

As a result, the total force acting on the end-effector during the copying state is:

$$f_{copy} = f_{\mathcal{T},c} + f_{\mathcal{T},\perp} + f_{\mathcal{T},v} + f_{lag}. \quad (7)$$

The rotational errors are compensated analogously:

$$m_{copy} = m_{\mathcal{T},c} + m_{\mathcal{T},\perp} + m_{\mathcal{T},v} + m_{lag}. \quad (8)$$

Resulting in the wrench:

$$w_{copy} = \begin{bmatrix} f_{copy} \\ m_{copy} \end{bmatrix}. \quad (9)$$

## RESULTS AND DISCUSSION

Figure 2a shows the teached and copied trajectory. The backdrivable robot (Virtuose 6D, Haption) was pushed away by hand to illustrate its off-trajectory behaviour. The combination of low-force behaviour along  $\mathcal{T}$  and stiff corrections when pushed off-trajectory allows for safe and flexible movement between desired endoscope positions during LSC. Figure 2b shows the error between the teached and copied trajectory. When no disturbance is applied, the mean error and standard deviation are 3 mm and 4 mm. A maximum error of 91 mm is observed after applying the disturbance force. By tuning the controller's parameters, the algorithm can be adapted for use in a variety of other surgical environments.

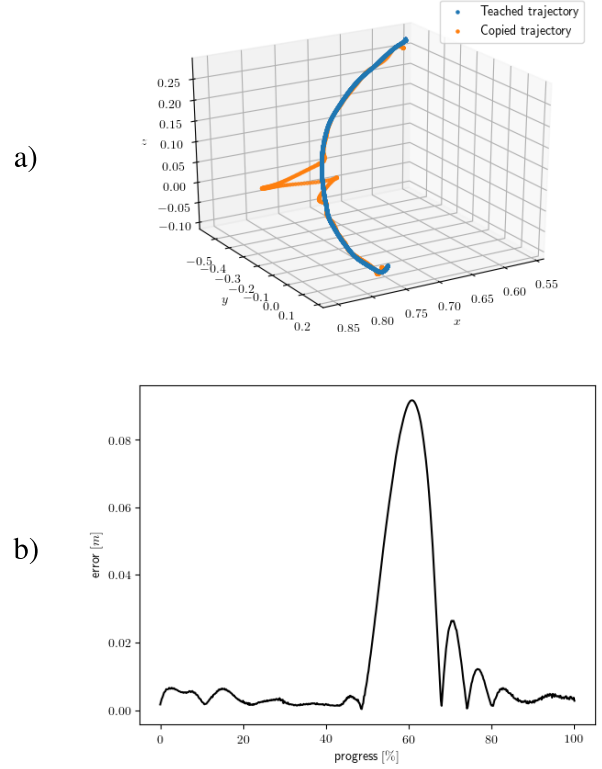


Figure 2: a) Teached and copied trajectory with disturbance applied by hand. b) Error between the teached and copied trajectory.

## REFERENCES

- [1] B. Haylen et al., “An International Urogynecological Association (IUGA) / International Continence Society (ICS) joint report on the terminology for female pelvic organ prolapse (POP),” 2016.
- [2] O. Gluck, M. Blagance, N. Veit-Rubin, C. Phillips, J. Deprest, B. O’reilly, I. But, R. Moore, S. Jeffery, J. M. Haddad, and B. Deval, “Laparoscopic sacrocolpopexy: A comprehensive literature review on current practice,” *European Journal of Obstetrics and Gynecology and Reproductive Biology*, vol. 245, pp. 94 – 101, feb 2020.
- [3] S. Pacqu e, K. Nawapun, F. Claerhout, E. Werbr uck, J. Veldman, A. Dhoore, J. Wyndaele, J. Verguts, D. De Ridder, and J. Deprest, “Long-Term Assessment of a Prospective Cohort of Patients Undergoing Laparoscopic Sacrocolpopexy,” *Obstetrics and gynecology*, vol. 134, pp. 323–332, aug 2019.
- [4] A. Park et al., “Patients Benefit While Surgeons Suffer: An Impending Epidemic,” 2010.

# Vision-guided Autonomous Robotic Electrical Bio-Impedance Scanning System for Abnormal Tissue Detection and Tracking

Zhuoqi Cheng, Veronica Penza, Jesús Ortiz, Darwin G. Caldwell, Leonardo S. Mattos

*Biomedical Robotics Lab, Advanced Robotics, Istituto Italiano di Tecnologia, Genova, Italy*

*{zhuoqi.cheng, veronica.penza}@iit.it*

## INTRODUCTION

In cancer surgery, correct localization of cancerous tissue is critical for the success of the surgery [1]. Specifically, it requires to remove the malignant tissue completely while preserving the maximum amount of healthy tissue. Robotic Minimally Invasive Surgery (RMIS) nowadays is widely used for cancer surgery and it brings significant benefits to both patients and surgeons. However, surgeons are still suffering from the limited availability of sensing capability for accessing tumor margin intra-operatively during RMIS. For instance, haptic sensing, which is commonly used in open surgery, cannot be used for discriminating healthy and cancerous tissue in this case. Therefore, there is a significant need for new sensing methods for RMIS.

Because of different cell compositions and cell organizations, the electrical bio-impedance characteristics can be very different among different tissue types, and also between healthy and pathological status of the same tissue type [2]. Consequently, this physical property can be used to discriminate different types of tissues and pathological conditions.

This paper proposes a vision-guided system for autonomous Electric Bio-Impedance (EBI) scanning in RMIS, aiming to acquire information for discriminating cancerous from healthy tissue intra-operatively, and to visualize the resulting impedance map on the endoscopic image using Augmented Reality (AR).

## MATERIALS AND METHODS

The system includes computer vision algorithms (tissue surface 3D reconstruction and tracking) and a high-level robot control interface for selecting the EBI scanning area directly on the endoscopic view. A monopolar forceps is fixed to the end-effector of a Panda robotic arm with its electrode connected to the EBI sensor. The EBI of the targeted tissue can be measured between the tip of the forceps and a reference electrode made from copper foil (70×40 mm), placed below the tissue.

The user is first required to use a standard computer interface device (mouse or tablet) to select the target area to be scanned on the endoscopic video image. A 2D triangular deformable mesh is created on the selected area [3] and tissue surface 3D reconstruction is done using a dense stereo-matching reconstruction algorithm [4]. Then, a set of 3D points  $p_i$  corresponding to the user-defined 2D mesh vertices are extracted.

Subsequently, the robot autonomously positions the EBI forceps on all  $p_i$  points based on the initial registration of the 2D mesh. It first places the tip of the forceps 15 mm above each target point, which is set as a safety distance to compensate for possible errors in the 3D reconstruction. Then, the robot arm slows down its speed and approaches  $p_i$ . When the tip of the forceps contacts the tissue, a change of EBI value under an empirically selected threshold is detected, and the robot starts to press the tissue for 2mm along the local tissue normal direction slowly. After the robot reaches the target depth, the system collects the EBI measurement [5] and then retracts the forceps along the same pressing direction for 15 mm.

Once measurement process is completed, the corresponding impedance value of each  $p_i$  is represented by a circle of a specific color selected according to the JET colormap. These 2D colored representations of measured impedance values are associated to the 2D mesh vertices. Then, the system automatically tracks tissue motions combining the 2D mesh with salient features tracking and a mass-spring-damper deformable model [4], adapting the impedance map in real time.

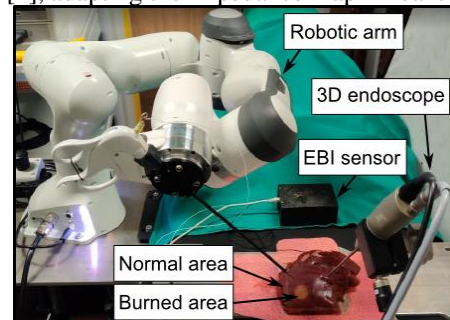


**Fig. 1** The setup of the proposed system.

In order to represent the AR information correctly and to control the robot with respect to the visual information, different calibrations are conducted. The calibration procedures include 3 steps: (i) stereo camera calibration, (ii) robot-forceps calibration, and (iii) camera-robot calibration. The error of the stereo camera calibration is 0.32 pixels, and the robot-forceps calibration error is 1.26 mm. Based on these calibrations, the camera-robot calibration can reach a high precision of 1.59 pixels.

In this study, a realistic experiment simulating a hepatic cancer resection surgery was conducted to demonstrate the effectiveness of the proposed system. As shown in Fig. 1, bovine liver was used, and a small area was



burned on the surface of the liver using a heating instrument in order to simulate abnormal tissue. When heating the tissue, the thermal effect caused different grades of protein denaturation in the area surrounding the heating point. In this case, the transition could realistically simulate the margin area between the tumor and normal tissue. In addition, the burned area could be easily seen since it was pink while the color of normal liver tissue was dark red.

During the experiment, the system was commanded to scan an area around the burned tissue autonomously, while the user only needed to select such area. Once the impedance map was obtained, the liver tissue was moved to evaluate the tracking system performance.

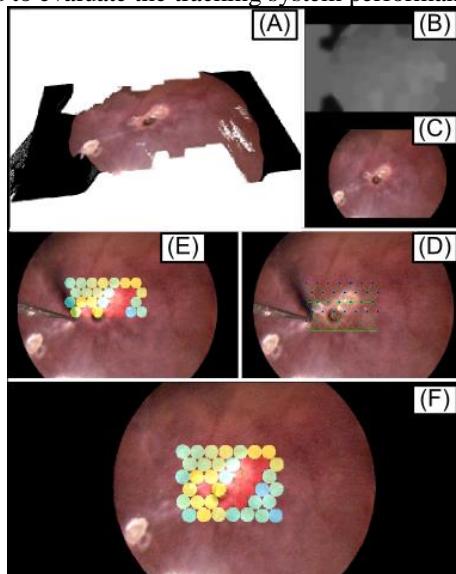


**Fig. 2** Experimental results: (A) liver surface 3D reconstruction; (B) disparity map; (C) rectified endoscope image; (D) the forceps was guided to measure EBI of the vertices on the mesh; (E) colored representation of the EBI measurement on rectified image; (F) the final scanning result.

## RESULTS

During the experiments, the vision system was demonstrated to perform the 3D reconstructions and generate the mesh successfully. As shown in Fig. 2(A), the 3D reconstruction was retrieved from the frame represented in Fig. 2(C). The corresponding disparity map is shown in Fig. 2(B). Given the target 3D points, the system could complete the EBI measurement on all the mesh vertices precisely (Fig. 2(D)). The EBI result was displayed in real time on the measurement position as shown in Fig. 2(E). The scanning area of Fig. 2 was about  $30 \times 30 \text{ mm}^2$ .

The overall precision of the system was calculated as the overlap between the correctly identified burned area (with an impedance value over a threshold) and the total burned area, manually segmented on the image. The precision was found to be 73%, indicating a good level of identification of the abnormal area.

The final scanning result is shown in Fig. 2(F), which has a clear position overlap with the normal tissue, abnormal tissue area and the transiting area. Moreover, a higher EBI value ( $3478.2 \pm 394.6 \Omega$ ) was detected in the

burned area, shown with red markers. A relatively lower EBI value ( $1743.1 \pm 443.2 \Omega$ ) was found in the transiting area and displayed in orange and yellow colors. Finally, the lowest EBI value ( $1429.1 \pm 336.4 \Omega$ ) was found in normal tissue where the markers were in blue and green. Furthermore, the system shows the capability of tracking the measured results in real time when the tissue was moving. In Fig. 3, we moved the tissue in two random positions during the experiment, and the results demonstrated that the system could track the mesh reliably even with small tissue deformation.

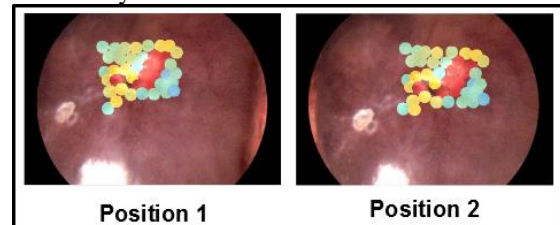


**Fig. 3** The tracking system could effectively track the measured results in real time when the tissue was moving after the scanning.

## DISCUSSION

The developed system effectively exploits a stereo vision system and a precise robotic arm to autonomously execute EBI scanning on tissue surfaces, aiming to assist surgeons in surgical margin assessment. The EBI sensing forceps press perpendicularly the tissue surface, obtaining the required measurements and tagging the tissue with AR markers to provide visual feedback to the user. In addition, the EBI results are associated to a deformable mesh tracking, allowing the tracking of the abnormal tissue. The experimental results demonstrate that the developed system can effectively measure, represent and track the EBI values of the tissues within a user-defined region of interest. In addition, the EBI scanning shows a gradual impedance change from the burned area to the normal area, which represents the transition area of tumor. This indicates a great potential of the system for assisting in determining resection margins. Future work will include an extended analysis of the system performance.

## REFERENCES

- [1] H. Gilles, et al. "Positive or close margins: reoperation rate and second conservative resection or total mastectomy?." *Cancer management and research* (2019).
- [2] Kalvøy, Håvard, et al. "Impedance-based tissue discrimination for needle guidance." *Physiological measurement* (2009).
- [3] Penza, Veronica, et al. "Hybrid Visual Servoing for Autonomous Robotic Laser Tattoo Removal." *2019 IEEE/RSJ International Conference on Intelligent Robots and Systems (IROS)*. IEEE, 2019.
- [4] Penza, Veronica, et al. "Dense soft tissue 3D reconstruction refined with super-pixel segmentation for robotic abdominal surgery." *International journal of computer assisted radiology and surgery* (2016): 197-206.
- [5] Cheng, Zhuoqi, et al. "SmartProbe: a bioimpedance sensing system for head and neck cancer tissue detection." *Physiological Measurement* (2020).

# Development of a resistive-based sensor for real time shape detection of a spring based flexible manipulator

S. K. Sahu<sup>1,2</sup>, I. Tamadon<sup>1,2</sup>, B. Rosa<sup>3</sup>, P. Renaud<sup>3</sup>, and A. Menciassi<sup>1,2</sup>

<sup>1</sup>The BioRobotics Institute, Scuola Superiore Sant'Anna, Pontedera, Italy

<sup>2</sup>Department of Excellence in Robotics & AI, Scuola Superiore Sant'Anna, Pontedera, Italy

<sup>3</sup>ICube, University of Strasbourg-CNRS-INSA, Strasbourg, France

[sujitkumar.sahu@santannapisa.it](mailto:sujitkumar.sahu@santannapisa.it)

## INTRODUCTION

Flexible robots can play a vital role in performing complex surgeries and diagnoses in minimally invasive procedures. Though they are good in adapting to various shapes, their control is difficult. Their flexibility creates uncertainty in their shape which may lead to damage of healthy tissues due to unwanted interactions. Therefore, the requirement of accurate and real time shape sensing is essential to achieve precise motion control of continuum manipulators. Image-based shape sensing [1] can suffer from the use of large radiation doses, dependence on nephrotoxic contrast agents, low resolution, and low signal-to-noise ratio. As an alternative, electromagnetic (EM) based shape sensing approaches are also used. Tully et al. [2] fused EM pose data with a kinematic model to reconstruct the shape of highly articulated snake robot. Song et al. [3] presented shape sensing of a flexible robot using the EM information from sensor and robot length. EM based methods have advantages like miniaturization, no obstruction of the line of sight, high sensitivity, etc. However, they suffer from disturbances due to presence of ferromagnetic material in the workspace. The tracking workspace is also limited on the EM field strength. To deal with these limitations, Sefati et al. [4] used a data driven method of regression modelling by taking information from Fiber Bragg Grating (FBG) sensors for shape reconstruction of a continuum manipulator. Liu et al. [5] used two modules, each consisting of three FBG nodes for shape sensing of continuum manipulators. These techniques show advantages such as fast response, miniaturization, high sensitivity, and negligible EM noise. However, their high cost and poor response to high strains limit their implementation in shape sensing. This paper presents the design of a flexible resistive shape sensor, fabricated by using a commercial conductive rubber, which is intended to detect the bending of a spring based mobile manipulator [6] using a constant curvature algorithm. The sensor shows several benefits in terms of cost, high elasticity, negligible electrical noise, freedom from high radiation doses, and large stretch-ability.

## MATERIALS AND METHODS

Reconstructing the shape of a flexible robot requires the estimation of arc parameters. A commercial conductive rubber of 2mm in diameter made of carbon infused rubber from adafruit industries (Product Id – 519, USA)

was cut into different lengths to be implemented as resistive sensor integrated in the spring based manipulator, available in the team [6]. Whenever the flexible manipulator bends, the length of the sensor changes and this in turn changes its resistance. Using this change in resistance, the arc parameters of the manipulator curvature can be estimated. The resistance of the material in relaxed state is 140-160 Ohm/cm, with a Young's Modulus  $E=11\text{MPa}$ . We assume that the sensor doesn't affect the performance of the manipulator because it imposes only an extra actuation force of 1.44% (difference between actuation force of the manipulator with and without sensor). In the next step, a prototype of 30mm length was prepared and used for hysteresis analyses. Using a Universal Testing Machine (Instron, Model-4464, Italy), tensile tests were performed and mechanical hysteresis was determined from the resulting stress-strain relationship. Since the manipulator we consider does not exceed 20% strain, the sample is also subjected to a 20% strain. We performed ten cycles to simulate multiple loading and unloading conditions, varying also the strain rates (10mm/min, 30mm/min, 50mm/min, 100mm/min and 200mm/min) to observe the effects on mechanical hysteresis behavior. A custom testbed was used for electrical characterization. 20% tensile strain, for one cycle and ten cycles, was applied on the sensor using a linear stage. The voltage across the sensor was measured using a DAQ system (NI USB-6259) while the sensor was connected to a DC voltage source through a voltage divider circuit. The voltage and strain data acquired were used for determining electrical hysteresis. Furthermore, one pre-stretched (5%) sensor was embedded on the periphery of the spring-based manipulator with the help of nine 3D printed holders. Five different bending deformations were applied manually by hand (figure 1) and voltage data was acquired at each deformation using the same voltage divider circuit. Finally, the relationship between voltage across the sensor and arc radii of manipulator generated manually was estimated by curve fitting a 3<sup>rd</sup> order polynomial. The unknown value of the arc radius can be estimated by acquiring the voltage data and using in the determined relationship.

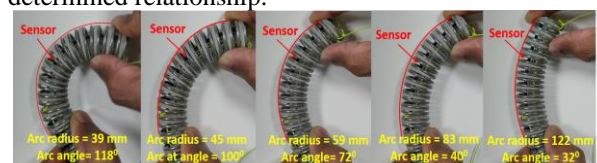


Figure 1: Bending deformations applied to the manipulator

## RESULTS

The mechanical hysteresis curve for the sensor is given in figure 2. To stretch the sample to 20% deformation, 2.7 MPa stress is required. In ten cycle experiments (figure 3) at different strain rates, mean hysteresis was found as 21% with standard deviation of 0.6%. The electrical hysteresis behavior of the sensor for single and multiple cycles can be seen from figure 4. The sensor produces 7.8% of voltage change for 20% elongation.

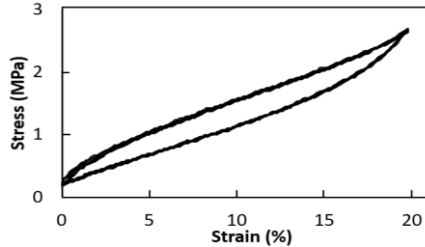


Figure 2 : Mechanical hysteresis for 10 cycles

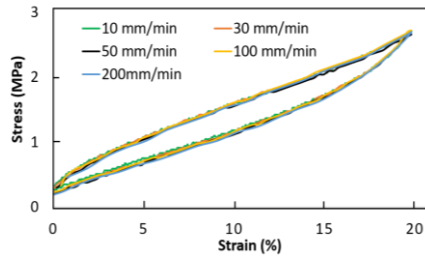


Figure 3 : Mechanical hysteresis at various strain rates

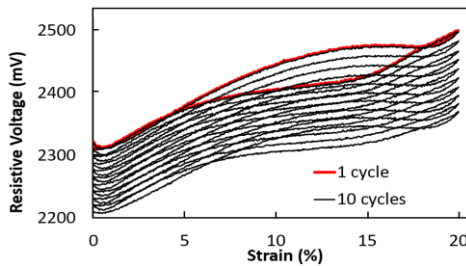


Figure 4 : Electrical hysteresis for 10 cycles

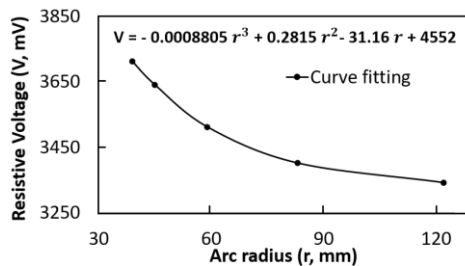


Figure 5 : Curve fitting and sensor calibration process

As discussed in the previous section, for sensor calibration the manipulator was bent into five different known radii manually (figure 1) and the voltage across the sensor was measured. The resulting voltage values were fitted into a third order polynomial with respect to arc radius as shown in figure 5. To verify the accuracy of this relationship generated, now four unknown bending deformations were applied to the manipulator manually and the voltage across the sensor was measured. The arc radius was estimated from the relationship shown in figure 5 and was compared to the arc radius calculated

geometrically (figure 6). Finally, the error in the arc radius estimation was found as 3% on average.

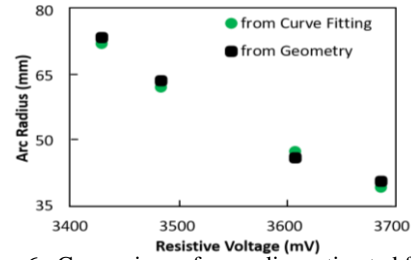


Figure 6 : Comparison of arc radius estimated from curve fitting and from geometry

## CONCLUSION AND DISCUSSION

In this paper we present the development of a flexible and stretchable resistive shape sensor using a commercial conductive rubber. The mechanical hysteresis curve is repetitive over 10 cycles. At higher strain rates, such as for 200 mm/min, the hysteresis behavior also remains nearly the same as for low strain rates such as 10mm/min and 30mm/min. In case of electrical characterization, it produces 7.8% voltage change for a deformation of 20%, which is enough to be measured. In successive loading cycles, the resistive voltage across the sensor reduces due to the presence of electrical hysteresis and delay in restoration of the original material behavior of the sensor after each cycle. This analysis of hysteresis can help to increase accuracy of the shape sensing methods. After characterization, the sensor is embedded into a spring-based manipulator and a relation between voltage across sensor and arc radius is determined by fitting a 3rd order polynomial. In future a constant curvature shape reconstruction algorithm will be implemented using three resistive sensors uniformly distributed across the periphery of the manipulator. The presented sensor could also be implemented in other systems such as cable driven manipulators using proper wiring management.

## REFERENCES

- [1] Hoffmann, M., et al. Semi-automatic catheter reconstruction from two views. MICCAI 2012. Springer.
- [2] Tully, S., et al. "Shape estimation for image-guided surgery with a highly articulated snake robot." 2011 IEEE/RSJ International Conference on Intelligent Robots and Systems
- [3] Song, S., et al., Real-time shape estimation for wire-driven flexible robots with multiple bending sections based on quadratic Bézier curves. IEEE Sensors Journal, 2015.
- [4] Sefati, S., et al. FBG-based position estimation of highly deformable continuum manipulators: Model-dependent vs. data-driven approaches. in 2019 ISMR.
- [5] Liu, H., et al., Shape Tracking of a Dexterous Continuum Manipulator Utilizing Two Large Deflection Shape Sensors. IEEE Sensors Journal, 2015.
- [6] Tamadon, Izadyar, et al. "Novel robotic approach for minimally invasive aortic heart valve surgery." IEEE EMBC 2018.

## ACKNOWLEDGEMENTS

This project has received funding from the European Union's Horizon 2020 research and innovation programme under the Marie Skłodowska-Curie grant agreement No 813782



# A fluid-driven mechanism for percutaneous needle insertion and fine-manipulation under image guidance

Lukas Lindenroth<sup>1</sup>, Agostino Stilli<sup>1</sup>, Saurabh Singh<sup>1,2</sup>, Steve Bandula<sup>1,2</sup>,  
Danail Stoyanov<sup>1</sup>

<sup>1</sup>Wellcome/EPSCRC Centre for Surgical and Interventional Sciences, University College London

<sup>2</sup> Interventional Oncology Service, University College London Hospital

*l.lindenroth@ucl.ac.uk*

## INTRODUCTION

Minimally-invasive image-guided interventions offer significant advantages over traditional surgical approaches for diagnosing and treating a variety of cancer types. The increasing number of procedures is enabled through advancements in real-time medical imaging and medical image computing. Such interventional procedures are commonly performed by clinicians inserting needle-shaped devices or probes into a patient's tumor. These procedures require skilled personnel as handling probes within the narrow bore of an MRI or CT scanner is considered highly challenging. Percutaneous needle insertion has become a prominent example for interventional procedures amongst robotics research due to its increased adoption in clinical workflows as well as its associated challenges for the operating clinician. To address such procedures, robotic systems have been developed which allow targeting and inserting probes and needles in a highly controlled manner [1]. Fluid-driven robotic systems can have significant advantages as motors and pumps can be placed away from the patient and outside the magnetic field in the case of MRI. He et al. have investigated the use of soft robotics technologies for MRI-guided needle guidance by creating a parallel inflatable mechanism [2]. In this work we present a novel design concept for a fluid-driven sliding mechanism which employs soft membranes to steer and drive a needle probe and discuss its preliminary characterization. While most state-of-the-art needle driving systems comprise of distinct mechanisms for clamping, inserting and steering the needle, the here-presented system combines these functions in a simple, easily-manufacturable and scalable mechanism which can retain MRI-compatibility.

## MATERIALS AND METHODS

The proposed system consists of a two-part mechanism, as shown in Fig. 1, which is based on inflatable actuation stages. Each stage is comprised of a rigid housing with three circumferentially-aligned bushings to allow for axial sliding motion via attached guiding rods, which is induced by an external hydraulic piston. The housing contains a central bore through which the needle can be fed as well as one or more flexible membranes to provide the desired contact with the needle, as shown in Fig. 1b). Whilst previous work has shown that such a membrane or bladder alone can be employed to efficiently provide

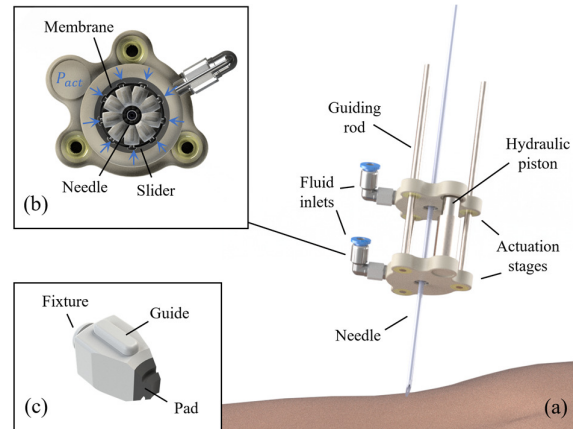


**Figure. 1** Overview of the fluid-driven needle insertion mechanism (a), with a cross-sectional view of an actuation stage with a single membrane (b) and a slider element (c)

directed forces on an inserted object, the small needle diameter hinders efficient actuation through a balloon alone due to the highly variable contact surface upon inflation. In the present design this is overcome by adding sliding elements linked to the membrane (Fig. 1c) which allow for efficient radial pressure transmission. The sliders are equipped with rubber tips to transmit occurring forces across the circumference of the needle and flexures to allow for needle tilting. Whilst a single, circumferential membrane equipped with radial sliders only actuates the clamping of the needle, directed motion in the plane of the actuation stage is achieved by sectioning the membrane and actuating the resulting sections individually. This not only allows translation of the needle, but also tilting when multiple actuation stages are combined.

To trial the viability of the proposed design, a finite element simulation study is carried out. Commercially-available FE software is employed (Ansys 19.0, ANSYS, Inc., USA) and static analyses are conducted for two-dimensional simplifications of the mechanism given a unit slice thickness (1m). Okamura et al. investigated forces typically occurring during biopsy needle insertion in the liver, yielding static forces up to 2.3N before puncture [3] which serves as reference measure for the here-presented design. Different elastic materials with varying Shore-A hardnesses are investigated for use in the deformable membrane (Dragon Skin™ 10, 20 and 30, Smooth-On Inc. USA). The silicone rubbers are modelled using a first-order Ogden formulation.



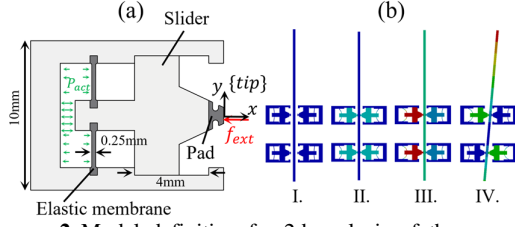


**Figure. 2** Model definition for 2d analysis of the proposed mechanism (a) and two-stage mechanism deformed results for initial deflated state b)-I., clamped state b)-II., translated state b)-III. and tilted state b)-IV.

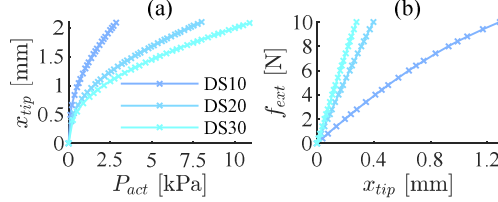


**Figure. 3** Slider displacement  $x_{tip}$  under actuation pressure  $P_{act}$  for different rubbers (a) and corresponding stiffness per unit thickness at 2mm extension under an external load  $f_{ext}$  (b)

Required model parameters have been fitted according to material data presented in prior research [4]. To determine the suitability of the design for the envisioned application, occurring slider motion for induced actuation pressures is investigated. Moreover, the effects of external forces are considered in steady state upon inflation. An overview of the model definition is shown in Fig. 2a).

The capabilities of a single stage to exert insertion forces are tested by inducing a clamping contact between two opposing sliders and an inserted needle under a defined actuation pressure (clamping force of approx. 15N) and inducing an axial displacement in the needle (0.3mm). The contact between pads and needle is modelled as static friction with a friction coefficient of 0.8.

Steering capabilities of two stages are investigated with a design which is comprised of two opposing inflatable membranes. An initial contact is provided between sliders and needle. Opposing sliders are actuated antagonistically in either opposite directions between both stages to achieve tilting of the needle or in parallel to enable planar translation motion. An overview of the investigated actuation configurations is provided in Fig. 2b).

## RESULTS

The response of an individual sliding element to a build-up of actuation pressure is shown in Fig. 3a). The local force-deflection response and hence stiffness of the slider at around 2mm extension is shown in Fig. 3b). For DS30 the stiffness per unit thickness of the system is substantially greater at 36.39N/mm compared to the DS10 and DS20 counterparts with 8.57N/mm and 25.63N/mm respectively. The contact behavior for an induced needle displacement is shown in Fig. 4. The simulation suggests an insertion force of approx. 10N before loss of contact.

The achievable motion of a two-stage system equipped with DS30 membranes is shown in Fig. 5. For a fixed

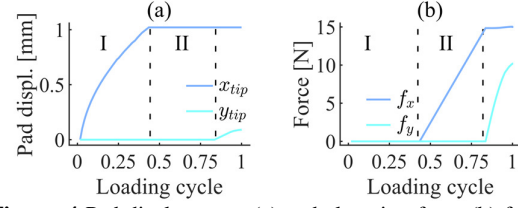


**Figure. 4** Pad displacement (a) and clamping force (b) for an induced needle sliding motion. The configuration of the system is indicated above the loading phase according to Fig. 2b).

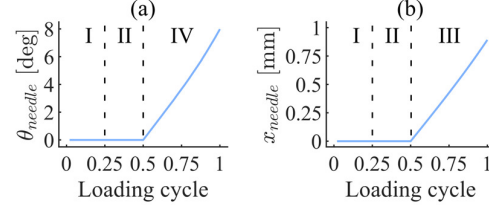


**Figure. 5** Induced needle motion in tilt  $\theta_{needle}$  (a) and planar translation  $x_{needle}$  (b). The configuration of the system is indicated above the loading phase according to Fig. 2b).

distance between the stages of 10mm and a housing bore diameter of 4mm the system reaches approx.  $\pm 8^\circ$  of tilt and  $\pm 0.83$ mm of planar translation can be achieved.

## CONCLUSION AND DISCUSSION

This work demonstrates the design of a novel needle driving system and a preliminary simulation-based feasibility study indicating the capabilities of the system. Despite the simplicity of the design, the 2d simplification of the mechanism indicates high system stiffness and driving forces. The results obtained at unit thickness suggest that a membrane of 6.3cm width could withstand the maximum force during insertion with only 1mm deflection. Additionally, mapping the obtained results for the needle insertion to two opposing semicircular membranes it can be anticipated that to achieve the required driving forces a circular membrane with a radius of  $\approx 8$ cm is required. Given the highly scalable design, miniaturization is possible by varying membrane thickness and material to increase stiffness further. The presented device could provide a viable solution for steering needles and other surgical instruments in confined spaces. Further investigations will be carried out into the fabrication of the system and a first physical prototype will be built and evaluated in the context of percutaneous needle insertion.

## REFERENCES

- [1] Tsekos, Nikolaos V., et al. "Magnetic resonance-compatible robotic and mechatronics systems for image-guided interventions and rehabilitation: a review study." Annual review of biomedical engineering 9 (2007).
- [2] Z. He et al., "Design of a Percutaneous MRI-Guided Needle Robot with Soft Fluid-Driven Actuator," IEEE Robot. Autom. Lett., vol. 5, no. 2, pp. 2100–2107, 2020.
- [3] Okamura, Allison M., et al. "Force modeling for needle insertion into soft tissue." IEEE transactions on biomedical engineering 51.10 (2004): 1707-1716.
- [4] Marechal, Luc, et al. "Toward a Common Framework and Database of Materials for Soft Robotics." Soft Robotics (2020).

# A Virtual Fetal Environment for TTTS Applications

A. Casella<sup>\*†</sup>, S. Moccia<sup>\*‡</sup>, F. Piccinotti<sup>\*</sup>, D. Paladini<sup>§</sup>

E. Frontoni<sup>‡</sup>, E. De Momi<sup>†</sup>, L. S. Mattos<sup>\*</sup>

<sup>\*</sup>Department of Advanced Robotics, Istituto Italiano di Tecnologia, Genoa, Italy

<sup>†</sup>Department of Electronics Information and Bioengineering, Politecnico di Milano, Milan, Italy

<sup>‡</sup>Department of Information Engineering, Università Politecnica delle Marche, Ancona, Italy

<sup>§</sup>Department of Fetal and Perinatal Medicine, Istituto “Giannina Gaslini”, Genoa, Italy

## INTRODUCTION

Twin-to-twin transfusion syndrome (TTTS) may occur during identical twin pregnancies when abnormal vascular anastomoses in the monochorionic placenta result in uneven blood flow between the fetuses. If not treated, the risk of perinatal mortality of one or both fetuses can exceed the 90% [1]. The most effective treatment to recover the blood flow balance is minimally invasive laser surgery in fetoscopy [2]. At the beginning of the surgical treatment, the surgeon identifies the inter-fetal membrane, which is used as a reference [3] to explore the placenta vascular network and identify vessels to be treated.

Limited field of view (FoV), poor visibility, high illumination variability, fetuses' movement, and limited maneuverability of the fetoscope make the membrane identification a challenging task. This results in increased surgery duration and risks of complications from the patients' side, as well as mental workload from the surgeons' side.

Recently, the Surgical Data Science (SDS) [4] community has focused more and more on developing mosaicking strategies to enhance surgeons' vision by extending the FoV. The literature approaches rely on instrument tracking or image analysis (i.e., no external hardware is required).

The work proposed by [5] integrates image processing with information on a fetoscope tip position, tracked by an electromagnetic tracker (EMT) to achieve rift-free mosaicking.

Among image analysis approaches, the first work proposed in [6] is based on the SIFT feature extractor for frame registration. Given the success of the deep learning techniques in vision tasks, researchers have exploited the potential of neural networks to extract features. In [7], a Siamese Network based on the VGG-16 backbone is proposed to extract vessel features combining region detection and stable image registration. In [8], the Lucas-Kanade algorithm was employed for frame registration of similar frames identified using bags of visual words based on VGG descriptors. The framework proposed in [9] uses a controlled data augmentation strategy and median outlier filter on estimated homography parameters for robust mosaicking. Most of the work in literature relies on a small dataset of fetoscopic images of the

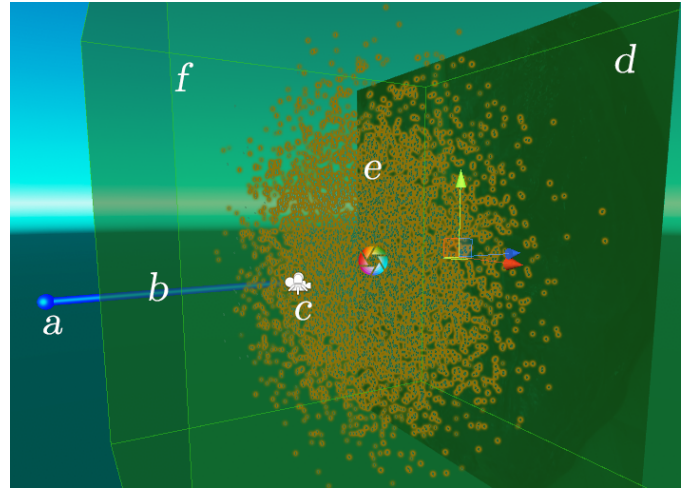


**Figure 1:** Overview of the scene elements in the virtual environment. *a* is the fulcrum of rotation of the instrument. On the tip of the sheath (*b*) the camera and a spot light (*c*) are attached. The ex-vivo placenta image is the texture of the image plane (*d*). The particle system (*e*) simulates the free-floating debris. All the elements are placed inside the amniotic volume *f*.

placenta acquired in-vivo (i.e., during the surgery), ex-vivo (i.e., using placentas removed after childbirth) or using phantoms.

The training and evaluation of deep learning approaches require ground truth data. Ground truth could be obtained by employing a fetoscope tracker, which, however, may not always be available. To overcome this limitation, we propose a virtual environment for simulated placenta exploration, starting from ex-vivo images. We implement the virtual environment on a modern 3D game development platform, offering the possibility to simulate all possible scenarios of fetoscopic images (e.g., different light conditions, amniotic fluid turbidity, insertion point, camera pose, and particle density).

## MATERIAL AND METHODS

In this preliminary study, our dataset is generated starting from three ex-vivo placenta images, acquired by clinicians right after TTTS surgery. The virtual environment can simulate both straight and 30 degrees fetoscope commonly used in TTTS surgery for the posterior and anterior placenta, respectively. An overview of the virtual

scene is shown in Fig. 1. The chosen ex-vivo placenta image is projected on the image plane (*d*).

The fetoscope sheath (*b*) is modeled as a cylinder rotating with respect to a fulcrum (i.e., the insertion point, *a*). At the tip of the sheath, a virtual camera and a light spot (*c*) simulates the fetoscope's fibers-optics. Camera and light parameters are qualitatively tuned to produce images as similar as possible to intra-operative TTTS video frames acquired in the clinical practice (in this work, 10 TTTS intra-operative videos are available for visual comparison).

The virtual fetoscope is immersed in the amniotic volume (*f*), modeled as a cube for simplicity. The cube is processed by a rendering pipeline to simulate the presence of the amniotic fluid. TTTS surgery is generally performed between the 16th and 25th weeks of pregnancy; in this period, the free-floating particulate is visible in the amniotic fluid. For this reason, we introduce a particle system (i.e., Unity module for the simulation of elementary particles, *e*) to simulate the particulate in the amniotic volume. Light intensity, amount of turbidity of the amniotic fluid, and particulate density can be changed during the simulation.

The virtual fetoscope can be moved to simulate different insertion points. After the operator has chosen the insertion point, the instrument can move freely or following a predefined trajectory through a keyboard. Other input controllers are allowed as well. During the free exploration, the user can start video capture and record the fetoscope's positions over time; it can be used later as a trajectory for further simulations or as an additional ground-truth datum. The user is provided with a small live reconstruction of the visited area at the bottom of the screen.

To experimentally evaluate the quality of the simulation, we decided to generate panorama using HomographyNet [10] trained on ex-vivo TTTS video frames generated with our environment. We chose this network given the promising results obtained in state of the art [9]. We computed the registration Root Mean Square Error (*RMSE*) [pixels] for each frame and compared to the ground-truth generated by the virtual environment to evaluate the panorama reconstruction quality.

## RESULTS AND DISCUSSION

The virtual environment enables us to acquire nine videos. Each one was acquired using one of the three ex-vivo placenta images in our dataset, different fetoscope trajectories (i.e., free, circular and spiral) and different configurations of the virtual environment (i.e., different light intensity, turbidity of the amniotic fluid, density of free particulate) for 120 seconds (750 frames at 25 fps).

Preliminary results using the HomographyNet trained model on simulated data achieved an average *RMSE* of 4.18 pixels. An example of the reconstructed panorama is shown in Fig. 2.

Future work will include an in-depth evaluation through clinician questionnaires. The virtual environment will be enriched implementing the following features: (i) optical



**Figure 2:** Example panorama reconstruction on video generated from virtual environment using HomographyNet [10].

distortion, (ii) placenta 3D models obtained from Magnetic Resonance Imaging (MRI) images, (iii) placenta texture generation using GAN networks with style-transfer, (iv) simulation of occlusions (e.g., fetuses) within the scene. The environment will be used to conduct further studies on more complex deep learning models for panorama reconstruction from in-vivo images.

## REFERENCES

- [1] A. Baschat, R. H. Chmait *et al.*, "Twin-to-twin transfusion syndrome (TTTS)," *Journal of Perinatal Medicine*, vol. 39, no. 2, 2011.
- [2] D. Roberts, J. P. Neilson *et al.*, "Interventions for the treatment of twin-twin transfusion syndrome," *Cochrane Database of Systematic Reviews*, vol. 2014, no. 1, 2014.
- [3] A. Casella, S. Moccia *et al.*, "Inter-foetus Membrane Segmentation for TTTS Using Adversarial Networks," *Annals of Biomedical Engineering*, vol. 48, no. 2, pp. 848–859, 2020.
- [4] L. Maier-Hein, S. S. Vedula *et al.*, "Surgical data science for next-generation interventions," *Nature Biomedical Engineering*, vol. 1, no. 9, pp. 691–696, 2017.
- [5] M. Tella-Amo, L. Peter *et al.*, "Pruning strategies for efficient online globally consistent mosaicking in fetoscopy," *Journal of Medical Imaging*, vol. 6, no. 03, p. 1, 2019.
- [6] P. Daga, F. Chadebecq *et al.*, "Real-time mosaicking of fetoscopic videos using {SIFT}," in *Medical Imaging: Image-Guided Procedures, Robotic Interventions, and Modeling*, R. J. Webster and Z. R. Yaniv, Eds. SPIE, 2016.
- [7] F. Gaisser, S. H. P. Peeters *et al.*, "Stable image registration for in-vivo fetoscopic panorama reconstruction," *Journal of Imaging*, vol. 4, no. 1, 2018.
- [8] L. Peter, M. Tella-Amo *et al.*, "Retrieval and registration of long-range overlapping frames for scalable mosaicking of in vivo fetoscopy," *International Journal of Computer Assisted Radiology and Surgery*, vol. 13, no. 5, pp. 713–720, 2018.
- [9] S. Bano, F. Vasconcelos *et al.*, "Deep sequential mosaicking of fetoscopic videos," in *International Conference on Medical Image Computing and Computer-Assisted Intervention*. Springer, 2019, pp. 311–319.
- [10] D. DeTone, T. Malisiewicz, and A. Rabinovich, "Deep image homography estimation," 2016.



# SmartProbe: an EBI sensing system for head and neck cancer tissue detection

Z. Cheng<sup>1</sup>, A. L. C. Carobbio<sup>2,3</sup>, L. Soggiu<sup>1</sup>, M. Migliorini<sup>1</sup>, L. Guastini<sup>2,3</sup>, F. Mora<sup>2,3</sup>, M. Fragale<sup>2,3</sup>, A. Ascoli<sup>2,3</sup>, S. Africano<sup>2,3</sup>, D. G. Caldwell<sup>1</sup>, F. R. M. Canevari<sup>2,3</sup>, G. Parrinello<sup>3</sup>, G. Peretti<sup>2,3</sup>, L. S. Mattos<sup>1</sup>

<sup>1</sup>Department of Advanced Robotics, Istituto Italiano di Tecnologia, Genova, Italy,

<sup>2</sup>Unit of Otorhinolaryngology – Head and Neck Surgery, University of Genoa, Genova, Italy

<sup>3</sup>IRCCS Policlinico San Martino, Genova, Italy

## INTRODUCTION

Head and neck squamous cell carcinomas (HNSCCs) are the sixth most common malignancy worldwide, accounting for over 500,000 new cases annually. In addition, it has been reported to result in a high mortality rate of approximately 1%–2% among tumor deaths, and approximately 10% of the patients die within six months after diagnosed. Traditional assessment of HNSCC is done under conventional examination (COE) or endoscopic bright white light (BWL). Since the morphological characteristics of SCCs under COE or BWL can be subtle and potentially confused with benign pathologies, especially in the early stages, biopsy is required on all the suspicious lesions for histopathological diagnosis. However, malignant tissues are known to present altered packing density and orientation of its cells, which also present increased water and mineral content and different membrane permeability than normal cells. Consequently, their electrical characteristics are significantly different from those of healthy tissue. Therefore, Electrical Bioimpedance (EBI) sensing can be an effective method for on-line cancer detection. In this study, we present the design and evaluation of SmartProbe [1], a needle-based EBI sensor device for the accurate identification of cancerous tissues in-vivo.

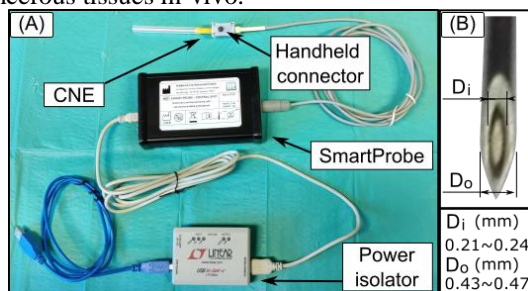


**Figure. 1.** The SmartProbe system.

## MATERIALS AND METHODS

The SmartProbe [1] was created and certified for clinical studies on the bioimpedance characteristics of both pathologic and healthy tissues from the head and neck region. As shown in Fig. 1(A), the SmartProbe system includes three main components: a data acquisition and processing unit, a handheld connector, and a power isolator. A disposable Concentric Needle Electrode (CNE) is directly connected to the handheld connector

for use. A pushbutton on the handheld connector allows the user to trigger the data collection process. The SmartProbe device integrates a microcontroller and a high precision impedance converter based on AD5933. The microcontroller controls the impedance converter and transfers the data to a connected computer for on-line visualization, storage and post-processing. The power isolator is required due to safety considerations since the system is designed for in-vivo use.

When the CNE is inserted into biological tissue, the tissue forms a frequency-dependent electrical load on its tip, including the impedance of the contacting material under test ( $Z_{MUT}$ ) and the electrode polarization impedance ( $Z_{EPI}$ ). Using the measured impedance values directly for tissue identification can have a relatively low accuracy considering the electrode polarization effect  $Z_{EPI}$  and the manufacturing tolerance of the CNE's inner diameter  $D_i$  and outer diameter  $D_o$  (Fig. 1(B)). The ideal calibration procedure requires the measurement with every CNE on different concentrations of saline solutions to remove this bias. This is time consuming and tedious. Therefore, a new calibration method is proposed in this study allowing the operator to calibrate each CNE with only one saline solution of known conductivity.

The proposed calibration process is based on statistical learning of training datasets measured on different concentrations of saline solutions. Each dataset is constructed by a series of impedance values measured from different saline solutions with known conductivity. These impedance values are measured using the same excitation frequencies, but different CNEs. Subsequently, principal components (PCs) of the covariance matrix for each dataset are calculated. Since the first PC can capture the maximum linear correlations between the features, the measured values of a new CNE can be calibrated by simply measuring one of the above saline solutions, and project this value to PC1 for obtaining the other estimated values. Furthermore, this allows computing the relationship between the material conductivity  $\sigma$  and the measured impedance value  $|Z|$ .

To evaluate the proposed calibration method, 40 CNEs were randomly selected, and three repeated measurements were performed for each needle in 6 different saline solutions (0.1% to 0.6% concentrations, 2 to 11 mS/cm). Subsequently, an experimental evaluation of SmartProbe was performed on different freshly excised ex-vivo human tissues from the head and



neck region, including both cancerous and healthy tissues. The experimental setup was installed in the operating room of Department of Otorhinolaryngology and Head and Neck surgery (San Martino Hospital, Genoa, Italy). For each patient, the practitioner first opened a new CNE and plugged it to the handheld connector. Then, calibration in a 0.4% saline solution was performed. Finally, SmartProbe was used for collecting the impedance value of tissues, recording them on a database. After the tissue was resected from the body, the practitioner first checked the tissue type and its pathologic status. Then the practitioner noted down the tissue location and features under measurement, and then the bioimpedance data was collected. The practitioner repeated the data collection 3 times at each measurement site, which were marked with colored ink for subsequent detailed histopathological examination. Once the histological report was generated, the pathologic status of all data collected was recorded on the database. The data was processed by calculating the conductivity of the measured tissue using the described calibration method. Both conductivity and phase angle information were used for tissue classification. A descriptive statistic based on principal component analysis (PCA) was used to reduce the dimensionality of the data. Furthermore, statistical analysis was performed on the 2D results (one dimension of conductivity and one dimension of phase) for classification between pathologic and normal tissues.

## RESULTS

The results of saline solution measurements in each excitation frequency were grouped as a dataset, and the PCs of every dataset were calculated. We retained only the maximum PC as a model for reconstructing the function  $|Z_S| = f(\sigma)$  for the CNE since its contribution was more than 90% in all the cases. Subsequently, the reconstruction accuracy of the calibration method was evaluated by comparing the reconstructed value  $|Z_S^*|$  and the actual measured value  $|Z_S|$ . In this study, 0.4% saline solution was chosen for the model reconstruction, since it was found to have the average lowest error ( $< 6\%$ ). This error rate is low enough for this application since the EBI differences between tissue's pathological and healthy status are generally much bigger.

The preliminary results of 10 patients are presented here, which includes four types of tissues from the head and neck region: muscle, mucosa, cartilage and salivary gland. In total, 586 data were collected, and each data includes 10 impedance modules  $|Z_i|$  and 10 phase angles  $\theta$  at 10 excitation frequencies from 10kHz to 100kHz. Except from 113 data whose pathologic status were not confirmed by the histologic report, the rest of the data were categorized according to the tissue type and pathologic status. The mean values and the standard deviation in different categories are shown in Fig. 2. In addition, the PCA method was applied for reducing the data dimension of both  $\sigma$  and  $\theta$ , resulting in one dimension of conductivity PCA( $\sigma$ ) and one dimension of phase PCA( $\theta$ ). Welch t-test was conducted to evaluate the statistical significance between pathological and

normal statuses of the same tissue type. The results demonstrated that the tissue status of cartilage (p-value = 0.018), muscle (p-value =  $1.6e-12$ ), and mucosa (p-value =  $2.5e-5$ ) can be successfully classified. However, it can be difficult to identify whether it is cancerous or not for the salivary gland tissue (p-value = 0.47).

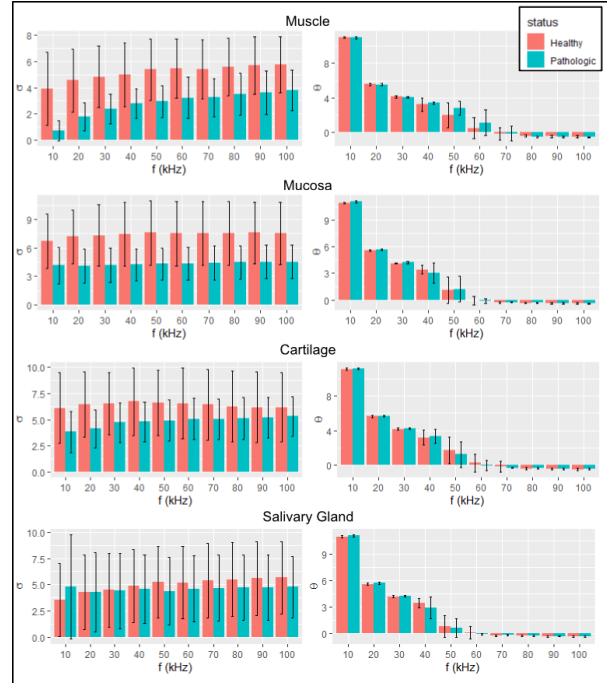


**Figure 2.** The  $\sigma$  (mS/cm) and  $\theta$  (rad) of four types of ex vivo human tissues in both pathologic status and healthy status.

## CONCLUSION AND DISCUSSION

This study presented SmartProbe, an EBI sensing system based on a CNE for in vivo on-line cancer detection. Considering the uncertainties in EBI measurements due to the CNE manufacturing tolerances and electrode polarization impedance, we proposed a calibration method based on statistical learning. In addition, an ex-vivo experiment was conducted for evaluating the system's capability to detect cancerous tissue. Four types of ex-vivo human tissues from the head and neck region, including both cancer and surrounding healthy tissue, were characterized using SmartProbe. The measured data was processed using dimensionality reduction and analyzed for tissue classification. The results show significant differences between pathologic and healthy tissues in muscle, mucosa and cartilage specimens based on their electrical property. These promising results indicate a great potential of SmartProbe in various cancer detection for in-vivo office-based assessments during routine consultations, and for intra-operative assessment of resection margins during surgical procedures. Future work will conduct the measurements with extended frequency range, potentially improving the detection capability for difficult tissue type such as salivary gland.

## REFERENCES

- [1] Cheng, Zhuoqi, *et al.* "SmartProbe: a bioimpedance sensing system for head and neck cancer tissue detection." *Physiological Measurement* (2020).

# Systems-Theoretic Process Analysis applied as a socio-technical safety analysis to support future fetoscope design

A. Adriaensen<sup>1</sup>, E. Reynaert<sup>1</sup>, M.A. Ahmad<sup>1</sup>, M. Ourak<sup>1</sup>, J. Deprest<sup>2</sup>, E. Vander Poorten<sup>1</sup>, L. Pintelon<sup>1</sup>

<sup>1</sup>*KU Leuven, Department of Mechanical Engineering, Celestijnenlaan 300, Leuven, Belgium,*

<sup>2</sup>*University Hospitals Leuven, Obstetrics & Gynecology, Leuven, Belgium  
arie.adriaensen@kuleuven.be*

## INTRODUCTION

Successful surgical interventions depend on the interaction of surgeons with medical teams, technical artefacts, organizational challenges and dynamic patient conditions. The dominant paradigm in industrial and healthcare safety management is based on root-cause thinking for accident analysis and energy-barrier thinking for subsequent safety mitigation. These two segments of the safety analysis are inherently based on a linear cause-effect reasoning [1]. Such sequential assumptions have received critique for not adequately describing the underlying complexity and dynamics of healthcare settings [1-2]. Therefore, non-linear safety analysis techniques like the Functional Resonance Analysis method (FRAM) and the Systems-Theoretic Process Analysis (STPA) gain importance [1-2]. They are both based on a systems-thinking approach of work systems. STPA is a hazard and risk analysis technique that belongs to a systemic causation model, called System Theoretic Accident Model and Processes (STAMP) [2]. The STPA technique treats safety as a dynamic control problem rather than an individual component failure. In our study, STPA is applied to a socio-technical work analysis of fetoscopic surgery during twin-to-twin transfusion syndrome (TTTS). TTTS is a severe complication of monochorionic twin pregnancies, characterized by the development of unbalanced chronic blood transfer from one twin, to the other through placental anastomoses [3]. We suggest using STPA to complement the knowledge about the TTTS surgical procedure from the perspective of engineers that are involved in design iterations of novel fetoscopic systems on the one hand with the expert knowledge provided by expert fetal surgeons on the other hand. Such comparison is also known as a Work-as-Imagined (WAI, here thus imagined by the engineers) vs. Work-as-Done (WAD, provided by the surgeons' practical expertise) [1]. This approach maximally takes into account the challenges experienced during the surgical procedure and transforms those into a methodical design aid to support the development of future fetoscope designs and design iterations. The analysis also provides systematic WAD knowledge transfer from surgeons to engineers. STPA has recently gained attention in relation to healthcare safety research

[4-5], which included a WAD perspective, although not explicitly labeled as such.

## MATERIALS AND METHODS

Data was gathered from 4 engineers (19 hours of interviews), whereas the WAD perspective was provided by an interview with one fetal surgeon (2 hours) and previous literature that specifically described operational guidelines, techniques and challenges of TTTS surgery [6-7], previously gathered by a number of fetal surgeons from two different hospitals. The scope of the analysis and interviews was to map the essential control elements (human & technological) of the TTTS procedure. Both HCS and unsafe control actions (see below) were based on the interviews. Engineers provided validation, whereas the surgeon complemented the engineers' HCS. The method follows the several steps of an STPA analysis, based on the three main principles of the STAMP causation model [2]: (i) safety is maintained by control constraints between human and technical controllers (system elements); (ii) the control constraints can be presented in a hierarchical structure with control & feedback loops between controllers of a work system (see Fig 1), and; (iii) automated/technical controllers have underlying mental models that can influence these control & feedback loops. From these steps emerges a functional representation of the work system. STPA subsequently produces a systematic analysis of how a set of previously defined system constraints can be violated. Any unsafe scenario can subsequently be identified and mitigated.

We applied these steps to the generic goals of fetoscopic surgery and produced a first generic hierarchical control structure (HCS) (Fig. 1). Such an HCS essentially maps the relations between human and technical system elements in terms of control action and feedback loops. Subsequently, we produced an HCS 2 (Fig. 2) where these generic controls and feedbacks are replaced by the physical actuators and sensors during current use of the fetoscope. Thirdly, during the interviews with the engineers suggestions for augmented actuator and sensor technologies were collected as topics for future design iterations to increase control and feedback accuracy in fetoscopic laser coagulation tasks. These were collected in HCS 3. Subsequently we analyzed (i) all unsafe control

actions generically defined by HCS 1; (ii) we subsequently assessed if HCS 2 meets the expected safety constraints, and (iii); if, by surgeon's expert knowledge, HCS 3 solutions are needed to increase mission success

## RESULTS

One part of the multi-step STPA approach is explained here for exemplary purposes. Figure 1 shows a small and simplified excerpt from HCS 1 with generic control actions for some activities performed during a fetoscopic laser coagulation surgery.

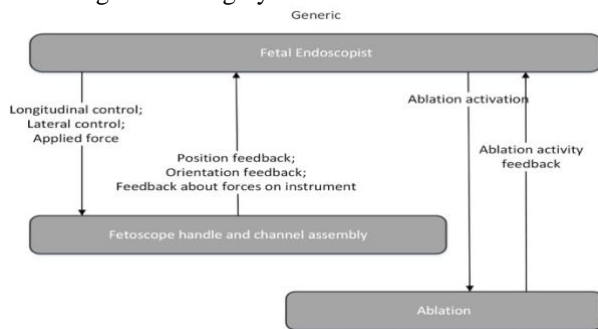


**Figure 1:** STAMP Hierarchical Control Structure - generic

This excerpt focuses on: (i) how the fetal endoscopist manipulates the fetoscope to reach the target by *applying longitudinal (zoom-in & out) and lateral control* with a certain degree of accuracy supported by corresponding feedbacks, such as *receiving position update from fetoscope tip*, and (ii) on *ablation activation and feedback*. In Figure 2, one can find an aggregated HCS 2+3: including the representation of the current actuators and sensors involved in a fetoscopic procedure (HCS 2, black), aggregated with future engineering solutions (HCS 3, red).

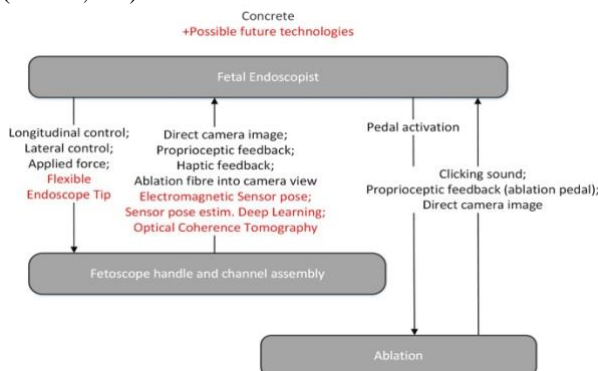


**Figure 2:** STAMP Hierarchical Control Structure – actuators and sensors

In figure 2, generic feedbacks from figure 1 like *position feedbacks* are now replaced by their physical equivalents such as *direct camera image*, *proprioceptive feedback*, and the like. Further STPA steps as described above were applied to look at how such controls can fulfill safety constraints in isolation and on systems level. The interviewed surgeon highlighted, from personal experience, that a TTTS with an anterior placenta provides the most challenging condition to reach the vascular equator with a correct laser fiber inclination, previously discussed in the literature [6-7]. Although

several techniques exist that take into account varying surgical practices, fetoscopic instruments and altered patient positions, surgeons are looking for technical improvement to treat the most extreme anterior placenta conditions [6-7]. Therefore, the generic control actions of longitudinal and lateral control (HCS1) are currently not met with the current instrumentation for all vascular equators in the case of an anterior placenta (HCS2). In STPA language this creates an unsafe control action. Because sufficient control is not provided to achieve mission success under all circumstances, the interviewed surgeon assigned the highest priority to the flexible fetoscope (HCS 3) engineering suggestion. Note that this specific design iteration produces systemic influences on other control actions in the HCS (not depicted here for space limitations). These include increased challenges for sterilizability of the fetoscope tip, transformation of coordination practice with the sonographer, unlearning old while acquiring new fetoscope manipulation skills, and the design of a contingency retraction mode to align fetoscope shaft and tip in case of emergency retraction.

## CONCLUSION AND DISCUSSION

Although we only presented one (highly prioritized) example from the STPA analysis, this result shows a system level constraint violation (being able to treat a maximal variety of vascular equator-placenta configurations) in the form of an unsafe control action. This can be addressed in future designs, but new systemic effects (both positive and negative) have been identified and need to be iteratively re-assessed to define new safety requirements (named control constraints in STPA). We believe that STPA as a safety analysis technique, in combination with WAD as a perspective for knowledge elicitation is a powerful combination for engineers as a design requirement and verification support to resolve remaining threats to patient safety and mission success.

## REFERENCE

- [1] Hollnagel, E., *Safety-I and Safety-II, The Past and Future of Safety Management*. 2014, Farnham, Surrey; Burlington, Vermont: Ashgate. 200.
- [2] Leveson, N.G., *Engineering a Safer World: Systems Thinking Applied to Safety*. 2011, Cambridge, Massachusetts; London, England: MIT Press.
- [3] Transfusion, Baschat, A. et al., *Twin-to-twin transfusion syndrome (TTTS)*. J Perinat Med, 2011. **39**(2): p. 107-12.
- [4] Patriarca, R., et al., *Systemic safety management in anesthesiological practices*. Safety Science, 2019. **120**: p. 850-864.
- [5] Pawlicki, T., et al., *Application of systems and control theory-based hazard analysis to radiation oncology*. Med Phys, 2016. **43**(3): p. 1514-30.
- [6] Deprest J., *Endoscopy in Fetal Medicine*. 2015, 3 ed.: Endo Press.
- [7] Van Der Veeke, L. et al., *Laser for twin-to-twin transfusion syndrome: a guide for endoscopic surgeons*. Facts, views & vision in ObGyn, 2019 **11**(3): p.197–205.

# ML Based Soft Capacitive E-skin Sensor for Soft Surgical Robots

Abu Bakar Dawood<sup>1</sup>, Hareesh Godaba<sup>2</sup>, Ahmad Ataka<sup>2</sup>, Kaspar Althoefer<sup>1,2</sup>

<sup>1</sup>*Centre of Advanced Robotics @ Queen Mary, School of Engineering and Material Sciences, Queen Mary University of London, E1 4NS, United Kingdom,*

<sup>2</sup>*Centre of Advanced Robotics @ Queen Mary, School of Electronics Engineering and Computer Science, Queen Mary University of London, E1 4NS, United Kingdom*  
*a.dawood@qmul.ac.uk*

## INTRODUCTION

Soft robots, when compared to conventional hard robots, because of their soft and compliant structure, have the advantage of being safe during Human-Robot Interaction (HRI). This property makes soft robots a better choice for Minimally Invasive Surgery (MIS), reducing the risk of damage when in contact with vital organs [1], [2]. On the other hand, soft robotics structures usually have an infinite number of degrees of freedom, making proprioception a challenging task. Apart from proprioception, a robot should also be able to physically interact with the environment in a meaningful way, making exteroception similarly important.

For exteroception and proprioception, resistive and capacitive sensing techniques have been applied individually [3]–[6]. Combinations of different sensing technologies have also been used for the detection of different stimuli [7]–[11]. However, the concept of multi-modality within one sensor skin is yet to be adequately explored. Recently there has been a great interest in using machine learning algorithms for proprioception and exteroception in soft robots [12], [13].

We present a silicone-based capacitive e-skin that can be integrated with the outside of a soft robot, enabling it to have a sense of its pose and to interact with the environment as well. The data collected from the skin is used to train a Machine Learning (ML) regression model to predict the applied global stretch and local indentation.

## MATERIALS AND METHODS

We fabricated the e-skin using Ecoflex 00-30. Our e-skin is made up of 4 silicone layers encapsulating 3 carbon grease terminal layers in between them. Fig. 1 shows an exploded view of the e-skin. The experimental setup for stretching was designed by attaching a SUNCOR stepper motor to an M8 lead screw. The clamps to hold the e-skin during stretching were 3D printed.

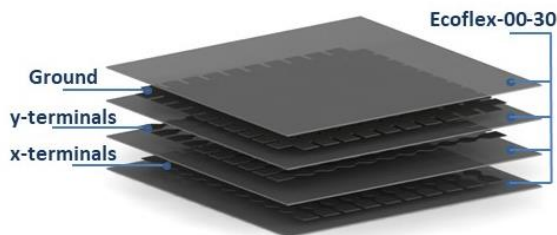


**Figure 1.** The e-skin. The x and y terminals are straight lanes, perpendicular to each other; the ground is another layer with a grid of perpendicular terminals.

To measure the capacitance of the skin, and integrated circuit CAV 424 was used. CAV 424 measures the capacitance and converts it to the voltage that is then read by an Arduino. CAV 424 was connected to the 10 x-terminals and 10 y-terminals through a couple of 16-1 multiplexers. The complete experimental setup is shown in Fig. 2.

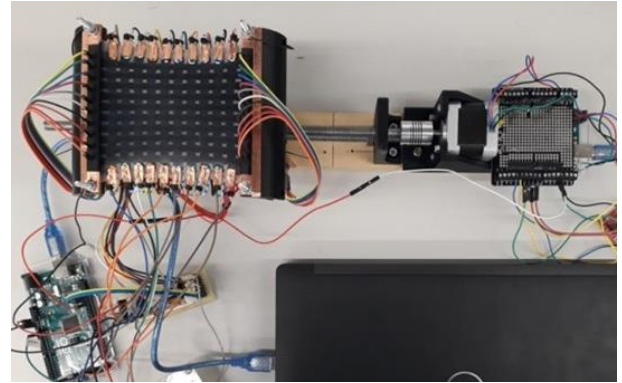


**Figure 2.** Shows the experimental setup for stretching the e-skin. Wires are connected from the e-skin terminals to the CAV 424 via multiplexers.

Data was collected by stretching the e-skin from stretch, i.e.  $\lambda=1$  to  $\lambda=1.2475$  with an increment of 5mm. A spherical indenter of 5mm diameter was 3D printed, and indentations of 5mm and 10mm at node (6,6) were applied for each stretch.

In work presented here, we train several machine learning algorithms to predict the indentation and the stretch corresponding to 20 input capacitance values. We collected 4 samples for all 15 states of different stretches and indentations. This data consisting of 60 samples, was used to train the machine learning algorithms. The data was stratified and split, resulting in 45/15 of 60 samples for training/testing. Linear Regression, K Neighbours Regressor and Linear SVR were trained using the training data. After training, predictions were made using the test data inputs, and these predictions were compared with actual outputs. To analyse the results, we calculated the Root Mean Squared Error and the Coefficient of Determination.

## RESULTS

The Root Mean Squared Error calculated for Linear Regression, K Neighbour Regressor, and Linear SVR methods are 0.3343, 3.5 and 5.11, respectively. The coeffi-



coefficient of determination for the above-mentioned algorithms were found to be 0.9789, 0.1915, and -1.2582. The plots of predicted stretch and indentation using linear regression on the test data are shown in Fig. 3 and 4.

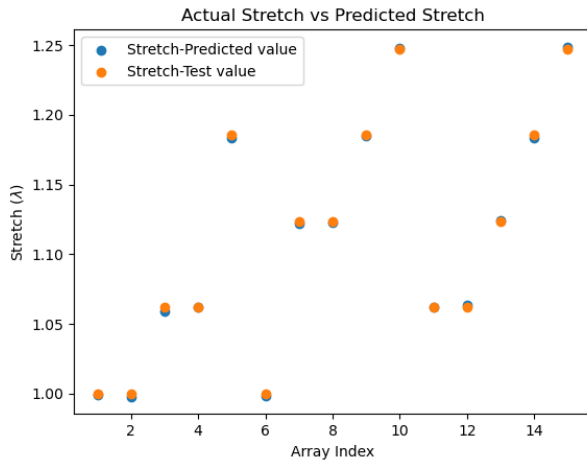


**Figure 3.** Shows the actual stretch from test data and the predicted stretch from the trained linear regression model.

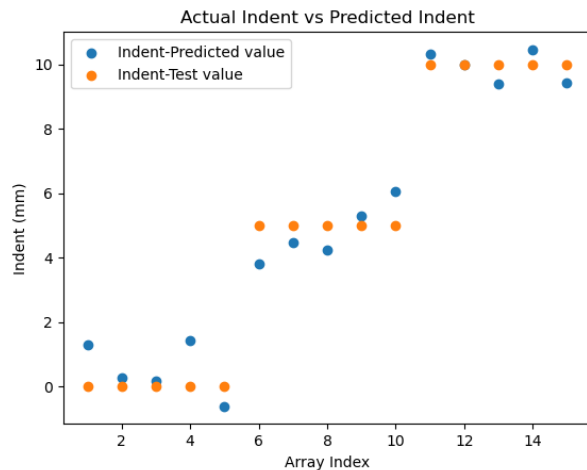


**Figure 4.** Shows the actual indent from test data and the predicted indent from the trained linear regression model.

## CONCLUSION AND DISCUSSION

We establish that machine learning techniques can be used to predict the global stretch as well as local indentation when applied simultaneously to a soft capacitive sensor skin. We were able to conclude that with the small data set we used; the linear regression model gives better results as compared to the other algorithms used. We can see in Fig. 3 that the predictions are accurate because capacitance and stretch are linearly related to each other [14]. Fig. 4 shows discrepancies in the actual and predicted values. The reason is that initially, capacitance changes linearly with indentation and then the curve saturates. The plot suggests that for indentation, we might have to employ a non-linear model for more accurate results. Our future work will explore enhancing the multimodality of capacitive e-skin by applying machine learning for predicting applied forces and localization of the force being applied in addition to the strains in the capacitive skin. Further, we will explore the use of our e-skin

in a soft robot tool, such as the STIFF-FLOP robot arm, for advanced interaction with soft tissue during MIS.

## REFERENCES

- [1] J. Fraś, J. Czarnowski, M. Maciaś, and J. Głowka, "Static modeling of multisection soft continuum manipulator for stiff-flop project," *Adv. Intell. Syst. Comput.*, 2014, doi: 10.1007/978-3-319-05353-0\_35.
- [2] M. Cianchetti *et al.*, "Soft Robotics Technologies to Address Shortcomings in Today's Minimally Invasive Surgery: The STIFF-FLOP Approach," *Soft Robot.*, 2014, doi: 10.1089/soro.2014.0001.
- [3] C. Larson *et al.*, "Highly stretchable electroluminescent skin for optical signaling and tactile sensing," *Science (80-. )*, 2016, doi: 10.1126/science.aac5082.
- [4] S. Y. Kim, S. Park, H. W. Park, D. H. Park, Y. Jeong, and D. H. Kim, "Highly Sensitive and Multimodal All-Carbon Skin Sensors Capable of Simultaneously Detecting Tactile and Biological Stimuli," *Adv. Mater.*, 2015, doi: 10.1002/adma.201501408.
- [5] J. Park *et al.*, "Giant tunneling piezoresistance of composite elastomers with interlocked microdome arrays for ultrasensitive and multimodal electronic skins," *ACS Nano*, 2014, doi: 10.1021/nn500441k.
- [6] T. Wang *et al.*, "A Self-Healable, Highly Stretchable, and Solution Processable Conductive Polymer Composite for Ultrasensitive Strain and Pressure Sensing," *Adv. Funct. Mater.*, 2018, doi: 10.1002/adfm.201705551.
- [7] D. H. Ho, Q. Sun, S. Y. Kim, J. T. Han, D. H. Kim, and J. H. Cho, "Stretchable and Multimodal All Graphene Electronic Skin," *Adv. Mater.*, 2016, doi: 10.1002/adma.201505739.
- [8] Q. Hua *et al.*, "Skin-inspired highly stretchable and conformable matrix networks for multifunctional sensing," *Nat. Commun.*, 2018, doi: 10.1038/s41467-017-02685-9.
- [9] P. Maiolino, M. Maggiali, G. Cannata, G. Metta, and L. Natale, "A flexible and robust large scale capacitive tactile system for robots," *IEEE Sens. J.*, 2013, doi: 10.1109/JSEN.2013.2258149.
- [10] V. Wall, G. Zoller, and O. Brock, "A method for sensorizing soft actuators and its application to the RBO hand 2," in *Proceedings - IEEE International Conference on Robotics and Automation*, 2017, doi: 10.1109/ICRA.2017.7989577.
- [11] M. Totaro, A. Mondini, A. Bellacicca, P. Milani, and L. Beccai, "Integrated Simultaneous Detection of Tactile and Bending Cues for Soft Robotics," *Soft Robot.*, 2017, doi: 10.1089/soro.2016.0049.
- [12] R. L. Truby, C. Della Santina, and D. Rus, "Distributed proprioception of 3d configuration in soft, sensorized robots via deep learning," *IEEE Robot. Autom. Lett.*, 2020, doi: 10.1109/LRA.2020.2976320.
- [13] T. G. Thuruthel, E. Falotico, F. Renda, and C. Laschi, "Model-Based Reinforcement Learning for Closed-Loop Dynamic Control of Soft Robotic Manipulators," *IEEE Trans. Robot.*, vol. 35, no. 1, pp. 127–134, 2019, doi: 10.1109/TRO.2018.2878318.
- [14] A. B. Dawood, H. Godaba, and K. Althoefer, "Modeling of a soft sensor for exteroception and proprioception in a pneumatically actuated soft robot," in *Lecture Notes in Computer Science (including subseries Lecture Notes in Artificial Intelligence and Lecture Notes in Bioinformatics)*, 2019, vol. 11650 LNAI, pp. 99–110, doi: 10.1007/978-3-030-25332-5\_9.

# Unscented Kalman filtering (UKF) with electrocardiogram (ECG) sensor fusion for heart state estimation and motion-compensation \*

Florian De Clercq<sup>1</sup>, Gianni Borghesan<sup>1,2</sup>, Wouter Oosterlinck<sup>3</sup>, and Emmanuel Vander Poorten<sup>1</sup>

<sup>1</sup>*Robot-Assisted Surgery Group, Department of Mechanical Engineering, KU Leuven, Belgium*

<sup>2</sup>*Core Lab ROB, Flanders Make, Belgium*

<sup>3</sup>*Department of Cardiovascular Sciences, UZ Leuven, Belgium*  
gianni.borghesan@kuleuven.be

## INTRODUCTION

Robust estimation and compensation of semi-periodic physiological movements play a key role in developments in the current robot-assisted surgery context as accurate motion tracking allows for more complex and less invasive procedures [1]. A particularly relevant case is the one where a robot-assisted bypass procedure of the heart (RACAB) is predominantly performed through keyholes with the exception of an incision the surgeon uses in order to stitch cardiac arteries. Motion-compensation contributes to rendering this incision obsolete as it would allow the surgeon to stitch through the robot (fig. 1).

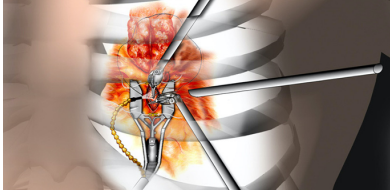


**Figure 1:** Thorax see-through during RACAB [2].

As opposed to the well-established strategies that exploit the periodicity of these motions, the possibility of the extraction of the electrocardiogram's (ECG) predictive information is rarely considered. As the ECG captures the same electrical heart activity that is responsible for muscle twitches and, in turn, the movement of the heart, a close physiological link between the two is in place. The ECG signal allows to anticipate changes of heart rate and anomalies such as skipped heart beats. In this work, a heart displacement model is used in combination with an unscented Kalman filter (UKF) to predict the heart motion. Principles of a strategy which aims to exploit the electrocardiogram (ECG) signal are then brought forward and embedded into the estimation procedure. After showing results of the system's validation, appropriate conclusions are drawn.

\*This work is part of the KUL C3 project BIOSERV

## HEART MODEL

In the considered scenario, the distance between a robotic instrument and the heart surface is measured in one dimension. By using a state estimator (the UKF) and leveraging the quasi-periodic nature of heart movement, it is possible to reduce the sensor noise and, most importantly, to predict the heart movement and regulate the robot accordingly. The UKF requires a model of the heart movement. This discrete-time dynamical model makes use of the fact that a periodic signal is decomposable into a sum of sines and a constant  $C$ . For the sake of clarity and without loss of generality, only two components are taken into account:

$$z_k = C_k + a_{1,k} \sin(\omega_k t + \phi_{1,k}) + a_{2,k} \sin(2\omega_k t + \phi_{2,k}) \quad (1)$$

Considering computational transparency, the time dependence is desirably implicit. The system update and measurement equations are therefore formulated as follows [3]:

$$\begin{bmatrix} C \\ a_1 \\ a_2 \\ \omega_0 \\ \theta_1 \\ \theta_2 \end{bmatrix}_{k+1} = \begin{bmatrix} 1 & 0 & 0 & 0 & 0 & 0 \\ 0 & 1 & 0 & 0 & 0 & 0 \\ 0 & 0 & 1 & 0 & 0 & 0 \\ 0 & 0 & 0 & 1 & 0 & 0 \\ 0 & 0 & 0 & \Delta t & 1 & 0 \\ 0 & 0 & 0 & 2\Delta t & 0 & 1 \end{bmatrix} \begin{bmatrix} C \\ a_1 \\ a_2 \\ \omega_0 \\ \theta_1 \\ \theta_2 \end{bmatrix}_k \quad (2)$$

$$z_k = C_k + a_{1,k} \sin \theta_{1,k} + a_{2,k} \sin \theta_{2,k} \quad (3)$$

## SENSOR FUSION

The filter compares the measured displacement  $\hat{z}_k$  with the predicted displacement  $z_k$  computed from the current state estimate  $\mathbf{x}_k$  through eq. (3). In order to take the ECG signal into account in the estimation, the UKF is expanded with a second output, a generated triangular pulse. A similar signal is composed making use of the measured ECG as follows.

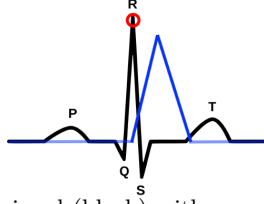


**Figure 2:** ECG signal (black) with generated pulse (blue). QRS peak detection is denoted by the red circle.

### Generated signal

The signal generated in association with the ECG curve is a triangular pulse train with pulse placement once every period. One of the most prominent characteristics of the ECG signal is used as reference mark: the peak in the QRS complex (fig. 2). Upon detection of this peak, a triangular pulse of fixed shape is generated. This large peak coincides with ventricular polarisation, a jump in the ventricular action potential. Subsequent depolarisation is in turn closely correlated with muscle twitch and concomitant heart movement. In short, the QRS complex designates upcoming heart movement. For simplicity, a constant time difference between ECG peak and heart movement peak of  $\Delta T_{\text{ecg,p}} = 400 \text{ ms}$  is assumed. As a result the peaks occur before the rising edges of the displacement, which is physiologically justifiable [4][5].

### Simulation

The UKF measurement noise covariance matrix contains two distinct parameters: the displacement and ECG signal noise variances. These are used to set the weight accredited to either signal. A heart displacement signal embodying process and measurement noise is generated along with its triangular pulses (see fig. 3). In a 3 s window the angular frequency increases by  $3 \text{ rad/s}$ . The resulting estimated heart rate is shown in fig. 4 (bottom) along with the real values and the conventionally estimated one without sensor fusion. When assimilation with the ECG signal finds place, the lagging estimation is updated towards a more accurate value. For this particular simulation involving non-negligible measurement noise, the resulting displacement and velocity estimations are respectively 35 and 50% better in terms of mean squared errors (MSE). The corresponding error signal for either estimation is also given by fig. 4 (top and middle respectively).

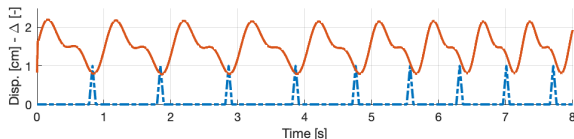


**Figure 3:** Generated displacement signal (full) with corresponding triangular pulses (dashed).

### DISCUSSION AND CONCLUSION

Because in this exemplary simulation only one association is made in every heart period, the estimated sig-

nal and the estimation errors tend to converge to the conventionally estimated ones after a while. This is a consequence of maintaining the introduced model which presumes a constant heart rate. More convergence towards the actual states can be achieved by recognising more parts of the signal through e.g. cross-correlation and making the impact of the individual elements of the generated signal smaller. I.e. by increasing the amount of elements (here triangles), decreasing their width and increasing the ECG signal measurement noise  $r_{0,\text{ECG}}$ . The generated triangular pulses spread out discrete-time information – the location of the next peak – over a range of time steps. This strategy therefore introduces a larger error with increasing pulse width which consequently manifests itself in a trade-off between suppressing this error and accreditation of the ECG information. The trade-off is tuned by  $r_{0,\text{ECG}}$  and the pulse shape. For signals with rapidly varying heart rates, narrow pulses are desired. In conclusion: the detection of a characteristic shape in the ECG signal along with a physiological assumption allow for predictive information to be used to increase UKF estimation accuracy. These findings suggest that future developments involve a more scrupulous ECG-displacement model with the aim of engendering a more continuous impact of the ECG measurement.

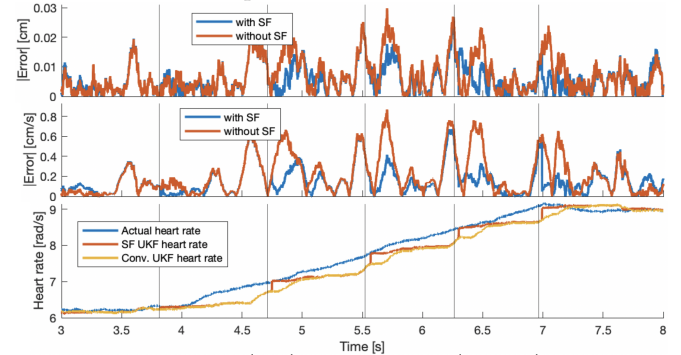


**Figure 4:** Position (top) and velocity (middle) errors between real and estimated values along with their heart rates (bottom). The conventionally estimated heart rates (yellow) are plotted against the ones obtained through sensor fusion (red) with the QRS peak times (grey vertical).

### REFERENCES

- [1] W. Gong et al., “Robot-assisted coronary artery bypass grafting improves short- term outcomes compared with minimally invasive direct coronary artery bypass grafting,” *Journal of Thoracic Disease*, pp. 459–468, 2016.
- [2] Intuitive Surgical Inc., *Copyright protected*.
- [3] S. Yuen et al., “Robotic motion compensation for beating heart intracardiac surgery,” *The International Journal of Robotics Research*, pp. 1355–1372, 2009.
- [4] T. Watanabe et al., “Ventricular action potentials, ventricular extracellular potentials, and the ecg of guinea pig,” *Circulation Research*, vol. 57, no. 3, pp. 362–373, 1985.
- [5] O. Bebek et al., “Intelligent control algorithms for robotic-assisted beating heart surgery,” *IEEE Transactions on Robotics*, pp. 468–480, 2007.

# Preliminary Analysis of Learning a Robot-Assisted Surgical Pattern-Cutting

Yarden Sharon<sup>1</sup>, Daniel Naftalovich<sup>2</sup>, Lidor Bahar<sup>1</sup>, Hanna Kossowsky<sup>1</sup>, Yael Refaely<sup>3</sup>, and Ilana Nisky<sup>1</sup>

<sup>1</sup>Department of Biomedical Engineering, Ben-Gurion University of the Negev, Israel

<sup>2</sup>Department of Computational & Mathematical Sciences, California Institute of Technology, USA, and Keck School of Medicine of USC, University of Southern California, USA

<sup>3</sup>Thoracic Surgery Unit, Soroka Medical Center, Israel

shayar@post.bgu.ac.il

## INTRODUCTION

Teleoperated robot-assisted minimally invasive surgery (RAMIS) is growing in popularity, but it is not clear how it is best to train robotic surgeons. Motor learning theories define *skill acquisition* either as an improvement in performance relative to previous performance levels or as the acquisition of completely novel abilities [1]. An important indicator of skill acquisition is an improvement in the speed-accuracy trade-off [2]. Another form of learning is *adaptation*, in which participants improve their performance in response to altered conditions, such as perturbing forces [1]. Different processes enable motor learning. For example, in error-based learning, the sensorimotor system estimates the gradient of the error between the desired outcome of a movement and the actual outcome. This error is then used in the tuning of motor commands in the following movement [3].

Recent findings in motor learning propose methods to affect learning that may be used to improve surgical skill acquisition. However, extrapolating simple adaptation mechanisms to the acquisition of surgical skill is not trivial. Therefore, we first need to deepen our understanding of human motor control in complex surgical tasks.

In this study we investigated how participants learned to perform a robotic surgical pattern-cutting task, and how external force perturbations affected their learning. In our experiment, the participants cut circles drawn on gauze, and were exposed to perturbations that pushed their hand in the radial direction. Since the desired path in this task was the drawn circle, such perturbations increased the error between the desired movement and the actual movement. We hypothesized that the motor system would adjust motor commands and reduce error [3]. This may result in greater improvements in performance by participants who trained with the perturbations, compared to those who trained without them.

## MATERIALS AND METHODS

The participants in this study performed a surgical pattern-cutting task using the da Vinci Research Kit (dVRK). The participants used their right hand to control curved scissors and cut a 5cm diameter circle drawn on a non-woven gauze (Fig. 1(a)).

As a first step towards understanding the effect of perturbing forces on the hand, we applied force

perturbations using the right Master Tool Manipulator (MTM), such that a planar radial force was applied on the participant's hand (Fig. 1(b)-(c)) – away from the center of the circle and toward the center, alternately:

$$(1) \vec{f}_M = A \left[ \frac{x_p}{\sqrt{x_p^2 + y_p^2}}, \frac{y_p}{\sqrt{x_p^2 + y_p^2}}, 0 \right],$$

where  $x_p$  and  $y_p$  are the x and y coordinates of the tip of the right Patient Side Manipulator (PSM), relative to the center of the circle, and A is the amplitude of the force.

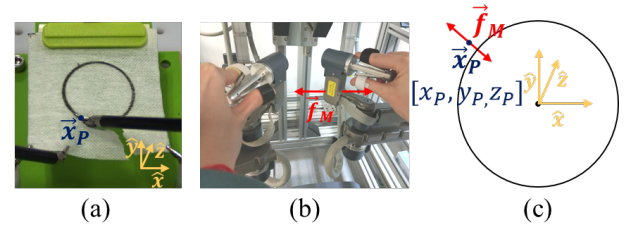


**Fig. 1** The pattern-cutting task. (a) The task board and the two PSM tools (right – curved scissors, left – large needle driver). (b) The MTMs. (c) The circle; the position of the right PSM's tip,  $\vec{x}_p$  (blue); the force applied on the participant's hand,  $\vec{f}_M$  (red); and the base reference frame (yellow).

The participants were divided into two groups: (1) 1Hz periodic perturbations, and (2) control – no perturbations. Each participant performed 24 consecutive trials:

- **Baseline (one trial – identical for both groups):** no perturbations –  $A = 0$ .
- **Training (20 trials):** force perturbations according to the condition group –  $A = \sin(2\pi t)$  for the 1Hz group, and  $A = 0$  for the control group.
- **Post training (3 trials – identical for both groups):** one trial without perturbations, one trial with 1Hz periodic perturbations, and one trial with nonspecific perturbations ( $A = \frac{\sum_1^5 \sin(2\pi f t)}{\sqrt{5}}$ ;  $f \sim U[0.3\text{Hz}, 1\text{Hz}]$ ).

The last two trials of the experiment were included to allow us to test the effect of training on the resistance to perturbations, but we will not elaborate on this point in this abstract. Here we present a preliminary analysis of the first 22 trials of 10 participants (five per group) using two basic metrics: task time and total error. The task time is the time elapsed between the initial contact of one of the tools with the gauze, and the moment the circle was completely removed from the gauze. To calculate the total error, we scanned the cut circles and used a custom-written image processing algorithm (MATLAB) to detect



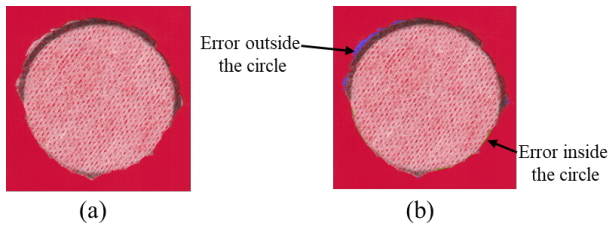


**Fig. 2** Example of total error calculation. (a) The cut circle. (b) The circle with marked error areas.

the error areas (Fig. 2). These are areas in which the cutting was not on the line (outside or inside the circle). The algorithm then counted the number of pixels in these areas.

## RESULTS

Fig. 3 shows the scissors' path when the participant cut the circle. The deviations from the circle in Fig. 3(b) are more prominent than those in Fig. 3(a), showing that the perturbations affect the scissors' path.

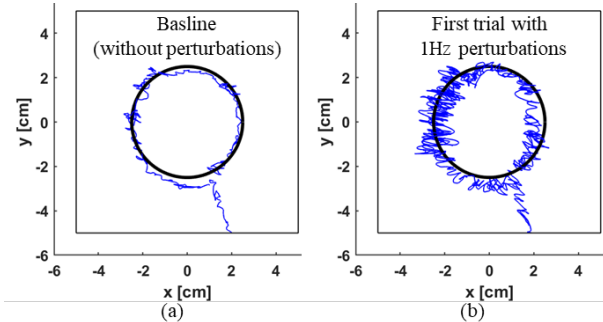


**Fig. 3** Examples of the recorded position of the scissors. (a) a baseline trial – without perturbations, and (b) the same participant's first training trial with 1Hz perturbations.

Fig. 4 shows the total time as a function of total error of the participants in the control (a) and the 1Hz (b) groups. Lower values represent smaller errors and shorter completion times and hence better performances. The trends of the dashed lines, drawn between trials 1 (baseline) and 22 (first post training), are towards the lower left corner in both graphs. This indicates that the participants in both groups improved their performance.

## DISCUSSION AND CONCLUSIONS

We showed a preliminary analysis of 10 participants. Due to the large variability between the participants, our current data are not sufficient for statistical testing whether participants who trained with the perturbations had a greater improvement. However, we learned important lessons about the protocol. For example, some of the metrics varied a lot between trials, and therefore one baseline or post-training trial is not sufficient. Our analysis highlights the different improvement paths in the time-error space – participants improved in what they had difficulty with. Participants who started with long task times improved the task time during training (Subject 5). Participants who started with both large errors and long task times improved in both (Subject 6). Another important result is the improvement of participants in the 1Hz group. Previous studies showed

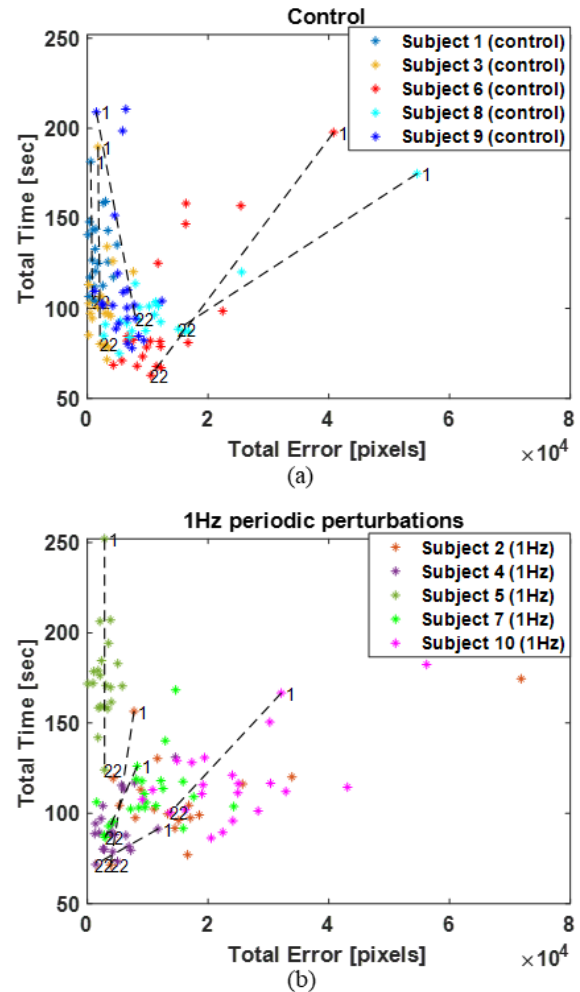


**Fig. 4** Total time vs. total error. The markers show the total time vs. the total error in each of the trials, each color represents a participant. We drew a dashed line between trial 1 (baseline) and trial 22 (first post training trial –without perturbations). (a) Control group. (b) 1Hz periodic perturbations group.

that participants do not adapt to time varying perturbations [4]. Although the motor system of participants in the 1Hz group may not adapt to the periodic perturbation, they did develop strategies to deal with it and to learn how to perform the task better. We are currently working on additional analyses that will shed light on the processes that enabled this learning.

## REFERENCES

- [1] J. W. Krakauer and P. Mazzoni, "Human sensorimotor learning: adaptation, skill, and beyond," *Current opinion in neurobiology*, vol. 21, no. 4, pp. 636–644, 2011.
- [2] J. Reis *et al.*, "Noninvasive cortical stimulation enhances motor skill acquisition over multiple days through an effect on consolidation," *Proceedings of the National Academy of Sciences*, vol. 106, no. 5, pp. 1590–1595, 2009.
- [3] D. M. Wolpert, J. Diedrichsen, and J. R. Flanagan, "Principles of sensorimotor learning," *Nature Reviews Neuroscience*, vol. 12, no. 12, pp. 739–751, 2011.
- [4] A. Karniel and F. Mussa-Ivaldi, "Sequence, time, or state representation: How does the motor control system adapt to variable environments?," *Biological cybernetics*, vol. 89, pp. 10–21, 2003.

# Bitrack: a friendly four arms robot for laparoscopic surgery

Josep Amat<sup>1,2</sup>, Alicia Casals<sup>1,2</sup> and Manel Frigola<sup>1,2</sup>

<sup>1</sup>Universitat Politècnica de Catalunya (UPC), <sup>2</sup>RobSurgical Systems SL (RSS)

alicia.casals@upc.edu

## INTRODUCTION

For years, robotic laparoscopic surgery has motivated research and initiatives with the development of robotic systems offering different kind of solutions, being Bitrack a new option. At present the market is dominated by DaVinci, which has become a benchmark in this speciality. Laparoscopic robots offer precision and accessibility since their instruments are endowed with 3 DoF, for their orientation, which are missing in standard laparoscopy. This paper presents the Bitrack system, which is a new laparoscopic surgical robot, designed at UPC, and currently undergoing the process of certification by a spin-off created for its exploitation, RSS. This new robot aims to obtain the same benefits and accuracy as the current benchmark but overcoming some dependencies that current robotic surgery poses. Many reports on studies that evaluate the contribution of robotics do not doubt on the improvements achieved with the use of robots in what refers to surgical quality and that more complex surgeries can be addressed than those performed by laparoscopy [1, 2]. The Bitrack system apart from these clear contributions of robotics also provides the concept of hybrid surgery. This concept implies the capability of performing an intervention alternating standard laparoscopy with other robot assisted phases according to the needs in each stage of the procedure. This performance has been achieved thanks to the Bitrack friendly design which allows a quick interchange of robotized instruments by their manual counterparts, less than a minute each, using the same conventional trocar. This paper presents the robot architecture and the experimental results achieved with the operational prototype.

## ARCHITECTURE

Bitrack has been conceived aiming to achieve an easy and quick set-up by providing just the minimum redundancy necessary to avoid collisions between the four arms, fig.1. Redundancy and collaborative control are necessary for and interactive human-robot system [3]. However, a high degree of redundancy generates a too high redundant number of configurations. The challenge has been defining a kinematic architecture that optimizes the compromise between collision avoidance and intuitiveness in the manual guidance along the setting-up of the operational work space. Being the set-up a manual operation, that is, the insertion of the four surgical instruments into the corresponding trocars by means of gestural movements made by the medical staff, this operation should be as easy and friendly as possible. A redundant degree of freedom implies unidimensional pose alternatives, which is intuitive for a human. More degrees of redundancy

involve a movement with higher dimensional pose alternatives, but not so evident for manual operation. The Bitrack system, fig.1, consists of a four-arms robot mounted on a column, which is provided with a vertical linear DoF. Each arm can pivot around the column independently from the others. The arms, with two different architectures are placed respectively in two levels.



Fig.1. The Bitrack system

All the arms operate with an elbow outside configuration, but the two upper arms have a SCARA type architecture to avoid interferences with those below. These two architectures are conceived to be able to operate in a quasi-coincident work space minimizing interference between the four arms. The upper arms can operate internally or externally with respect to the lower arms and can be used indistinctly for camera guidance or as auxiliary arm. The lower arms are the operational ones. Fig.2 show the kinematics of the two types of arms.

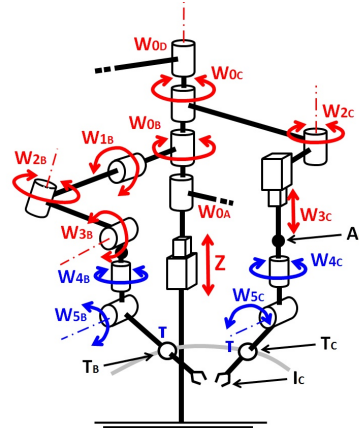
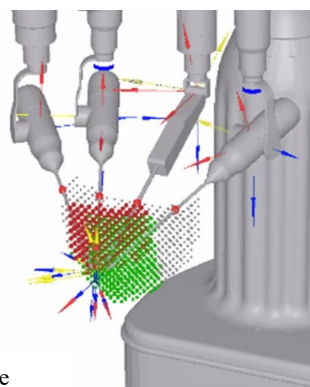


Figure. 2. Kinematics with indication of the DoF of the two kind of arms (B and C)

The DoF of the lower arms are three rotations:  $W_0$  around the column axis and  $W_1$  and  $W_2$  which allow the wrist  $A(x_A, y_A, z_A)$  to reach any position in the working space.  $W_3$ , the fourth joint adds a degree of redundancy allows reaching the target position in different orientations and thus optimize the shared workspace by shifting the other joints conveniently. The wrist supports the instrument (I), which movement is restricted as it pivots over the trocar

$T(x_T, y_T, z_T)$ . Once in the target position,  $W_4$  and  $W_5$  provide the orientation compatible with the trocar. The difficulty to control the coordinates of the instrument tip  $I(x_I, y_I, z_I)$  compatible with the intermediate point  $T$ , the trocar, requires knowing its position. DaVinci solves this problem by subjecting the trocar with active joints. Doing this way, the trocar keeps steady all along the intervention and thus not posing a problem to the kinematics computation. In the Bitrack system, to ensure its continuous adaptation to the patient and transient variations in gas pressure in the abdominal cavity and at the same time facilitate the set-up, these two DoF are passive and therefore they do not force the movement of the operator who can smoothly insert the instrument. By freeing the trocar, its position becomes a variable, but the Bitrack system continuously computes its position with enough precision. The free movement of the trocar with respect to the arm, although requiring its computation to control teleoperation, avoids strains on the abdominal surface that can produce bruising and also gas leaks during the procedure. In addition, the Bitrack architecture enables the use of conventional trocars and thus the possibility of changing from robotic surgery to standard laparoscopy at any time during an intervention. The architecture of the upper arms, also shown in fig. 2, has no redundancy and joint  $W_3$  is changed from angular to linear, a vertical displacement to minimize volume occupancy. The lower arms, with redundancy, are those that avoid collision with the upper ones. A simulation of this architecture, Fig. 3, has allowed modelling the working volume that show an accessibility for each instrument of about a 35x45x55 cm spheroid.



**Figure 3.** Working volume

## RESULTS AND DISCUSSION

With this architecture, the Bitrack system becomes very versatile and offers an easy set-up process having reduced as much as possible the redundancies that avoid collisions. Instead of the multiple redundant DoFs of DaVinci, which provide more configurations free of collision in broader spaces, Bitrack has only one redundant DoF for each lower arm, in addition to the common DoF for the Z movement of the column that supports the four arms. However, in the set-up, when the surgeon or medical staff should take decisions on movements dealing with redundancy of the arms, the additional DoFs of redundancy increase the time to reach an acceptable arms configuration and without

guaranteeing reaching an optimal solution. The Bitrack architecture simplification thus results in a shorter set-up time, but also in a smaller occupancy in the O.R, less weight and less cost. From the long evaluation phase in the experimental operating room, with animal models (mini pigs), the insertion and retrieval of instruments has been of 1,6 minutes in average (considering that some of them didn't have previous experience with Bitrack) in front of the 20 minutes that can be achieved with the Da Vinci Xi model after a training course. The quick interchange of instruments, together with the more reduced space occupancy in the OR makes the combination of robot and manual surgery feasible. This hybrid surgery allows a significant reduction in intervention time as many surgical tasks that do not require robot performance are executed quicker manually. Thus, the main contribution of Bitrack is not improving efficacy, since precision is not the problem in surgical robotics, but efficiency, understood as a balance between value and cost.

The architecture with multiple arms on a unique column has been chosen in front of other solutions as, Titan or CMR with configuration one column - one arm, since it is a more compact solution that occupies less space in the O.R. when four arms are needed.

The Bitrack system has been extensively tested in the experimental operating room Fig 4, in renal, hepatic and gynaecologic surgeries, as well as other less frequent surgeries that surgeons wanted to test, achieving a considerable reduction in operation time compared to fully robotic surgery.



**Figure 4.** The operational Bitrack system performing a surgery in the experimental Operating Theater.

## REFERENCES

- [1] Sally K. Longmore, Ganesh Naik and Gaetano D. Gargiulo, Laparoscopic Robotic Surgery: Current Perspective and Future Directions, Robotics, Vol 9, Issue 2, 2020
- [2] Alicia Casals, Albert Hernansanz, Narcís Sayols and Josep Amat, Assistance Strategies for robotized laparoscopy Robot 2019: Fourth Iberian Conference, Springer
- [3] Hang Su, Chenguang Yang, Giancarlo Ferrigno, and Elena De Momi. Improved Human-Robot Collaborative Control of Redundant Robot for Teleoperated Minimally Invasive Surgery, IEEE Robotics and Automation Letters, Vol 4, N 2, April 2019

## CRAS 2020 Support



UNIVERSITAT POLITÈCNICA  
DE CATALUNYA  
BARCELONATECH



ISTITUTO  
ITALIANO DI  
TECNOLOGIA



UNIVERSITÀ  
di **VERONA**  
Dipartimento  
di **INFORMATICA**



UNIVERSITÀ DEGLI STUDI DI NAPOLI  
**FEDERICO II**



# CRAS

Conference on Computer/Robot Assisted Surgery



# CRAS 2020

Proceedings of the 10<sup>th</sup> Conference on  
New Technologies for Computer/Robot Assisted Surgery

---